

NEURAL NETWORKS FOR ESTIMATING THE CERAMIC PRODUCTIVITY OF WALLS

Assist. Prof.: Dr. Sawsan Rasheed Mohammed
University of Baghdad
College of Engineering
Department of Civil Engineering

Ali Sabri Tofan
University of Baghdad
College of Engineering
Department of Civil Engineering

ABSTRACT

Productivity estimating of a construction operation is an essential tool for the successful completion of the construction process. Productivity of a construction operation is defined as output of the system per unit of time.

In this research Artificial Neural Networks approaches are presented. The main reason for using neural networks for construction productivity estimation is the requirement of performing complex mapping of environment and management factors to productivity.

A generic description of the artificial neural networks model is provided, followed by summarized factors that affect ceramic labor productivity, then neural-network model are developed for Estimating ceramic walls productivity, the input data for the model based on experienced superintendents employed by a leading construction general contractor, test results show that the ANN approach can produce a sufficiently accurate estimate with a limited data-collection effort, and thus has the potential to provide an efficient tool for construction productivity estimation.

الخلاصة

تخمين الإنتاجية لعملية البناء هي وسيلة أساسية من أجل النجاح في إتمام عملية البناء و تعرف إنتاجية البناء على انها ناتج النظام لكل وحدة من الوقت. في هذا البحث استخدمت الشبكات العصبية الاصطناعية. السبب الرئيسي لاستخدام الشبكات العصبية لتقدير إنتاجية البناء هو متطلبات رسم الخرائط المعقدة للبيئة و عوامل ادارة الانتاجية.

وضع وصف عام لنموذج الشبكات العصبية الاصطناعية ، يليها تلخيص العوامل التي تؤثر على إنتاجية عمال السيراميك ، ثم طور نموذج من الشبكات العصبية المتقدمة لتخمين إنتاجية السيراميك للجدران ، والبيانات المدخلة للنموذج اعتمدت على المراقبين ذوي الخبرة و الموظفين من قبل المقاول العام للانشاء ، تشير نتائج الاختبار الى أن الشبكات العصبية الاصطناعية يمكن ان تؤدي إلى تخمينات دقيقة بما فيه الكفاية مع جهود جمع بيانات محدودة ، وبالتالي فإن الاختبار لديه القدرة على توفير أداة فعالة لتخمين إنتاجية البناء.

KEYWORDS: NEURAL, NETWORKS, ESTIMATING, CERAMIC, PRODUCTIVITY, WALLS

INTRODUCTION

Estimating is an essential tool for successful completion of a construction process. The process for a construction activity can be broadly divided into the direct costs and the indirect costs plus contingency and profit. The direct costs include costs for materials, labors and equipment. The direct costs are reached when combining the quantitative finite factors to the qualitative subjective factors in the estimating process. The quantitative factors include unit prices of materials, labor wages and equipment depreciation. The qualitative subjective factors are more difficult to determine. They include, among others, productivity rates and associated construction risks. (*Gould 2002*)

Experienced estimators rely on their personal expertise to incorporate the effect of qualitative factors in their estimate. Less experienced estimators could benefit from tools that would incorporate such effects. Neural networks are tools that attempt to mimic the human brain functions. Like the brain, neural networks learn from past trails. They attempt to generalize on the data provided.

OBJECTIVES

The main objective of this research is to introduce alternative approach of using neural network for estimating productivity of ceramic. This objective is to be justified through the following procedures:

- a- gathering background information by reviewing the previous studies related on the estimating the productivity of project activities techniques.
- b- adjust the factors that affect the productivity rates of ceramic activities and there data gathering.
- c- developing neural network model capable of predicting the productivity rates of ceramic for walls.

PRODUCTIVITY

One of the most contentious areas in construction claims is the calculation or estimation of lost productivity. Unlike direct costs, lost productivity is often not tracked or cannot be discerned separately and

contemporaneously. As a result, both causation and entitlement concerning the recovery of lost productivity are difficult to establish. Compounding these situations, there is no uniform agreement within the construction industry as to a preferred methodology of calculating lost productivity. There are, in fact, numerous ways to calculate lost productivity. Many methods of calculation are open to challenge with respect to validity and applicability to particular cases -- thus making settlement of the issue on a particular project problematic. (*CII 1984*)

“Productivity is measured generally by the output per hour of input. (*Kavanaugh 1978*)

PRODUCTIVITY AND PRODUCTION

All too often in construction, the terms “productivity” and “production” are used interchangeably. This is, however, incorrect. Production is the measure of output (i.e., things produced) whereas productivity is the measurement of the production. The following two formulas can be used to calculate these two terms.

$$\begin{aligned} \text{Productivity} &= \text{Output (units completed)} / \\ &\text{Input (work or equipment hours)} \\ \text{Productivity Factor} &= \text{Actual} \\ &\text{Productivity} / \text{Baseline or Planned Productivity} \end{aligned}$$

Given this set of operating terms, it is therefore possible for a contractor to achieve 100% of its planned production but not achieve its planned productivity. That is, a contractor could well be accomplishing the planned rate of production of 300 linear feet of pipe/day in the ground but be expending twice the amount of labor planned to accomplish this daily production rate, for example. In this case, the contractor would be accomplishing 100% of planned production but operating at 50% productivity. (*AACE 2004*)

THE FACTORS THAT AFFECT THE PRODUCTIVITY

Mukherjee and sing (1975) classified these factors into two groups which are:

- External factors that we cannot control them.
- Internal factors that we can control them.

Prokopenko (1987) classified these factors into three groups:

- Work related factors.
- Input or resource related factors.
- Boundary related factors.

Burnham (1982) made the best classification which classified into four levels:

- a- State level that contains:
 - 1- Human recourses as general education level, work motivation systems, work circumstances cooperation in the decision making, age and experience of the laborers.
 - 2- Technology and the activities researchers and development.
 - 3- Instruction and the laws of work.
- b- Sectors level that contains:
 - Product design and quantity engineering application.
 - Machine and equipment usage.
 - Training and development.
 - Production volume for each person.
- c- Work quality level.
- d- Man power level.

PERFORMANCE

The word performance contains two related concepts they are:

- Performance is the results that individual can achieve in work.
- Performance is all that individual do to affect the work results. (*Lefton 1982*)

Which means that the performance is continues operation the action refers to the inputs and the results are the outputs. (*Feldman 1983*)

On the other hand Bain (1982) found another definition for (performance) as mathematic equality as the following:

- Performance = skill + motivation
- Skill = training + experience
- Motivation = attitude + environment

The last mentioned definition is so important, that we have the two performance's elements (skill + motivation) to get a particular performance level, so at any level there is no copasity to compensate the lake of skill by increasing motivation or the reverse.

Scientifically, it can't put a maximum level for the motivation but it is possible to find maximum man capability according to the indicators of mantel and physical nature of human body.

ARTIFICIAL NEURAL NETWORKS

Over the past two decades there has been an increased interest in a new class of computational intelligence systems known as Artificial Neural Networks (ANNs). This type of networks (i.e. ANNs) has been found to be powerful and versatile computational tools for organizing and correlating information in ways that have proved to be useful for solving certain types of problems which are too complex to understand, too poorly to analyze, or too resource-intensive to tackle using more traditional computational methods.

ANNs have been successfully used for many tasks including pattern recognition, function approximation, optimization, forecasting, data retrieval, and automatic control. As ANNs can be useful complement to more traditional numerical and statistical methods, their use merits continued investigation. (*TRB, 1999*)

ARTIFICIAL NEURAL NETWORK STRUCTURE AND OPERATION:

A typical structure of ANNs consists of a number of artificial neurons variously known as processing elements (PEs), or nodes, or units that are usually arranged in layers: an input layer, an output layer and one or more intermediate layers called hidden layers.

The input from each (PE) in the previous layer (x_i) is multiplied by an adjustable connection weight (w_{ij}) at each PE, the weighted input signals are summed, and a threshold value (θ_j) may be added. This combined input (I_j) is then passed through a transfer (activation) function ($f(.)$) to produce the output of the PE (y_j). The output of one PE provides the input to the PEs in the next layer. This process is summarized in equations:

$$I_j = \sum w_{ij}x_i + \theta_j \quad (1)$$

Summation

$$y_j = f(I_j) \quad (2)$$

transfer

Where

I_j = the activation level of node j;

W_{ij} = the connection weight between nodes i and j ;
 x_i = the input from node i , $i = 0, 1, \dots, n$;
 θ_j = the bias or threshold for node j ;
 y_j = the output of node j ; and
 $f(.)$ = the transfer (activation) function

The propagation of information in ANNs starts at the input layer where the input data are presented. The network adjusts its weights on the presentation of a training data set and uses a learning rule to find a set of weights that will produce the input/output mapping that has the smallest possible error. This process is called 'learning' or 'training'. Once the training phase of the model has been successfully accomplished, the performance of the trained model has to be validated using an independent testing set.

As described above, ANNs learn from data examples presented to them and use these data to adjust their weights in an attempt to capture the relationship between the model input variables and the corresponding outputs. Consequently, ANNs do not need any prior knowledge about the nature of the relationship between the input/output variables, which is one of the benefits that ANNs as compared with most empirical statistical methods. (*Shahin 2003*)

TRANSFER (ACTIVATION) FUNCTIONS

Transfer functions can take a variety of forms. The logistic sigmoid and hyperbolic tangent transfer functions are the most common functions in neural networks. The logistic sigmoid function is usually used when the desired range of output values is between 0 and 1, whereas the hyperbolic tangent function is often used when the desired range of output values is between -1 and 1. The logistic sigmoid and hyperbolic tangent transfer functions are shown in figure and equations, respectively. Usually, the same transfer function is used for all processing elements in a particular layer. (*Shahin 2003*)

$$f(I_j) = \frac{1}{1 + e^{-(I_j)}} \quad (3)$$

$$f(I_j) = \frac{e^{(I_j)} - e^{-(I_j)}}{e^{(I_j)} + e^{-(I_j)}} \quad (4)$$

TYPES OF NEURAL NETWORKS:

FEED-FORWARD NEURAL NETWORK:

The feedforward neural network was the first and arguably simplest type of artificial neural network devised. In this network, the information moves in only one direction, forward, from the input nodes, through the hidden nodes (if any) and to the output nodes. There are no cycles or loops in the network. (*Roman 2009*)

RADIAL BASIS FUNCTION (RBF) NETWORK:

Radial Basis Functions are powerful techniques for interpolation in multidimensional space. A RBF is a function which has built into a distance criterion with respect to a centre. Radial basis functions have been applied in the area of neural networks where they may be used as a replacement for the sigmoid hidden layer transfer characteristic in Multi-Layer Perceptions. RBF networks have two layers of processing: In the first, input is mapped onto each RBF in the 'hidden' layer. The RBF chosen is usually a Gaussian. In regression problems the output layer is then a linear combination of hidden layer values representing mean predicted output. The interpretation of this output layer value is the same as a regression model in statistics. In classification problems the output layer is typically a sigmoid function of a linear combination of hidden layer values, representing a posterior probability. Performance in both cases is often improved by shrinkage techniques, known as ridge regression in classical statistics and known to correspond to a prior belief in small parameter values (and therefore smooth output functions) in a Bayesian framework. (*Roman 2009*)

KOHONEN SELEF – ORGANIZING NETWORK:

The self-organizing map (SOM) invented by Teuvo Kohonen performs a form of unsupervised learning. A set of artificial neurons learn to map points in an input space to coordinates in an output space. The input space can have different dimensions and topology from the output space, and the SOM will attempt to preserve these. (*Roman 2009*)

RECURRENT NETWORK:

Contrary to feed forward networks, recurrent neural networks (RNs) are models with bi-directional data flow. While a feed forward network propagates data linearly from input to output, RNs also propagate data from later processing stages to earlier stages, there are many types of recurrent network, and these types are: (Roman 2009)

- **Simple recurrent network:**
- **Hopfield network:**
- **Echo state network:**
- **Long short term memory network:**

STOCHASTIC NEURAL NETWORKS:

A stochastic neural network differs from a typical neural network because it introduces random variations into the network. In a probabilistic view of neural networks, such random variations can be viewed as a form of statistical sampling, such as Monte Carlo simulation, Boltzman machine. (Roman 2009)

MODULAR NEURAL NETWORK:

Biological studies have shown that the human brain functions not as a single massive network, but as a collection of small networks. This realization gave birth to the concept of modular neural networks

NEURO – FUZZY NETWORKS:

A neuro-fuzzy network is a fuzzy inference system in the body of an artificial neural network. Depending on the *FIS* type, there are several layers that simulate the processes involved in a *fuzzy inference* like fuzzification, inference, aggregation and defuzzification. Embedding an *FIS* in a general structure of an *ANN* has the benefit of using available *ANN* training methods to find the parameters of a fuzzy system. (Roman 2009)

IDENTIFICATION OF ANN MODEL VARIABLES

The neural network application for ceramic productivity estimation is *an* example of causal forecasting. This type of forecasting considers a number *of* variables that affect the variable to be predicted. This type of forecasting is more powerful than the traditional methods. The purpose of productivity estimation is to predict or estimate the productivity from known or assumed values of other variables related to it. One of the most important tasks of this objective is to determine

which variables are important indicators. Once the appropriate variables have been determined, the productivity estimation can be performed either using a neural network or any other tool, such as regression analysis.

This research describes the development of neural network models of ceramic activity productivity based on current projects data. The initial impetus for the research was the paucity of data available that can provide reliable information about the *productivity*. The data collection method used in this study is the direct data gathering from projects and the direct interview with the concerned engineers and foremen. This method faces a great difficulty nowadays because of the unsecured status of the country, and the shortage in projects.

Independent variables were carefully selected and well defined as follows:

- V1 Ganger experience.
- V2 Ganger age.
- V3 Number of assistant laborers.
- V4 Area of ceramic tile.
- V5 Site complication.
- V6 Height level of the work.
- V7 Climate status (Weather).

MODEL INPUTS AND OUTPUTS

It is generally accepted that seven parameters have the most significant impact on the productivity estimation of ceramic activity, and are thus used as the *ANN* model inputs.

The output of the model is the total productivity of ceramic activity. A code is used in this chapter to identify the names of the different models developed. The code consists of two parts separated by a hyphen. The first part represents an abbreviation of the current output (i.e. Total productivity, ID). The second part denotes the model number. Hence, for example "TP—1" represents Total productivity model. The available data extracted from the database in appendix A.

PRE-PROCESSING AND DATA DIVISION

Data processing is very important in using neural networks successfully. It determines what information is presented to create the model during the training phase. It can be in the form of data scaling, normalization and transformation. Transforming the output data into some known forms (e.g. log.,

exponential, etc) may be helpful to improve ANN performance.

The next step in the development of ANN models is the division of the available data into their subsets, training, testing and validation sets. Trail-and-error process was used to select the best division, by using *Neuframe* software. The network that performs best with respect to testing error was used in this work (compared with other criteria to evaluate the prediction performance, training error and correlation of validation set). Using the default parameters of the software, a number of networks with different divisions were developed and the results are summarized in Table below.

It can be seen that the best division is 60% for training set, 30% for testing set, and 10% for validation set, according to the highest coefficient of correlation (r) and the low difference between the values of testing error. Thus, this division was adopted in the model.

The effect of using different choices for divisions (i.e. striped, blocked, and random) was investigated and shown in Table below. It can be seen that the performance of ANN model was relatively insensitive to the method of division. The better performance was obtained when the striped division was used.

SCALING OF DATA

Once the available data have been divided into their subsets, the input and output variables are pre-processed by scaling them to eliminate their dimension and to ensure that all variables receive equal attention during training. Scaling has to be commensurate with the limits of the transfer functions used in the hidden and output layers (i.e. —1.0 to 1.0 for tanh transfer function and 0.0 to 1.0 for sigmoid transfer function). The simple linear mapping of the variables' extremes to the neural networks practical extremes is adopted for scaling, as it is the most commonly used method, (*Shahin, 2003*). As part of this method, for each variable x with minimum and maximum values of x_{\min} and x_{\max} , respectively, the scaled value x_n , is calculated as follows:

$$x_n = \frac{x - x_{\min}}{x_{\max} - x_{\min}} \quad (5)$$

MODEL ARCHITECTURE, OPTIMIZATION AND STOPPING CRITERIA

One of the most important and difficult tasks in the development of ANN models is the determination of the model architecture (i.e. the number and connectivity of the hidden layer nodes). A network with one hidden layer can approximate any continuous function, provided that sufficient connection weights are used, (*Shahin et al 2002*).

Consequently, one hidden layer is used in this research. The general strategy adopted for finding the optimal network architecture and internal parameters that control the training process is as follows: a number of trials were carried out using the default parameters of the software used with one hidden layer and starting with one hidden node and then slightly increasing the number of the nodes until no significant improvement in the model performance, was gained.

The network that performs best with respect to the lowest testing error followed by training error and high correlation coefficient of validation set was retrained with different combinations of momentum terms, learning rates and transfer functions in an attempt to improve model performance.

Consequently, the model that has the optimum momentum term, learning rate and transfer function was retrained a number of times with different initial weights until no further improvement occurred.

Using the default parameters of the software (learning rate = 0.2 and momentum term = 0.8 and the transfer functions in hidden and output layer nodes are sigmoid), a number of networks with different numbers of hidden layer nodes were developed and results are summarized in Table below for ANN model, since maximum no. of nodes equal to $(2I+1)$ where (I) the number of input nodes. (i.e. max. nodes=15).

It can be seen from that there are slightly differences in testing error. Therefore, one hidden node was chosen in this model. It is believed that the network with one hidden node is considered optimal.

The effect of the internal parameters controlling the back-propagation algorithm (i.e. momentum term and learning rate) on the model performance was investigated for the model with one hidden layer node. The effect of the momentum term on model performance is summarized in Table below:

It can be seen from that the performance of the ANNs model is relatively insensitive to the variation of

the momentum term, particularly in the range 0.01 to 0.5. Then the test errors slightly decrease at the range 0.55 to 0.95. Thus, the obtained optimum value for the momentum term is 0.9 which have the lowest values of testing error (8.88%) and training error (9.34%) and maximum correlation coefficient (r) (87.68%), hence it was used in this model. In addition, the effect of the learning rate on the model performance was investigated (momentum term = 0.9). The results are summarized in Table below. The optimum value for learning rate is 0.6 which has the lowest prediction error, hence it used in this model.

It can be seen from that the performance of the ANN model is relatively insensitive to the variation of the learning rate. Thus, the obtained optimum value for the learning rate is 0.6, which has the low value of testing error, low value training error and high coefficient of correlation (86.33%); hence it was used in this model.

The effect of using different transfer functions (i.e. sigmoid and tanh) was investigated and it was shown in Table below. It can be seen that the performance of ANN model was relatively insensitive to the type of the transfer function. The better performance was obtained when the sigmoid transfer function was used for both hidden and output layers.

To ensure the data that were carried out by *Neuframe* software for training, testing, and validation sets to represent the same statistical population, a statistical parameters estimation was carried out, including the mean, standard deviation, minimum, maximum, and range, as shown in Table:

The results indicated that the training, testing, and validation sets are generally statistically consistent.

SENSITIVITY ANALYSIS OF THE ANN MODEL INPUTS

In an attempt to identify which of the input variables have the most significant impact on the *output* predictions, a sensitivity analysis was carried out on the ANN model. A simple and innovative technique proposed by *Garson (1991)* {AS Mentioned in *Shahin et.al, 2002*} was used to interpret the relative importance of the input variables by examining the connection weights of the trained network. For a network with one hidden layer, the technique involves a process of partitioning the hidden output connection weights into components associated with each input node. For this model, the method is illustrated as follows. The model has seven input nodes, one hidden

node, and one output node with connection weights as shown in Table:

The computational process proposed by Garson (1991) is as follows:

- For each hidden node i , obtain the products P_{ij} (where j represents the column number of the weights mentioned above) by multiplying the absolute value of the hidden-output layer connection weight by the absolute value of the hidden-input layer connection weight of each input variable j .
- For each hidden node, divide P_{ij} by the sum of all input variables to obtain Q_{ij} . For each input nodes, sum Q_{ij} to obtain S_j . in this case the Q_{ij} will be equal to S_j .
- Divide S_j by the sum for all input variables to get the relative importance of all output weights attributed to the given input variable. The results of the above technique were presented in Table:

These results indicate that the variable (V6) have the most significant effect on the predicted total productivity with a relative importance (27.93%). The results also indicate that (V1, V2 and V5) have a moderate impact on prediction with a relative importance equals to 11.77%, 18.97% and 15.31% respectively, while the variables (V3, V4 and V7) have the smallest impact on prediction with the relative importance of 8.51%, 9.97% and 7.53% respectively. The results are also presented in the figure:

ANN MODEL EQUATION:

The small number of connection weights obtained by *Neuframe* for the optimal ANNs model enables the network to be translated into relatively simple formula. While as connection weights and threshold levels (bias) are summarized in Table below:

Using the connection weights and the threshold levels shown in Table above, the prediction of the equation total productivity for wall ceramic can be expressed as follows:

$$TP = \frac{1}{1 + e^{(-3.3789 + 4.4862 \tanh x)}} \quad (6)$$

Where:

$$X = \{ \theta_8 + (W_{8,1} * V1) + (W_{8,2} * V2) + (W_{8,3} * V3) + (W_{8,4} * V4) + (W_{8,5} * V5) + (W_{8,6} * V6) + (W_{8,7} * V7) \} \quad (7)$$

And it can be written as:

$$TP = \frac{(-3.3789 + 4.4862 \tanh x)}{1 + e} + 0.94 \quad (8)$$

It can be noted that, before using Equation (2), all input variables (i.e. V1, V2 ,V7) need to be scaled between 0.0 and 1.0 and the data ranges in the ANN model training. It should also be noted that the predicted value of the total productivity obtained from Equation (1) is scaled between 0.0 and 1.0.

CONCLUSIONS

Through the research work, there are groups of conclusions that can be summarized by the following points:

- The study shows that neural networks are able to model the complex relationships between the job conditions and the productivity of an operation and achieve an acceptable accuracy in estimation.
- The presented approach agrees well with the way in which a contractor makes an intuitive estimate, based on developed experience that comes from observation. However, the superiority of the approach over a pure empirical method is that it generalizes the cause-effect relationships and provides a binding mechanism to maintain the consistency of an estimate.
- The model was never designed to replace the estimator, only to be another tool to formulate final labor productivity for an estimate. An estimator's judgment would always be the final approval before a labor productivity estimate is completed.
- The productivity rate models derived in this research enable planners and construction operation researchers studying the ceramic productivity more accurately than previous approaches.
- The sensitivity analysis indicated the following:
- **The** results obtained using this model indicate that the variable (V6) have the most significant

effect on the predicted total productivity with a relative importance (**27.93%**).

- The results also indicate that (V1, V2 and V5) have a moderate impact on prediction with a relative importance equals to **11.77%**, **18.97%** and **15.31%** respectively,
- while the variables (V3, V4 and V7) have the smallest impact on prediction with the relative importance of **8.51%**, **9.97%** and **7.53%** respectively.

RECOMMENDATIONS:

The construction management should also be familiar with powerful estimate tools such as ANN. This invitation is not optional, but rather inevitable, if the challenges of the forthcoming period, which Iraq is marching towards, are to be faced and overcome.

REFERENCES

- AACE International Recommended Practice No. 25R-03 " **Estimating Lost Labor Productivity in Construction Claims**", TCM Framework: 6.4 – Forensic Performance Assessment / 2004.
- **Ali Sabri Tofan** "Neural Networks for Estimating the Productivity Ceramic of Walls and Floors" *M.Sc. Thesis, College of Engineering, Al-Baghdad University* /2009
- Bain, D. "**The Productivity Prescription**", McGraw Hill, New York, 1982.
- Burnham, D.C. "**Productivity; an Overview**", Handbook of Industrial Engineering, John Wiley & Sons, 1982.
- Construction Industry Institute (CII), "**An Analysis of the Methods for Measuring Construction Productivity**", SD-13, Austin, Texas, 1984
- Feldman, D.C. and Arnol, H.J. "**Managing Group and Individual**

Behavior in Organization", McGraw Hill; 1983.

- Gould, F. Managing *"The Construction Process: Estimating, Scheduling, and Project Control"* 2nd Ed. Prentice-Hall. Upper Saddle River. N. d. Halligan. D.W. Demset2. L.A. Brown. J.d and Pacc, C.B 2002.
- Kavanaugh, Thomas C., Frank Muller & James J. O'Brien, *"Construction Management: A Professional Approach"*, McGraw-Hill Book Company, New York, 1978.
- Lefton, R.E. and Fellows *"Effective Motivation Through Performance Appraisal"*, John Wiley & Sons, 1982.
- Mukherjee, S.K. and Sing, D. *"Towards High Productivity"*, Report of a Seminar on Higher Productivity in Public Sector Production Enterprises, New Delhi – Bureau of Public Enterprises, 1975.
- Prokopenko, J. *"Productivity Management"*, a Practical Handbook, International Labor Office, Geneva, 1987.
- Roman M. Balabin, Ekaterina I. Lomakina. "Neural network approach to quantum-chemistry data: Accurate prediction of density functional theory energies", 2009.
- Shahin, M.A. *"Use of Artificial Neural Networks for Predicting Settlement of Shallow Foundations on Cohesionless Soils"*, Ph. D. Thesis, Department of Civil and Environmental Engineering, University of Adelaide, 2003.
- TRB, *"Use of Artificial Neural Networks in Geotechnical and Pavement Systems"*, Transportation Research Circular No. e-c012, (1999).

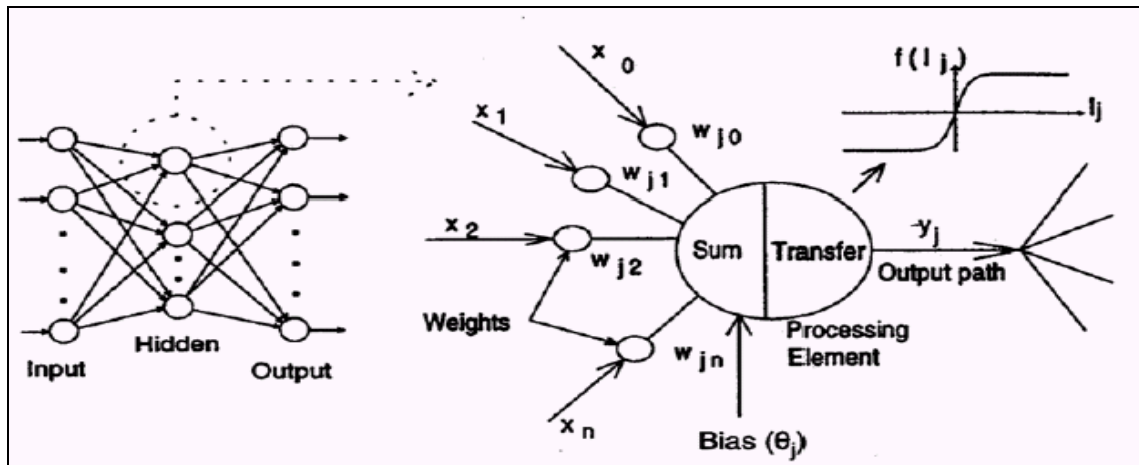
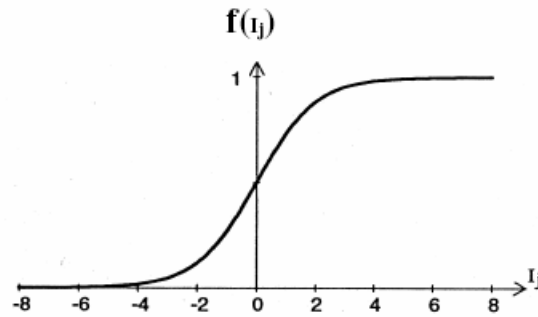
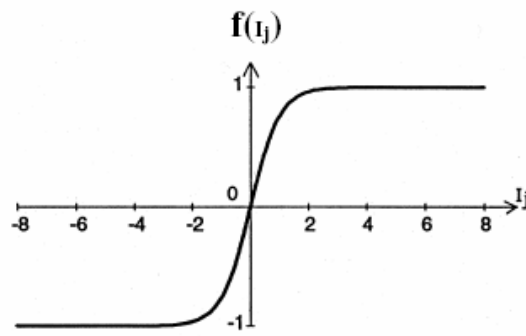


Figure (1) Typical structure and operation of ANNs (Shahin 2003).



(a) The logistic sigmoid function



(b) The hyperbolic tangent function

Figure (2) The logistic sigmoid and hyperbolic tangent transfer functions. (Shahin 2003)

Table (1) Divisions developed and results.

Data Division %			Training Error %	Testing Error %	Coefficient of Correlation (r) %
Training	Testing	Querying			
70	10	20	8.09	9.38	72.53
68	12	20	7.78	14.28	76.34
66	14	20	8.35	8.70	73.50
65	15	20	8.36	9.04	78.52
65	20	15	8.28	11.94	76.57
60	20	20	7.98	11.06	77.52
60	25	15	8.93	9.23	66.57
60	30	10	9.51	8.99	88.23
56	24	20	8.11	10.31	75.80
55	30	15	9.81	7.99	71.94



55	25	20	9.81	7.99	-63.64
55	20	25	9.81	7.99	-79.43
50	30	20	8.56	9.31	77.77
50	35	15	8.79	9.24	77.07
45	35	20	8.11	10.31	-61.30

Table (2) Effect of using different choices of divisions.

Data Division %			choices of division	training error%	testing error%	coefficient correlation(r)%
Training	Testing	Querying				
60	30	10	Striped	9.51	8.99	88.23
60	30	10	Blocked	9.51	8.99	-66.24
60	30	10	Random	8.04	9.73	34.34

Table (3)), Effect on networks with different numbers of hidden layer nodes .

No. of Nodes	Training Error %	Testing Error %	Coefficient of Correlation (r) %
1	9.51	8.99	88.23
2	9.54	9.17	88.25
3	9.58	9.11	88.37
4	9.65	9.15	89.07
5	9.74	9.26	89.41
6	9.67	8.98	88.63
7	9.75	9.15	89.04
8	9.82	9.05	89.13
9	9.92	8.96	88.65
10	9.73	8.98	88.99
11	9.30	9.01	89.04
12	9.79	9.56	90.70
13	9.81	9.10	89.42
14	9.68	9.62	90.31
15	9.77	9.19	89.71

Table (4) effect of the momentum term on model performance.

Parameters Effect	Momentum Term	Training Error %	Testing Error %	Coefficient Correlation(r)%
Model No. 1 Choices of division (striped) Learning Rate (0.2) No. of Nodes (1) Transfer function in hidden layer (sigmoid) Transfer function in output layer (sigmoid)	0.01	9.80	9.02	88.49
	0.05	9.81	9.02	88.48
	0.1	9.80	9.02	88.49
	0.2	9.78	9.02	88.49
	0.3	9.76	9.02	88.49
	0.4	9.72	9.02	88.48
	0.5	9.71	9.02	88.47
	0.55	9.67	9.01	88.45
	0.6	9.66	9.01	88.44
	0.7	9.59	9.01	88.36
	0.8	9.51	8.99	88.23
	0.9	9.34	8.88	87.68
	0.95	9.19	9.08	87.25

Table (5) Effect of the learning rate on the model performance .

Parameters Effect	Learning Rate	Training Error %	Testing Error %	Coefficient Correlation(r)%
Model No. 1 Choices of division (striped) Momentum Term (0.9) No. of Nodes (1) Transfer function in hidden layer (sigmoid) Transfer function in output layer (sigmoid)	0.02	12.47	11.34	82.01
	0.05	9.65	8.99	88.40
	0.1	9.50	8.95	88.19
	0.15	9.41	8.86	87.94
	0.2	9.34	8.88	87.68
	0.3	9.28	8.70	87.34
	0.4	9.24	8.82	86.94
	0.5	9.21	9.17	86.60
	0.55	9.21	8.98	86.53
	0.6	9.20	8.65	86.33
	0.7	9.22	8.41	85.80
	0.8	9.78	8.28	85.90



Table (6) Effect of using different transfer functions.

Parameters Effect	Transfer Function		Trainin g Error %	Testing Error %	Coefficient Correlation(r)%
	Hidden Layer	Output Layer			
Model No. 1 Choices of division (striped) No. of Nodes (1) Momentum Term (0.9) Learning Rate (0.6)	Sigmoid	Sigmoid	9.20	8.65	86.33
	Sigmoid	Tanh	62.14	66.76	---
	Tanh	Sigmoid	9.26	9.89	79.47
	Tanh	Tanh	62.14	66.76	---

Table (7) Data statistical parameters.

Statistical parameter	Output	Input Variables						
	productivity	V1	V2	V3	V4	V5	V6	V7
	Training set							
MAX	3.83	15	46	2	0.1	1	2	2
MIN	0.94	3	26	1	0.06	0	0	0
RANGE	2.89	12	20	1	0.04	1	2	2
MEAN	2.0335	9.45	36.13333	1.416667	0.086	0.466667	0.45	0.283333
S.D	0.636571	4.114567	7.247365	0.497167	0.01924	0.503098	0.648989	0.490301

	Testing set							
MAX	3.07	15	46	2	0.1	1	2	1
MIN	0.9	3	26	1	0.06	0	0	0
RANGE	2.17	12	20	1	0.04	1	2	1
MEAN	1.866667	10	37	1.566667	0.084	0.533333	0.6	0.333333
S.D	0.449623	3.99137	7.22066	0.504007	0.019931	0.507416	0.723974	0.479463
	Validation set							
MAX	3.12	15	46	2	0.1	1	1	1
MIN	1.33	3	26	1	0.06	0	0	0
RANGE	1.79	12	20	1	0.04	1	1	1
MEAN	2.021	10.1	37.1	1.6	0.084	0.5	0.4	0.1
S.D	0.519154	3.984693	7.340148	0.516398	0.020656	0.527046	0.516398	0.316228

Table (8) Output nodes with connection weights.

Hidden Nodes	Weights							
	V1	V2	V3	V4	V5	V6	V7	output
Hidden 1	0.929928	1.498832	-0.67265	-0.787878	1.209671	2.206048	0.594394	-4.486283



Table (9) Technique results.

Input Variables	Weights (from input to hidden) absolute	Hidden node	Weights (from hidden to output) absolute	Output node	P_{ij}	$Q_{ij}=P_{ij}/\sum P_{ij}$	$S_{ij}=\sum Q_{ij}$	R.I%
V1	0.929928377880479	1	4.4862833213507	1	4.171922172	0.117721328	0.117721328	11.77%
V2	1.4988328523284				6.724188827	0.189739983	0.189739983	18.97%
V3	0.672650849930333				3.017702289	0.085152097	0.085152097	8.51%
V4	0.787878018353824				3.534644013	0.099738914	0.099738914	9.97%
V5	1.20967140631394				5.426928654	0.153134508	0.153134508	15.31%
V6	2.20604809276063				9.896956765	0.279267649	0.279267649	27.93%
V7	0.594394785685078				2.666623413	0.075245519	0.075245519	7.53%
				$\sum P_{ij}=$	35.43896613	$\sum S_{ij}=$	1	100.00%

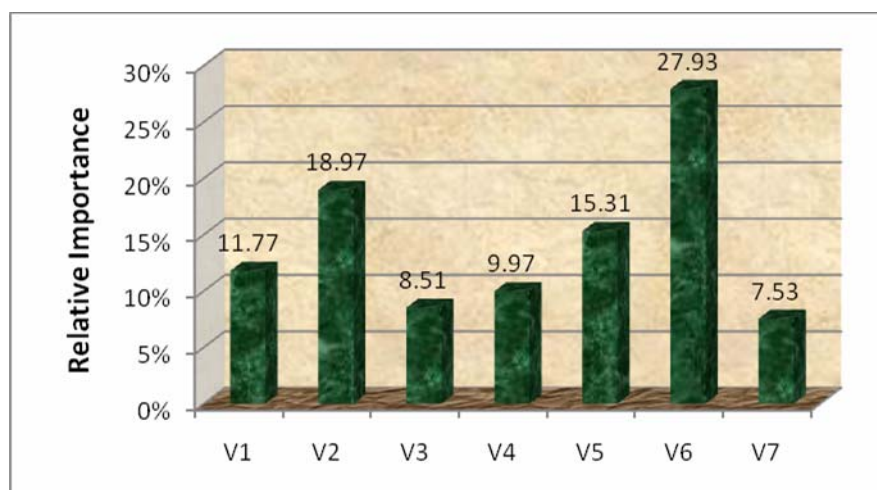


Figure (3) Relative importance of the input variables for the Model

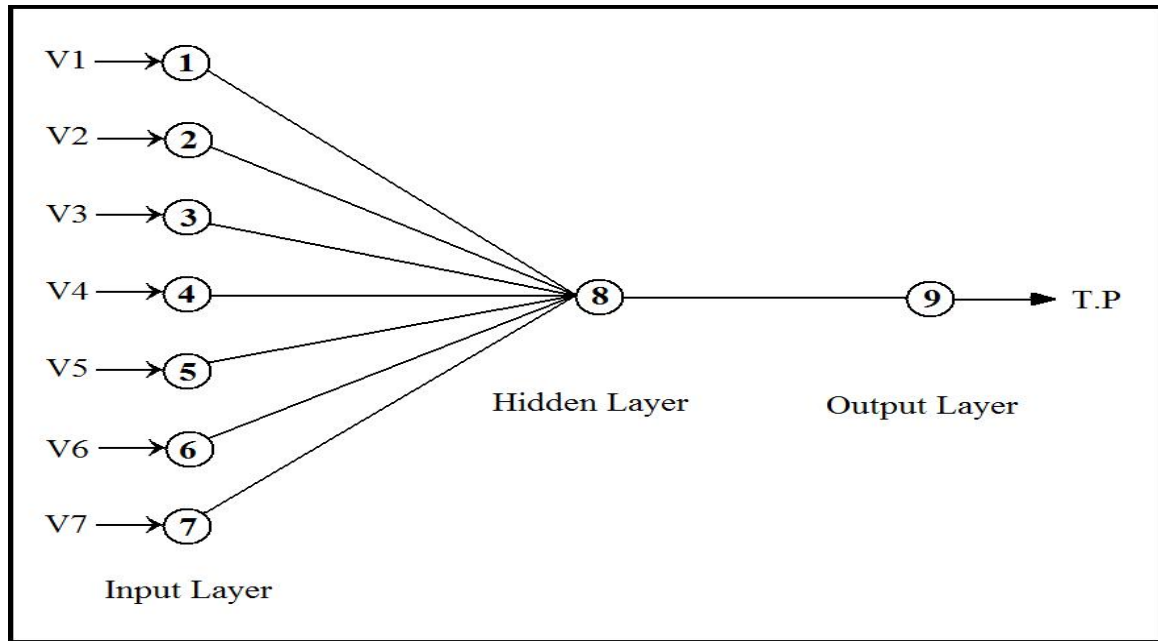


Figure (4) Structure of the ANNs optimal model

Table (10) Connection weights and threshold levels of model.

Hidden layer nodes	W_{ji} (weight from node i in the input layer to node j in the hidden layer)							Hidden layer threshold θ_j
	$i=1$	$i=2$	$i=3$	$i=4$	$i=5$	$i=6$	$i=7$	
$j=8$	0.9299	1.4988	-0.6726	-0.7878	1.2096	2.2060	0.5943	0.4247
Output layer nodes	W_{ji} (weight from node i in the hidden layer to node j in the output layer)							Output layer threshold θ_j
	$i=8$	-	-	-	-	-	-	
$j=9$	-4.4862	-	-	-	-	-	-	3.3789

APPENDIX A: INPUTS AND OUTPUT VARIABLES USED FOR MODEL

Productivity	Height	complication	Labors	Age	Experience	Weather	Area of ceramic
1.64	0	1	2	35	10	0	0.06
0.9	1	1	2	35	10	0	0.06
1.94	0	1	2	35	10	0	0.06
1.82	0	1	2	35	10	0	0.06
2.1	0	0	2	35	10	0	0.06
1.22	1	1	2	35	10	0	0.06
1.2	2	1	2	35	10	0	0.06
1.36	1	1	2	35	10	0	0.06
1.32	0	1	2	35	10	0	0.06
1.44	0	1	2	35	10	0	0.06
1.7	1	1	2	35	10	0	0.06
1.1	2	1	2	35	10	0	0.06



1.9	0	0	2	35	10	0	0.06
1.6	0	1	2	35	10	0	0.06
1.49	0	1	1	35	10	0	0.06
3.15	0	0	2	35	10	0	0.06
0.94	2	1	1	35	10	0	0.06
1.68	0	1	1	35	10	0	0.06
1.59	0	1	1	35	10	0	0.06
1.63	1	1	1	35	10	0	0.06
1.86	0	0	1	46	15	0	0.06
1.84	0	0	1	46	15	0	0.06
1.8	1	0	1	46	15	0	0.06
1.76	0	0	2	46	15	0	0.06
2.08	0	0	2	46	15	0	0.06
2.12	0	0	2	46	15	0	0.06
1.7	0	0	2	46	15	0	0.06
1.4	0	1	2	46	15	0	0.06
1.37	0	1	2	46	15	0	0.06
1.42	0	1	1	46	15	0	0.06
1.33	1	1	1	46	15	0	0.06
1.6	2	0	2	46	15	0	0.06
1.88	1	0	2	46	15	1	0.06
1.49	1	0	2	46	15	1	0.06
2.32	0	0	1	46	15	1	0.06
1.92	0	0	2	46	15	1	0.06
1.87	0	0	2	46	15	1	0.06
1.82	0	0	2	42	12	1	0.1
2.15	0	0	1	42	12	1	0.1
1.67	1	0	1	42	12	1	0.1
2.37	0	0	2	42	12	0	0.1
2.08	0	0	2	42	12	0	0.1
1.57	0	0	1	42	12	0	0.1
1.9	0	0	1	42	12	0	0.1
1.76	1	0	1	42	12	0	0.1
1.89	0	0	1	42	12	0	0.1
1.88	0	0	1	42	12	0	0.1
1.76	0	0	1	42	12	0	0.1
2.02	0	0	1	42	12	0	0.1
1.87	0	0	1	42	12	0	0.1
1.56	1	0	1	42	12	1	0.1
2.76	0	0	2	42	12	1	0.1
3.07	0	0	2	42	12	0	0.1
1.76	0	0	1	42	12	1	0.1
1.49	2	0	1	42	12	1	0.1
2.05	0	0	2	42	12	0	0.1
1.69	0	0	1	41	12	1	0.1
2.17	0	0	2	41	12	2	0.1
1.78	0	0	1	41	12	1	0.1

1.43	1	0	1	41	12	0	0.1
2.31	0	0	1	41	12	0	0.1
2.33	0	1	2	41	12	0	0.1
2.13	1	1	2	41	12	0	0.1
1.79	0	1	1	41	12	0	0.1
1.92	1	1	1	41	12	0	0.1
2.07	0	1	1	41	12	0	0.1
3.03	0	1	2	41	12	0	0.1
2.33	1	1	1	41	12	0	0.1
1.76	1	1	1	29	6	0	0.1
2.33	0	1	1	29	6	0	0.1
2.23	1	1	2	29	6	0	0.1
1.95	1	1	1	29	6	1	0.1
2.39	1	1	1	29	6	0	0.1
2.13	1	1	1	29	6	1	0.1
1.54	1	1	1	29	6	1	0.1
2.86	1	1	1	29	6	0	0.1
2.51	1	1	1	29	6	1	0.1
1.88	2	1	1	29	6	0	0.1
2.46	1	0	1	29	6	0	0.1
2.46	1	1	2	29	6	1	0.1
3.12	0	0	2	29	6	0	0.1
2.17	0	1	1	29	6	1	0.1
1.94	2	1	1	29	6	0	0.1
2.17	1	0	2	26	3	1	0.1
2.79	0	0	2	26	3	0	0.1
3.67	0	0	2	26	3	1	0.1
2.73	0	1	2	26	3	1	0.1
2.08	1	1	2	26	3	0	0.1
3.7	0	0	2	26	3	0	0.1
1.07	2	1	2	26	3	0	0.1
2.09	0	1	2	26	3	0	0.1
1.24	1	1	2	26	3	0	0.1
1.23	2	1	1	26	3	1	0.1
1.76	0	1	1	26	3	1	0.1
3.08	0	0	1	26	3	0	0.1
3.83	0	0	1	26	3	0	0.1
2.45	1	0	1	26	3	0	0.1
2.68	0	0	1	26	3	0	0.1
1.77	1	0	1	26	3	1	0.1
2.26	0	1	1	26	3	0	0.1



EFFECT OF OPENINGS WITH OR WITHOUT STRENGTHENING ON PUNCHING SHEAR STRENGTH FOR REINFORCED CONCRETE FLAT PLATES

Asst. Lect. Abeer H.H. Al-Shammari
Civil Engineering Department
College of Engineering/ Al-Mustanseryah University

ABSTRACT

Reinforced concrete slabs with openings are usually designed with help of traditional rules proposed by building codes. Such methods introduce limitations concerning size, location of openings and magnitude of applied loads. Furthermore, there are some traditional approaches to strengthen reinforced concrete slabs with openings which can be either cumbersome or expensive. This paper studies variable locations of an opening with respect to a central column in reinforced concrete flat plates, and presents a good approach to strengthen this opening by using steel plates.

Nine reinforced concrete flat plates are cast with dimensions (length, width and thickness) equal to (850, 470 and 50) mm) using a single concrete mix with average compressive strength (f_{cu}) equals 30 MPa. Each slab contains a square cross-section opening (side length =75 mm) and supported by a central square cross-section column (side length =75 mm). The variables of this study are: the type of opening (with or without strengthening) and the clear distance between the opening and the column which takes the values (0.0d, 2d, 4.5d and 7d), where d is the effective depth. The specimens are tested over a simply supported span at four edges.

The test results show that, the ultimate load reaches the maximum value for slab without opening while this load reaches the minimum value for slab with a non-strengthening opening and lies in the pattern of the failure zone (where the clear distance between the column and the opening equals 4.5d).

When a comparison is made between the test results ,it is concluded that ;strengthening the slab opening with steel plates causes increasing in the ultimate load by (19.44 ,19.51 ,35.13 and 13.46) % for the specimens (0.0d ,2d ,4.5d and 7d) respectively.

KEY WORD: Punching Shear, Flat Plate, Slab with Opening.

:

()

(50 470 850) ()
30 (75=)
(: (75 =)

(7 4.5 2 0)

(

)

.(4.5

(7 4.5 2 0.0) % (13.46 35.13 19.51 19.44)

INTRODUCTION

Openings in slabs are usually required for different purposes such as for fire protection pipes, plumbing, heat and ventilation ducts and air conditioning (Mota and Camara 2005). These openings can severely weaken the slab due to the discontinuity of both concrete and steel. There are some traditional approaches to strengthen opening including use of embedding reinforcing steel bars next to the opening, the addition of columns at the edges of openings and the good approach is the use of carbon fiber reinforced polymer (CFRP) systems, but this approach is expensive (Seliem and Sumner 2008).

In many cases only strengthening along opening edges is advised by adding reinforcing steel bars next to the opening. One practical method of reinforcement arrangement that consists in applying skew bars in opening corners. A big advantage in application of this method can be obtained since bars are situated perpendicular to the direction where the main crack is to appear (Rusinowsk 2005).

This study gives a clear understanding on the behavior and failure mechanisms of a proposed concrete slab with opening of different locations. Also gives a good approach to strengthen this opening with steel plates in section conforms to the opening. The output of this study will be beneficial to produce an efficient strengthening method to slab with opening. If the concept of strengthening using steel plates is commercially accepted, thus a strengthening process can be conducted much easier with equally satisfactory solutions.

EXPERIMENTAL WORK

Experimental Program

The test program consists of fabricating and testing of nine reinforced concrete slabs with a central column and a single opening using a concrete mix with average cube compressive strength (f_{cu}) equal to (30 MPa). All slab specimens have the same dimensions (length,

width and thickness) equal to (850, 470 and 50mm) and concrete cover of (15 mm); see Fig. 1. The variables investigated in this study are the type of opening (with or without strengthening) and the clear distance between the column and the opening in the slab specimen. Deformed welded wire fabric mesh (WWF) with (6mm) diameter and (75mm) c/c spacing each way are used as flexural reinforcement placed in tension faces. The average yield strength (f_y) of deformed wires is (438MPa). The specimens are divided into two groups, each of them includes four specimens, the specimens of the first group are with non strengthening openings while the specimens of second group are with strengthening openings, the ninth specimen is cast without opening and considered as a reference. Table 1 shows the detail of the specimens. All specimens are tested over a simply supported span at four sides using a steel frame made for this purpose.

MATERIALS

The materials used in manufacturing the test specimens are reported and presented in Table 2 with descriptions; the tests of materials are presented in Tables 3, 4 and 5 and the concrete mix proportions are reported and presented in Table 6.

Details of Moulds and Openings

Steel moulds are used for casting control specimens while wooden moulds are used for casting slab specimens, the central column of slab is fabricated by using a hollow wooden square cross-section box (clear side length = 75mm) and a solid wooden box is used to fabricate the opening in specimens of group A, Fig. 2a shows details of mould of group A and Fig. 2b shows the reinforcement details of the column.

The same moulds are used to fabricate specimens of group B, but the strengthening of opening is made by using steel plates in square

cross-section (side length =75 mm, thickness of plates =3mm). Bond between steel plates and concrete is obtained by using bolts welded to the steel plates (two bolts of diameter 17 mm in each side) as shown in Fig.3.

Mixing, Casting, Compacting and Curing Procedure

The mixing procedure was as follows:-

- Before mixing, all quantities are weighted and packed in clean containers.
- Saturated surfaces dry crushed gravel and dry sand are added to the rotary drum mixer of (0.18m³) volume capacity and mixed for several minutes.
- The cement is then added to the mixer, and water is added gradually to the mix. The total mixing time is (8-10 minutes).
- The moulds are coated with oil before putting the reinforcing bar, or casting the control specimens.
- Before placing the concrete in the mould, steel reinforcement is placed in the mould and the specimen is cast in two layers. Then, column is cast continuously (monolithically) with slab. Specimens were compacted by a table vibrator with a compaction time (2minutes) for each layer; some of these procedures are explained in Fig.4. After casting, the slab specimens and control specimens are covered with polythene sheets and after (24 hours) they are stripped of the moulds and placed in water for other (27days) and then tested.

Test Measurement and Instrumentation

A hydraulic universal testing machine (MFL system) is used to test the specimens as well as control specimens. Central deflection has been measured by means of (0.01mm) accuracy dial gauge (ELE type) and (30mm) capacity. The dial gauges are placed underneath the bottom face of each span at mid, Fig. 5 shows the test instrumentation. All tests are made in the Laboratory of Structures in Al-Mustansiriya University, College of Engineering.

RESULTS AND DISCUSSIONS

Engineering Properties of Hardened Concrete

Control specimens ,which contain four standard cylinders, three cubes and one standard prism with each slab specimen ,are tested at age of 28 days to determine the engineering properties of hardened concrete ,which include concrete compressive strength, modulus of elasticity E_c , splitting tensile strength f_{sp} and modulus of rupture f_r . Table 7 shows the engineering properties.

SLAB SPECIMENS

In this study, eight opened slabs are tested in addition to another slab without opening (reference). These slabs are identical in size and ratio of steel reinforcement, but different in the type of opening and in the clear distance between the column and the opening in the slab specimen. According to these variables, ultimate loads, crack patterns as well as shapes of failure are different from each other.

Crack Pattern

The test results of cracking and ultimate loads are reported and presented in Table 8. When load is applied to these slab specimens, the first cracks form at about (15.5-20.4) % of the ultimate load for the slab specimens. At ultimate load, punching shear failure occurs suddenly for all specimens

The first crack appears around the sides of the column on the tension face of the slab and other cracks form at the central region of the slab. By increasing the load, these cracks widen and increase in number. At ultimate load, punching shear failure occurs suddenly for all slabs. Fig. 6 illustrates crack patterns and failure modes of specimens. From Fig. 6 it is evident that the capillary cracks appear in the tensile face of the slabs when the moment generated from the applied load reaches to the crack moment. Also it is clear that the punching cracks for the specimens of group B do not enclose around themselves because the presence of steel plates strengthen the area around the opening.

Load-Deflection Behavior

The deflection results of all specimens are illustrated in Table 9. The test results show that, the deflection at ultimate load increases as the ultimate load increases (specimens A₄, B₄ and R have maximum deflection due to maximum ultimate load). Also Fig. 7 and Fig. 8 show the load-deflection relationships of the slabs. From these figures, it is observed that the specimens have a convergent load-deflection behavior

because of the size of specimens which is rather small.

Ultimate Loads

Ultimate load capacity for punching failure is illustrated in Table 8. The test results show that:-

- The ultimate load reaches the maximum value for the specimen (R) of no opening
- Strengthening the slab opening with steel plates causes increasing in the ultimate load by (19.44, 19.51, 35.13 and 13.46) % for the specimens (0d, 2d, 4.5d and 7d) respectively.
- The ultimate load is about (51.79, 59.00, 42.86 and 84) % and about (64.30, 73.21, 66.07 and 96.43) % of the ultimate load of the reference (R) for the specimens ($A_1 - A_4$) and for the specimens ($B_1 - B_4$) respectively.
- The ultimate loads increase as the clear distance between the column and the opening is increased, except specimens A_3 and B_3 because the opening lies in the pattern of the failure zone (where the clear distance between the column and the opening equals 4.5d) (Al-Hafiz 2009). See Fig. 9.

Area of Failure Zone

The areas and perimeters of the punching failure zones are measured for the specimens (A_1 , A_2 , A_4 and R) only because the opening of the specimen A_3 lies in the pattern of the failure zone where the clear distance between the column and the opening equals 4.5d (Al-Hafiz 2009) (i.e. the failure zone does not enclose around itself). Also the areas of the punching failure zones of specimens of group B do not be measured because the steel plates strengthen the area around the opening (also the failure zones do not enclose around itself), see Fig. 6.

From Table 10, it is concluded that the area of failure zone of the specimen A_2 is greater than that of the specimen A_1 by about 56% (i.e. the area of failure zone increase as the clear distance between the column and the opening is increased), while the area of failure zone of A_4 is smaller than that of A_2 by about 10% because the position of the column is out of the area of the failure zone.

Comparison of Experimental Results with ACI-318 Code (2008) and BS 8110 (1997)

Many codes and researchers have presented different formulas for predicting punching shear

strength of slabs based on their understanding of punching behavior, the ACI-318 Code (2008) is considered in this study and compared with its results. Punching strength is predicted by considering the effect of opening on the value of b_o according to the item 11.12.5 of chapter eleven of ACI 318 Code; see Table 11 and Fig. 10.

From Fig. 10, it is evident that the punching shear strength v_u increases as the clear distance between the column and the opening is increased because of the decreasing of the effect of this distance on the value of b_o as it is increased. Also it is clear that the punching shear strengths for all slabs are safe (the experimental results are larger than the computed results) except the specimen A_3 because the opening lies in the pattern of failure zone as mentioned before.

BS 8110-1 (1997) is also considered in this study, punching strength is calculated by considering the effect of opening on the value of u (perimeter of failure zone) according to the item 3.7.7 of section three of the BS, see Table 12.

From Table 12 it is clear that the punching shear strength v_u increases as the clear distance between the column and the opening is increased for the same reason above.

$$f_{cu}=30\text{MPa}$$

When the clear distance between the column and the opening is greater than 6d, the opening has no effect on the value of u according to BS 8110-1.

CONCLUSIONS

Depending on the test results of this study, the following conclusions are obtained:-

- The first cracks form at about (15.5-20.4) % of the ultimate load for the slab specimens.
- At ultimate load, punching shear failure occurs suddenly for all specimens
- The ultimate load reaches the maximum value for slab without opening while this load reaches the minimum value for slab with a non-strengthening opening and lies in the pattern of the failure zone (where the clear distance between the column and the opening equals 4.5d).
- The ultimate loads increase as the clear distance between the column and the opening is

increased except specimens with opening lies in the pattern of the failure zone (where the clear distance between the column and the opening equals $4.5d$) which have smaller ultimate load.

- Strengthening the slab opening with steel plates causes increasing in the ultimate load by (19.44, 19.51, 35.13 and 13.46) % for the specimens (0.0d, 2d, 4.5d and 7d) respectively.
- The punching shear strength v_u according to both ACI 318 Code and BS 8110-1 increases

as the clear distance between the column and the opening is increased.

NOTATION

b_o : perimeter of failure zone;

d : Effective depth of slab;

f_c : Ultimate cylinder compressive strength;

f_{cu} : Ultimate cubic compressive strength

f_y : Yield tensile strength;

f_u : Ultimate tensile strength;

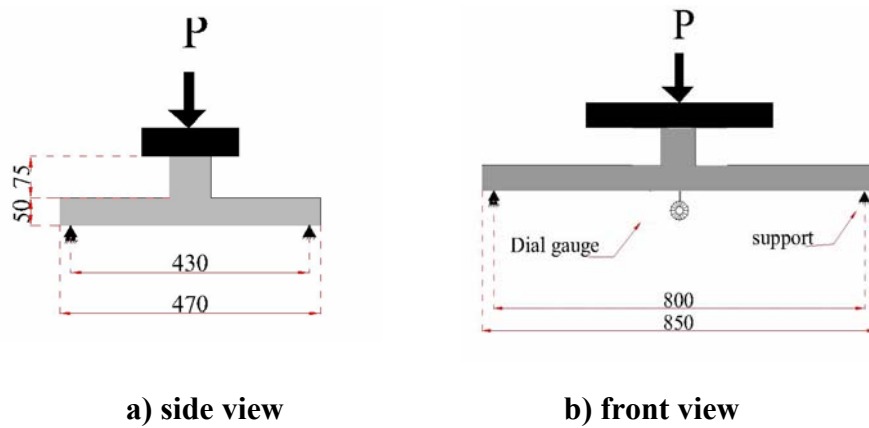
X : Clear Distance between the column and the opening.

REFERENCES

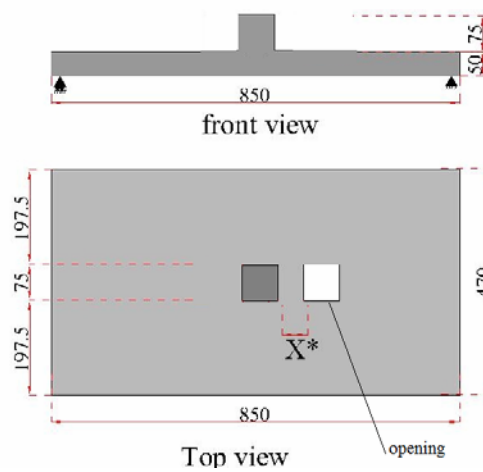
- ACI Code (318-08), "**Building Code Requirements for Reinforced Concrete**", ACI, Detroit, March, 2008.
- Al-Hafiz, A.M., " Experimental Study of Punching Shear for Reinforce **Concrete Flat Plates With Coupled Columns**"
-

M.Sc. Thesis, Civil Engineering Department, Al-Mustansiriya University, January-2009.

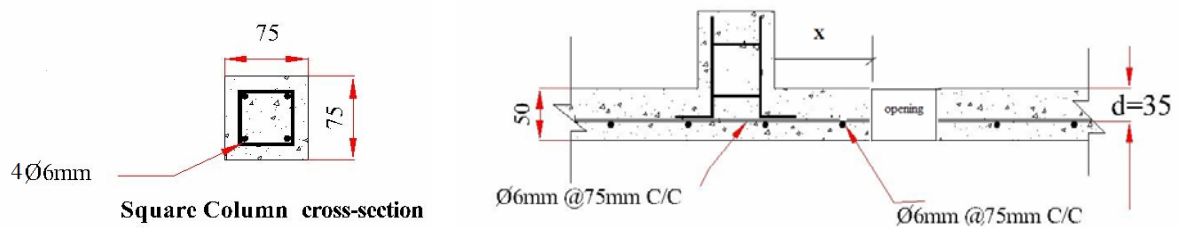
- BS 8110-1 (1997), "**Code of Practice for Design and Construction**", British Standard Institution, 1997.
- Mota, M., and Kamara, M., "Floor Opening in Two-Way Slabs", Portland Cement Association, Skokie, Illinois, paper from Internet, 2005.
- Rusinowski, P., "Two-way Concrete Slabs with Openings", M.Sc. Thesis, Civil and Environmental Engineering Department, Division of Structural Engineering, Lulea University of Technology 2005.
- Seliem, H.M., Sumner, E.A. and Seracino, R., "Field testing of RC Slabs with Openings Strengthened with CFRP ", Fourth International Conference on FRP Composites in Civil Engineering (CICE2008), Zurich, Switzerland.
- المواصفات العراقية رقم 5 " السمنت البورتلاندى ، الجهاز المركزى للتقييس والسيطرة النوعية " بغداد 1984، ص 8.
- المواصفات العراقية رقم 45 لسنة 1984 " ركام المصادر الطبيعية المستعملة فى الخرسانة والبناء، ص(5-20).



Details of Slab Specimen Test and its Loading Arrangement



Details of Slab Dimensions.



Details of specimen cross-section

Fig. 1: Details of Slab Specimen.

Notes: All dimensions are in mm.

(*)X is a variable distance; its values are given in Table 1.



Table 1: Dimension Details of Tested Slabs

Group	Designation	Column side length (mm)	Opening side length (mm)	Clear distance between Column and opening (X)
A	A ₁	75×75	75×75	0.0 d [*]
	A ₂			2 d
	A ₃			4.5 d
	A ₄			7 d
B	B ₁			0 d
	B ₂			2 d
	B ₃			4.5 d
	B ₄			7 d
Reference	R			Without opening

(*) d (the effective depth) = 35 mm.

Table 2: Description of Construction Materials

Material	Descriptions
Cement	Ordinary Portland Cement (Type I), properties of this cement are shown in Tables 3a and 3b, which comply with the Iraqi Standard Specification No.5/1984 Requirements.
Sand	Natural sand from Al-Ukhaider region with maximum size of (4.75mm). The grading of the fine aggregate is shown in Table 4, which complies with the Iraqi Standard Specification No.45/1984.
Gravel	Crushed gravel with maximum size of (10mm) from Al-Nibae area. The grading of the coarse aggregate is shown in Table 5, which complies with the Iraqi Standard Specification No.45/1984.
Reinforcing Bars	Deformed welded wire fabric mesh (WWF) with (6mm) diameter and (75mm) c/c spacing each way are used as flexural reinforcement placed in tension faces. The average yield strength (f_y) is (438MPa) and the average ultimate strength (f_u) is (580MPa).
Water	Tap water.

Table 3a:
chemical properties of cement #.

#All chemical tests are made in the National Center for Construction Laboratories and Researches

Oxides		%	IQS 5:1984 Limits
Calcium Oxide	Ca O	63.19	5.00 max. 2.80 max. 4.00 max. 1.50 max. 0.66-1.02
Silicon Oxides	SiO ₂	20.06	
Aluminum Oxides	Al ₂ O ₃	5.28	
Ferric Oxides	Fe ₂ O ₃	4.10	
Magnesium Oxides	Mg O	2.28	
Sulfur Trioxides	SO ₃	1.98	
Loss on Ignition	L.O.I	2.45	
Insoluble Residue	I.R	0.47	
Lime Saturation Factor	L.S.F	0.94	
Bogue's Potential Compound		%	
Tricalcium Silica	C ₃ S	57.11	
Dicalcium Silica	C ₂ S	16.23	
Tricalcium Aluminates	C ₃ A	3.29	
Tetra Calcium Aluminaferite		13.23	
C ₄ AF			

Table 3b:
Physical Properties of Cement[#]

Physical Properties	Test Result	IQS 5:1984 limits
Fineness: Specific surface, Blaine(cm ² /gm)	3329	2300 min.
Soundness, Autoclave %	0.19	0.8 max.
Setting time ,Vicat s method:- Initial (min) Final (min)	175 255	45 min. 10 max.
Compressive strength of cement (MPa) 3 day 7days	32.4 40.5	15 min. 23 min.

#All physical tests are made in the National Center for Construction Laboratories and Researches

Table 4: Grading of Fine aggregate (Sand)[#]

No.	Sieve (mm)	%Passing	
		Fine aggregate %	IQS 45:1984 Zone(2)
1	5	100	90-100
2	2.36	83.75	75-100
3	1.18	63.84	55-90
4	0.6	35.84	35-59
5	0.3	5.84	8-30
6	0.15	0.64	0-10

All tests are made in the Laboratory of Materials in Al-Mustansiriyah University, College of Engineering.

Table 5 : Grading of Coarse aggregate (Gravel)[#]

No.	Sieve (mm)	%Passing	
		Coarse aggregate %	IQS 45:1984 size (5-14)mm
1	14	100	90-100
2	10	74.5	50-85
3	5	3.5	0-10
4	2.36	0	-

All tests are made in the Laboratory of Materials in Al-Mustansiriyah University, College of Engineering.

Table 6: Mix Proportions by Weight

Mix proportions	W/C ratio	Water (L/m ³)	Cement (kg/m ³)	Sand (kg/m ³)	Gravel (kg/m ³)
1:1.5:3	0.45	225	500	750	1500

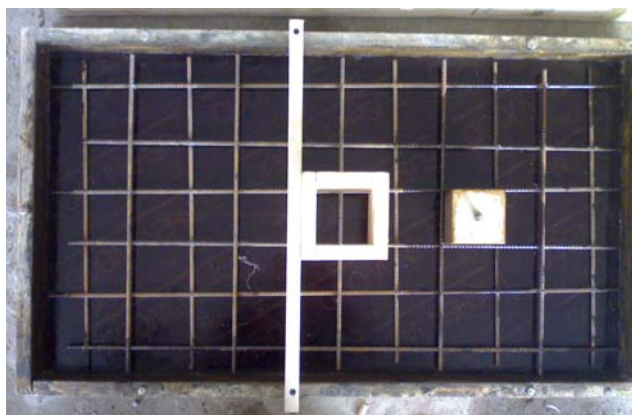

Fig. 2a: Details of mould of group A

Fig. 2b: Reinforcement of column



Fig. 3: Details of mould of group B



Fig.4: Casting Procedure



Fig. 5: Test Instrumentation.

**Table 7: Engineering Properties of Hardened Concrete**

Specimen	Average compressive strength f_c (MPa)	Average compressive strength f_{cu} (MPa)	Measured Static Modulus of Elasticity GPa	Measured Splitting Tensile Strength (f_{sp}) (MPa)	Measured Modulus of Rupture f_r (MPa)
A ₁	22.1	29.1	25.5	2.50	3.36
A ₂	21.8	32.8	26.5	2.62	4.50
A ₃	22.5	31.3	26.1	2.59	4.08
A ₄	23.5	30.5	26.2	2.59	3.85
B ₁	21.9	29.3	25.5	2.58	3.38
B ₂	22.3	28.8	25.1	2.40	3.21
B ₃	23.8	29.3	25.6	2.57	3.37
B ₄	22.7	29	25.3	2.48	3.30
R	23.78	31.5	26.2	2.60	4.15

Table 8: First Crack and Ultimate Loads of Slabs

Group	Designation	Clear distance between column and opening		f_{cu} (MPa)	First crack load (P_{cr}) (kN)	Ultimate Load (P_u) (kN)	$\frac{P_{cr}}{P_u}$ (%)
		(X) mm	X/d				
A	A ₁	0	0	29.11	4.5	29	15.5
	A ₂	70	2	32.8	5.5	33	16.6
	A ₃	157.5	4.5	31.33	4	24	16.6
	A ₄	245	7	29.33	8	47	17
B	B ₁	0	0	28.88	6.5	36	18.1
	B ₂	70	2	29.33	7.5	41	18.3
	B ₃	157.5	4.5	32.22	6	37	16.2
	B ₄	245	7	29.78	11	54	20.4
Reference	R	without opening		31.5	10	56	18

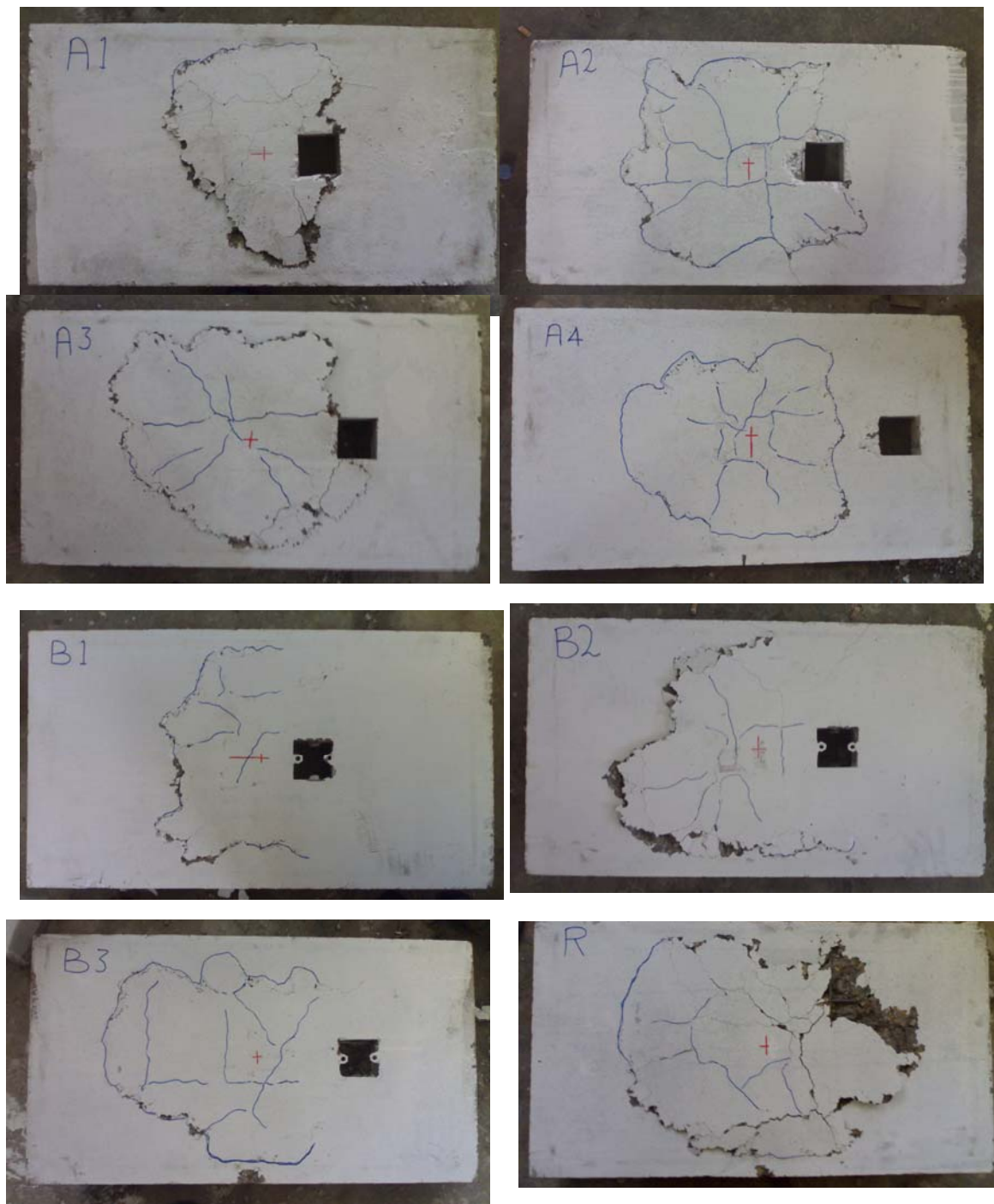
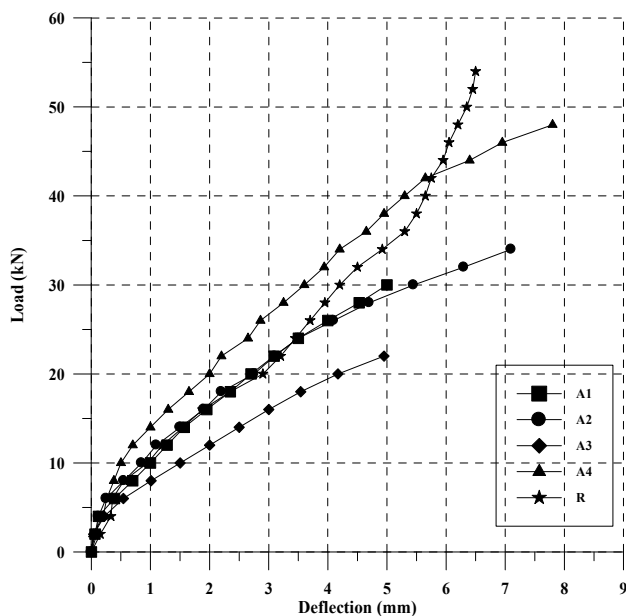
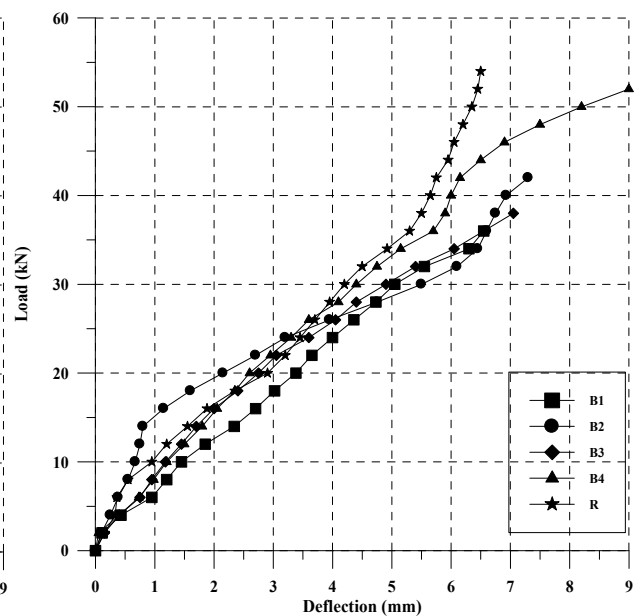


Fig. 6: Crack Patterns at a Bottom face of Slabs at Failure Stage.

Table 9: Load and Deflection Characteristics at First Crack and at Ultimate Loads

Group	Specimen	Deflection at first crack (mm)	Deflection at ultimate load (mm)
A	A ₁	0.16	5
	A ₂	0.2	7.1
	A ₃	0.22	5
	A ₄	0.38	7.8
B	B ₁	0.98	6.55
	B ₂	0.5	7.3
	B ₃	0.75	7.05
	B ₄	1.35	9
Reference	R	0.95	6.5


Group A

Group B
Fig. 7: Load-Deflection Relationship for groups A and B

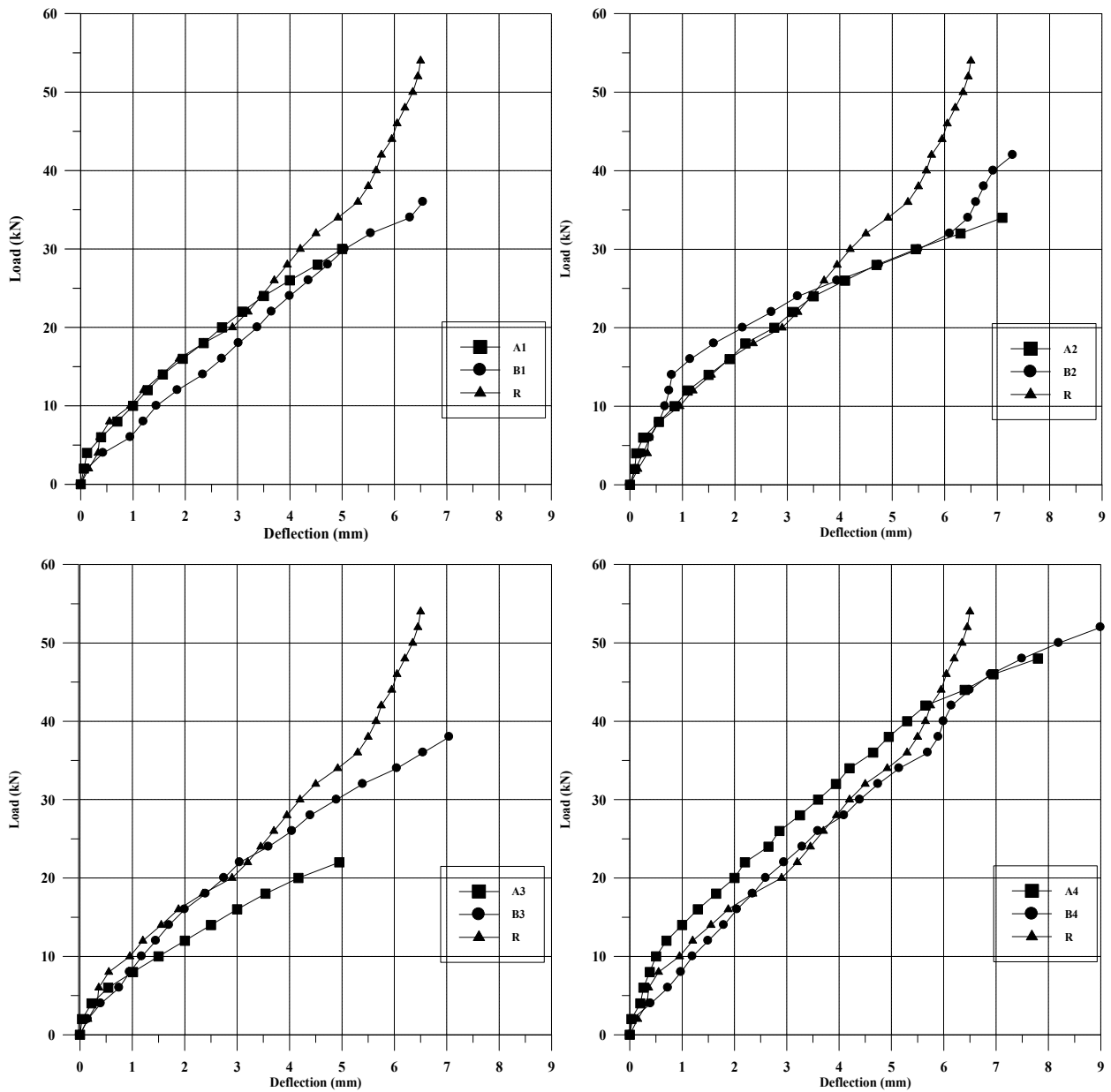


Fig. 8: Comparison of Load-Deflection Relationships between Group A and Group B

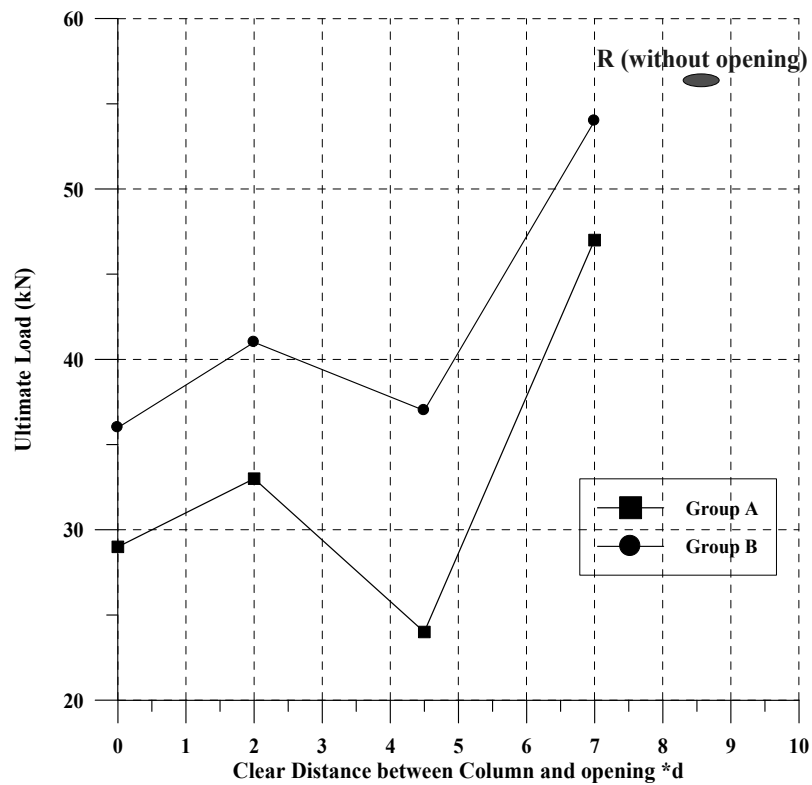


Fig.9: Ultimate Load – Clear Distance between column and opening relationship

Table 10: Area and Perimeter of the Failure Zone

Slab	Measured area (mm ²)	Measured perimeter (mm)
A ₁	88702	1363
A ₂	138283	1477
A ₄	125637	1484
R	170016	1835

Table11: Punching Shear strength of Slabs according to ACI 318 Code

Specimen	$P_{u(Exp)}$ kN	b_o (mm)	v_u (kN) using ACI Code $v_u = \frac{1}{3} \sqrt{f'_c} b_o d^*$
A ₁	29	365	20.42
A ₂	33	421	23.57
A ₃	24	432	24.10
A ₄	47	435	24.32
B ₁	36	365	20.42
B ₂	41	421	23.57
B ₃	37	432	24.10
B ₄	54	435	24.32
R	56	440	24.62

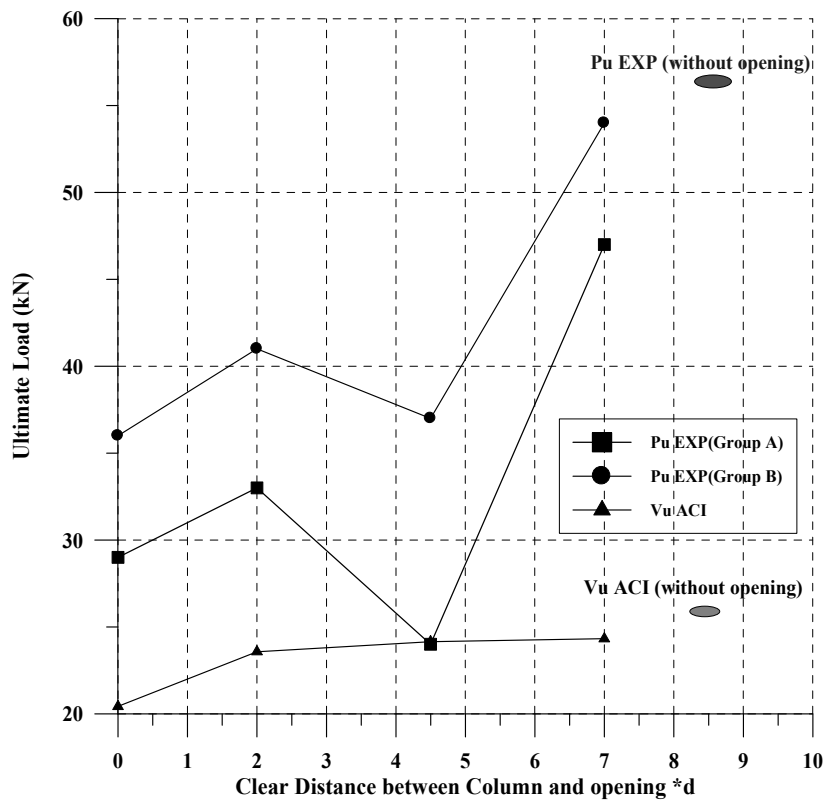
(*) $f'_c = 23$ MPa

Fig. 10: Ultimate Load – Clear Distance between column and opening relationships

**Table12: Punching Shear strength of Slabs according to BS 8110-1.**

Specimen	$P_{u(Exp)}$ kN	u (mm)	v_u (kN) using BS $v_u = v_{ck} u d$
A ₁	29	540	29.90
A ₂	33	657	36.38
A ₃	24	685	38.00
A ₄	47	720	39.87
B ₁	36	540	29.9
B ₂	41	657	36.38
B ₃	37	685	37.00
B ₄	54	720	39.87
R	56	720	39.87



MEMBRANES SEPARATION PROCESS FOR OILY WASTEWATER TREATMENT

Hasan Ferhood Makki, Ahmed Faiq Al-Alawy, Maha H. Al-Hassani and Zaid Waadulla Rashad
Chemical Engineering Department – College of Engineering – University of Baghdad – Iraq.

ABSTRACT

Pilot-scale dead end microfiltration membranes were carried out to determine the feasibility of the process for treating the oily wastewater which discharge from some Iraqi factories such as power station of south of Baghdad and the general company of petrochemical industries. Polypropylene membranes (cylindrical shape) with different pore diameters (1 and 5 micron) were used to conduct the study on micromembrane process. The variables studied are oil concentration (100 – 1000 ppm), feed flow rate (20 – 40 l/h), operating temperature (31 – 50°C) and time (0 – 3 h). It was found that the flux increases with increasing feed flow rate, temperature and pore size of membrane, and decreases with increasing oil concentration and operating time. It was found also that the effect of feed oil concentration has the greatest effect on the fouling of membrane among other variables. The percent rejection of oil improved significantly with decreasing oil concentration but decreased with increasing feed temperature, pore size of membrane and operating time. Feed flow rate has slightly effect on oil rejection. The type of oil used in this work is 20W-50 gasoline and diesel engine oil.

A general model of dead end filtration mode has been successfully evaluated to explain fundamental mechanisms involved in flux decline during dead end microfiltration of oily water emulsions. Analysis of the fall in flux with time for the polypropylene membrane (5 µm) indicates that intermediate and standard pore models give the best prediction for experimental behavior. Empirical correlations for the prediction of the flux and percent reject of oil were determined in this study. These equations have the correlation coefficient 98.87% and 91.49% respectively.

KEYWORDS: Membrane Separation; Microfiltration; Oil; Wastewater; Polypropylene Membranes.

5 1) . (1000 – 100) ((3 – 0) (° 50 – 31) (/ 40 – 20) (()) () 20W-50

(5)

%91.49 %98.87

INTRODUCTION

Oily water emulsions are one of the main pollutants emitted into water by industry and domestic sewage (1). If oil and greases are not removed from wastewater before discharging, they can cause subsequent difficulties in surface waters. Oils can blind the pores of activated carbon, ion-exchange resins, membranes, reverse osmosis and ultrafiltration units in water and wastewater treatment plants and reduce the effectiveness and life of such plants (2). Other environmental problems caused by oil and grease are toxicity to soil and aquatic organism, damages to humans, taste and odor problems, and high chemical oxygen demand (COD). Typical oil concentrations from various industrial sources are (3): petroleum (10 – 7200 mg/l), Metals (100 – 5000 mg/l), food processing (14 – 10550 mg/l), wool (3000 – 20000 mg/l), textiles (20 – 12260 mg/l) and cooling and heating (7 – 1200 mg/l). Iraqi requirements for the oil in the discharge water are 10 mg/l (4). Various types of technologies exist for treatment of oily waters. These methods are gravity separators, dissolved air flotation, coalescers, biological treatment and activated carbon adsorption (5). Over the past several years, advances have been made in developing an industrial wastewater reclaim system for a separation process for oily industrial wastewater which is extremely effective and economical in recycling of aqueous parts washing solutions. This process is based on a membrane technology that has major technical and commercial advantages over other approaches that have been tried for this application (6).

Membrane processes are those in which a membrane is used to permeate high-quality water while rejecting the passage of dissolved and suspended solids. In the water industry, the membrane processes have been used for demineralization and for removal of both dissolved and suspended particles. Tremendous improvements have been made in recent years, and the utilization of membrane technology has dramatically increased in potable water treatment. It is expected that membrane processes will be used more and more in the future as more

stringent drinking water quality standards will likely become enforced. Therefore, Membrane processes such as microfiltration (MF), ultrafiltration (UF), nanofiltration (NF) and reverse osmosis (RO) are increasingly being applied for treating oily wastewater (7). Membranes have several advantages such as more widely applicable across a wide range of industries, the quality of the treated water (the permeate) is more uniform regardless of influent variations, no extraneous chemicals are needed, making subsequent oil recovery easier, membranes can be used in-process to allow recycling of selected waste streams within a plant, concentrates up to 40±70% oil and solids can be obtained by UF or MF, membrane equipment has a smaller foot print, energy costs are lower compared to thermal treatments and the plant can be highly automated and does not require highly skilled operators (8, 9).

Microfiltration (MF) is the oldest membrane technology but it seems to be remaining in its childhood much longer than its relative's ultrafiltration and reverse osmosis (10). Microfiltration refers to filtration processes that use porous membranes to separate suspended particles with diameters between 0.1 and 10 µm. Thus, microfiltration membranes fall between ultrafiltration membranes and conventional filters. Currently there are three basic types of membranes being offered for microfiltration systems (11, 12): (a) Polymer types such as polysulfones and polypropylene are popular due to their low cost, (b) Ceramic membranes typically have a sintered metal membrane such as zirconium or titanium oxide over the support structure of an aluminum oxide tube and (c) Carbon/graphite fiber tubes use a sintered carbon membrane surface for microfiltration.

Although MF membranes can successfully treat produced waters, they experience a decline in permeate throughput or flux as a result of fouling. This flux decline is due to the adsorption and accumulation of rejected oil, suspended solids, and other components of

produced water on the membrane surface (external fouling) or in the membrane pores (internal fouling). This fouling can be irreversible or resistant to cleaning, making the original flux unrecoverable. Fouling can be reduced through the use of different or surface modified membrane materials, various operating strategies and pretreatments, and hydrodynamic techniques (13). However, specific fouling mechanisms and reduction strategies during microfiltration of produced water are not well understood (14). In the present study, to achieve low content of oil in permeate and high permeate flux, effects of operating parameters (oil concentration, temperature, feed flow rate, pore diameters and time) in a microfiltration unit were studied. Simple models have also been employed to help analyze the polypropylene membrane-fouling process. The experimental results of the oily wastewater treatment in the membrane process can be formulated in a form of empirical correlations.

MEMBRANE FOULING MODELS

Fouling is widely perceived to be the most significant issue affecting the design and operation of membrane filtration facilities (15). The permeation flux of particle-free water across a clean membrane can be described by Darcy's law as:

$$J = \frac{\Delta P}{\mu R_m} \quad (1)$$

Where J is the permeation flux, ΔP the transmembrane pressure, μ the absolute viscosity of the water and R_m the membrane resistance (16). For any constant pressure dead-end filtration, fouling of the membrane can be analyzed using different pore blocking models namely complete pore blocking model, standard pore blocking model, intermediate pore blocking model and cake filtration model (17).

The complete blocking filtration assumed that each particle reaching the membrane participates in the blocking phenomenon by pore sealing, which leads to the assumption that particles are not superimposed one upon the other (18). In standard blocking model, the particle diameter is much less than the pore diameter, thus, the particles can enter most pores, deposit on the pore walls, and thus reduce the pore volume. The decrease of pore volume is also proportional to the permeate volume (1). Intermediate blocking occurs when the size of the solute particles are

similar to the membrane pore size. In this model, it is assumed that a membrane pore is not necessarily blocked by the solute particles and some particles may settle over others. Therefore, the non-blocked membrane surface area diminishes with time and some particles are expected to obstruct the membrane pore entrance without blocking the pore completely (19). In the cake filtration model, it is assumed that the flux decline is due to the accumulation of a cake at the surface of the membrane and that cake thickness increases proportionally with the volume of permeate produced.

For microfiltration at a constant transmembrane pressure, the permeation fluxes under each of these case may be given as:

- a. Complete pore blocking model

$$J = J_0 \exp(-k_b t) \quad (2)$$

- b. Standard pore blocking model

$$J = J_0 \left(1 + \frac{1}{2} K_s (AJ_0)^{0.5} t\right)^{-2} \quad (3)$$

- c. Intermediate pore blocking model

$$J = J_0 (1 + K_i AJ_0 t)^{-1} \quad (4)$$

- d. Cake filtration model

$$J = J_0 (1 + 2K_c (AJ_0)^2 t)^{-0.5} \quad (5)$$

Where J_0 depends on the transmembrane pressure, membrane resistance and viscosity of the filtrate and is expressed as $J_0 = \Delta P / \mu R_m$. The various K terms represent mass transfer coefficients for the associated filtration laws. In the case of constant pressure filtration, the term (AJ_0) is constant and the filtration laws can be simplified to:

- a. Complete pore blocking model

$$\ln(J) = \ln(J_0) - k_b t \quad (6)$$

- b. Standard pore blocking model

$$(1/J^{0.5}) = (1/J_0^{0.5}) + k_s t \quad (7)$$

- c. Intermediate pore blocking model

$$(1/J) = (1/J_0) + k_i t \quad (8)$$

- d. Cake filtration model

$$(1/J^2) = (1/J_0^2) + k_c t \quad (9)$$

Where $k_s = (1/2) K_s A^{0.5}$, $k_i = K_i A$, $k_c = 2K_c A^2$.

Consequently plotting the left-hand side flux functions for each model against time are the tests to determine the more appropriate model and the means to obtain the mass transport parameters from the slope. Therefore, a plot of $\ln(J)$ vs. t , $(1/J^{0.5})$ vs. t , $(1/J)$ vs. t and $(1/J^2)$ vs. t shall be a straight line with slope of k_b , k_s , k_i and k_c , with y-intercept of $\ln(J_0)$, $(1/J_0^{0.5})$, $(1/J_0)$ and $(1/J_0^2)$ for complete pore blocking, standard pore blocking, intermediate pore blocking and cake filtration model, respectively. The appropriate fitness and competence of various fouling models can be confirmed by comparing the values of coefficient of correlation (R^2) obtained from the linear regression analysis (20).

MEMBRANE OIL REJECTION

The rejection percentage ($R\%$) is a combination factor between the oil concentration in feed (C_F) and oil concentration in the product (C_P). It is calculated according to the following formula.

$$R\% = \left(1 - \frac{C_P}{C_F}\right) * 100 \quad (10)$$

The decrease of oil concentration in permeate will increase the rejection percentage and vice versa (21).

EXPERIMENTAL

Materials

The Pentek PS5-10C Smooth Core Filter Cartridge is a spun polypropylene filter cartridge used to reduce dirt, sandy, rust and sediment from water. Also known as part number 255694-43. Ideal applications include water, organic acids, oils, concentrated alkalis, organic solvents and electroplating solutions. The Ametek, Pentek, USA Filter PS510C Specifications:

- Manufactured from pure 100% polypropylene.
- Designed for purity and chemical compatibility.
- Spun fibers from a true gradient density from outer to inner surfaces.
- Micron Rating: 5 and 1.
- Temperature Range: 4.4 °C to 62.8 °C

- Dimensions: $L = 25\text{ cm}$ & $d = 6.5\text{ cm}$
- Effective area: 0.051 m^2

This filter should be changed every 3 – 6 months based on water quality and usage.

Equipments

Oil – water emulsions were prepared by vigorous mixing of oil and water in the QVF glass vessel (30 l), using a stirrer (JANKE & KUNKEL GmbH, CokG, England, 1 KA – WERK, RW 14 H, Staufen) at an agitation speed of 0 - 2000 rpm. Classic oil 20W-50 (gasoline and diesel engine oil), was used for the preparation of the oil-water emulsions. Demineralized water, of 15 – 25 $\mu\text{S/cm}$ conductivity, was used for preparing emulsion with oil concentration of 100, 500 and 1000 ppm. Pressure gauge is used in the feed line to indicate the feed pressure (range of 0 – 6 bar). The physical and chemical properties of the oil are given in Table 1.

Experimental Procedure

The experimental setup is shown schematically in Figure 1. The feed was pumped by means of a centrifugal pump (11.4 – 54.6 l/min, 3 – 13.7 m. H, 210 Watt, STUART TURNER LTD. HENLEY ON THAMES ENG, England) to pass through membranes (5 μm and 1 μm) to remove oil from oil – water emulsions. The feed temperature was varied between 31 and 50 °C by means of a submersible electrical coil (220 Volt, 1000 Watt) and thermostat of range from 0 to 80 °C. The water flow rate was regulated by means of globe valve connected at the discharge of the pump (the main feed line), and measure with a calibrated rotameter with range flow (10 – 100 l/hr). Furthermore, a by-pass line with valve was located at the outlet of the pump to direct any excess flow of water back to the feed vessel (Q.V.F. cylindrical vessel of 30 liter capacity).

Permeate (filtered water) was collected every 15 minutes and volume of the permeate during the interval was measured and recorded. Concentration of oil in permeate was measured by UV-ultraviolet/visible spectrophotometer (Shimadzu model UV-160 A). Figure 2 show the calibration curve for the oil in water. The filtration flux was calculated by dividing the permeate volume by the product of effective membrane area and time. After recording the results, the solution

(remaining in feed vessel), was drained by means of a drain valve. The whole system was washed by warm water for 20 min, and then drained away. Also, detergent solution was allowed to circulate through the equipment for further 20 min, and then drained. Finally the equipment was flushed away with distilled water.

RESULTS AND DISCUSSION

Effect of Oil Concentration

Figures 3 to 4 show the effect of oil concentration on membrane flux and oil rejection for polypropylene membrane (5 μm). All experiments have been carried out at a temperature of 31°C and transmembrane pressure of 0.8 bar. It can be seen that the permeation fluxes is a decreasing function of filtration times. The flux and oil rejection decreases with increasing concentration of oil. The results show that permeation fluxes of oil feed concentrations 100, 500 and 1000 ppm decrease steeper at early filtration times (0.25 – 2 h) and by increasing the time from 2 to 3 hour, the flux slowly change and remained approximately constant.

However, when the concentration increases to 1000 ppm, the flux decreases because a layer of oil forms on the membrane surface. At lower concentrations, an oil layer formed on the membrane surface can be removed by hydrodynamic action of flow. But at higher concentrations, the hydrodynamic action cannot remove the oil layer. By increasing the operation time, this layer becomes thicker and the flux decreases as well as increasing of oil concentration in permeate i.e. decreasing the rejection of oil.

Effect of Feed Flow Rate

The effect of flow rate on flux through membrane and oil rejection is shown in Figures 5 and 6 for polypropylene membrane (5 μm). The flux increased (363.3 to 726.6 $\text{l/m}^2\cdot\text{h}$) with an increase in feed flow rate (20 to 40 l/h) at time equal to 0.25 hour due to a concomitant increase in the Reynolds number and the transition to turbulent flow (i.e. increasing the feed flow rate prevents the concentration buildup in the solution at the vicinity of the membrane surface, and resulting in decreasing the concentration of

oil in product and increasing flux). Increasing of flow rate will slightly decrease the concentration of oil in permeate (50 to 34 mg/l) at $t = 0.25$ h, and cause increase in oil rejection (90 to 93.2%) at $t = 0.25$ h.

EFFECT OF TEMPERATURE

As the operating temperature of feed increase, the flux will increase. This is shown in Figure 7. The viscosity of feed dramatically decreases with increasing temperature from 31°C to 50°C, and as a result, its permeation through the membrane becomes easier. This enhances permeate flux. Increasing temperature also increases oil content in permeate. Therefore, the rejection percentage of oil decreased with increase in operating temperature. This is shown in Figure 8. It must be mentioned that by increasing temperature, the flux increased, but higher temperatures increase the operational cost of the unit. Thus, temperatures higher than 40°C are not recommended.

EFFECT OF PORE SIZE OF MEMBRANE

Figure 9 presents the variation of permeate flux with time for polypropylene membranes with pore sizes of 5 μm and 1 μm . For two membranes, the order of water flux and ejection of oil are:

$$\begin{aligned} \text{Flux (for 5 } \mu\text{m)} &> \text{Flux (for 1 } \mu\text{m)} \text{ and } \text{Rejection} \\ \text{Oil (for 5 } \mu\text{m)} &< \text{Rejection Oil (for 1 } \mu\text{m)} \end{aligned}$$

Membrane pore size of 5 μm has a high water flux because it has high pore size which easier the flow through membrane. Figure 10 illustrates the effect of pore size on rejection percentage for oil. The fact that the permeate concentration does not generally increase with membrane pore size provides further support for the filtration being controlled by the fouling layer rather than the membrane. Generally, both membranes showed a similar trend in the relationship of permeate flux and rejection of oil.

THE FILTRATION MODELS

Figures 11 – 15 show model prediction and experimental data for different cases of Hermia's model. In most cases the models exhibit

a reasonable agreement with experimental data giving linear correlations. The model correlations for each case are given in figures. The estimation of the flux at $t = 0$ (J_0), from the intercept, gives the following values, 375.7, 381.05, 387.9 and 409.57 $\text{l/m}^2\cdot\text{h}$ for the complete pore blocking, standard pore blocking, intermediate pore blocking and cake filtration models, respectively. These values are different from the initial experimental flux, measure at 391 $\text{l/m}^2\cdot\text{h}$. The best agreement with experimental data is given by the intermediate pore blocking model and came in second level, the standard model for polypropylene membrane (5 μm).

CORRELATION ANALYSIS

The experimental data obtained from the membrane separation process experiments were correlated as a relationship between the flux (J) with different operating conditions namely; the feed oil concentration (C_F), feed flow rate (Q_F), operating temperature (T) and time (t), for polypropylene membrane (5 μm). The resulting correlation is:

$$J = 21.229 C_F^{-0.0519} Q_F^{1.018} T^{0.195} t^{-0.188} \quad (10)$$

The correlation coefficient for the above equation is 98.87%.

Also the empirical correlation of the rejection percentage of oil $R\%$ as function of C_F , Q_F , T and t lead to the following equations:

$$R\% = 213.323 C_F^{-0.094} Q_F^{0.0819} T^{-0.0164} t^{-0.155} \quad (11)$$

The correlation coefficient for the $R\%$ equation is 91.49%. The curve fitting procedure was done by STATISTICA software to find the constants and powers in Equations 10 and 11. Figures 16 and 17 show the observed values versus predicted values of flux and oil rejection obtained from Equations 10 and 11 respectively.

CONCLUSION

- The polypropylene membrane is inexpensive and available commercially. Through three hours from operating it showed efficiencies higher than 50%; therefore, this membrane can be recommended for oily wastewater treatment.

- The time of the experiment was run for three hours in order to keep the membrane and the possibility of cleaning. Then used again in other experiments.
- The flux of the membrane increases with increasing operating temperature, feed flow rate and pore size of membrane. While, the flux decreases with increasing feed oil concentration and operating time.
- The rejection of oil increases with increasing flow rate and pore size of membrane. While, the rejection decreases with increasing feed oil concentration and feed temperature.
- The flux and oil rejection decreases with increasing operating time because the fouling deposited on the surface of the membrane.
- High flow rates are suitable in order to remove the oil layer from the membrane surface. Also, temperatures higher than 40°C are not recommended because higher temperatures increased operational costs.
- The 5 μm polypropylene membrane is more permeable and exhibits a higher flux than does the 1 μm polypropylene membrane. The polypropylene membrane (1 μm) has high oil rejection.
- Experimental results in this work were in excellent agreement with intermediate pore blockage and standard models.
- The flux (J) and rejection percentage of oil $R\%$ from membrane unit are correlated to include the effect of different variables. These equations have the correlation coefficient 98.87% and 91.49% respectively.

REFERENCES

- Mohammadi, T., Kazemimoghadam, M. and Saadabadi, M., 2003, "Modeling of Membrane Fouling and Flux Decline in Reverse Osmosis During Separation of Oil in Water Emulsions", *Desalination* (157), 369 – 375.
- Percy, J.A., 1982, "Benthic and Intertidal Organisms Oil and Dispersant in



- Canadian Seas", Environment Canada Report EPS3 – EC-82-2, Ottawa, Canada.
- Jassim, M.K., 2008, "Using of Local Bentonite for Removal of Oil Contaminants from Industrial Wastewater", M.Sc. Thesis, University of Baghdad.
 - Iraqi limits for rivers maintenance system from pollution and specialized with discharge water discarded to water sources (rivers) No. 25, 1967.
 - Shams Ashaghi, K., Ebrahimi, M. and Czermak, P., 2007, "Ceramic Ultra- and Nanofiltration Membranes for Oilfield Produced Water Treatment: A Mini Review", The Open Environmental Journal, (1), 1-8.
 - Mike, P. and Ivan, A.C., 2008, "Ultrafiltration for Oily Industrial Water", NC AWWA-WEA conference November 17.
 - Syed, R.Q. Edward, M.M. and Guang Z., 2000, "Water Works Engineering: Planning, Design, and Operation", Prentice – Hall, Inc., USA.
 - Cheryana, M. and Rajagopalanb, N., 1998, "Membrane Processing of Oily Streams. Wastewater Treatment and Waste Reduction", Journal of Membrane Science (151), 13 – 28.
 - Cheryan, M., 1998, "Ultrafiltration and Microfiltration Handbook", Technomic, Lancaster, PA.
 - Rune, G., 1985, "Microfiltration – State of the Art", Desalination (53), 363 – 372.
 - John, A.B., 2003, "Feasibility of Cross-Flow Microfiltration for Combined Sewer Overflows", M.Sc. Thesis, Pittsburgh University.
 - Mohammed, B., 2008, "Membrane Separation Process for Treatment and Reuse of Water from Effluents of Cooling Towers", M.Sc. Thesis, University of Baghdad.
 - Zaidi, A., Simms, K., Kok, S. and Nelson, R., 1992, "Recent Advances in the Application of Membrane Technology for the Removal of Oil and Suspended Solids from Produced Water", in J.P. Ray and E.R. Engelhart (Eds.) Produced Water, Plenum Press, New York, 1992.
 - Jeffrey, M., Yanwei, C. and Robert H.D., 1997, "Crossflow microfiltration of oily water", Journal of Membrane Science (129), 221– 235.
 - John, C.C., Rhodes, R.T., David, W.H., Kerry, J.H., and George, T., 2005, "Water Treatment: Principles and Design", John Wiley & Sons, Inc., 2nd Ed.
 - Lim, A.L., and Renbi, B., 2003, "Membrane Fouling and Cleaning in Microfiltration of Activated Sludge Wastewater", Journal of Membrane Science (216), 279– 290.
 - Hermia, J., 1982, "Constant pressure blocking filtration laws-application to power-law non-Newtonian fluids", Chem. Eng. Res. Des., (60), 183–187.
 - Ohyaa, H., Kimb, J.J., Chinena, A., Aiharaa, M., Semenovaa, S.I., Negishia, Y., Moric, O., and Yasudac, M., 1998, "Effects of pore size on separation mechanisms of microfiltration of oily water, using porous glass tubular membrane", Journal of Membrane Science (145), 1– 14.
 - Nandi, B.K., Moparathi, A., Uppaluri, R. and Purkait, M.K., 2010, "Treatment of oily wastewater using low cost ceramic membrane: Comparative assessment of pore blocking and artificial neural network models", chemical engineering research and design, journal homepage: www.elsevier.com/locate/cherd.
 - Peng, H. and Tremblay, A.Y., 2008, "Membrane regeneration and filtration modeling in treating oily wastewaters", Journal of Membrane Science (324), 59 – 66.
 - Ahmed, F.H., 2000, "Study of The Factors Affecting the Efficiency of Reverse Osmosis Process", M.Sc. thesis, Baghdad University.

**NOMENCLATURE**

Symbol	Definition	Units
ΔP	Transmembrane Pressure	bar
A	surface area of the membrane	m^2
C_f	Feed Concentration	ppm
C_p	Product Concentration	ppm
J	Permeation Flux	$l/m^2.h$
J_0	Initial filtrate Flux through the Membrane	$l/m^2.h$
k_b	constant in complete blocking model	h^{-1}
k_c	constant in cake filtration model	h^{-1}
k_i	constant in intermediate pore blocking model	h^{-1}
k_s	constant in standard pore blocking model	h^{-1}
Q_F	Feed Flow Rate	l/h
R	rejection	
R_m	Membrane Resistance	m^{-1}
t	Time	h
T	Temperature	$^{\circ}C$
Greek Symbols		Units
Symbol	Definition	
μ	Absolute Viscosity of the Water	Pa s

Table 1 The Physical and Chemical Properties of Oil

Viscosity grade	20W-50
Colour	Amber
Physical State	Liquid at ambient temperature
Odour	Characteristic mineral oil
Vapour Pressure	Expected to be less than 0.5 Pa at 20 $^{\circ}C$
Initial Boiling Point	Expected to be above 280 $^{\circ}C$
Solubility in Water	Negligible
Density	888 kg/m^3 at 15 $^{\circ}C$.
Flash Point	215 $^{\circ}C$
Flammable Limits - Upper	1% (V/V)
Flammable Limits - Lower	10% (V/V)
Auto-Ignition Temperature	Expected to be above 320 $^{\circ}C$
Kinematic Viscosity	157 mm^2/s at 40 $^{\circ}C$
Pour Point	-27 $^{\circ}C$

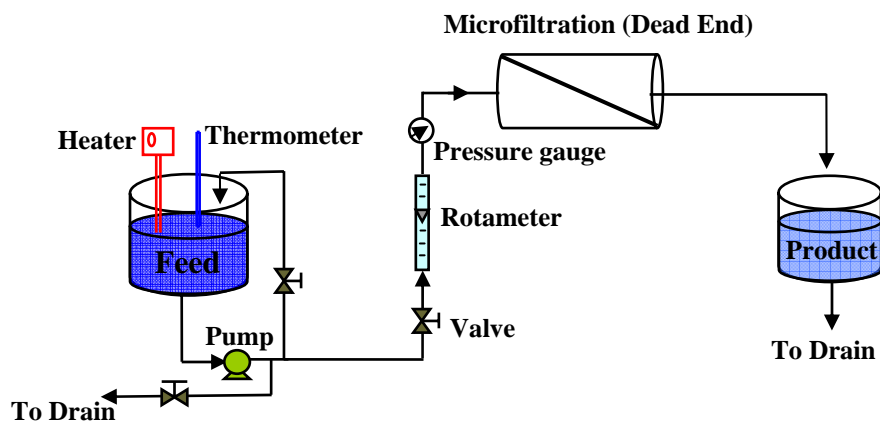


Fig. 1 Schematic Diagram of Microfiltration Process

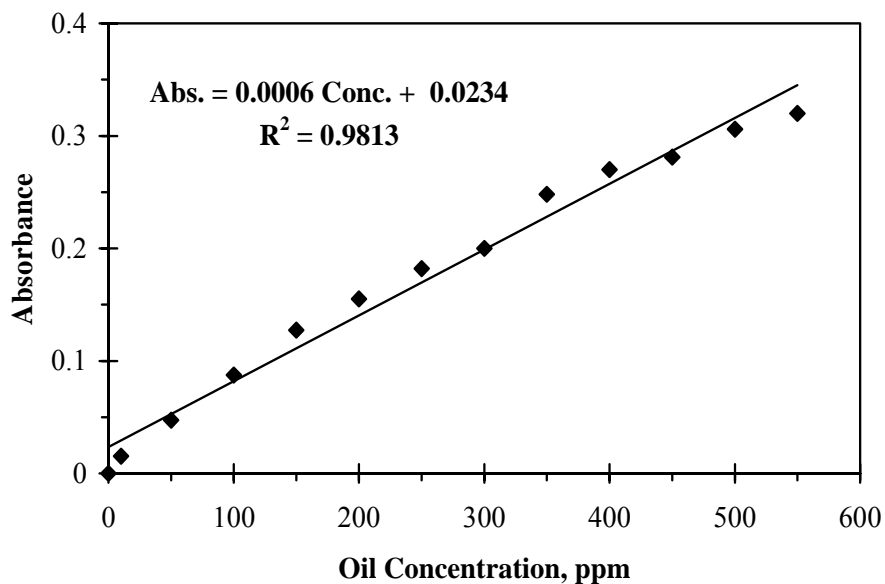


Fig. 2 Oil Concentrations vs. Absorbance (Calibration Curve)

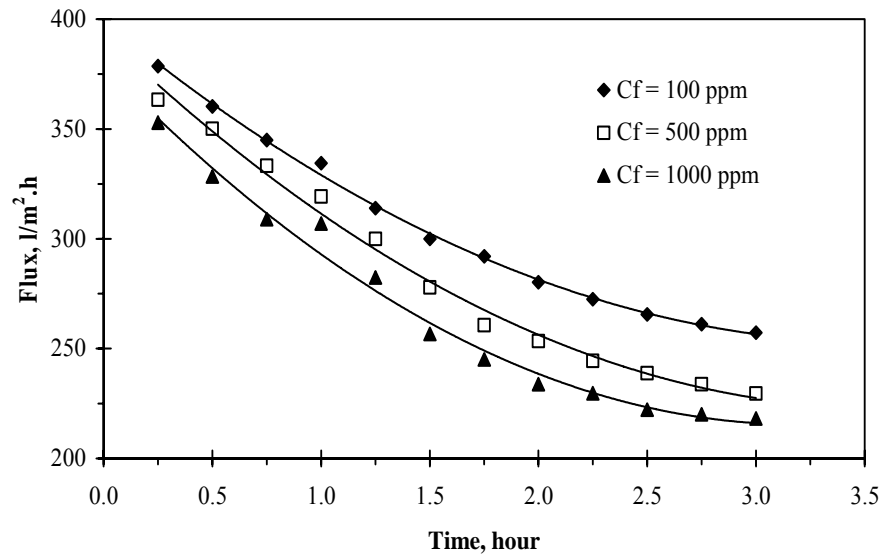


Fig. 3 Flux vs. Time at Different Oil Concentrations ($Q_F = 20$ l/h and $T = 31^\circ\text{C}$)

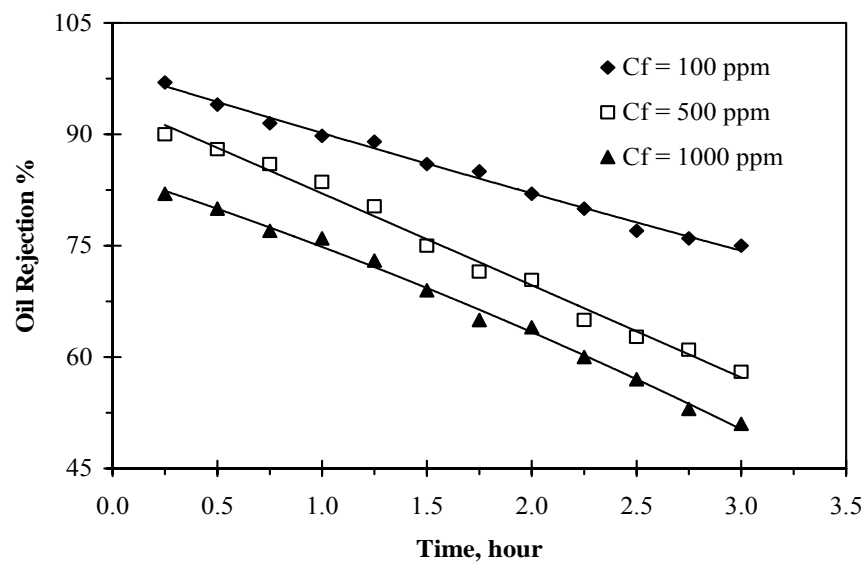


Fig. 4 Oil Rejection vs. Time at Different Oil Concentrations ($Q_F = 20$ l/h and $T = 31^\circ\text{C}$)

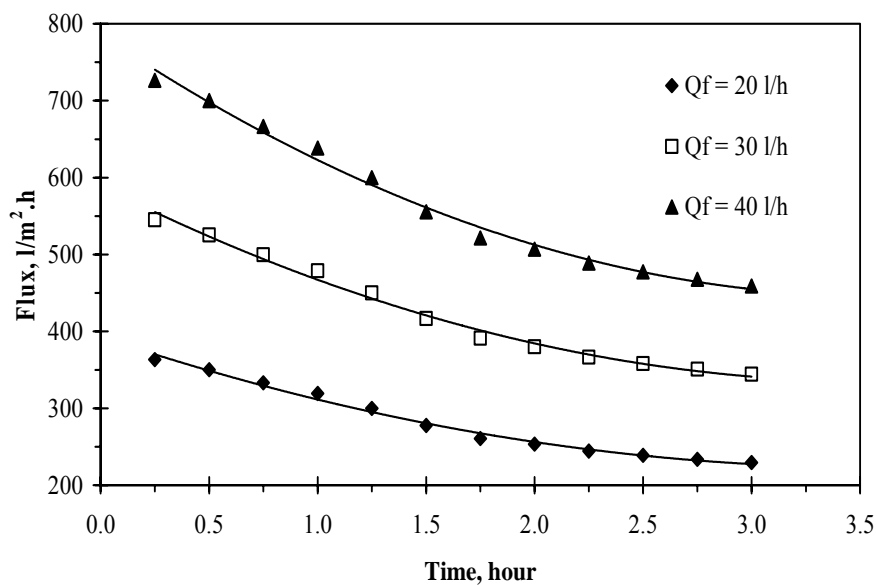


Fig. 5 Flux vs. Time at Different Feed Flow Rate ($C_F = 500$ ppm and $T = 31^\circ C$)

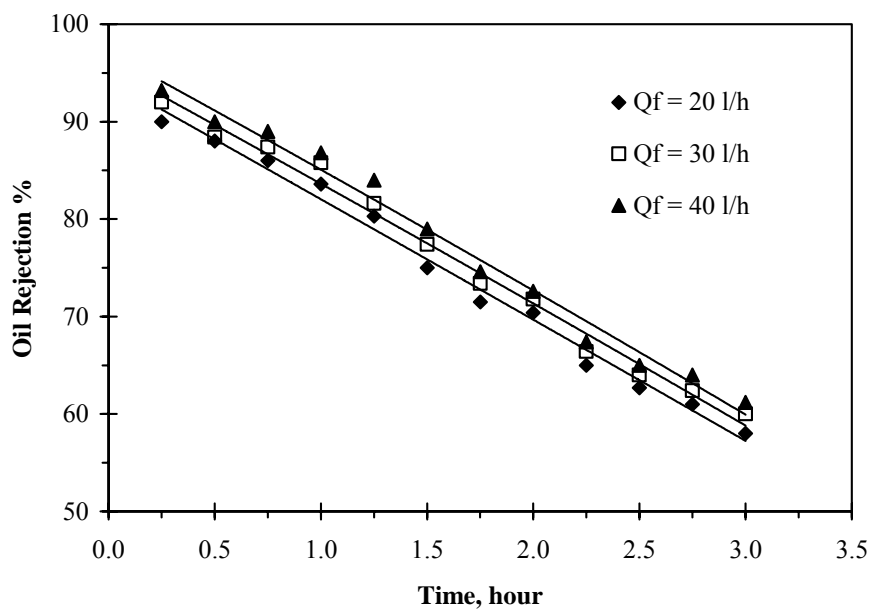


Fig. 6 Oil Rejection vs. Time at Different Feed Flow Rate ($C_F = 500$ ppm and $T = 31^\circ C$)

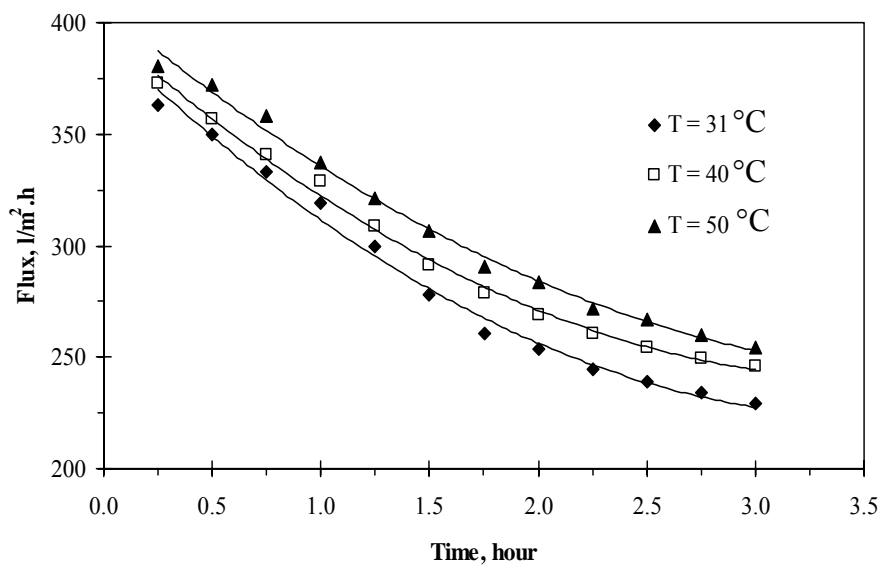


Fig. 7 Flux vs. Time at Different Feed Temperature ($C_F = 500$ ppm and $Q_F = 20$ l/h)

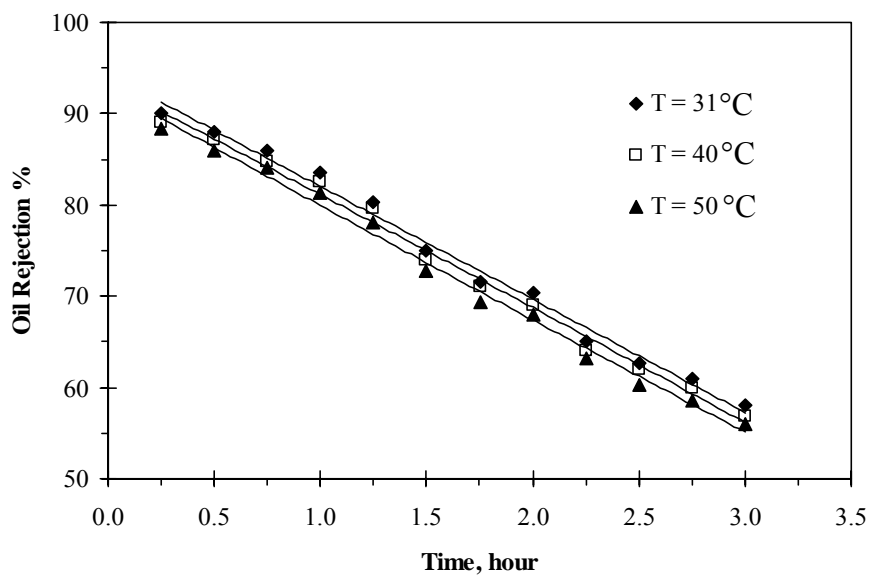


Fig. 8 Oil Rejection vs. Time at Different Feed Temperature ($C_F = 500$ ppm and $Q_F = 20$ l/h)

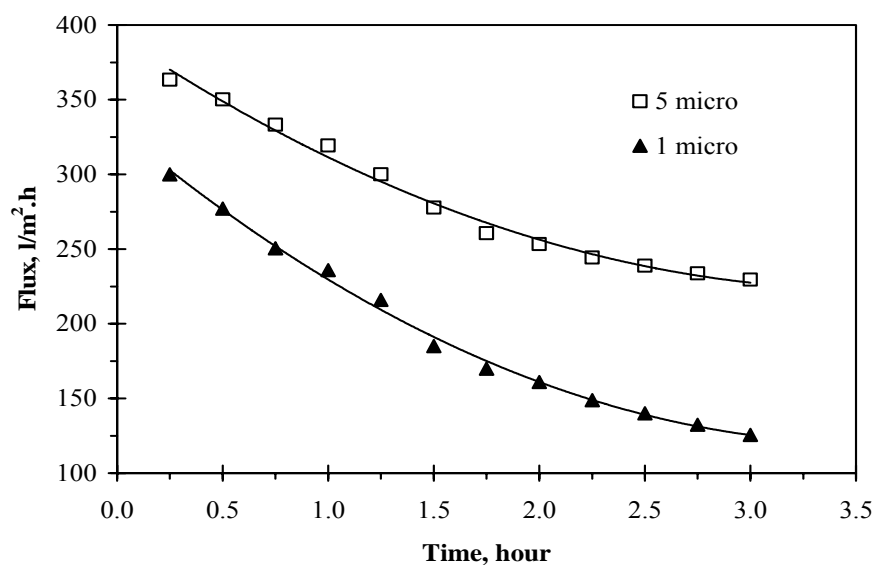


Fig. 9 Flux vs. Time at Different Pore Size ($C_F = 500$ ppm, $T = 31^\circ\text{C}$ and $Q_F = 20$ l/h)

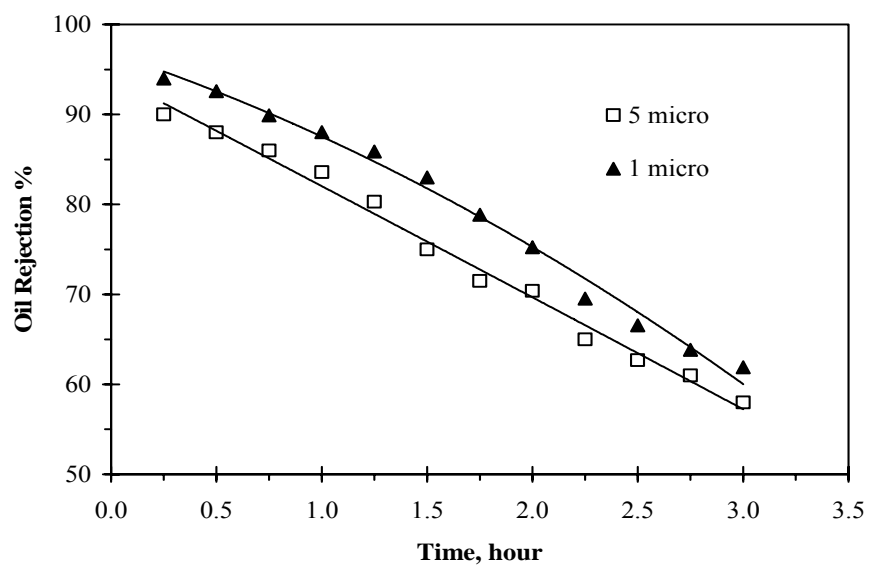


Fig. 10 Oil Rejection vs. Time at Different Pore Size ($C_F = 500$ ppm, $T = 31^\circ\text{C}$ and $Q_F = 20$ l/h)

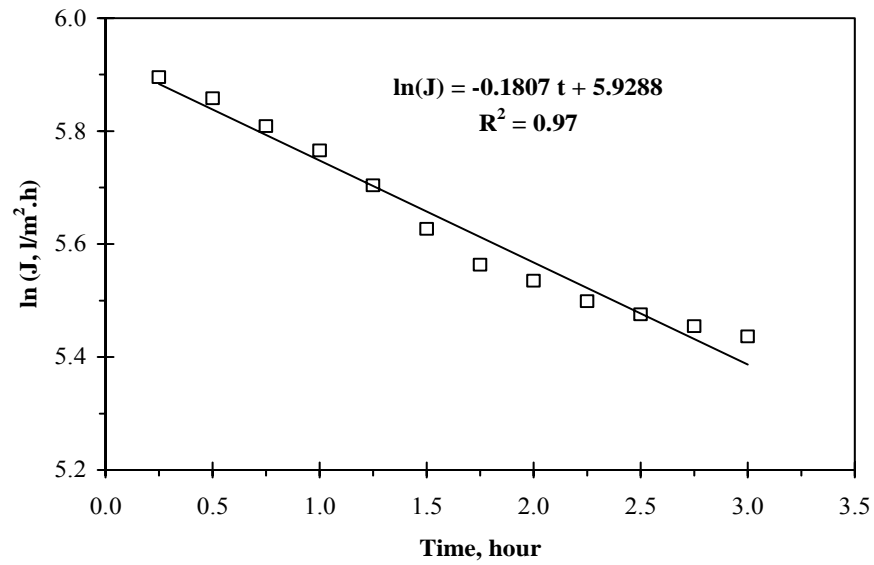


Fig. 11 Complete Pore Blocking Model ($C_F = 500$ ppm, $T = 31^\circ\text{C}$ and $Q_F = 20$ l/h)

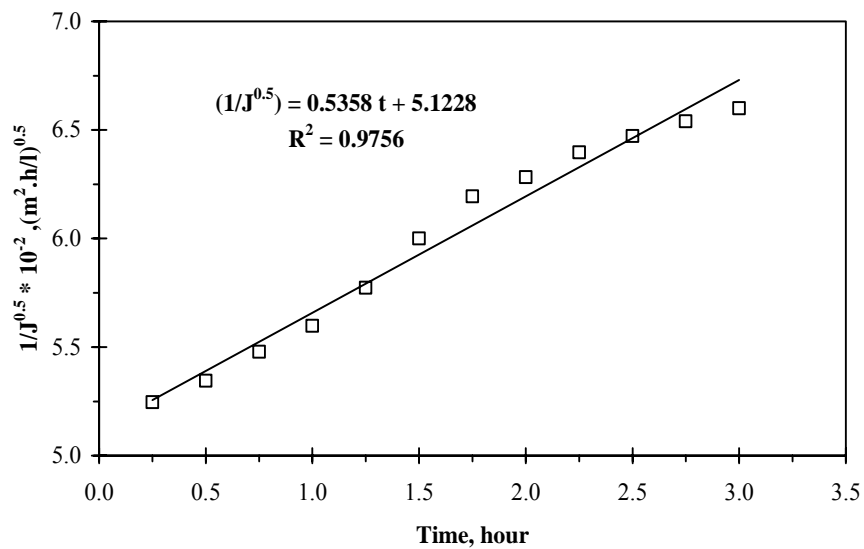


Fig. 12 Standard Pore Blocking Model ($C_F = 500$ ppm, $T = 31^\circ\text{C}$ and $Q_F = 20$ l/h)

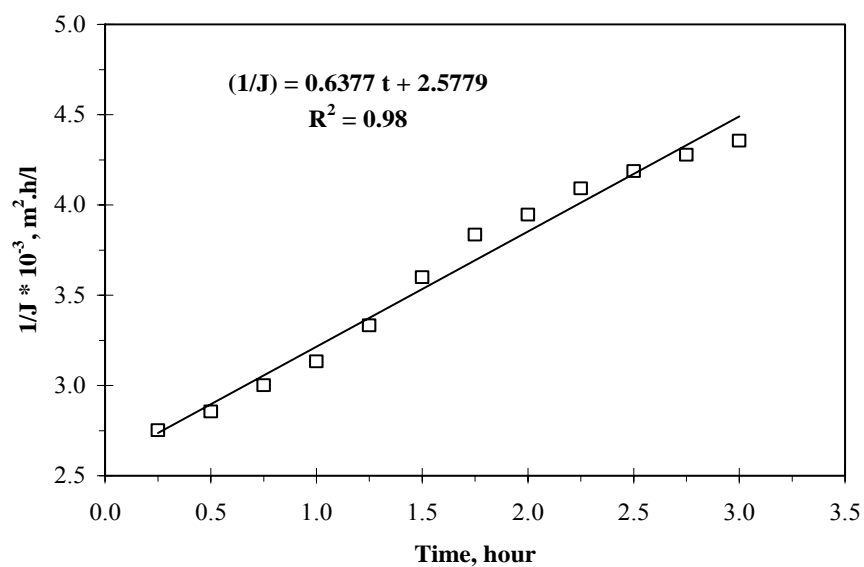


Fig. 13 Intermediate Pore Blocking Model ($C_F = 500$ ppm, $T = 31^\circ\text{C}$ and $Q_F = 20$ l/h)

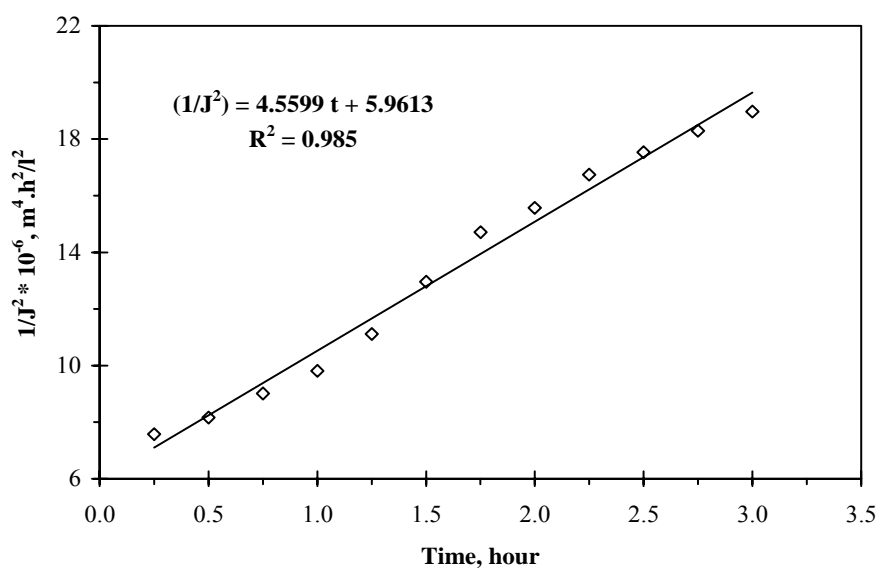


Fig. 14 Cake Filtration Model ($C_F = 500$ ppm, $T = 31^\circ\text{C}$ and $Q_F = 20$ l/h)

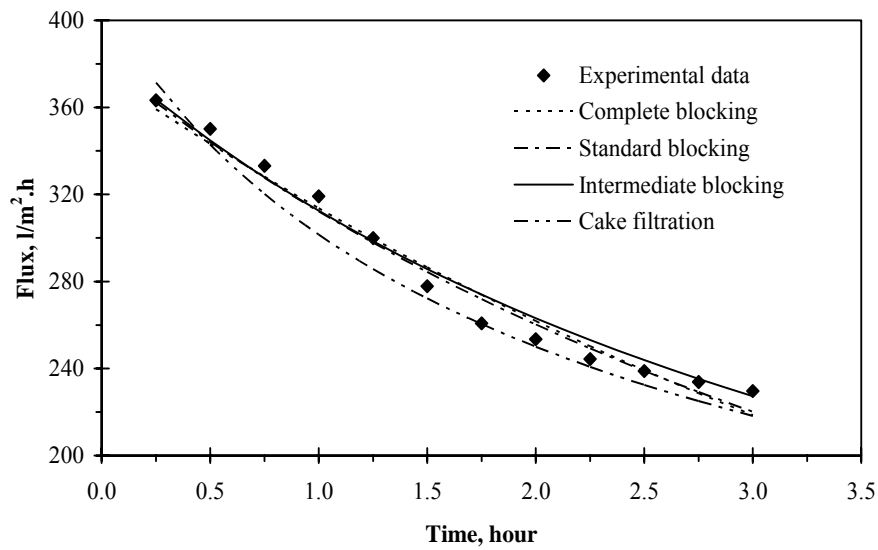


Fig. 15 Comparison of Filtration Model Prediction with Experimental Data for Polypropylene Membrane (5 μm)

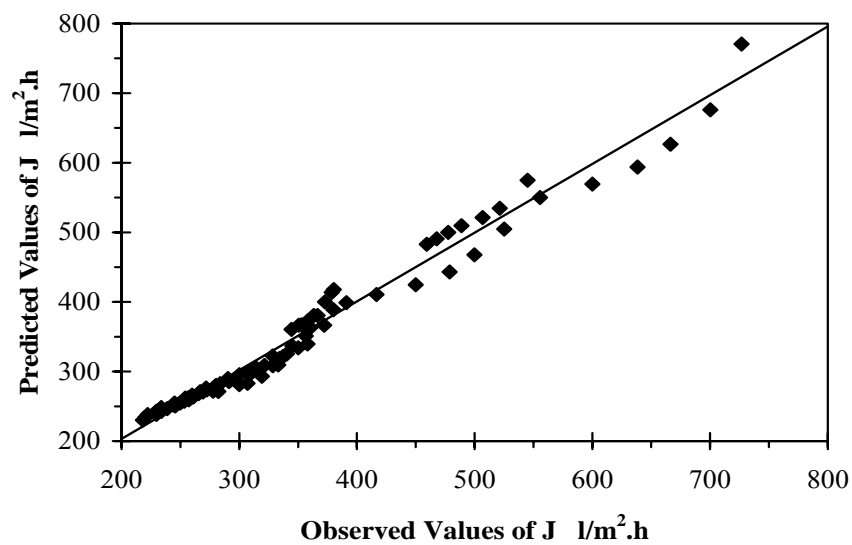


Fig. 16 Observed Versus Predicted Values of Flux

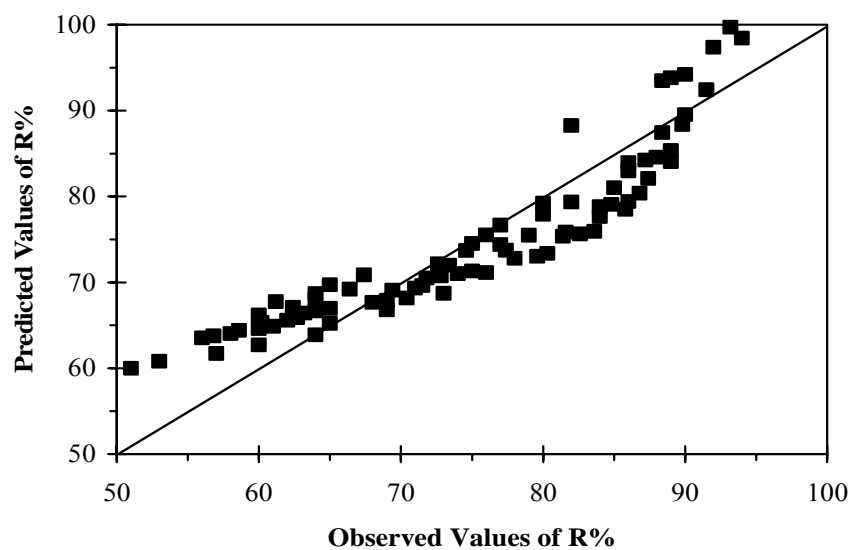


Fig. 17 Observed Versus Predicted Values of Oil Rejection

OILY WATER TREATMENT USING CERAMIC MEMBERANE

Sama Mohammed Abdullah

College of Engineering – University of Baghdad – Iraq.

ABSTRACT

This research was conducted using ceramic microfiltration membrane for treatment of oily wastewater in the pilot-scale dead-end filtration system designed in the laboratory under the influence of conditions of feed flow rate 15-35 l/h, feed temperature 32-48°C, oil feed concentration 300-1200 ppm, feed solution pH 2.6-9.8. The influence of these conditions on the permeate flux rate and oil rejection percent were investigated. Experimental results indicated that when feed flow rate increased to 35 l/h permeate flux rates increased to 100 l/m².h and oil rejection percent decreased to 70.1%, and when feed temperature increased to 48 °C permeate flux rate increased to 62 l/m².h and oil rejection percent decreased to 56.44%. But when oil feed concentration increased to 1200 ppm permeate flux rate decreased to 17.2 l/m².h and oil rejection percent increased to 99.7%. Also basic feed solution (pH=9.8) gave high permeate flux rate (44.51 l/m².h) and low oil rejection percent (84%) in comparison with acidic feed solution (pH=2.6) which gave low permeate flux rate (26.42 l/m².h) and high oil rejection percent (99.46%). Four classical models were investigated to flux decline and the results showed that the experimental data was consistent ($R^2 = 0.9883$) with the complete blocking filtration model.

الخلاصة

تم في هذا البحث استخدام غشاء سيراميك مايكرو فلتر لمعالجة المياه الملوثة بالزيت في منظومة ترشيح مختبرية ذات النهاية المسدودة المصممة في المختبر تحت تأثير ظروف تشغيلية من معدل جريان التغذية 15-35 لتر/ساعة و درجة حرارة 32-48 °م و تركيز زيت ابتدائي 300-1200 جزء بالمليون ودرجة حامضية 2.6-9.8. تم هنا دراسة تأثير هذه المتغيرات على معدل تدفق الراشح ونسبة طرح الزيت. النتائج المختبرية أثبتت أنه عند زيادة معدل جريان التغذية الى 35 لتر/ساعة يزداد معدل تدفق الراشح الى 100 لتر/متر². ساعة و تنخفض نسبة طرح الزيت الى 70.1% وأن زيادة درجة الحرارة الى 48 °م ترفع معدل تدفق الراشح الى 62 لتر/متر². ساعة و تقلل نسبة طرح الزيت الى 56.44%. لكن زيادة التركيز الابتدائي للزيت في التغذية الى 1200 جزء بالمليون تقلل معدل تدفق الراشح الى 17.2% وترفع نسبة طرح الزيت الى 99.7%. أيضا عندما يكون محلول التغذية قاعديا (pH = 9.8) فإنه يعطي معدل تدفق الراشح أعلى (44.51 لتر/متر². ساعة) و نسبة طرح الزيت أقل (84%) بالمقارنة مع محلول التغذية الحامضي (pH = 2.6) الذي يعطي معدل تدفق الراشح أقل (26.42 لتر/متر². ساعة) و نسبة طرح الزيت أعلى (99.46%). تم دراسة اربعة موديلات لتنبؤ بسلوك تدفق الراشح وظهرت النتائج ان النتائج العملية متطابقة ($R^2 = 0.9883$) مع موديل انسداد المرشح التام.

INTRODUCTION

Nowadays, considerable attention has been focused on the discharge of oily wastewater and its influence on the environment. Pollution of water by oily hydrocarbon is especially harmful to the aquatic life, as it attenuates the light and perturbs the normal oxygen transfer mechanism (Srijaroonrat et al. 1999). In the recent years, the application of vegetable oils in industries has a great attention because vegetable oils are renewable, non-toxic and environmentally friendly resource. Vegetable oils are considered to be potential candidates to substitute conventional mineral oil-based lubricating oils and synthetic esters as a result of the stringent requirement of resource conservation and environmental protection (Hua et al. 2007). The main source of vegetable oil effluent are : degumming, deacidification, deodorization steps, the blow down of the boiler and wash water from de-oiling of the bleaching earth also contribute to the effluent in small amounts (Sridhar et al. 2002).

Typical composition ranges of "Produced water" generated in the oily wastewater oil, and gas industrial processes include 50-1000 ppm of total oil and grease and 50-350 ppm of total suspended solids (TSS). Stricter environmental legislations enforce the maximum total oil and grease concentration in discharge waters to be 10-15 ppm. Major pollution in wastewater (also Known as produced water) generating from oil field is oil which may range between 100 and 1000 ppm or more depending on emulsification efficiency and crude oil nature (Abbasi et al. 2010 and Abbasi et al. 2010). The small quantity of remaining oil in water must be reduced to an acceptable limit before the water can be discharged into the sea or rivers or reinjected for water flooding. Purification of this water is urgent issue so that it can be reused to save water resources and to protect the environment (Li et al. 2006 and Abbasi et al. 2010).

In wastewater treatment plants, there exist several techniques for separation. Typical ones include gravity separation and skimming, dissolve air flotation, demulsification, coagulation and flocculation, which have several disadvantages such as low efficiency, high operation costs, corrosion and recontamination problems (Mohammadi et al. 2003 and Li et al. 2006). The emulsified oily wastewater from the processing of petroleum products (particularly in oil

exploitation) was difficult to treat by using these above common methods because in addition to above reasons, those operations could create a series of problems in the application. These problems not enclosed by upsetting equipment's surface and potentially choke reservoir, but also create huge waste with the rejected wastewater containing significant amount of crude oil and lead to serious environmental pollution (Wang et al. 2009).

One of the treatment techniques used for oil separation from emulsified oily wastewater is membrane filtration (Salahi et al. 2010). Membrane separation has enjoyed great candidate since 1973 and is becoming attractive technology due to low energy consumption, no chemical additives are needed to break the emulsion, high COD removal efficiencies, and treatment facilities are quite compact and fully automated (Hua et al. 2007 and Wu et al. 2008). One troublesome problem encountered in many membrane plants is fouling which can cause a decrease in flux due to pore blocking, solute aggregation (which lead to the formation of cake, or gel layer, on the surface of the membrane) or adsorption (Brinck et al. 2000). Obtaining membranes that are capable of lowering the solutes tendency to deposit on the membrane surface will minimize fouling (Masuelli et al. 2009). Also, the development of effective membrane cleaning method is desirable for diminishing this phenomenon such as backwashing by liquid or gas (Peng and Tremblay 2008).

Ceramic membranes have been Known for years and used in many different applications depending on their numerous advantages: stability at high temperatures and pressure resistance, good chemical stability, high mechanical resistance, long life and antifouling properties (Abbasi et al. 2010). Ceramic microfiltration membranes can be made from alumina, mullite, cordierite, silica, spinel, zirconia and other refractory oxides. These membranes are very cheap because they can be prepared by extruding and calcining kaolin clay (Abbasi et al. 2010 and Abbasi et al. 2010).

Many studies focused on empirical models based on non-linear correlations for the description of permeate flux decline with time. Such these correlations that the empirical models were presented by Hermia 1982, which used to identify the fouling mechanism occurred during

microfiltration process (Grenier et al. 2008, Nandi et al. 2010 and Salahi et al 2010).

The objective of this paper is to investigate oily water treatment using ceramic membrane and the influence of feed flow rate, feed temperature, oil feed concentration and feed solution pH on the permeate flux and oil rejection percent. Determination the most appropriate applicable model to the experimental data for ceramic membrane microfiltration of oily water emulsion was investigated using the empirical models presented by Hermia 1982.

THEORY

The importance of applying filtration models for flux decline to predict the variation in flux rate with time during filtration process has led to various fouling mechanisms to be proposed to better characterize the flux performance (Hu and Scott 2008 and Nandi 2010).

There are four classical filtration models were proposed by Hermia 1982 are often used to describe fouling in relations correlate the permeate flux rate with the operating time (Ohya et al. 1998, Grenier et al. 2008 and Nandi 2010). These models are:

- Complete blocking filtration assumes a seal of pores entrances and prevention of any flow through them because the large size of particles such that the particles are not superimposed one upon the other.

$$\ln(F) = \ln(F_0) - K_{\text{comp}}.t \quad (1)$$

- Intermediate blocking filtration assumes a seal of pore entrances by a fraction of particles and some particles may settle over other.

$$1/F = 1/F_0 + K_{\text{inter}}.t \quad (2)$$

- Standard blocking filtration (or sometimes called Gradual pore blocking) assumes an accumulation inside the pore walls of the membrane causing proportional decreasing in pore volume with filtrate volume.

$$1/F^{0.5} = 1/F_0^{0.5} + K_{\text{standr}}.t \quad (3)$$

- Cake filtration assumes an accumulation of particles on the membrane surface forming cake layer, its thickness increases with time that adds a hydraulic resistance to filtration.

$$1/F^2 = 1/F_0^2 + K_{\text{cake}}.t \quad (4)$$

Plotting the left hand side flux function of each model verse time must be a straight line, and then plotting flux from experimental data and that is determined by these four models versus time. Often the model which best fits the experimental data is claimed to capture the fouling mechanism.

EXPERIMENTAL STUDY

Materials

The commercial tubular ceramic microfiltration membrane (0.8-0.3 μ) used in this research was made of kaolin (inside diameter: 1.5 cm, outside diameter: 4.6 cm. and length: 22 cm.). Ceramic membrane was put in the filter cartridge (100 % poly propylene). Oil-in-water emulsion (oily wastewater feed solution) was prepared by mixing edible vegetable oil (bizec oil made in Turkey, density: 910 kg/m³ and viscosity: 4.37 $\times 10^{-2}$ kg/m.sec.) and tap water using homogenizer. 1M of NaOH solution (99.97% purity was purchased from BDH Chemicals Ltd) and H₂SO₄ (95.97% purity was purchased from Fluka) were used to adjust pH of feed solution.

Experimental Setup

Fig.1 shows the pilot-plant used in all the experiments. The pilot was operated in a dead-end cell. This system was consisted of a glass feed tank with a capacity of 30 l. supplied with automatic heater to heat the feed and keep it at a constant temperature and stirrer to keep the feed homogeneous. The feed was pumped through the system by means of centrifugal pump. Permeate from the system was collected in a 500 ml cylinder to determine permeate flux.

A sample of feed solution was withdrawn immediately before filtration started while sample of permeate was withdrawn periodically every 15 min. to be analyzed. The analysis of samples was attempted using ultraviolet visible light spectra photometer (Shimadzu model UV-160A) at wave length 303 nm. Periodically and after each run the membrane was regenerated physically and due to its rigidity and without any problem it was cleaned with hot water (60°C). The effectiveness of the filtration process was denoted in terms of oil rejection percent and permeate flux rate. Oil rejection percent is determined as:

$$R \% = (1 - C_p / C_f) \times 100 \quad (5)$$

While permeate flux rate is determined as:

$$F = V / A.t \quad (6)$$

RESULTS AND DISCUSSIONS

Feed Flow Rate Effect

The effect of flow rates (15, 25 and 35 l/h). on the treatment process performance were investigated with the operation conditions of feed temperature 32°C, oil feed concentration 300 ppm, and feed solution pH 6.86. Fig.2 and Fig.3 show the effect of feed flow rate on the permeate flux rate and the oil rejection percent. As shown increasing flow rate leads to increase permeate flux rate but decrease rejection percent.

This behavior may be attributed to the fact that at dead end filtration the cake/gel layer can be formed easily due to absence applied shear. Therefore increasing flow rate leads to removing the oil layer from the membrane surface. Due to extent of mixing over the membrane surface, this can reduce accumulate of oil drops which essentially acts as a dynamic membrane, as a result the oil drops on the membrane surface diffuse back to the bulk solution. The results obtained here are in good agreement with Mohammadi et al. (2003) and Wu et al. (2008).

Feed Temperature Effect

Fig. 4 and Fig.5 present the effect of temperature on the treatment efficiency at conditions of feed flow rate 15 l/h, oil feed concentration 300 ppm, and feed solution pH 6.86. While temperatures 32, 40 and 48°C was chosen for this study.

It can be observed that increasing feed temperature causes increasing in permeate flux and decreasing oil rejection percent. This can explain as at high temperatures oil/water emulsion viscosity decreases and lower viscosity eases fluid permeate through the membrane surface. These results agree with Wang et al. (2009) and Abbasi et al. (2010).

Oil Feed Concentration Effect

Oil feed concentrations of 300, 600 and 1200 ppm were investigated with the operation conditions of feed flow rate 15 l/h, feed temperature 32°C, and feed solution pH 6.86. The

influence of oil feed concentrations are shown in Fig.6 and Fig.7.

According to the results the lower oil concentration the higher permeation flux of the membrane, but the oil rejection decreasing with the decreasing of oil concentration in the feed. These results are attributed to the formation of oil layer on the membrane surface with thickness increases with increasing oil feed concentration specially at dead end filtration process because there is no hydrodynamic action causes removing this layer. These results agree with Wu et al. (2008) and Abassi et al. (2010).

Feed Solution pH Effect

The effect of feed solution pH was illustrated in Fig.8 and Fig.9, at conditions of feed flow rate 15 l/h, feed temperature 32°C, and oil feed concentration 300 ppm at different feed pH of 6.86, 9.8 and 2.6. As can seen from the figure the permeate flux was increase at steady rate at the basic medium while decreased sharply at the acidic medium, but the reverse behavior can be seen for oil rejection.

This behavior was explained by former researcher as that the permeate flux under different pH was effected by the properties of the solute (droplet) in addition to the characteristics of the membrane. The stability of the oil in water emulsion was more stable at pH 4-6 than at pH of 6-10. Therefore the emulsion didn't coagulate under stable condition and so the lower level of flux was observed at low pH. While the cake layer become more open at high pH due to the inter-droplet repulsion, and this increased the permeability, resulting in higher permeate flux. It's noticeable to mention the thickness of cake layer reduced due to the particle deposition prevented by the inter-droplet repulsion. While, corresponding to the membrane surface properties, it was found that at lower feed solution pH the membrane becomes hydrophilic and at higher feed solution pH the membrane becomes hydrophobic. Hydrophobic membrane tends to absorb foulant (oil), while leads to oil attachment on the membrane surface and therefore high oil passage. This result is agree with A-Jeshi and Nevill (2008).

Model Analysis

Models are investigated for the run with conditions of feed flow rate 15 l/h, feed temperature 32°C, oil feed concentration 300 ppm



and feed solution pH 6.86, and the Fig.'s 10-14 show model prediction and experimental data for Hermia's model in different cases. The complete blocking filtration model explained the experimental data very well, as previously mentioned, the complete pore blocking happens when pore entrance blockage, which cause reduction the area to flow and leads to prevention of any flow through it. .

CONCLUSIONS

The experimental results of this work showed that using of ceramic microfiltration membrane process was effective for treatment oily water. It was obtained that F increases with increasing feed flow rate, feed temperature and feed solution pH, but decreases by increasing oil feed concentration. The results also proved that increasing oil feed concentration, acidity of the feed solution causes increasing R %, but it decreases when feed flow rate and feed temperature increase. Comparing experimental data with Hermia's model showed the best consistency corresponds to the complete blocking filtration model.

REFERENCES

- Abbasi M., Salahi A., Mirfendereski M., Mohammadi T. and Pak A., 2010, "Dimensional analysis of permeation flux for microfiltration of oily wastewater using mullite ceramic membranes", *Desalination*, 252, 113-119.
- Abbasi M., Mirfendereski M., Nikbakht M., Golshenas M. and Mohammadi T., 2010, "Performance study of mullite and mullite-alumina ceramic MF membranes for oily wastewaters treatment", *Desalination*, xxx, xxx-xxx.
- Al-Jeshi S. and Neville A., 2008, "An experimental evaluation of revers osmosis memberane performance in oily water", *Desalination*, 228, 287-294.
- Brinck J., Jönsson A.-S., Jönsson B., Lindau J., 2000, "Influnce of pH on the adsorption fouling ultrafiltration memberanes by fatty acid", *Journal of Membrane Science*, 164, 187-194.
- Grenier A., Meireles M., Aimar P. and Carvin Ph., 2008, "Analysis flux decline in dead-end filtration", *Chemical Engineering Research and Design*, 86, 1281-1293.
- Hu B. and Scott K., 2008, "Microfiltration of water in oil emulsions and evaluation of fouling mechanism", *Chemical Engineering Journal*, 136, 210-220.
- Hu F.L., Tsang Y.F., Wang Y.J., Chan S.Y., Chua H., Sin S.N., 2007, "Performance study of ceramic microfiltration membrane for oily wastewater treatment", *Chemical Engineering Journal*, 128, 169-175.
- Li Y.S., Yan L., Xiang C. B. and Hong L.J., 2006, "Treatment of oily wastewater by organic-inorganic composite tubular ultrafiltration (UF) membranes", *Desalination*, 196, 76-83.
- Masuelli M., Marchese J. and Ochoa N.A., 2009, "SPC/PVDF membranes for emulsified oily wastewater treatment", *Journal of Membrane Science*, 326, 688-693.
- Mohammadi T., Kazemimoghadam M. and Saadabadi M., 2003, "Modeling of membrane fouling and flux decline in reverse osmosis during separation of oil in water emulsion", *Desalination*, 157, 369-375.
- Nandi B.K., Moparthi A., Uppaluri R. and Purkait M.K., 2010, "Treatment of oily wastewater using low cost ceramic membrane: Comparative assessment of pore blocking and artificial neural network models", *Chemical Engineering Research and Design*, xxx, xxx-xxx.
- Ohya H., Kim J.J., Chinen A., Aihara M., Semenova S.I., Negishi Y., Mori O. Yasuda M., 1998, "Effects of pore size on separation mechanisms of microfiltration of oily water, using porous glass tubular membrane", *Journal of Membrane Science*, 145, 1-14.

- Peng H. and Tremblay A.Y., 2008, "Membrane regeneration and filtration modeling in treating oily wastewater", Journal of Membrane Science, 324, 59-66.
- Salahi A., Abbasi M. and Mohammadi T., 2010, "Permeate flux decline during UF of oily wastewater: Experimental and modeling", Desalination, 251, 153-160.
- Sridhar S., Kale A. and Khan A.A., 2002, "Reveres osmosis of edible vegetable oil industry effluent", Journal of Membrane Science, 205, 83-90.
- Srijaroonrat P., Julien E. and Aurelle Y., 1999, "Unstable secondary oil/water emulsion treatment using ultrafiltration: fouling control by backflushing", Journal of Membrane Science, 159, 11-20.
- Wang Y., Chen X., Zhang J., Yin J. and Wang H., 2009, "Investigation of microfiltration for treatment of emulsified oily wastewater from the processing of petroleum products", Desalination, 249, 1223-1227.
- Wu C., Li A., Li L., Zhang L., Wang H., Qi X. and Zhang Q., 2008, "Treatment of oily water by a poly (vinyl alcohol) ultra filtration membrane", Desalination, 225, 312-321.

NOMENCLATURES

A	Effective Membrane Area (m^2)
C_f	Oil Concentration in The Feed (ppm)
C_p	Oil Concentration in The Permeate (ppm)
F	Permeate Flux Ratio ($\text{l}/\text{m}^2.\text{h}$)
F_0	Initial Permeate Flux Ratio ($\text{l}/\text{m}^2.\text{h}$)
K_{cake}	Y-intercept of cake filtration model ($(\text{m}^2/\text{l})^2$)
$K_{\text{comp.}}$	Y-intercept of complete blocking filtration model (unit less)
$K_{\text{inter.}}$	Y-intercept of intermediate blocking filtration model (m^2/l)
$K_{\text{standr.}}$	Y-intercept of standard blocking filtration model ($(\text{m}^2/\text{l})^{0.5}$)
R	Oil Rejection
t	The Run Time (h)
V	Permeate Volume (l)

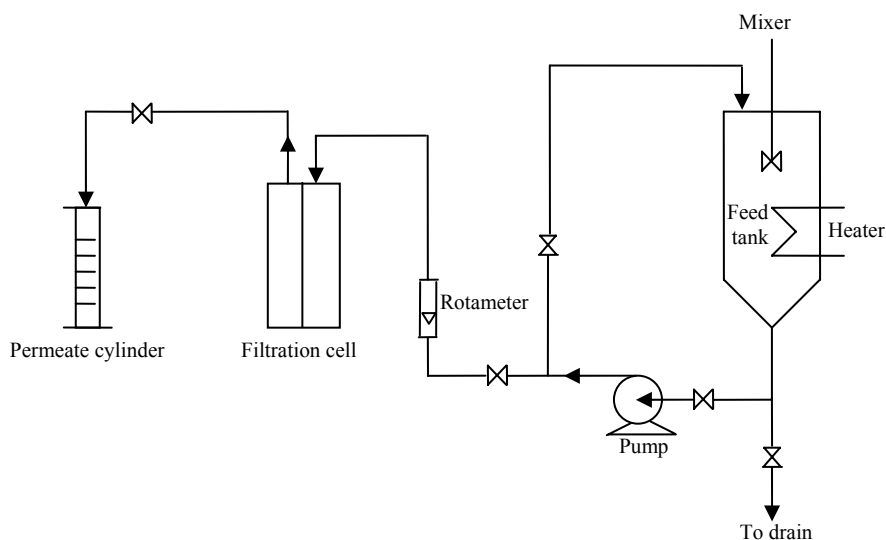


Fig.1 Experimental Set-Up

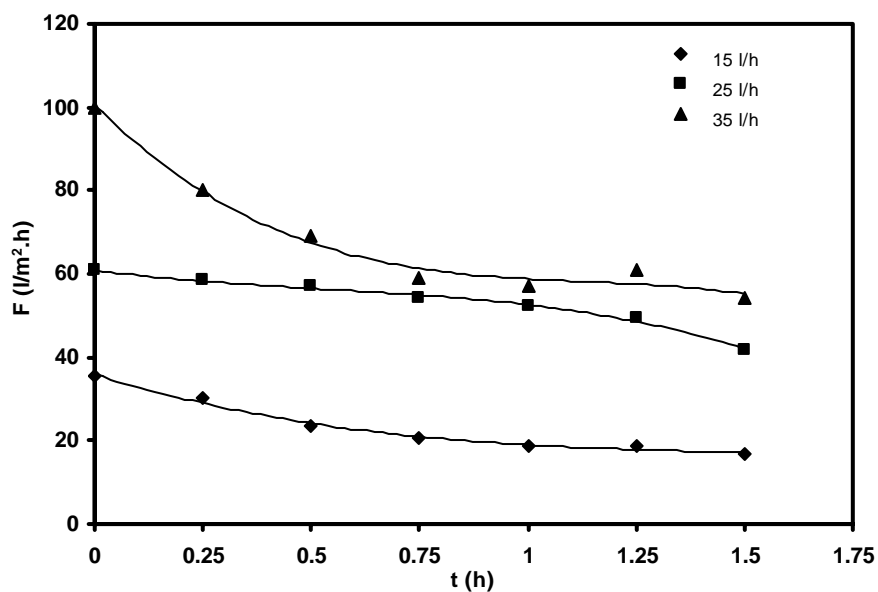


Fig.2 Time vs permeate flux rate at different feed flow rate
Feed temperature 32°C, oil feed concentration 300 ppm, and feed solution pH 6.86

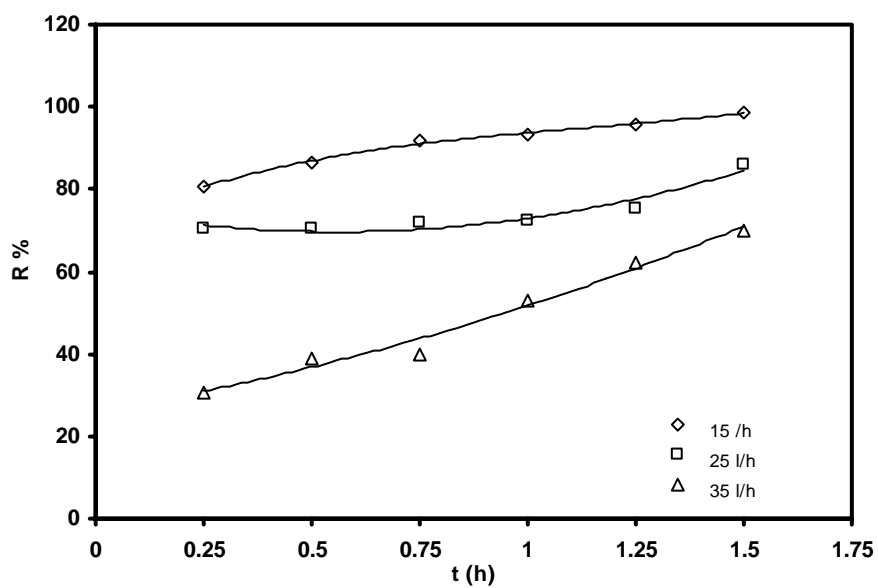


Fig.3 Time vs oil rejection percent at different feed flow rate
Feed temperature 32°C, oil feed concentration 300 ppm, and feed solution pH 6.86

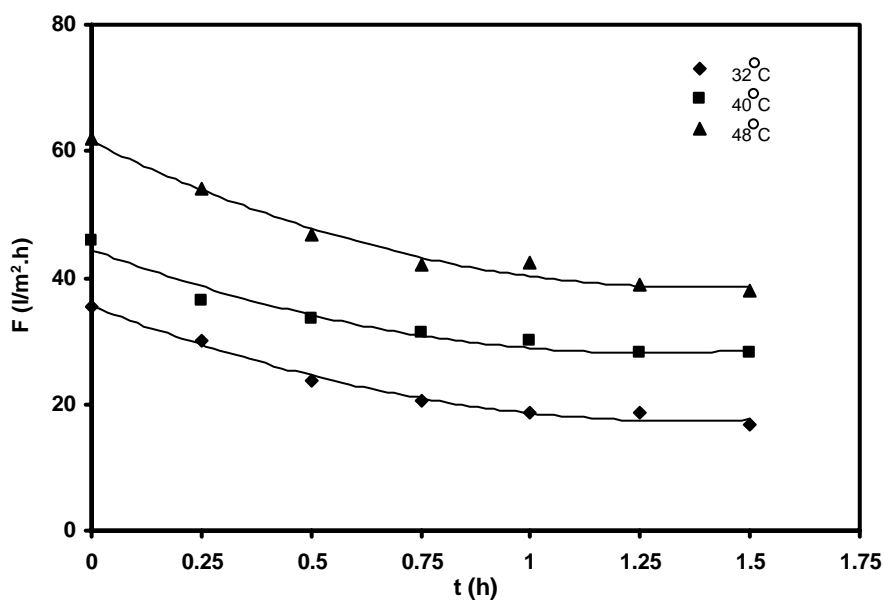


Fig.4 Time vs permeate flux rate at different feed temperature

Feed flow rate 15 l/h, oil feed concentration 300 ppm, and feed solution pH 6.86

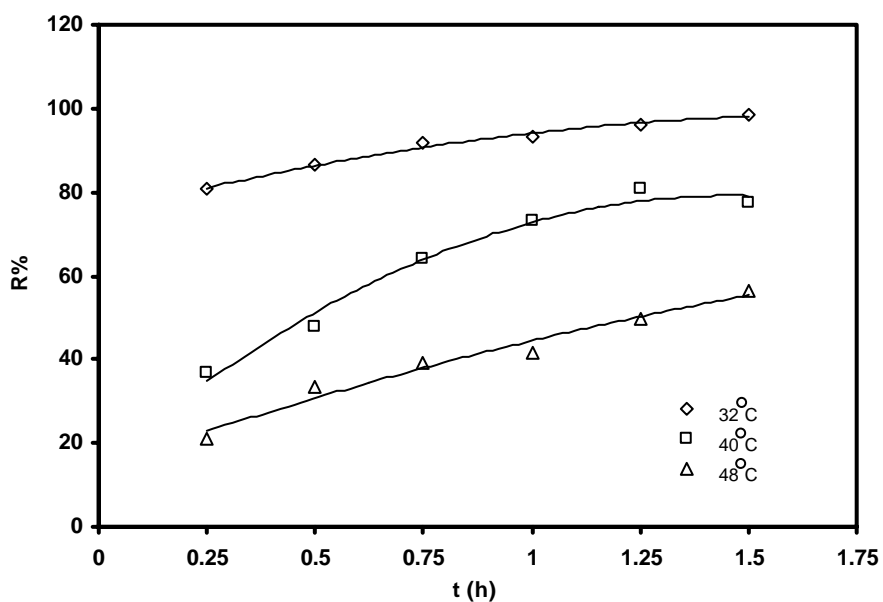


Fig.5 Time vs oil rejection percent at different feed temperature

Feed flow rate 15 l/h, oil feed concentration 300 ppm, and feed solution pH 6.86

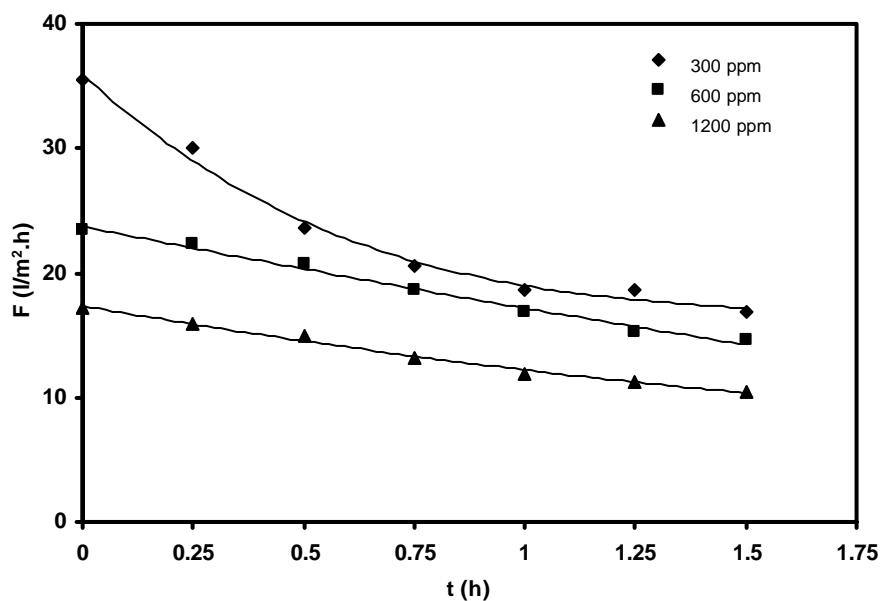


Fig.6 Time vs permeate flux rate at different oil feed concentration
Feed flow rate 15 l/h, feed temperature 32°C, and feed solution pH 6.86

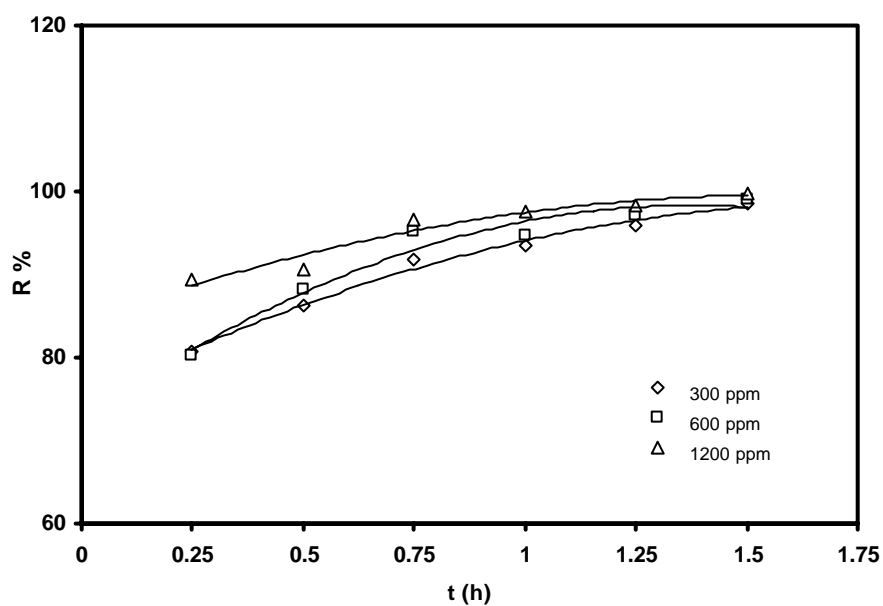


Fig.7 Time vs oil rejection percent at different oil feed concentration
Feed flow rate 15 l/h, feed temperature 32°C, and feed solution pH 6.86

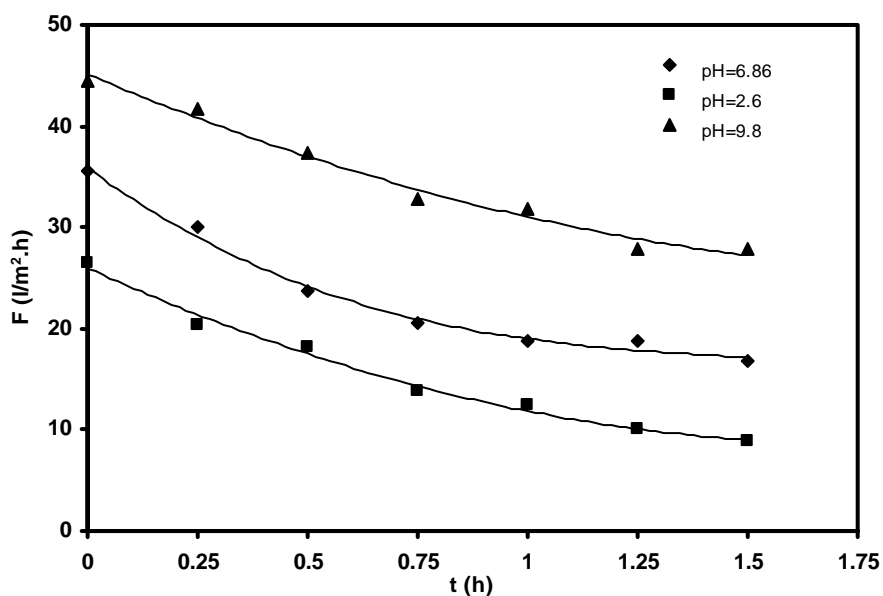


Fig.8 Time vs permeate flux rate at different feed solution pH
Feed flow rate 15 l/h, feed temperature 32°C, and oil feed concentration 300 ppm

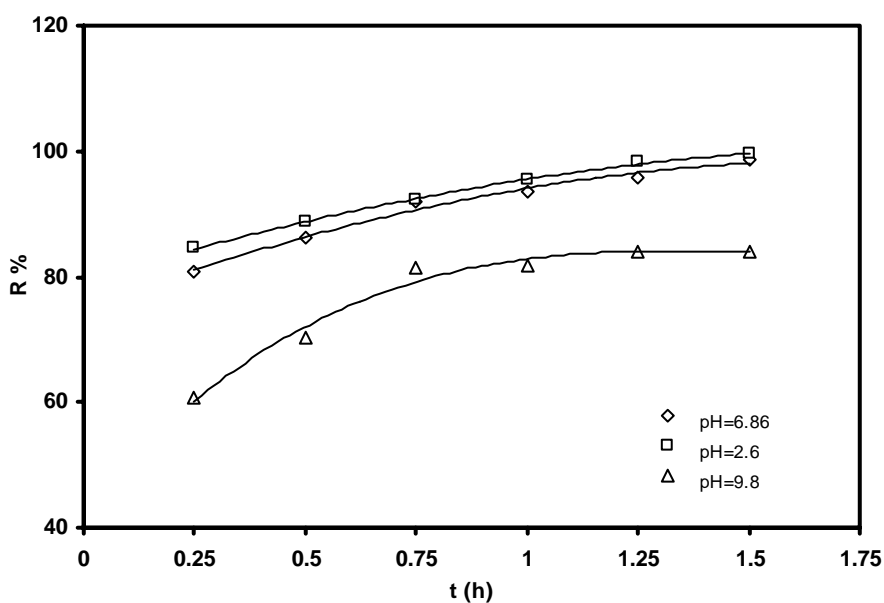


Fig.9 Time vs oil rejection percent at different feed solution pH
Feed flow rate 15 l/h, feed temperature 32°C, and oil feed concentration 300 ppm

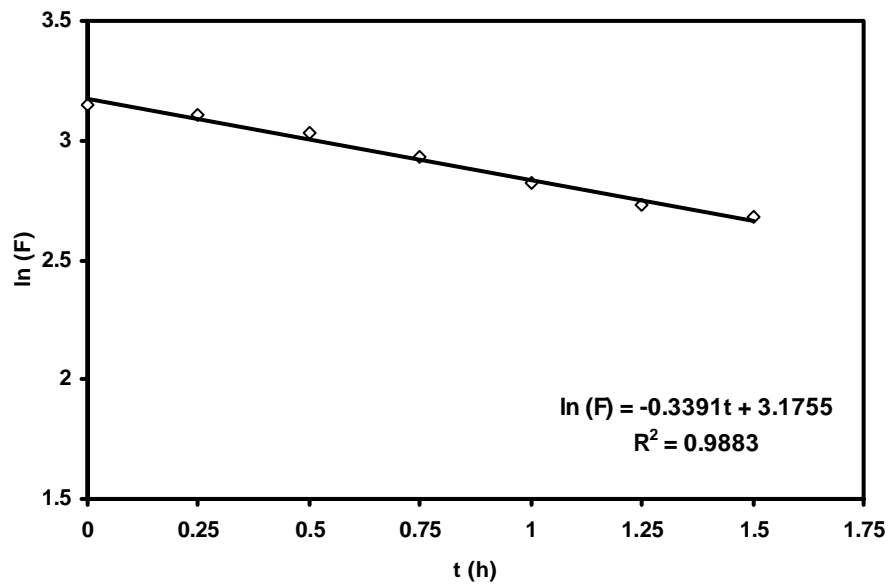


Fig.10 Complete blocking filtration model

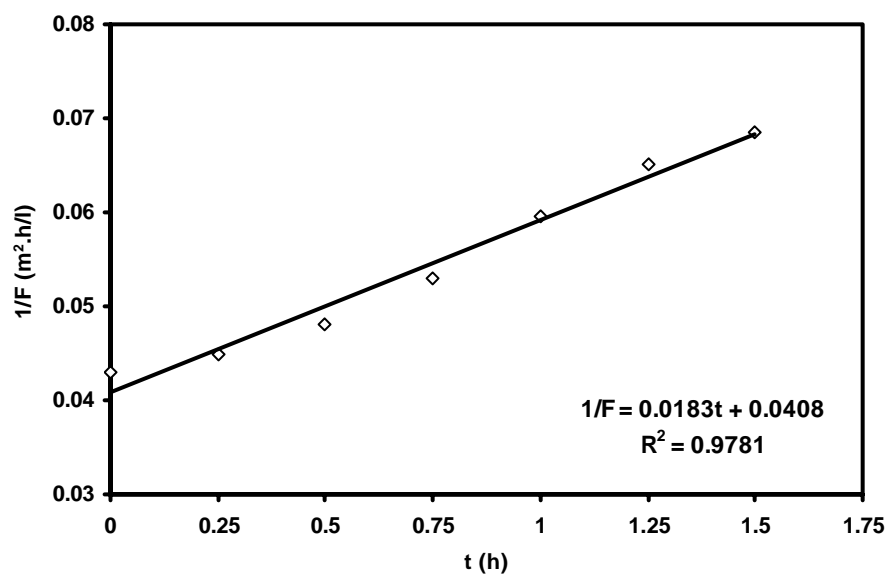


Fig.11 Intermediate blocking filtration model

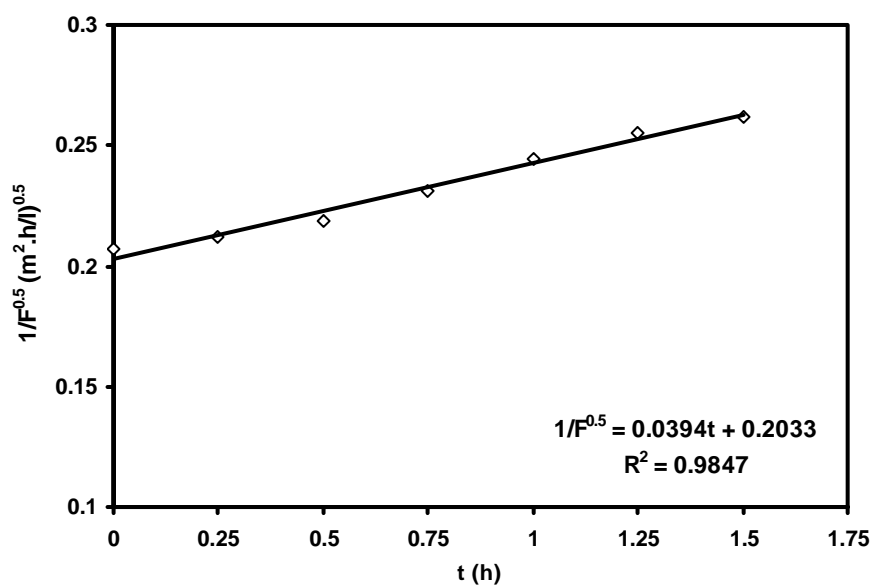


Fig.12 Standard blocking filtration model

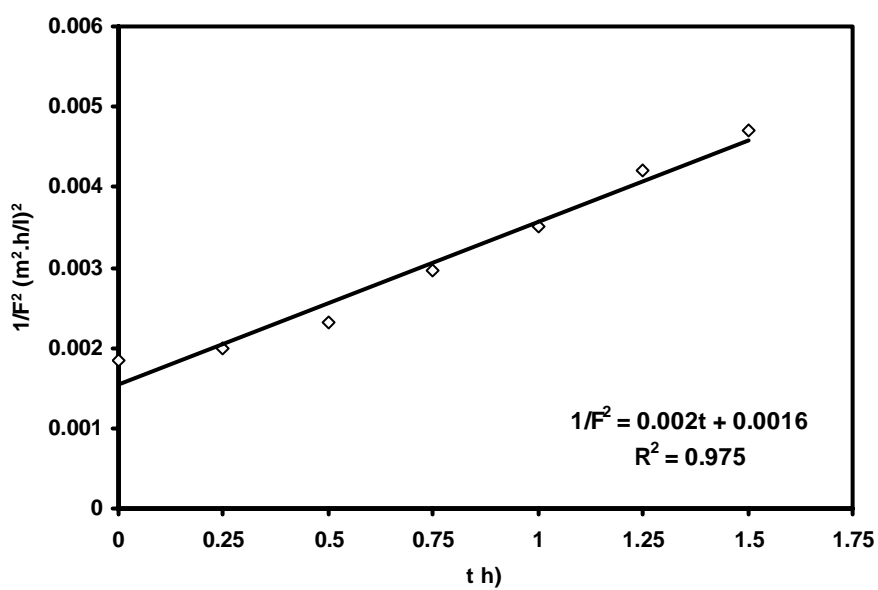


Fig.13 Cake filtration model

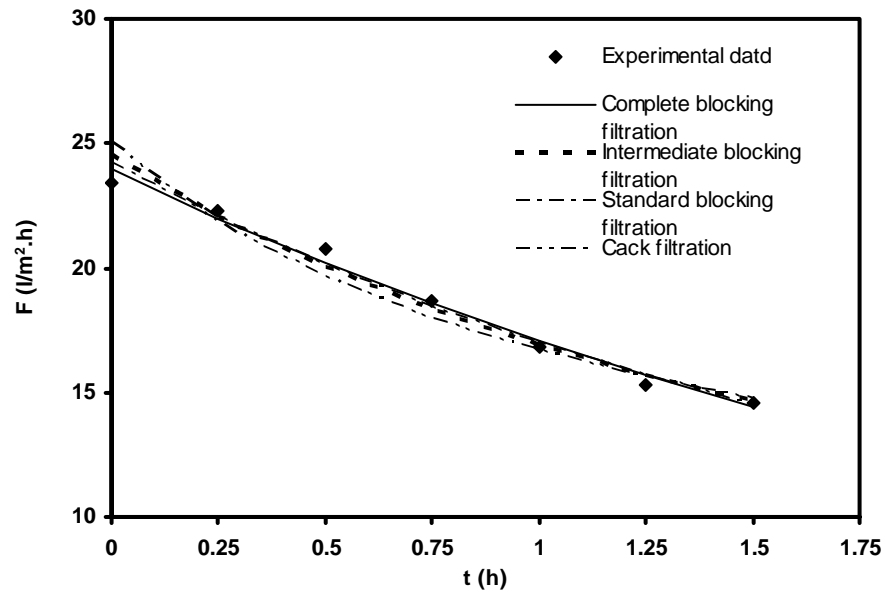


Fig.14 Comparison of experimental data with filtration model prediction



ROBUST CONTROLLER DESIGN FOR LOAD FREQUENCY CONTROL IN POWER SYSTEMS USING STATE-SPACE APPROACH

The late
Prof. Dr. Ismail A. Mohammed
University of Baghdad
Electrical Eng. Dept.

Prof. Dr. Rami A. Mahir
University of Technology
Control & Systems Eng. Dept.

Dr. Ibraheem K. Ibraheem
University of Baghdad
Electrical Eng. Dept.

ABSTRACT:

In this paper a robust governor has been designed using H_∞ techniques to replace the conventional governor of the steam turbine of the power system to regulate the frequency of the power grid. The robust governor is synthesized using state-space approach with time variations, neglected dynamics, and constant main steam pressure are considered in the design process. The proposed approach ensures internal stability, satisfying both frequency and time domains requirements, and obtaining minimal performance H_∞ -norm of the closed-loop system in one burden. The simulations are carried out using MATLAB and the results show that the overall system output performance can be improved using the proposed H_∞ robust governor.

(H_∞)

(H_∞ -norm)

MATLAB

KEYWORDS: robust control, load frequency control, steam turbine, H_∞ -norm, system uncertainty, load disturbance.

BACKGROUND AND MOTIVATION

Modern power systems are highly complex and non-linear and their operating conditions can vary significantly over a wide range. Power system stability can be defined as that property of a power system that enables it to remain in state of operating equilibrium under normal operating conditions and to regain an acceptable state of equilibrium after being subjected to a disturbance [1, 2]. The quality of power supply must meet certain minimum standard requirements with regard to the following factors:

- Constancy of frequency.
- Constancy of voltage.
- Level of reliability.

The main concern in this work is regarding the first factor mentioned above. Most universal method of electric generation is accomplished using thermal generation, and the most common machine for this production is the steam turbines. In the world most of the generation is powered by steam-turbine-driven generators. The size of these generating units has increased over time and the steam used in electric production is produced in steam generators or boilers using either fossil or nuclear fuels as primary energy sources [2].

Ideally, the load must be fed at constant voltage and frequency at all times. In practical terms this means that both voltage and frequency must be held within close tolerances so that the consumer's equipments may operate satisfactorily. For example, reduction of the system frequency of only a few hertz may lead to stalling of the motor loads on the system [2]. Subsequent large change in the system frequency might cause cascade trips of the generating power plants and results in system breakup. Thus it can be accurately stated that the power system operator or automatic control system must maintain a very high standard of continuous electrical service [2].

Poor balancing between generated power and demand can cause the system frequency to deviate away from the nominal value, and create inadvertent power exchanges between control areas. To avoid such a situation, Load Frequency Controllers (LFC) are designed and implemented to automatically balance between generated power

and the demand power in each control area [1, 3, 4].

The problem of load frequency control has been investigated by many researchers. In [5] speed governors have been designed based on PID techniques with different philosophies because of its simplicity and ease of implementation. Fuzzy sliding mode controller for LFC has been designed in [6] to account for the system's parameters variations and the governor backlash. Genetic Algorithm (GA) is a global search optimization technique. The researchers in [7] used GA for tuning the control parameters of the Proportional-Integral (PI) control subject to the H_∞ constraints in terms of LMI. Modern control techniques have been reported in [8, 9] in which a load frequency controller for power systems has been designed using LQR techniques. The work in [10] investigated the design problem of robust load frequency controller using LMI methods for solving the H_∞ control problem.

This paper is organized as follows: in section 2 a brief introduction to the robust control theory and H-infinity techniques is given. Section 3 describes the mathematical modeling of the steam turbine system and the design objectives. Section 4 presents the design procedure of the robust governor and Section 5 is devoted to the performance evaluation and simulation results. Collusions are given in section 6.

ROBUST CONTROL AND H-INFINITY TECHNIQUES

Central to the development of feedback control theory has been the notion of uncertainty. Uncertainty refers to the differences or errors between models and reality. It can be defined as discrepancy between the physical plant and the mathematical model used for controller design. A good model should be simple enough to facilitate design, yet complex enough to give the engineer confidence that designs based on the model will work on the true plant.

For a scalar stable transfer function $G(s)$, the H_∞ -norm is simply the peak value of $|G(j\omega)|$ as a function of frequency (i.e. maximum of Bode plot) [11, 12, 13]:

$$\|G(s)\|_{\infty} = \sup_{\omega} |G(j\omega)| \quad (1)$$

Where \sup is the supremum or the least upper bound, it is the same as max value and it is used here instead of max because the maximum may only be approached as $\omega \rightarrow \infty$ and may therefore not actually be achieved. The H_{∞} stands for **Hardy Space** which is a functional space containing all analytic and bounded transfer functions in the RHP and the symbol ∞ implies that it is designed to accomplish minmax restrictions in the frequency domain.

The shaping of a multivariable transfer function is based on the idea that a satisfactory definition of gain (range of gain) for matrix transfer function is given by the singular values σ of the transfer function. By multivariable transfer function shaping, therefore it is meant that the shaping of singular values of appropriately specified transfer functions such as the loop transfer function $L = KG$ or possibly one or more closed-loop transfer functions [14,15]. Two essential objectives are required for the closed-loop system, these are [15]:

- For disturbance rejection we have to make $1/\bar{\sigma}(S) \geq |W_p|$, where W_p is the performance bound.
- While for robust stability against a multiplicative perturbation $G_p = G(I + \Delta)$ we have to make $\bar{\sigma}(T) \leq |W_I^{-1}|$ where W_I^{-1} is the robustness bound.

The two mentioned requirements cannot all be met at the same time. Feedback is therefore a tradeoff over frequency of conflicting objectives.

Weighted Performance and Weighting Filters Selection Criteria

The performance objectives of the feedback system can usually be specified in terms of requirements on the sensitivity S and /or complementary sensitivity T functions or in terms of some other closed-loop transfer functions like control sensitivity function R as defined below:

$$S = \frac{c}{d} = \frac{1}{1+L} \quad (2)$$

$$R = \frac{u}{r} = \frac{K}{1+L} = K S \quad (3)$$

$$T + S = I \Rightarrow T = \frac{c}{r} = I - S = \frac{L}{(1+L)} \quad (4)$$

To achieve the two essential requirements mentioned early, the following have to be satisfied [14,15]:

- For disturbance rejection minimize $\bar{\sigma}(S)$ over the low frequency range. To do this one could select a weighting filter $W_p(s)$ that has low-pass filter characteristics with bandwidth equal to the bandwidth of the disturbance. The optimal robust control problem is then solved by finding a stabilizing controller that minimizes $\|W_p S\|_{\infty}$.
- The $\bar{\sigma}(T)$ needs to be minimized as large as possible at high frequencies to account for unstructured uncertainties that appear in that frequency range. To achieve this goal, a weighting filter $W_I(s)$ has to be chosen such that it has high magnitude at high frequencies and low at low frequencies with the condition that $\|W_I T\|_{\infty}$ is minimized.
- Finally, the control sensitivity R should be kept at low values to limit the magnitude of the control signal u to prevent saturation of the actuators. To get this done, the control sensitivity R has to be reshaped with a weighting filters such that $\|W_U R\|_{\infty}$ is minimized in the specified frequency range.

The minimization process to the closed-loop transfer functions is achieved at different frequency regions especially for S and T to keep the equation $S + T = I$ valid over the entire frequency range. This can be done via the selection of corresponding weighting filters with different frequency characteristics as explained above. From the above discussion the requirements for the performance become [14,15,16]:

$$\begin{aligned}\|W_P S\|_\infty \leq 1 &\Rightarrow \bar{\sigma}(S(j\omega)) \leq \bar{\sigma}(W_P^{-1}(j\omega)) \\ \|W_I T\|_\infty \leq 1 &\Rightarrow \bar{\sigma}(T(j\omega)) \leq \bar{\sigma}(W_I^{-1}(j\omega)) \quad (5) \\ \|W_U R\|_\infty \leq 1 &\Rightarrow \bar{\sigma}(R(j\omega)) \leq \bar{\sigma}(W_U^{-1}(j\omega))\end{aligned}$$

The selection of the weighting filters is not an easy task for a specific design problem and often involves ad hoc, and fine tuning. It is very hard to give a general formula for the weighting filters that will work in every case. Finally the selection of the uncertainty weighting filter depends on the dynamics of the system and the nominal model chosen [14,15].

There are many ways in which feedback problems can be casted as H_∞ optimization problem, one of them is afforded in **Fig. 1**.

The closed-loop transfer functions from w to z is given by the Linear Fractional Transformation (LFT) [17,18]:

$$z = T_{zw} w = F_l(P, K) w \quad (6)$$

$$T_{zw} = F_l(P, K) = P_{11} + P_{12}K(I - P_{22}K)^{-1}P_{21} \quad (7)$$

Where P is the open-loop generalized plant that includes the plant transfer function in addition to the weighting filters and is the H_∞ controller K . It should be said that the H_∞ algorithms, in general, find a suboptimal controller, that is, for a specified γ a stabilizing controller is found for which $\|F_l(P, K)\|_\infty < \gamma$. If an optimal controller is required then the algorithm can be used iteratively, reducing γ until the minimum is reached within a given tolerance [14,15,18].

The standard H_∞ suboptimal control problem for **Fig. 1** is to find all stabilizing controllers $K(s)$ which minimize [14,15,18]:

$$\|T_{zw}\|_\infty = \|F_l(P, K)\|_\infty = \max_{\omega} \bar{\sigma}(F_l(P, K)(j\omega)) \quad (8)$$

For the general control configuration of **Fig. 1**, there exist a stabilizing controller $K(s)$ such that $\|F_l(P, K)\|_\infty < \gamma$ if and only if [18,19,20]:

(i) $X_\infty \geq 0$ is a solution to the following algebraic Riccati equation:

$$A^T X_\infty + X_\infty A + C_1^T C_1 + X_\infty (\gamma^{-2} B_1 B_1^T - B_2 B_2^T) X_\infty = 0 \quad (9)$$

Such that

$$Re(\lambda_i[A + (\gamma^{-2} B_1 B_1^T - B_2 B_2^T) X_\infty]) < 0, \forall i; \text{ and}$$

(ii) $Y_\infty \geq 0$ is a solution to the following algebraic Riccati equation:

$$A Y_\infty + Y_\infty A^T + B_1 B_1^T + Y_\infty (\gamma^{-2} C_1^T C_1 - C_2^T C_2) Y_\infty = 0 \quad (10)$$

Such that

$$Re(\lambda_i[A + Y_\infty (\gamma^{-2} C_1^T C_1 - C_2^T C_2)]) < 0, \forall i; \text{ and}$$

(iii) $\rho(X_\infty Y_\infty) < \gamma^2$

Moreover, when these conditions hold, one such controller $K(s)$ is given with the following state-space representation [14,15,16,17,20]:

$$K_{sub}(s) \triangleq \begin{bmatrix} A_\infty & -Z_\infty L_\infty \\ \hline F_\infty & 0 \end{bmatrix} \quad (11)$$

$$A_\infty = A + \gamma^{-2} B_1 B_1^T X_\infty + B_2 F_\infty + Z_\infty L_\infty C_2$$

$$F_\infty = -B_2^T X_\infty, \quad L_\infty = -Y_\infty C_2^T, \quad Z_\infty = (I - \gamma^{-2} Y_\infty X_\infty)^{-1}$$

STEAM TURBINES AND SPEED GOVERNING SYSTEM

A steam turbine converts stored energy of high pressure and high temperature steam into mechanical energy, which is in turn converted into electrical energy by the generator. The heat source for the boiler supplying the steam may be a nuclear reactor or a furnace fired by fossil fuel (coal, oil, or gas) [1, 21].

Steam turbines normally consist of two or more turbine sections or cylinders coupled in series. Most units placed in service in recent years have been of the tandem-compound design,

in which, the sections are all on one shaft, with a single generator. Typical configuration of tandem-compound steam turbine with single reheat is shown in Fig. 2.

A typical mechanical-hydraulic speed governing system consists of a Speed Governor (SG), a Speed Relay (SR), a Hydraulic Servomotor (SM), and Governor-Controller Valves (CVs). In steam turbine-generator system, the governing is accomplished by a speed transducer, a comparator, and one or more force-stroke amplifiers. Fig 3 depicts the complete system block diagram of a steam turbine generator [2].

The transfer function of each individual block is derived as follows [1,2,4,21,22]:

Speed Governor (SG):

$$S_G = \frac{1}{R} \quad (12)$$

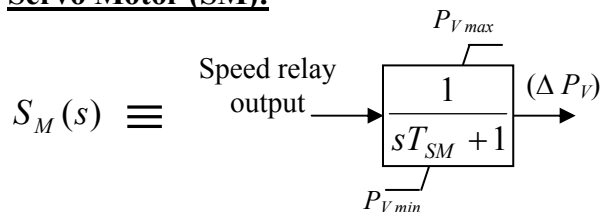
Where R is the steady-state speed regulation. The value of R determines the steady-state speed load characteristic of the generating unit.

Speed Relay (SR):

$$S_R(s) = \frac{1}{sT_{SR} + 1} \quad (13)$$

Where T_{SR} is the time constant of the speed relay.

Servo Motor (SM):



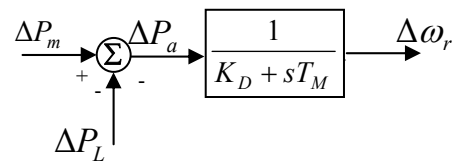
Where T_{SM} is the time constant of the servomotor.

Steam Turbine (ST):

$$S_T(s) = \frac{\Delta P_m}{\Delta P_V} = \frac{(F_{HP}(sT_{CO} + 1)(sT_{RH} + 1) + F_{IP}(sT_{CO} + 1) + F_{LP})}{(sT_{CH} + 1)(sT_{CO} + 1)(sT_{RH} + 1)} \quad (14)$$

Where T_{CO}, T_{RH}, T_{CH} are the time constants for the cross over, reheater, and steam chest respectively.

Machine Dynamics (MD):



Where T_M is the mechanical starting time.

ΔP_m is the incremental change of the turbine mechanical power.

ΔP_L is the incremental change of load power.

ΔP_a is the incremental change of accelerating power.

$\Delta\omega_r$ is the deviation of the angular speed of the synchronous generator.

Speed Disturbance Spectrum (SD)

$$W_{D3}(s) = \frac{1}{s + 2\pi f_o} \quad (15)$$

The model of the complete steam turbine system has been derived with typical values of parameters of the model shown in Fig. 3. This model is applicable to a tandem-compound single reheat turbine of fossil-fuelled units are listed in Table 1 [1,2,22].

1. H_∞ CONTROLLER DESIGN FOR THE UNCERTAIN STEAM TURBINE SYSTEM: A STATE-SPACE APPROACH

This section summarizes the design procedure of the H_∞ robust governor design for the steam turbine system based on state-space techniques in which the system will be represented by four system matrices $\{A, B, C, D\}$.

For steam turbine system, the design requirements that have to be satisfied are summarized as follows:

- **Time-domain requirements:**
 - Good and swift disturbance rejection with steady-state error less than 0.2 % .
 - The closed-loop system is stable at all operating conditions.
 - Undershoot of the output frequency deviation is as minimum as possible.
 - Control signal (u) lies in the range [0,1] in response to step load change.
- **Frequency-domain requirements:**
 - Phase margin $> 40^\circ$.
 - Gain margin > 10 dB.
 - High frequency roll-off to the controller.

In designing a robust governor the parameter variations have to be taken into consideration in the design process since the variations are a common phenomenon in many practical applications, one of them is the steam turbine system.

This can be done by designing the H_∞ robust controller for the nominal model $G_{nom}(s)$ rather than the original one $G(s)$. Usually the nominal model $G_{nom}(s)$ is of a transfer function which is simpler than the original transfer function $G(s)$ or perturbed one $G_p(s)$. One possible proposed choice of the nominal model for the steam turbine system is:

$$G_{nom}(s) = G_{1nom}(s) \cdot G_{2nom}(s) = \frac{(F_{HP} T_{RH} s + 1)}{(T_{CH} s + 1)(T_{RH} s + 1)} \cdot \frac{1}{(T_M s + K_D)} \quad (16)$$

Where the dynamics that represents the speed relay $SR(s)$, servo motor $SM(s)$, and the crossover piping in the turbine transfer T_{CO} have been neglected as they have very small time constants. These neglected high frequency dynamics will be represented as an output multiplicative uncertainty in the design stage,

where the original model $G(s)$ will be replaced by a nominal model $G_{nom}(s)$ together with uncertainty filter $W_I(s)$ usually of finite and low order. In addition, real perturbations are added to the system by allowing specific parameters to vary in their ranges. In this model two parameters are assumed to be uncertain. With the aid of **Table 1**, the characteristics of these two uncertain parameters are listed in **Table 2**.

At this end the nominal model $G_{nom}(s)$ has been chosen based on simplification in the original model $G(s)$. With perturbations added to the two parameters mentioned above, the nominal model becomes:

$$G_{1nom}(s) = \frac{(1 + sF_{HP}\bar{T}_{RH})}{(1 + s\bar{T}_{CH})(1 + s\bar{T}_{RH})} \quad (17)$$

$$G_{2nom}(s) = \frac{1}{(T_M s + K_D)} \quad (18)$$

$$G_{nom}(s) = G_{1nom}(s) \cdot G_{2nom}(s) = \frac{(2.1s + 1)}{(0.25s + 1)(7s + 1)} \cdot \frac{1}{(8s + 2)} \quad (19)$$

While the perturbed transfer function $G_p(s)$ is given by:

$$G_p(s) = \frac{1}{0.1s + 1} \cdot \frac{1}{0.2s + 1} \cdot \frac{0.3(0.4s + 1)(T_{RH}s + 1) + 0.4(0.4s + 1) + 0.3}{(T_{CH}s + 1)(0.4s + 1)(T_{RH}s + 1)} \cdot \frac{1}{8s + 2} \quad (20)$$

Where T_{CH} and T_{RH} are uncertain, their ranges are defined in table 1 and, \bar{T}_{CH} , \bar{T}_{RH} are the nominal values of their respective variables. Their values can be obtained from table 5.1. Based on the above analysis, the next step is to design the uncertainty filter $W_I(s)$ which represents the neglected dynamics as well as the variations in T_{CH} and T_{RH} . The uncertainties of these two parameters will contribute in the design of the uncertainty weighting filter $W_I(s)$.

Now, the H_∞ design procedure will be carried out on the nominal plant $G_{nom}(s)$ together with the uncertainty filter $W_I(s)$ that compensates for the modeling errors (neglected dynamics plus parameter perturbations).

With output multiplicative uncertainty has been incorporated into the system, the open-loop generalized plant will be represented by $P(s)$:

$$P(s) = \begin{bmatrix} 0 & 0 & 0 & W_I G_1 \\ 0 & 0 & 0 & W_U \\ W_p G_2 & -W_p G_2 & W_p W_{D3} & W_p G_1 G_2 \\ -G_2 & G_2 & -W_{D3} & -G_1 G_2 \end{bmatrix} := \begin{bmatrix} A & B_1 & B_2 \\ C_1 & D_{11} & D_{12} \\ C_2 & D_{21} & D_{22} \end{bmatrix} \quad (21)$$

While the weighted closed-loop transfer function matrix T_{zw} is given by:

$$T_{zw} = \begin{bmatrix} -W_I T & W_I T & -W_I G_1 K S W_{D3} \\ -W_U K G_2 S & W_U K G_2 S & -W_U K S W_{D3} \\ W_p G_2 S & -W_p G_2 S & W_p S W_{D3} \end{bmatrix} \quad (22)$$

The block diagram of the augmented plant $P(s)$ including the performance and uncertainty weighting filters ($W_p(s)$, $W_U(s)$ and $W_I(s)$) together with plant is shown in Fig. 4, where an output multiplicative uncertainty is assumed in the system as indicated by the uncertainty weight $W_I(s)$ and the input d_1 .

Selection of the Weighting Filters

Two kinds of weighting filters have been designed in the H_∞ optimization process:

- **Performance weighting filters:** Two performance weighting filters have been used. The performance weighting filter $W_p(s)$ reflects the requirements of disturbance rejection. While the second weighting filter $W_U(s)$, is included to limit the value of the control signal (u) to avoid the saturation of the actuators. After deep analysis it is found that the following weighting filters that are suitable for the problem at hand [23]:

$$W_p(s) = \frac{s + 0.29}{s + 2.9 * 10^{-6}} \quad , \quad W_U(s) = \frac{1}{10}$$

- **Uncertainty weighting filter:** This weighting filter represents the neglected dynamics in the model in addition to the parametric uncertainties in the variables T_{CH} and T_{RH} and is given as follows [23]:

$$W_I(s) = W_{I1}(s) = \frac{4500s + 1067}{s + 3333}$$

Up to this point all the weighting filters have been designed. Applying the H_∞ design procedure to the generalized plant $P(s)$, the optimization process ends with the following results [23]:

- $\gamma_{\min} = 0.9631$ and the H_∞ -norm of the closed-loop transfer function is $T_{zw}(s) = 0.963054$.
- The H_∞ controller is suboptimal, strictly proper, and of 6th order:

$$K(s) = \frac{41176293.2898(s + 3333)(s + 4)(s + 2.975)(s + 0.2588)(s + 0.1429)}{s(s + 5.41 * 10^4)(s + 6.499 * 10^4)(s + 66.89)(s + 0.959)(s + 0.4825)}$$

SIMULATIONS AND RESULTS

In this section the time and frequency domain simulations have been carried out on the closed-loop configuration of the steam turbine system as shown in Fig. 5 and have been done using MATLAB software.

Where,

$$K(s) = \text{the designed } H_\infty \text{ robust governor } K(s)$$

$$G_1(s) = SR(s) * SM(s) * ST(s),$$

$$G_2(s) = MD(s).$$

$$\Delta P_L = \text{Load disturbance signal,}$$

$$\Delta P_m = \text{Output Mechanical power of the turbine,}$$

$$\Delta \omega_r = \text{Output frequency deviation } (\Delta \omega_r = 0 \text{ if } \Delta P_L = 0),$$

$$d_3 = \text{Speed disturbance signal,}$$

u = Control signal (output of the governor),

The frequency response of the compensated system $G(s) * K(s)$ is drawn in **Fig. 6**. The controller has an integrating action as planned for which tends to damp the low frequency disturbances as it is clear in the time response simulations. Also the controller has a high frequency roll-off of 20 dB/decade. The controller gives a very good phase margin about 72.42° with 3.908 rad/sec phase crossover frequency and gain margin of about 35 dB with gain crossover frequency of 0.26 (rad/sec).

Since all the roots of $1 + G(s) * K(s)$ lie in the open left half s -plane, then nominal stability is guaranteed. Both robust stability and nominal performance tests are illustrated in **Fig. 7**. The figure confirms that the nominal performance condition has been satisfied. As seen the bound $1/W_p$ covers the sensitivity S with wide gap between them. Since the uncertainty in the system is unstructured and is modeled in multiplicative form, the verification of the robust stability is performed by plotting the singular values of T and comparing it with the frequency response of the bound $1/|W_l|$. This is shown in **Fig. 7**. RP is automatically satisfied when the subobjectives of NP and RS are satisfied.

To check the stability of the system against the variations of the system parameters, the two uncertain parameters has been set to two extreme values as depicted in **Fig. 8** where the transient behavior of the output speed deviations due to load disturbance step of 0.02 p.u ($\Delta P_L = 0.02$ p.u) is plotted. As seen in the figure, the system exhibits clear performance degradation due to the parametric perturbations of the uncertain variables. But, evidently the system ensures stability even when the uncertain parameters vary over their entire range.

The nature of the generating unit with reheat turbine when subjected to 0.04 p.u step

change in the load (load disturbance) is illustrated in **Fig. 9**. These responses have been computed by using the typical parameters listed in table 1. Values shown are in per unit of the step change. As can be seen from the figure, the increase in P_L causes the frequency to decay at a rate determined by the inertia of rotor. As the speed drops, the turbine mechanical power begins to increase. This in turns causes a reduction in the rate of decrease of speed with undershoot of $8.5 * 10^{-3}$, and then an increase in speed when the turbine power is in excess of the load power (this starts beyond 10.7 sec). The speed will ultimately return to its reference value within 23 sec settling time and steady-state error of about 0.17% and the steady-state turbine power is increased by an amount equal to the additional load.

CONCLUSION

The robust governor has been designed and the simulations had showed that the closed-loop of the steam turbine system with this robust governor exhibits a very good results and it satisfy both the time and frequency domain requirements. The robust governor designed by the H_∞ techniques based on the state-space approach ensures both robust stability and robust performance of the closed-loop system against parametric variations and neglected dynamics for the steam turbine system.

REFERENCES

- Kundur P., "Power System Stability and Control", McGraw-Hill Inc., 1994.
- Anderson P. M. and Fouad A. A., "Power System Control and Stability", John Wiley and Sons Inc., 2003.
- Khodabakhshian A. and Golbon N., "Robust load frequency controller design for hydro power systems", IEEE Conference on Control Applications, Toronto, Canada, pp. 1510-1515, August 28-31, 2005.
- Hadi S. "Power System analysis", McGraw-Hill Inc., 1999.



- Khodabakhshian A. and Golbon N., "Unified PID design for load frequency control", IEEE Conference on Control Applications, Taipei, Taiwan, pp. 1627-1632, September 2-4, 2004.
- Ha Q. P., "A fuzzy sliding mode controller for power system load frequency control", IEEE Second International Conference on Knowledge-Based Intelligent Electronics Systems, Adelaide, Australia, pp.179-154, April 21-23, 1998.
- Rerkpreedapong D., Hasanovic A., and Felischi A., "Robust load frequency control using genetic algorithms and linear matrix inequalities", IEEE Transactions on Power Systems, Vol. 18, No. 2, pp. 855-861, May 2003.
- Azzam Mohyi el-din, "An optimal approach to robust controller design for load frequency control", IEEE/PES, Transmission and Distribution Conference and Exhibition, Asia Pacific, Vol. 1, pp. 180-183, 2002.
- Kamal Al-Tahan Iman, "Micro-computer based turbine governor", M.Sc. Thesis, Baghdad University, Elect. Eng. Dept., 1993.
- Kanchanaharuthai A. and Jutong N., "Robust load frequency controller design for interconnected power systems with circular pole constraints via LMI approach", IEEE, SICE Annual Conference, Sapporo, Hokkaido Institute of Technology, Japan, pp. 344-349, August 4-6, 2004.
- Green M. and Limebeer D. J. N., "Linear Robust Control", Prentice-Hall Inc., 1995.
- Francis B. A., "A course in H_∞ Control Theory", Volume 88 of Lecture Notes in
- Control and Information Sciences, Springer-Verlag, 1st edition, 1987.
- Clausen S. Tøffner, "System Identification and Robust Control", Springer-Verlag
- Inc., London, 1996.
- Zhou K., Doyle J. C., and Glover K., "Robust and Optimal Control", Prentice Hall, Upper Saddle River, New Jersey, 1996.
- Skogestad S. and Postlethwaite I., "Multivariable Feedback Control Analysis and Design", John Wiley & Sons Ltd, England, 2005.
- Balas G., Chiang R., Packard A., and Safonov M., "Robust Control Toolbox", MATLAB User's Guide, V. 3, the Mathworks Inc., 2005.
- Burl J. B., "Linear Optimal Control", Addison Wesley Longman Inc., Menlo Park, California, USA, 1999.
- Zhou K. and Doyle J. C., "Essentials of Robust Control", Prentice Hall, Upper Saddle River, New Jersey, USA, 1998.
- Mackenroth U., "Robust Control Systems Theory and Case Studies", Springer-Verlag, Berlin, Heidelberg, Germany, 2004.
- Gu D. W., Petkov P. Hr., and Konstantinov M. M., "Robust Control Design with Matlab", Springer -Verlag Inc., London, England, 2005.
- Al-Azzawi F. J., "Training course on Stability of Electrical Power Systems", IEE Cigre, Amman, Jordan, August 31-September 5, 1996.
- IEEE Committee, "Dynamics models for steam and hydro turbines in power system studies", IEEE Transactions on Power Apparatus Systems, pp. 1904-1915, December, 1973.
- Ibraheem K. braheem, "Polynomial and State-Space Based H-Infinity Robust Controller Design for Load Frequency Control in Power Systems", Ph.D thesis, University of Baghdad, College of Engineering, Elect. Eng. Dept., November 2006.

LIST OF SYMBOLS

$F_l(P, K)$	lower linear fractional transformation
H_∞	subspace containing all analytic and bounded transfer functions in the
$Re(x)$	real value of the complex number x
$\ G\ _\infty$	H-infinity norm of G
\sup	is the supremum or the least upper bound
$\rho(G)$	maximum eigenvalue of the matrix G
$\sigma_i(G)$	i-th singular values of the matrix G
$\bar{\sigma}$	maximum singular values of the matrix G
λ	eignvalue of the matrix G
γ	solution of the H_∞ optimization
X_∞	solution of the riccati equation
Y_∞	solution of the riccati equation
T_{zw}	weighted closed-loop transfer function

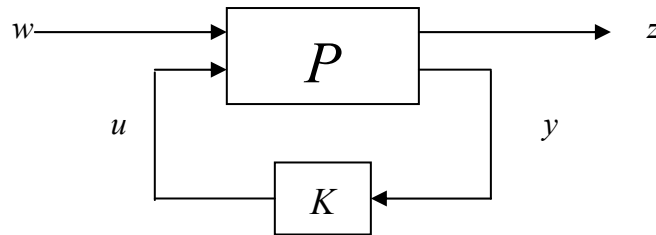


Figure 1: General control configuration.

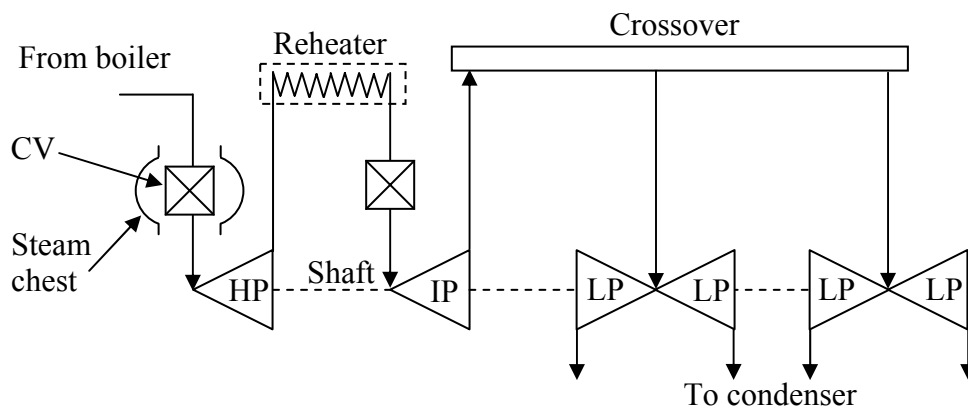


Figure 2: Tandem-compound single reheat steam turbine Configuration.

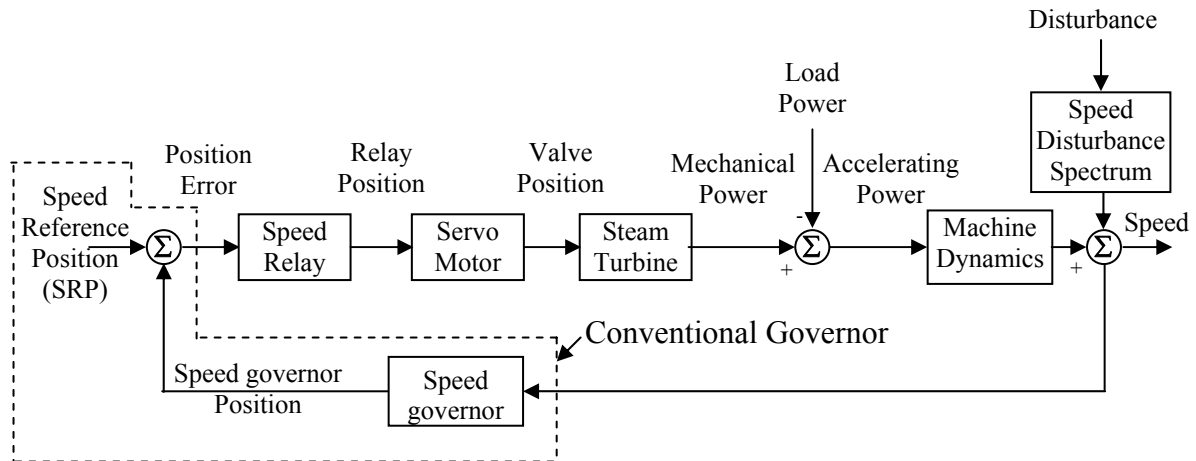


Figure 3: Block diagram of steam turbine control system.

Table 1: Description of the Steam Turbine System Parameters.

Parameter	Description	Value	Unit
K_D	Damping factor = torque (pu) / speed (pu)	2	pu
T_M	Mechanical starting time	8	sec
F_{IP}	IP turbine power fraction	0.4	-
F_{LP}	LP turbine power fraction	0.3	-
F_{HP}	HP turbine power fraction	0.3	-
T_{CO}	Crossover time constant	0.4	sec
T_{SR}	Speed relay time constant	0.1	sec
T_{SM}	Servomotor time constant	0.2	sec
T_{CH}	Steam chest time constant	0.25	sec
T_{RH}	Reheater time constant	7	sec
P_{Vmax}	Maximum valve position	1	pu
P_{Vmin}	Minimum valve position	0	pu
f_0	Speed disturbance bandwidth	0.5-2	Hz

Table 2: Specifications of uncertain parameters.

Parameter	Nominal symbol	Nominal Value/sec	Range/sec
Steam Chest time (T_{CH})	\bar{T}_{CH}	0.25	0.1-0.4
Reheat Time (T_{RH})	\bar{T}_{RH}	7	3-11

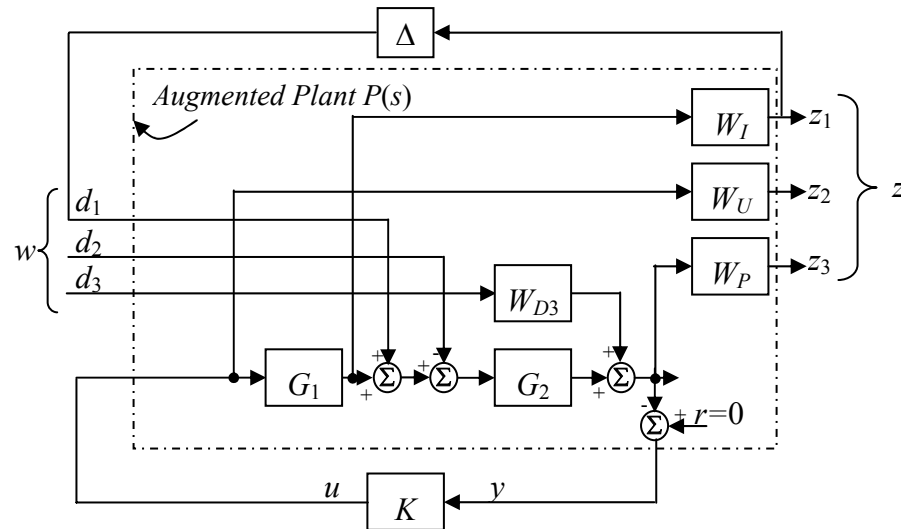


Figure 4: Augmented Plant for the H_∞ Control Problem.

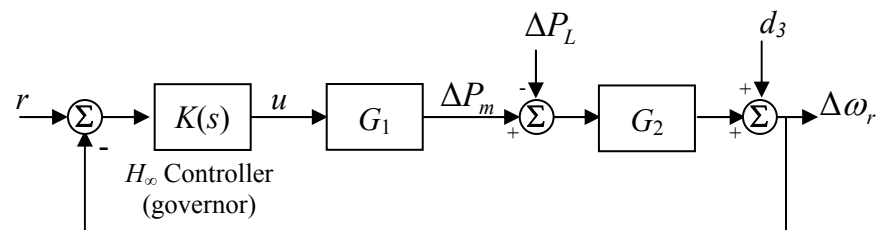


Figure 5: Closed loop of the steam turbine system.

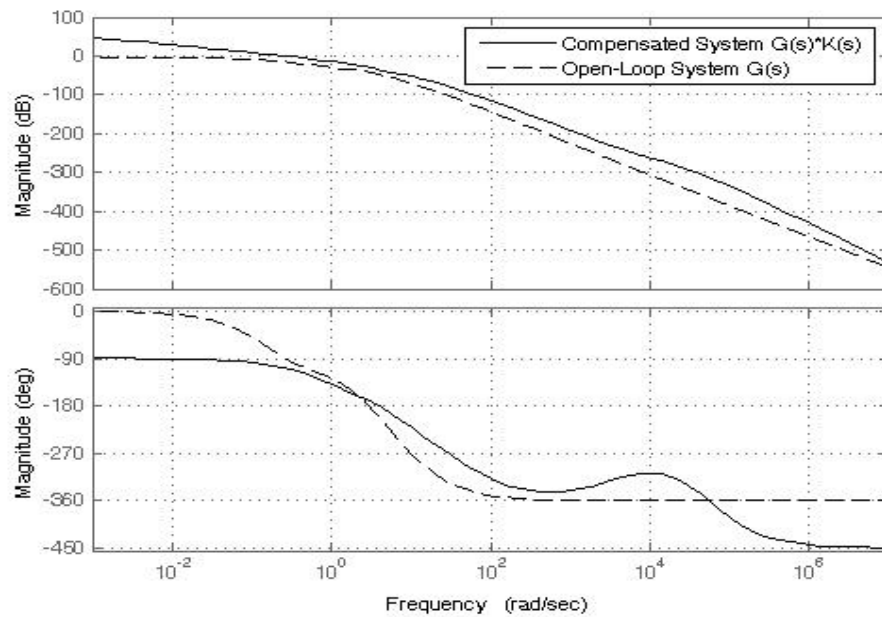


Figure 6: Frequency response of the system

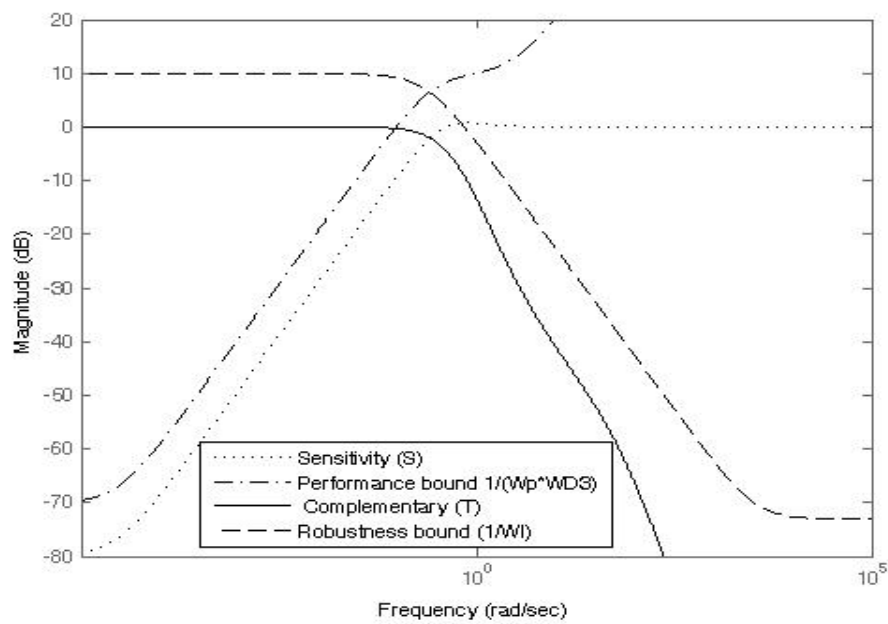


Figure 7: Singular values of S , T , and their Performance bounds.

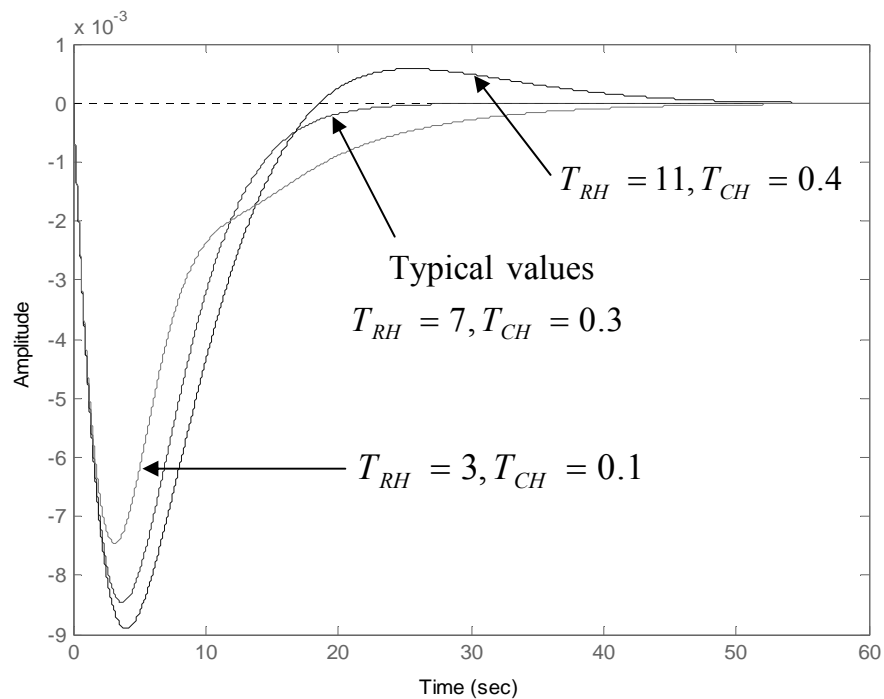


Figure 8: Response of $\Delta\omega_r$ for extreme values of the uncertain parameters T_{RH} and T_{CH} .

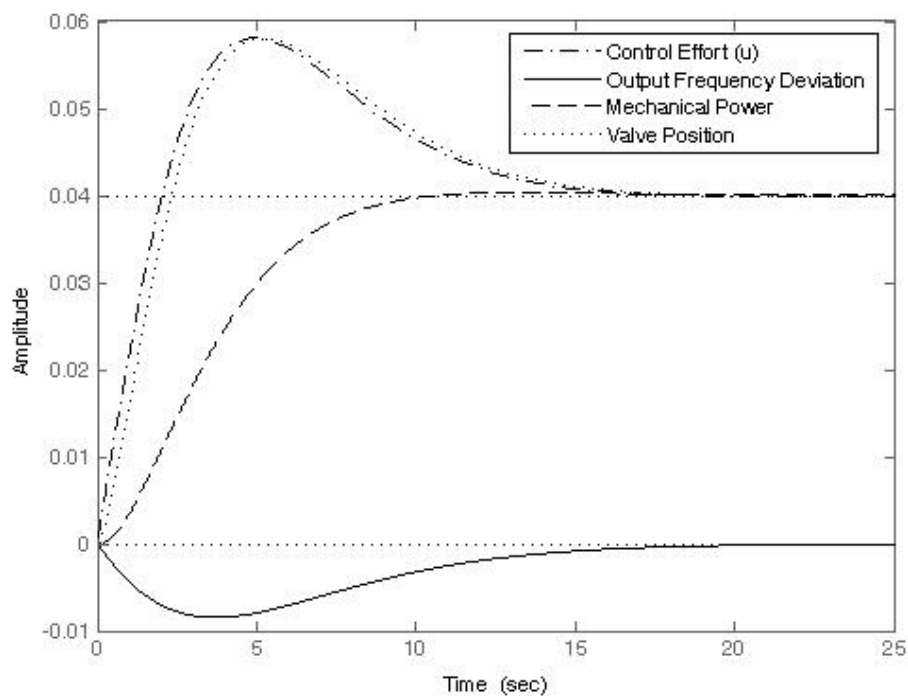


Figure 9: Transient response of the closed-loop system to a small step increase ΔP_L .



DESIGN AND EVALUATION OF A WEB BASED VIRTUAL DSP LABORATORY USING GUI AND HTML

Dr. Ashwaq Q. Hamid

Burak Abedulhadi

Electromechanical Engineering Department, University of Technology

HTML GUI

DSP

الخلاصة :

التعليم الهندسي يجب ان يشترك فيه المختبر العملي وذلك لأسناد الجانب النظري وتطوير مهارات الطالب .ان لهذه المختبرات بعض المشاكل مثل الكلفة العالية جدا كما أنها تتطلب أشرف بالإضافة الى المحددات الزمنية والمكانية. يقدم البحث الحالي تصميم وتقييم لمختبر افتراضي تم بناءه باستخدام صفحات الويب لتدريس مادة معالجة الإشارة الرقمية (DSP) لطلبة الدراسات الأولية في قسم الهندسة الكهروميكانيكية في الجامعة التكنولوجية. التجارب المختبرية المنفذة ستضمن أنواع الاشارات ، نظرية النمذجة ، متسلسلة فورير ، متسلسلة فورير المركبة، محول فورير، معكوس محول فورير، محول فوريرالمتقطع، محول فورير السريع (FFT) ، الألتفاف ، محول-Z ، المرشحات الرقمية . واجهة المستخدم الرسومية (GUI) المميزة لبرنامج (MATLAB) تم استخدامها لاعطاء الطالب طريقة سهلة ومرئية في ادخال البيانات بينما تم استخدام لغة ترميز النصوص التشعبية (HTML) في توضيح الأسس النظرية. لقد تم استخدام الاستفتاء ومقياس ليكرت ذي الخمس نقاط في إجراء عملية التقييم . أظهرت نتائج التقييم أن مختبر (DSP) الافتراضي المقترح ساعد الطلبة في فهم مباديء (DSP) ، كما أضاف تأثيرات إيجابية في أداء ورغبات الطلبة بالمقارنة مع طرق التعليم التقليدية.

ABSTRACT:

Engineering education should involve practical laboratory to support theoretical foundation and develop student skills. These hands on laboratories have some disadvantages such as expensive, supervision required, time and place restrictions. This paper presents design and evaluation of a web based virtual laboratory for teaching Digital Signal Processing (DSP) to undergraduate students in Electromechanical Engineering Department at the University of Technology. The laboratory experiments includes classification of signals, sampling theorem, Fourier series, complex Fourier series, Fourier transform, inverse Fourier transform, discrete Fourier transform, Fast Fourier Transform (FFT), convolution , Z-transform, and digital filters. Graphical User Interface (GUI) feature of MATLAB have been used to provide students with a friendly and visual approach in specifying input parameters while Hyper Text Markup Language (HTML) was used to illustrate theoretical foundations. The questionnaire survey and five point Likert scale are utilized in performing evaluation. Results of this evaluation showed that the proposed virtual DSP laboratory was helped students in DSP concepts, made positive effects on students' achievements and attitudes when compared to traditional teaching methods.

KEYWORDS: Engineering Education, Virtual laboratory, DSP, Internet, GUI, HTML

I. INTRODUCTION

Digital Signal Processing (DSP) course have been taught at Electromechanical Engineering Department, University of Technology. This course involves a large number of complicated mathematical equations that need some explanation to appreciate underlying concepts. The hands on laboratory can be used to help students in illustrating these conceptual concepts and developing their practical skills [Feisel, 2005]. However, these hands on laboratories have some drawbacks such as expensive, supervision required, time and place restrictions [Nedic, 2003; Balamuralithara,2008].

In the last decade, there has been a growing trend in the utilization of simulation-based virtual laboratories for undergraduate students in the engineering and science colleges. However, these modern laboratories are cost effective [Wolf,2009], increase the student performance [Macias,2001;Campbell,2004], encourage self learning by providing hands on activities [Chu,1999], and suitable for use in distance learning when the World Wide Web (WWW) access is available [Agrawal,2008]. Several authors have presented researches in engineering education covered a wide range of disciplines, such as electrical engineering [Tanyildizi, 2009], mechanical engineering [Gil, 2000], control engineering [Uran, 2008], chemical engineering [Murphy,2002] , and civil engineering [Budhu,2002], while other authors were introduced researches in science education [Stone,2007; Jimenez,2003].

Nowadays, virtual laboratory is used as prevalent alternative to the traditional hands on laboratory and must be performed the same learning outcomes. However, some universities already have been started to utilize virtual laboratories in the engineering colleges such as John Hopkins University in USA [Karweit], Polytechnic University of Valencia in Spain [Tejedor,2008], Warsaw University of Technology in Poland [Sobczuk,2007], University of Pisa in Italy [D'andrea,2008], and many others.

Virtual laboratories can be broadly classified into three types: **First**, simulation laboratories that use software and web server to emulate the physical laboratory [Nedic, 2003; Balamuralithara,2008] . In these laboratories, the users can modify the parameters of the simulation and observe the changes in the system. **Second**, remote laboratories allow users to view, control

and acquire data from a physical experiment through a web server [Nedic, 2003; Balamuralithara,2008]. **Third**, recorded experiments allow users to view actual experiments and work with real data [Sidhu,2010;Chan,1998].

Virtual laboratory has been assessed by several researchers and they have concluded that there is no significant difference in student learning results from using virtual learning laboratory versus physical laboratory [Campbell, 2002]. However, complete removal of physical laboratory from the syllabus would not be accepted by students according to their feedback [Wiesner,2004].

This paper presents design and evaluation of web-based virtual DSP laboratory developed by the authors as an instructional tool for undergraduate students at the Electromechanical Engineering Department /University of Technology [Burak ,2008]. The developed virtual laboratory has been evaluated by (30) undergraduate students and (5) lecturers from the Electromechanical Engineering Department / University of Technology.

II. LABORATORY IMPLEMENTATION

The implementation of the virtual DSP laboratory required a variety of tools to facilitate the use of different presentation methods. Two important software programs in the development of the virtual DSP laboratory included Hyper Text Markup Language (HTML) and MATLAB Graphical User Interface (GUI).

1) Hyper Text Markup Language (HTML)

The HTML version 4 has been used to demonstrate theory information of DSP in a web page form. The main web page of the developed virtual DSP laboratory will begins with the presentation screen shown in Fig. 1. As can be seen from this main web page, the student can study and perform required experiments in any of the following topics by clicking on the button **1)** Classification of signals, **2)** Sampling theorem, **3)** Fourier series, **4)** Complex Fourier series, **5)** Fourier transform, **6)** Inverse Fourier transform,**7)** Discrete Fourier transform, **8)** Fast Fourier Transform (FFT), **9)** Convolution,**10)** Z-transform, and **11)** Digital filters. These topics constitute the core structure of DSP course that is presently introduced to the undergraduate students in Electromechanical Engineering Department.



The HTML code for the main web page is generated dynamically through the Hypertext Preprocessor (PHP) as shown in Fig.2. The PHP code is interpreted by a web server to generate the web page of virtual DSP laboratory. The PHP is available as a processor for most modern web servers and as a standalone interpreter on most operating systems and computing platforms.

2) Graphical User Interface

The Graphical User Interface (GUI) is a MATLAB based toolbox with the following features: **1)** User friendly environment, (drag and drop) approach, **2)** Developing a model needs short time **3)** No knowledge in computer programming required to perform an experiment, **4)** The student can set the desired parameters in any experiment and plot result using mouse clicks. Therefore, GUI has been utilized to perform mathematical

calculation for any DSP model used herein in this paper. MATLAB implements GUI through Graphical User Interface Development Environment (GUIDE) which allows the user to create figure windows containing graphical objects. In order to start create models in GUI type GUIDE in the MATLAB prompt window that will cause appearing GUIDE program as shown in Fig.3. This window is separated equally into right side window which is called (open existing GUI) used to open an already exist model in the workspace while the left side window is called (create new GUI) which is used to build new GUI model with the help of four GUIDE templates; blank GUI, GUI with uicontrols, GUI with axes and menu, and modal question dialog.

By clicking on the blank GUI in GUI beginning window and clicking on save new figure to save model with name SIGNALS_GUI as shown in Fig.4. The component palette at the left side of the GUI layout editor contains the pushbuttons, toggle buttons, lists, menus, text boxes, and so forth components that will be used to build simulation program for stepper motor. This component palette can display with its names.

Note that due to space limitation the authors cannot presents all programming steps, for further

details see [Burak]. The following are experiments of the developed virtual DSP laboratory.

Experiment (1): Classification of signals

In this experiment, the student can conducts experiment on five types of signals as shown in Fig.5. Each experiment has a menu on the left hand side includes objective, theory, example, exercise, equation, and question. The objectives of the experiment can be obtained by pressing on the objective button. The necessary information and theory bases for this experiment will displayed after pressing on the theory button as shown in Fig.6. Example button can be used to present solved example as shown in Fig.7. The exercise button is

intended for conducting the required experiment on continuous, discrete time, and digital signal using GUI. The last two buttons are used for mathematical description of the experiment and to perform self test after complete experiment as shown in Fig.8 and Fig.9 respectively.

The exercise of experiment (1) shown in Fig.10 was designed in MATLAB GUI. The student can perform experiment on three different types of signals, sine, triangle and square wave. The frequency, sampling rates, and the number of bits per sample of the selected signal can be changed through using slider menu .After selection of input signal parameters, one can plot experiment results by pressing on display button.

Experiment (2): Sampling Theory

The experiment of sampling theory is shown in Fig.11. This experiment can be accessed through clicking on the sampling theory button in the main web page. The student can explore this experiment with the help of the menu on the left hand side which has six different buttons. When the student clicks on the first button, this will cause in viewing of experiment objectives while clicking on the second button will cause to display experiment theory as shown in Fig.12.

It is possible to view a number of solved examples in sampling theory through clicking on the third button

as shown in Fig.13. These examples can help students to understand basic principles of sampling theorem and prepare them to practical exercise. Fig.14 shows an interactive exercise which has been developed in MATLAB GUI to deal with continuous and discrete time domain signals. Furthermore, the effects of signal aliasing can also be studied. The student can change the frequency as well as the phase for the aforementioned signals either by using slider or by entering required value in appropriate box and then observe the frequency spectrum of the signal in a three displays. A web page containing all the necessary equations for this experiment can be reached by clicking on the equation button in the left menu of experiment (2) as shown in Fig.15. Finally, in order to complete this experiment, the student should be able to correctly answer on a number of questions as shown in Fig.16.

Experiment (3): Fourier series

This experiment starts with reviewing some historical background for the famous Fourier paper as shown in Fig.17. The basic principles for representing any periodic signal by means of Fourier series were illustrated in a web page as shown in Fig. 18. It is possible to demonstrate solved examples that can be helpful to explain how to obtain coefficients in Fourier series as shown in Fig.19. From the excise menu of this experiment, the student can choose from the GUI menu one of the following signals: **1) Square wave, 2) Triangle wave, 3) Ramp and Saw tooth waves, 4) Full wave rectified sine, 5) Full wave rectified cosine, 6) Half wave rectified sine, 7) Half wave rectified cosine** to perform exercise in Fourier series as depicted in Fig.20. This exercise has been designed to be flexible enough in changing frequency of the selected signal by placing mouse on the

slider. All the necessary equations for this experiment were prepared in web page as shown in Fig.21. For evaluation purpose the student should be passed a self test as shown in Fig.22.

Experiment (4): Complex Fourier series

In preceding experiment we have learned representation of signals by using Fourier series. Now, the advantageous to use complex representation of the sine and cosine signals we will be discussed in this experiment as shown in Fig.23.

The theory behind using complex Fourier series in the analysis of signals as a superposition of complex exponentials was introduced in a web page as shown in Fig.24. Normally, the principles of complex Fourier series rely on sophisticated equations that cannot be understood by student without solved examples as shown in Fig.25.

The exercise for this experiment has been developed in MATLAB GUI as shown in Fig.26, with the following features: **1) There are so many built in wave forms which can be obtained by clicking on the slider to perform required experiment. 2) Changing the amplitude, period and width of any desired signal is quite simple by using slider. 3) There are three display windows used to observe and plot results.**

All the necessary equations were given in Fig.27 while the self test was prepared using multiple choose as shown in Fig.28.

Experiment (5): Fourier Transform

This experiment addresses the use of Fourier transform in converting signals from time domain to frequency domain. The Fourier transform of continuous and discrete signals will be discussed in details. It can access this experiment by clicking on the Fourier transform button in main web page as shown in Fig.29.

A brief description of the basic ideas and theorems of Fourier transform can be obtained after clicking on the theory button as shown in Fig.30. A solved example that illustrates the power of this technique in handling signals will be available by clicking on the example button of the experiment as shown in Fig.31.

The exercise of this experiment has been developed in MATLAB GUI for use in conducting Fourier transform experiments in time domain as well as frequency domain. This exercise will be ready to start performing certain experiments after clicking on the exercise button as shown in Fig.32.

There are many features has been added to facilitate perform this exercise such as variety of



signals, change of signal magnitude and phase in time domain as well as frequency domain is very simple because it is based on slider, has four display to monitor results uses two for time domain and the rest for frequency domain.

The derivations of Fourier transform equations and some explanation can be found by clicking on the

theory button as shown in Fig.33. The student should perform multiple-choice self-test as shown in Fig.34. The grading of this test appears after complete test.

Experiment (6): Inverse Fourier Transform

The inverse Fourier transforms used to convert frequency series of complex values into the original time series. We have been developed an experiment to study this conversion and it can be get access to this experiment by clicking on inverse Fourier transform button as shown in Fig.35. In order to get more information on the theory basis of inverse Fourier transforms press on the theory button as shown in Fig.36.

There is a solved example which may increase student perception can be viewed by clicking on the example button as shown in Fig.37.

The MATLAB GUI has been used to develop inverse Fourier transform exercise in such away the student can perform experiment in short time with clear steps. To start this exercise you should press on the exercise button as shown in Fig.38. The essential equations and derivation for inverse Fourier transform could be very helpful in underline some basic concepts. Therefore, these equations can be obtained if we clicking on the equation button as shown in Fig.39.

Evaluating what students have learned throughout this exercise can be accomplished in multiples choose test which can be accessed by clicking on the question button as shown in Fig.40.

Experiment (7): Discrete Fourier Transform

There are many applications that use Discrete Fourier Transform (DFT) to perform a specific task. Generally, the DFT is difficult topic due to

their inherent mathematical equations. Therefore, we have been developed this experiment to help student in understanding basic concepts of DFT. To start this experiment, click on the DFT button in the main web page as shown in Fig.41. We have been designed a series of options on the left hand side of this experiment which give access to the different sections, for example to get information on theory basis, click on the theory button as shown in Fig.42.

It is possible after complete reading theory basis to view some solved example on DFT concepts by clicking on the example button as shown in Fig.43. The exercise for this experiment has been developed in MATLAB GUI to give students more insight into DFT and remove any confusion might be happen due to their misunderstanding of complicated mathematical equations.

The exercise can launch by clicking on the exercise button as shown in Fig.44. There are four types of signals could be used to perform experiments such as sine wave, square wave, triangle wave, and saw tooth wave. These signals can be selected by placing cursor at the signals menu. Also, the number of cycles in the selected signal can be changed similarly. To get detailed mathematical equations and derivation of DFT press on the equations button as shown in Fig.45. The end of this experiment include multiple choose test that should be performed by any participated student and this test could be launched by clicking on the question button as shown in Fig.46. If the students did not get good score in this test, they should repeat experiment again.

Experiment (8): Fast Fourier Transform

The Fast Fourier Transform (FFT) is a mathematical approach aims to reduce computational power of DFT. The FFT have a wide range of applications in communication, biomedical engineering, and radar systems. Therefore, the FFT has become an invaluable analysis tool and every enrolled student in this course should have good expertise to use this tool. Fig.47 shows FFT experiment which can be launched to perform experiments by clicking

The student can obtain more information on basic concepts of FFT to increase intuitive development by clicking on the theory button as shown in Fig.48. An 8-points solved example was used to intuitively justify the FFT algorithm. This example will be launched by pressing on the example button as shown in Fig.49. From this example one should be note that the FFT owes its success to the fact that the algorithm reduces the number of multiplications and additions in the computation. By clicking on the exercise button the student can start performing experiments on FFT as shown in Fig.50. The graph of FFT spectrum can be displayed on the three small windows. Fig.51 shows part of the FFT equations which can be browsed by clicking on the equation button. As with the preceding experiments, the student should answer on a number of questions in order to complete this experiment and this test could be started by clicking on the question button as depicted in Fig.52. The minimum score to pass this experiment is 50 percent.

Experiment (9): Convolution

The convolution can be defined as a mathematical operation on two functions f and h , producing a third function that is viewed as a modified version of one of the original functions. The convolution is of great importance due to its wide range of applications from signal and image processing to acoustics and probability theory. Fig. 53, shows the convolution experiment which can be launched by pressing on the convolution button. When the student pressing on the theory button a web page as shown in Fig.54 which gives detailed information on convolution fundamentals.

A solve example can be accessed by clicking on the example button as shown in Fig.55. The purpose of this example is for assistance in learning convolution. Now, the student can perform experiment on convolution by pressing on the exercise button as shown in Fig.56. It is possible to choose the desired signal to conduct convolution from a button called get $x(t)$. Three displays were used to monitor two input signals, multiplication and convolution results, respectively. The equations of convolution theorem are shown in Fig.57. The self test question of this exercise is shown in Fig.58.

Experiment (10): Z-Transform

The Z-transform is very powerful mathematical tool used in design, analysis and monitoring of systems. The importance of this experiment comes from the fact that knowledge of Z-transform is essential to design of digital filters. This experiment will be started by clicking on the Z-transform button as shown in Fig.59. In this experiment, the definition of the Z-transform from the Laplace transform of a discrete-time signal as well as the properties of Z-transform is presented.

A useful aspect of the Z-transforms is the representation of a system in terms of the locations of the poles and the zeros of the system transfer function in a complex plane can be found by clicking on the theory button as shown in Fig.60. Several examples illustrating the physical significance of Z-transform and their effect on the frequency response of a system is available by clicking on the examples button as depicted in Fig.61.

An interactive and user friendly software program has been developed in MATLAB GUI to conduct experiments in z-transform. This exercise can be accessed by pressing on the exercise button as depicted in Fig. 62. The developed Z-transform exercise has the following features: **1)** Students can add poles and zeros by mouse click or by input required poles and zeros in box. **2)** Poles and zeros can be moved around the Z-plane by selecting them and pulling the mouse around, with the instant update of the system frequency impulse response. **3)** System transfer function or filter coefficients were used to indirectly specify poles and zeros. The derivation of the so-called Z-plane, and its associated unit circle, from sampling the S-plane of the Laplace transform can be accessed by pressing on the equations button as shown in Fig.63. A multiple choose test should be performed by students to measure learning at the various cognitive levels. This test can be started by clicking on the question button as shown in Fig.64.

Experiment (11): Digital Filter

This is the last experiment in the developed virtual DSP laboratory. In this experiment, the students can conduct experiments on the digital filters for both Infinite Impulse Response (IIR) and Finite Impulse Response (FIR) by clicking on the digital filter button as shown in Fig.65.



A digital filter is an electronic filter usually linear used in removing undesirable elements of a signal or compensating for some frequency dependent distortion within the signal. For more information on these filters as well as advantageous and disadvantageous can be reached by clicking on the theory button as depicted in Fig.66. Numerous numbers of solved examples in digital filters have been added into this experiment to help students in understanding theoretical concepts. These examples will be viewed by pressing on the example button as shown in Fig.67.

The exercise of this experiment will be started after pressing on the exercise button as shown in Fig.68. From this figure, it is clear that, the upper GUI model can be used to perform FIR filter experiments while the middle GUI model used to conduct IIR filter experiments. The features of the developed exercise can be summarized as: **1)** Students easily can select filter type to conduct experiment such as a low pass, high pass, band pass, and band stop filter from the popup menu. **2)** Allow to change filter order, frequency (1) and frequency (2) using the slider. **3)** Options, such as rectangular, bartlett, hamming, hanning, and blackman windowing functions are also available to be applied using slider. **4)** The pole- zero placements and the magnitude of the filter can be observed by using two display screens (see lower figure in Fig.68). The mathematical equations of FIR and IIR filters can be obtained by clicking on the equations button as shown in Fig.69. The student should be exposed to a test consists of multiple choice questions each question has two answers. This test could be started by pressing on the question button as shown in Fig.70.

III-Evaluation

The developed Virtual DSP Laboratory has been evaluated by fifteen final year students (10 males and 5 females). All the participants in the survey were from Electromechanical Engineering Department, University of Technology. The Likert scale will be used to analyze the results of the questionnaire survey. This scale measure either positive or negative response to a statement. The responding to a Likert questionnaire item, respondents specify their level of agreement to a statement. A recent empirical study found that a five point or seven point scale may produce

slightly higher mean scores relative to the highest possible attainable score, compared to those produced from a ten point scale, and this difference was statistically significant [Dawes,2008]. Therefore, in this paper, the students were asked in questionnaire survey to provide their degree of agreement using five-point Likert scale (strongly disagree **1**, disagree **2**, neither agree nor disagree **3**, agree **4**, and strongly agree **5**).

The evaluation statements were designed to assess the students' attitudes toward using the developed virtual DSP laboratory in the course, make sure that it's achieve course objectives, and to determine if the students would find the presentation and the contents of the developed virtual DSP laboratory beneficial to their performance, learning, and understanding in the laboratory course.

Means and standard deviations of the survey results are presented in Table 1. As indicated in Table (1) the students generally agreed that the developed virtual DSP laboratory provides a convenient environment for learning. It was also confirmed that developed virtual DSP laboratory is fairly easy to use in the sense of moving around different menus rapidly. Furthermore, they were able to take as much time as they wished to review the material. The best part of developed virtual DSP laboratory turned out to be, as intended, its user-friendly environment and easy accessibility. Majority of students thought that the virtual laboratory was helped them to get a better understanding of signal processing and that they were able to visualize some of the concepts.

Conclusions

In this paper, a web based virtual DSP laboratory has been developed in MATLAB GUI and HTML to enhance the understanding of concepts taught in the undergraduate DSP course. The proposed virtual laboratory is affordable, interactive, and can be used in distance learning via using World Wide Web (WWW). Furthermore, offers an excellent and suitable platform to prepare undergraduate students before they are going into the actual laboratory.

There are 11 experiments have been performed using the developed virtual DSP laboratory and all of these experiments were selected from the curriculum of the Electromechanical Engineering Department /University of Technology. A methodology for evaluation of developed virtual DSP laboratory based on five point Likert scale was outlined. The results of

questionnaire survey indicate that the majority of the students felt that the developed virtual DSP laboratory was beneficial in understanding of DSP algorithms, make learning an enjoyable experience and it had further aroused their interests. It is expected that the virtual laboratories as promising technology will increasingly use in engineering and sciences colleges to complement hands on laboratories but not to substitute them.

References

- Agrawal, J.P. and Cherner , Y.E ,(2008) " A Classroom/Distance Learning Engineering Course on Wireless Networking with Virtual Lab ," *Proceedings of the IAJC-IJME International Conference*, pp.1-9.
- Balamuralithara, B. , and Woods, P.C.,(2008)" Virtual Laboratories in Engineering Education: The Simulation Lab and Remote Lab," *Computer Applications in Engineering Education*, vol.17, issue 1, pp. 108 – 118.
- Budhu , M.,(2002) " Virtual Laboratories for Engineering Education ," *International Conference on Engineering Education* , Manchester ,UK, pp.1-6.
- Burak, Abdulhadi, (2008), *Techniques of Distance Learning for Digital Signal Processing, MSc Thesis, Electromechanical Engineering Department, University of Technology.*
- Campbell, J. O., Bourne, J., Mosterman, P., and Brodersen, A. J. , (2002) "The Effectiveness of Learning Simulations for Electronic Laboratories," *Journal of Engineering Education*, vol.91, no. 1, pp.81-87.
- Campbell, J. O. , Bourne, J.R. , Mosterman, P.J. , Nahvi, M., Rassai, R., Brodersen, A.J. ,and Dawant, M. , (2004)" The Effectiveness of Simulated Electronics Laboratories for Distributed Online Learning, " *Journal of Asynchronous Learning Networks*, vol. 8, no. 3, pp.1-8.
- Chan, T. Y., and Bradbeer, R., (1998) "An Online Multimedia Learning System for First Year Laboratory", *Proceedings of 3rd IEEE Conference on Multimedia Engineering and Education (MMEE)* , Hong Kong, pp.1-4.
- Chu, K. C. , (1999) " What are the Benefits of a Virtual Laboratory for Student Learning, " *HERDSA Annual International Conference*, Melbourne, pp.1-9.
- D'andrea, A.N. , Giannetti, F., Manara, G., Michelini , M., and Nepa , P., (2008) " A Virtual Educational Laboratory for Telecommunications Engineering ," *International Journal of Engineering Education* , vol.24, no.1, pp.144-152.
- Dawes, J. , (2008), " Do Data Characteristics Change According to the number of scale points used? An experiment using 5-point, 7-point and 10-point scales", *International Journal of Market Research*, vol. 50, no.1, PP. 61–77.
- Feisel, L.D., and Rosa, A.J.,(2005) " The Role of Laboratory in Undergraduate Engineering Education," *Journal of Engineering Education*," vol.94, pp.121-130.
- Gil, L., Blanco, E. and Maria, J., (2000)" The Virtual Laboratory Concept to Strain Measurements," *European Journal of Engineering Education*, vol. 25, no. 3, pp.243-251.
- Jimenez, P. M., Pedrajas, A. P., Bellido, M. S. C., and Cozar , J. P., (2003) "Learning in Chemistry With Virtual Laboratories, " *Journal of Chemical Education*, vol.80, no.3,pp.346-352.
- Karweit, M. , " A Virtual Engineering / Science Laboratory Course ," <http://www.jhu.edu/~virtlab/virtlab.html>.
- Macias , M. E. , Cazares , V. M. , and Ramos, E. E. , (2001), "A Virtual Laboratory for Introductory Electrical Engineering Courses to Increase the Student Performance, *31st ASEE/IEEE Frontiers in Education Conference*,vol.3,pp. S2C-13, Oct.10-13.
- Murphy, T., Gomes , V.G., and Romagnoli , J.A., (2002)" Facilitating Process Control Teaching and Learning in a Virtual Laboratory Environment ," *Computer Applications in Engineering Education*, vol. 10, issue 2, pp.79-87.
- Nedic, Z., Machotka, J. and Nafalskt, A., (2003)" Remote Laboratories versus Virtual and Real Laboratories," *33rd ASEE/ IEEE Frontiers in Education Conference*, vol.1, pp.T3E1-T3E6, Nov. 5-8.
- Sidhu, M.S.,(2010), *Technology Assisted Problem Solving for Engineering Education Interactive Multimedia Applications*, Engineering Science Reference, Hershey, USA.
- Sobczuk , D.L. ,(2007) " Internet Based Teaching of Pulse Width Modulation for Three Level Converters ," *Eurocon, International Conference on Computer as a Tool* , Warsaw, Poland, pp.2479-2484.



Stone, D.C. , (Sept., 2007) “ Teaching Chromatography Using Virtual Laboratory Exercises,” *Journal of Chemical Education*, vol. 84, no.9, pp. 1488–1496.

Tanyildizi, E., and Orhan , A.,(2009) " A Virtual Electric Machine Laboratory for Effect of Saturation of the Asynchronous Machine Application ," *Computer Applications in Engineering Education*, vol. 17, issue 4, pp.422-428.

Tejedor , J.A. G. , Martinez, G. M. , and Vidaurre , C. B. ,(2008) " An Online Virtual Laboratory of Electricity ," *International Journal of Distance Education Technology*, vol.6 , issue 2, pp.21-34.

Uran, S., and Jezernik , K., (2008)" Virtual Laboratory for Creative Control Design Experiments ," *IEEE Transactions on Education*, vol. 51, no. 1, pp.69-75.

Wiesner, T. and Lan, W., (2004) "Comparison of Student Learning in Physical and Simulated Unit Operations Experiments," *Journal of Engineering Education*, vol. 93, no.3, pp.195–204.

Wolf, T., (2009)"Assessing Student Learning in a Virtual Laboratory Environment," *IEEE Transaction on Education*, vol.52, issue 3, pp. 1 – 7.

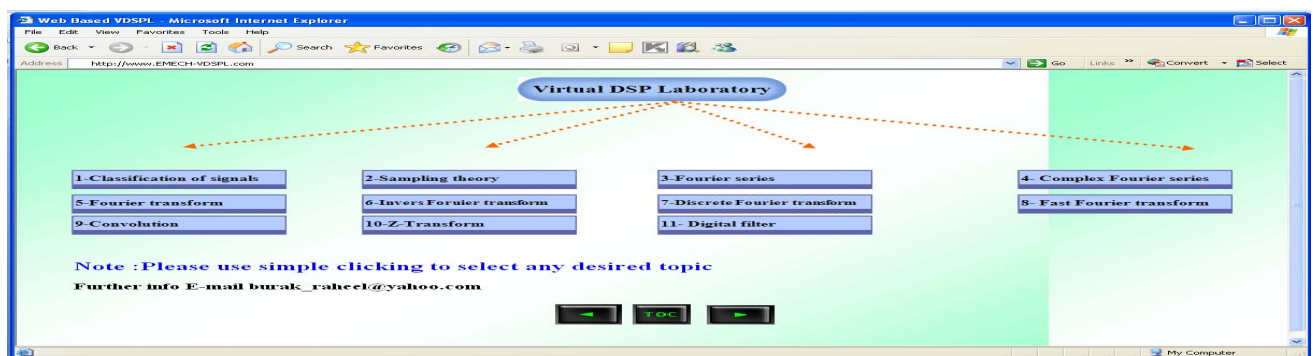


Fig.1 Main web page of virtual DSP laboratory.

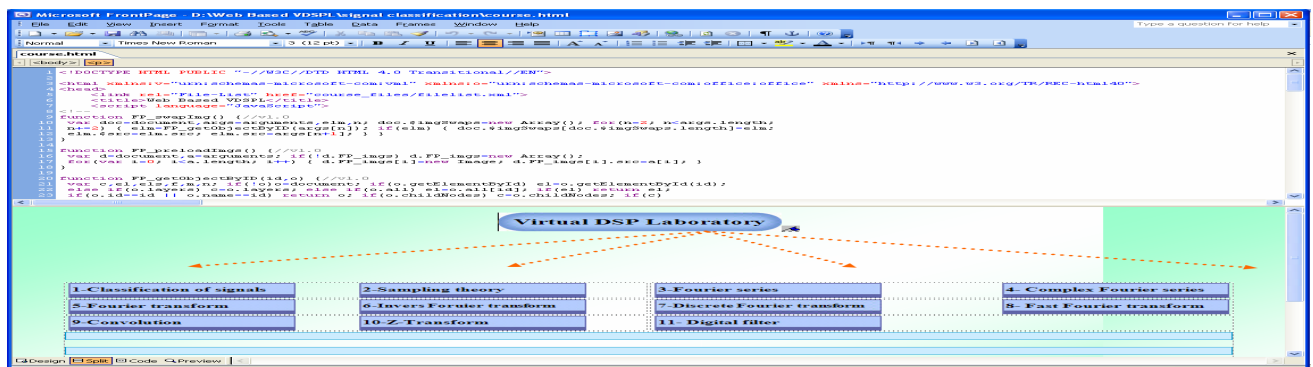


Fig.2 HTML code of the main web page.

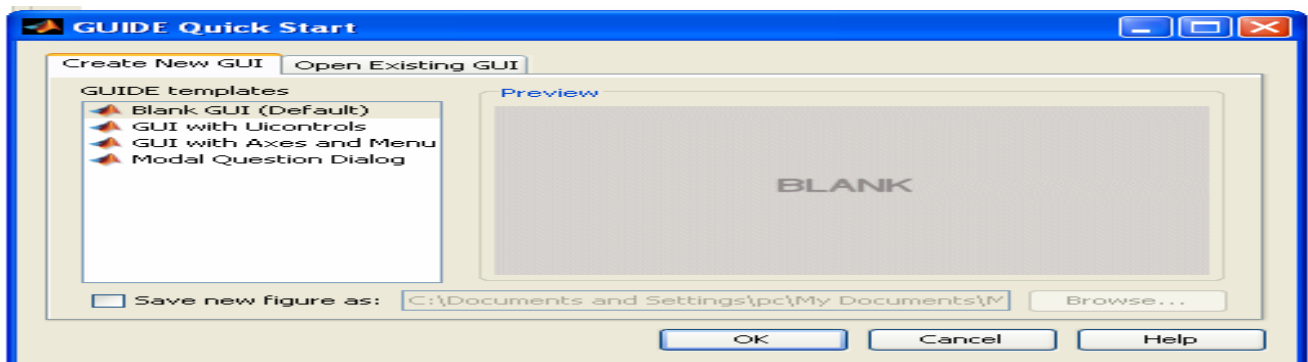


Fig.3 GUIDE quick start dialog box.

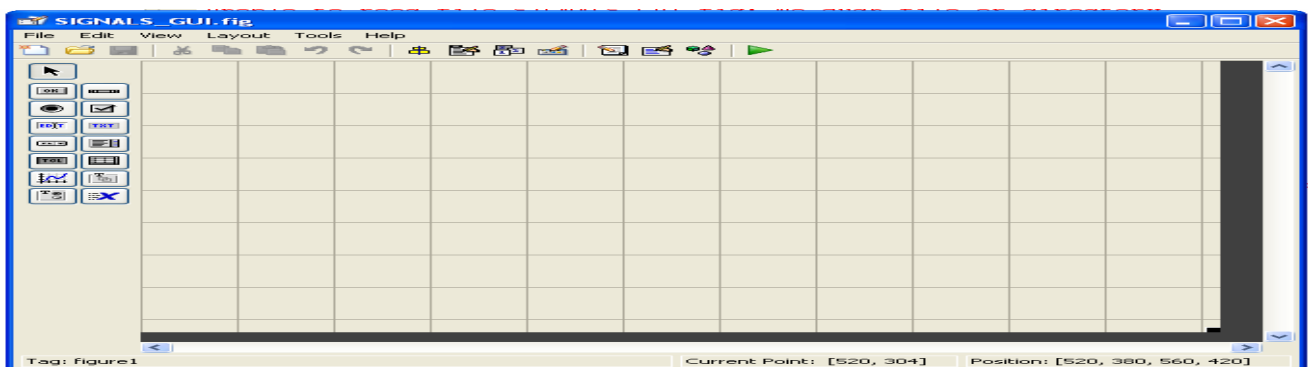


Fig.4 GUI layout editor.

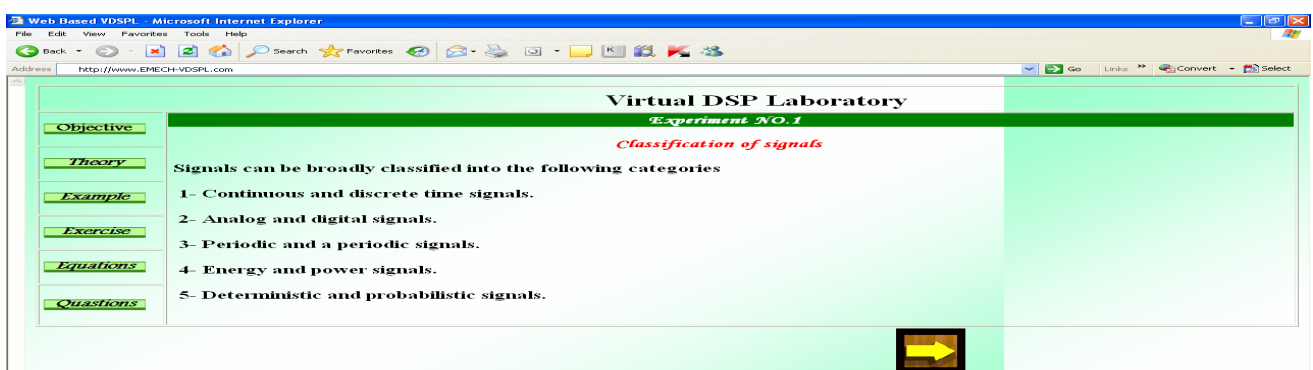


Fig.5 Web page of experiment (1).

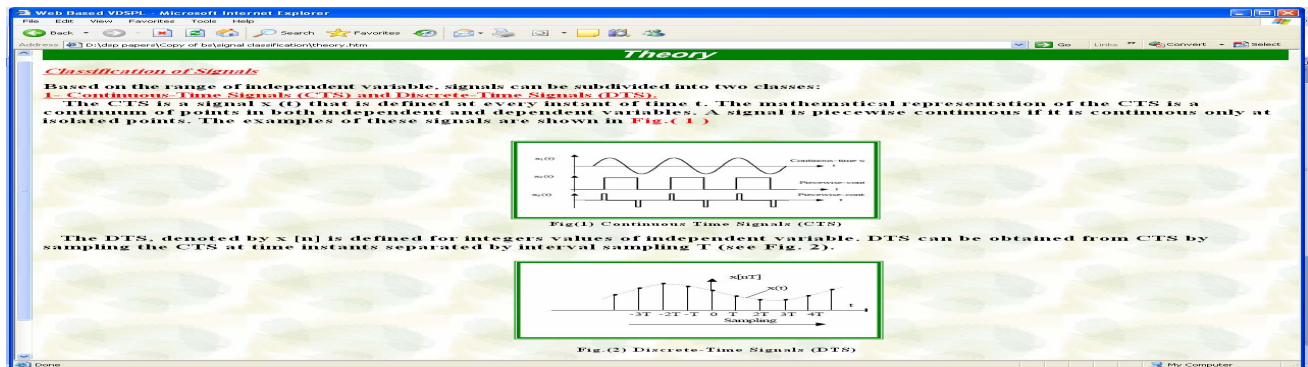


Fig.6 Web page of theory bases for experiment (1).

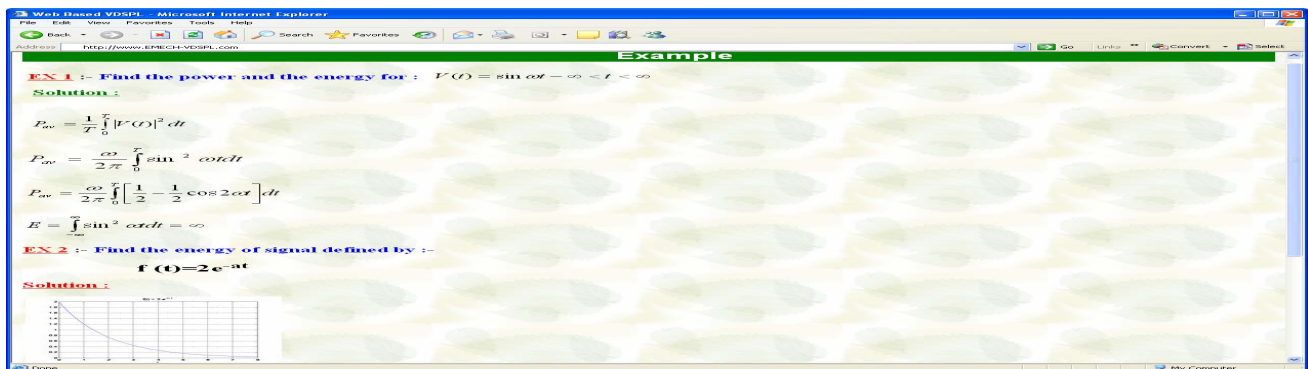


Fig.7 Web page of solved example introduced in experiment (1).

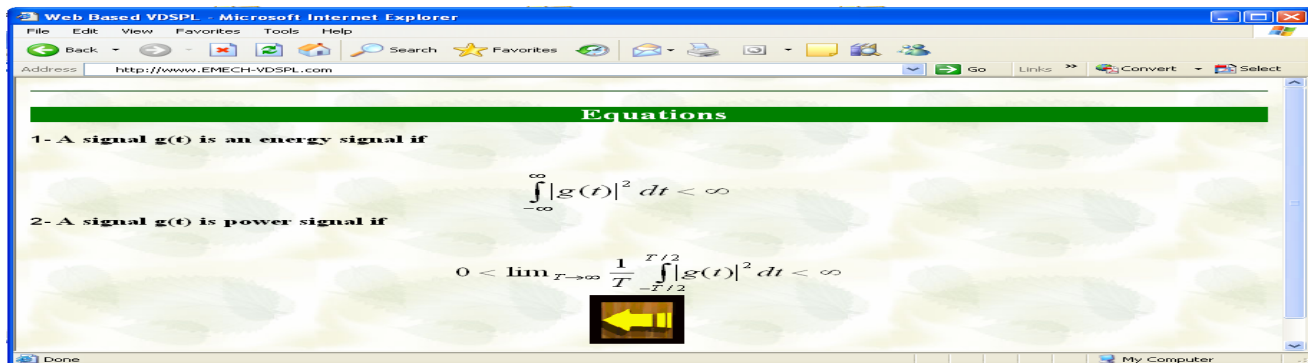


Fig.8 Web page of equations used in experiment (1).

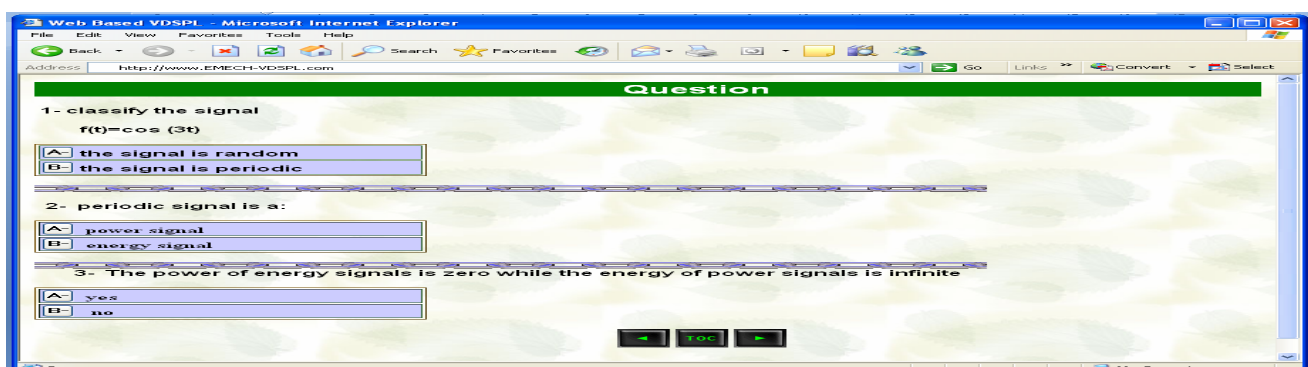


Fig.9 Web page of self test questions applied to experiment (1).

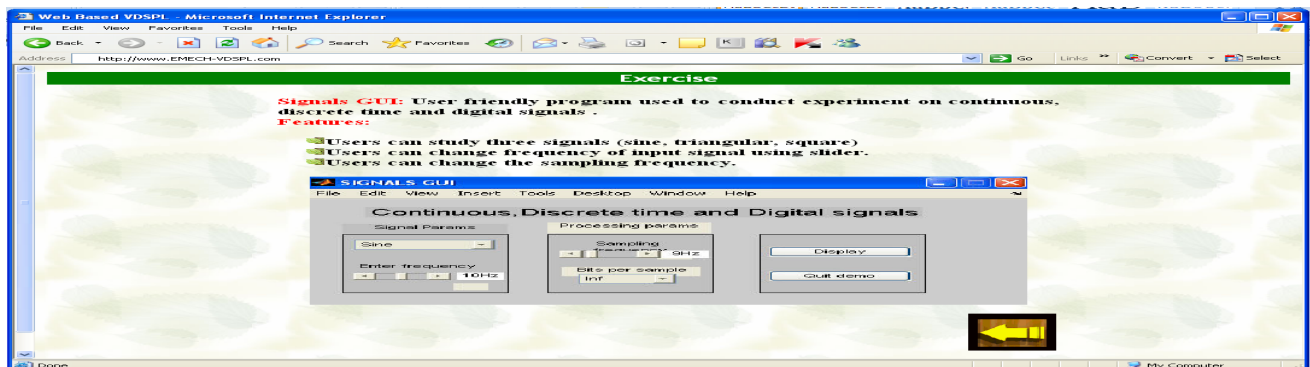


Fig.10 Web page of exercise for experiment (1).

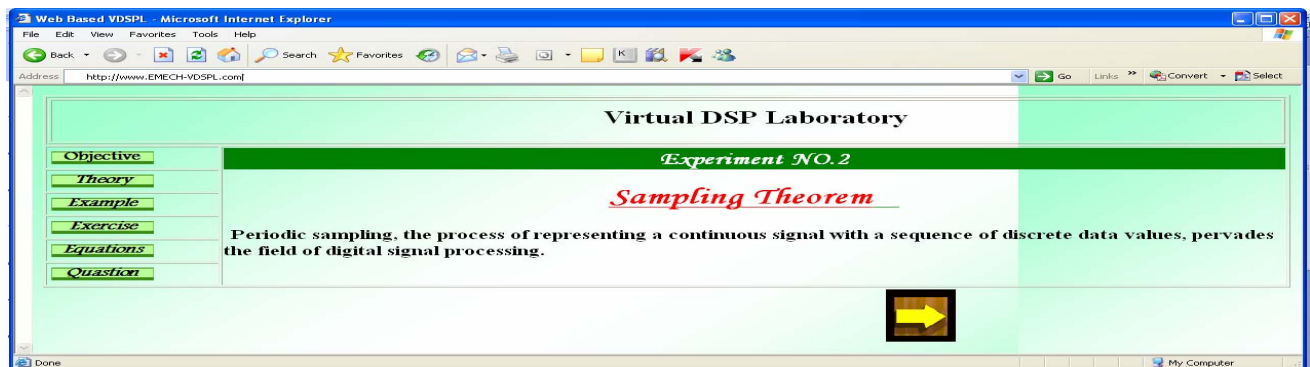


Fig.11 Web page of experiment (2).

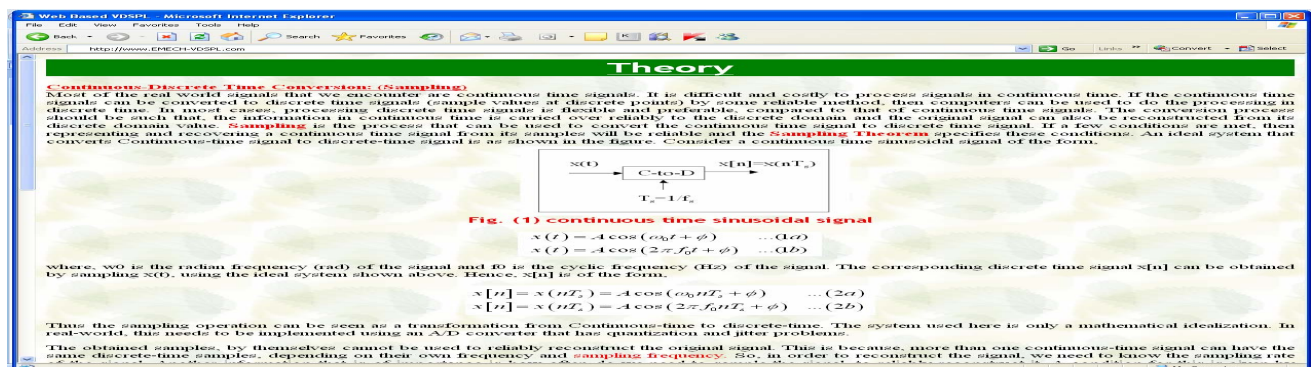


Fig.12 Web page of theory bases for experiment (2).

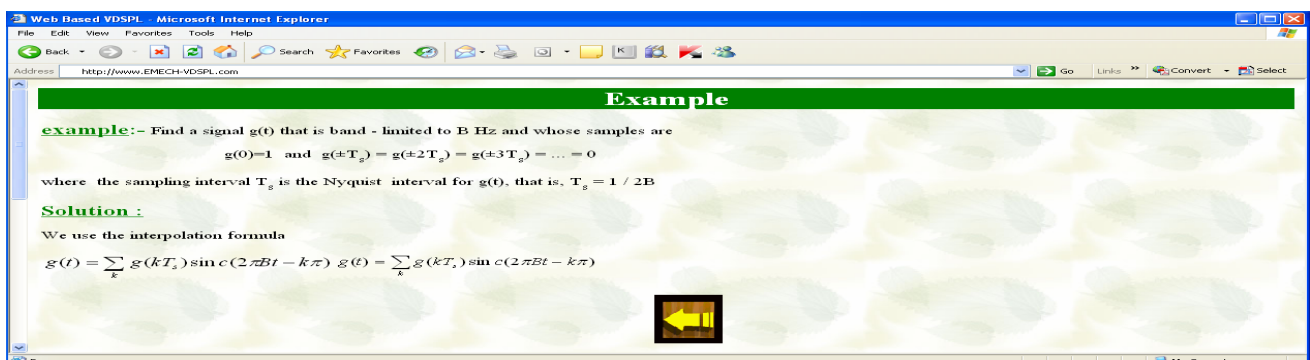


Fig.13 Web page of solved example used in experiment (2).

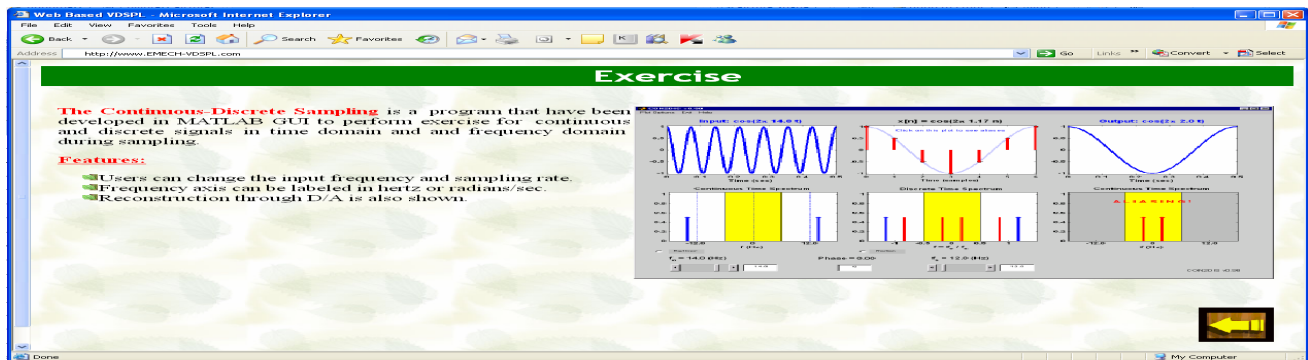


Fig.14 Web page of exercise for experiment (2).

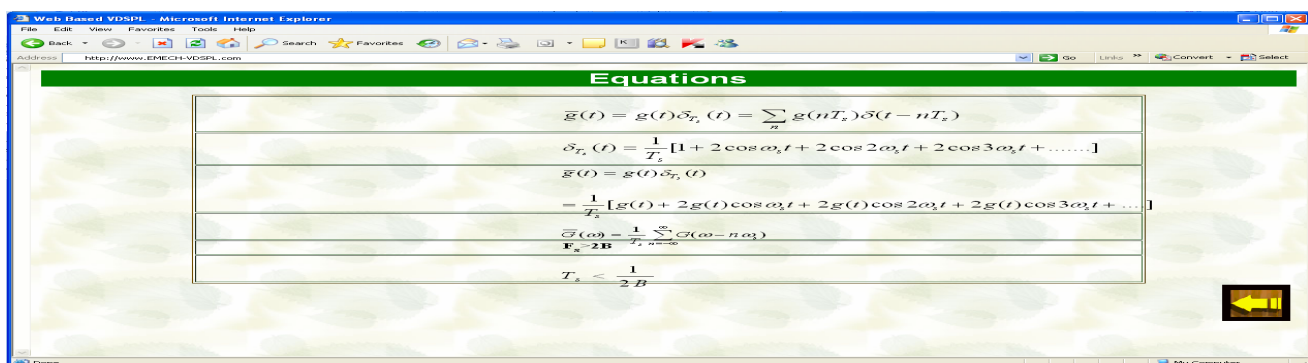


Fig.15 Web page of equations used in experiment (2).

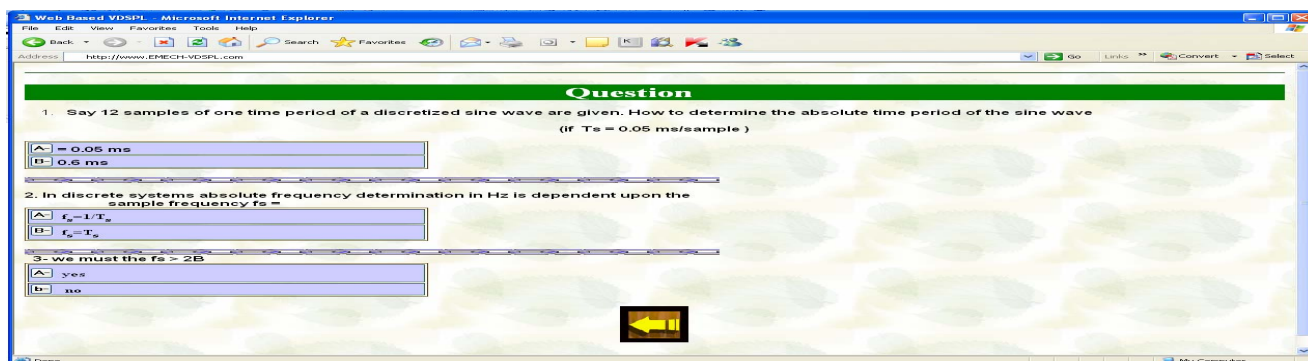


Fig.16 Web page of self test questions applied to experiment (2).

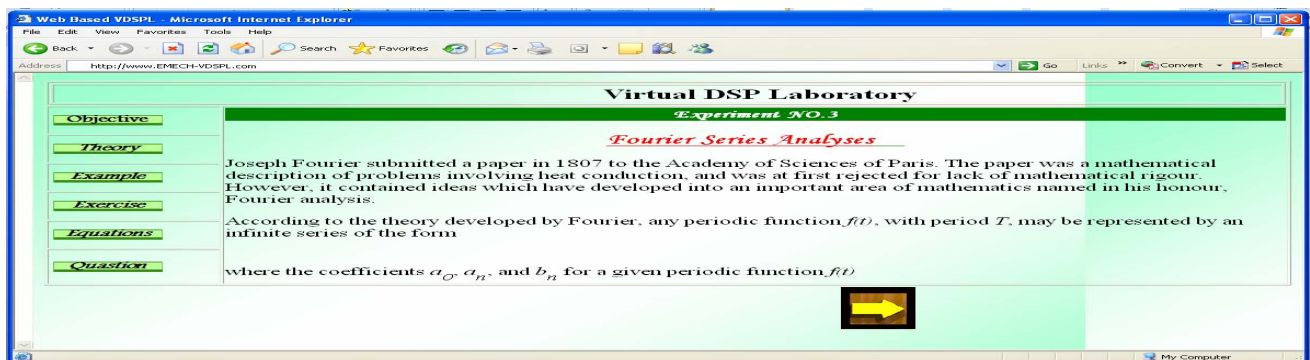


Fig.17 Web page of experiment (3).

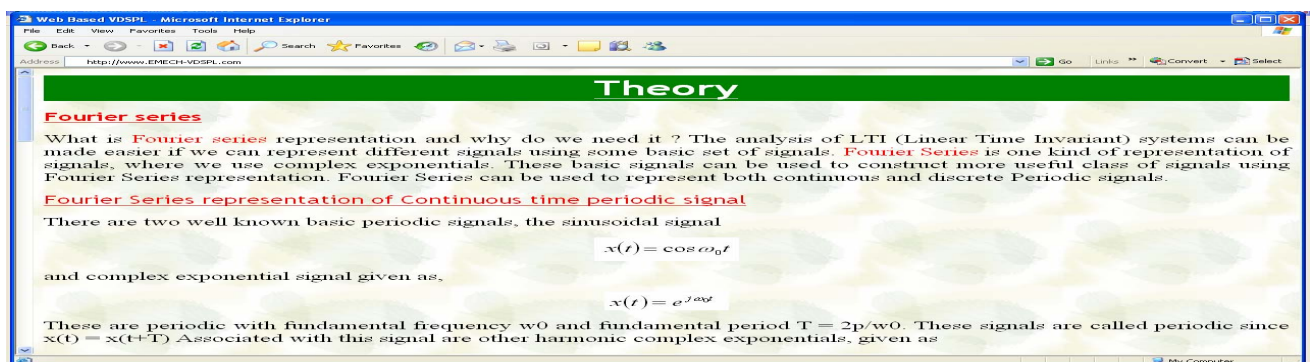


Fig.18 Web page of theory bases for experiment (3).

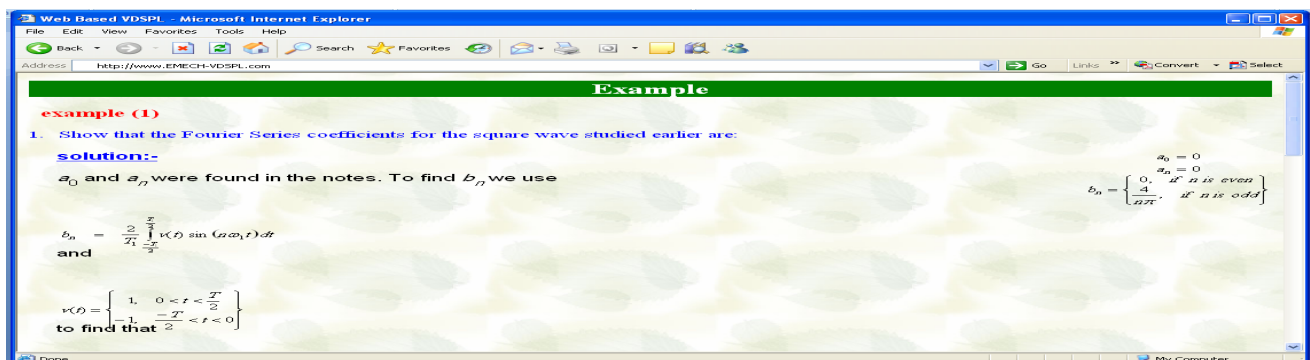


Fig.19 Web page of solved example used in experiment (3).

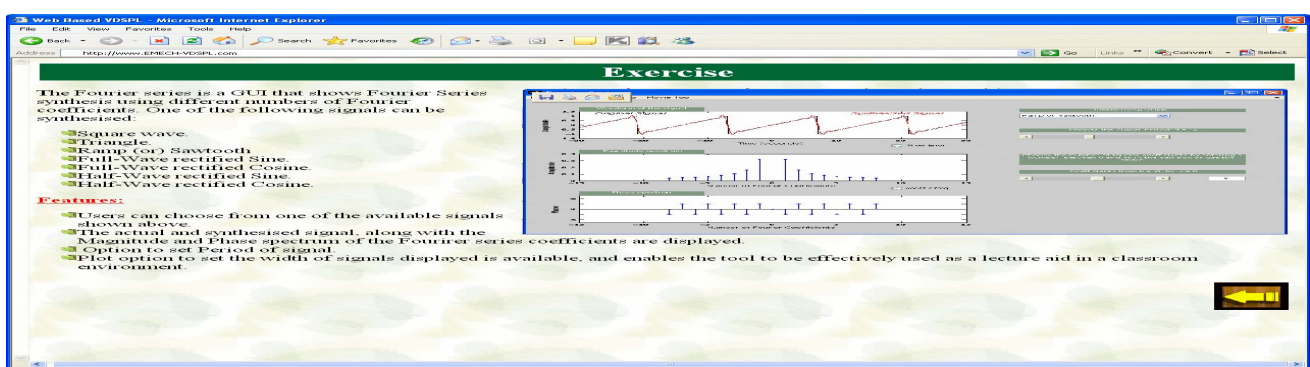


Fig.20 Web page of exercise for experiment (3)

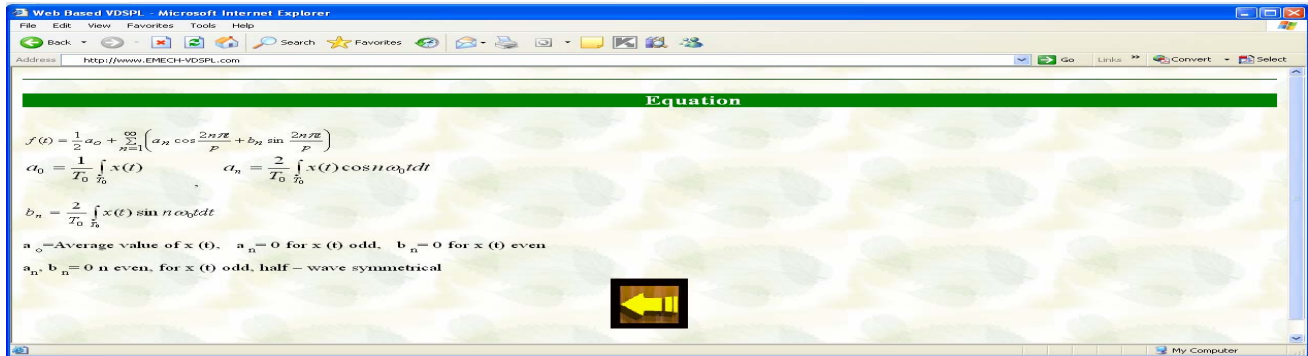


Fig.21 Web page of equations used in experiment (3)

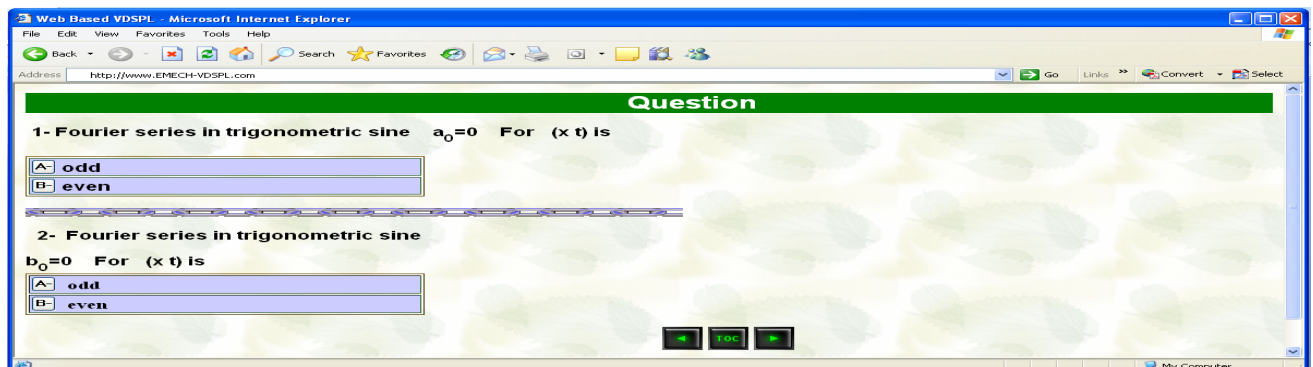


Fig.22 Web page of self test questions applied to experiment (3).

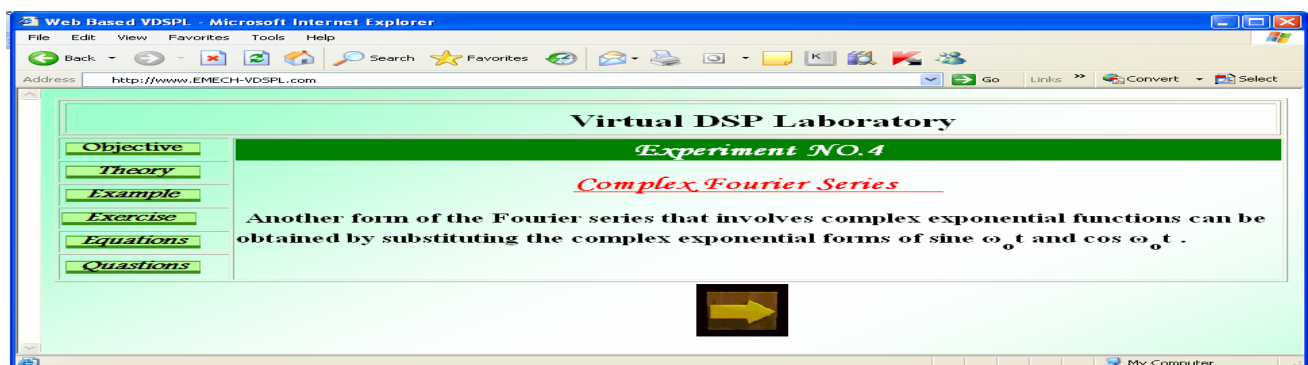


Fig.23. Web page of experiment (4).

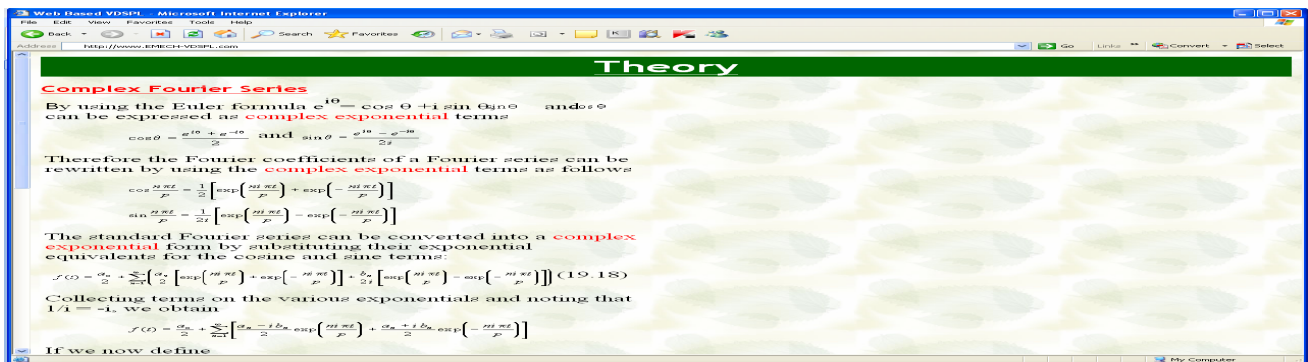


Fig.24 Web page of theory bases for experiment (4).

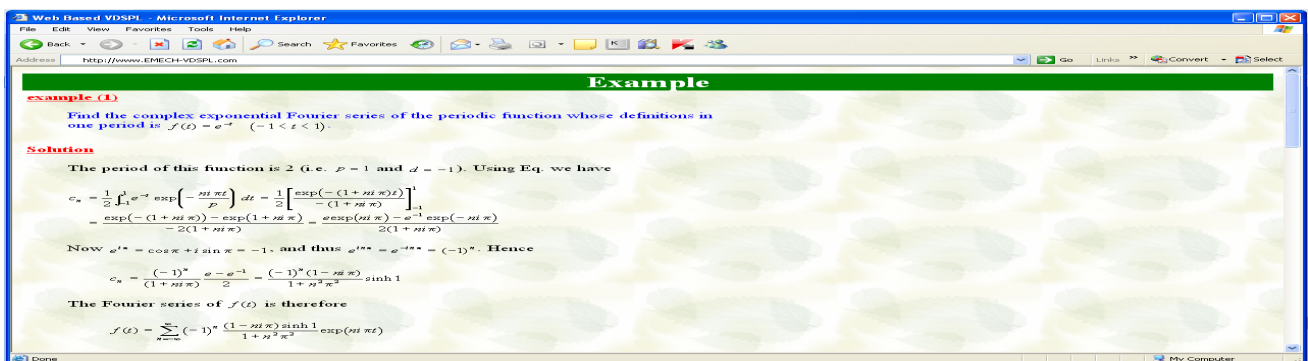


Fig.25 Web page of solved example used in experiment (4).

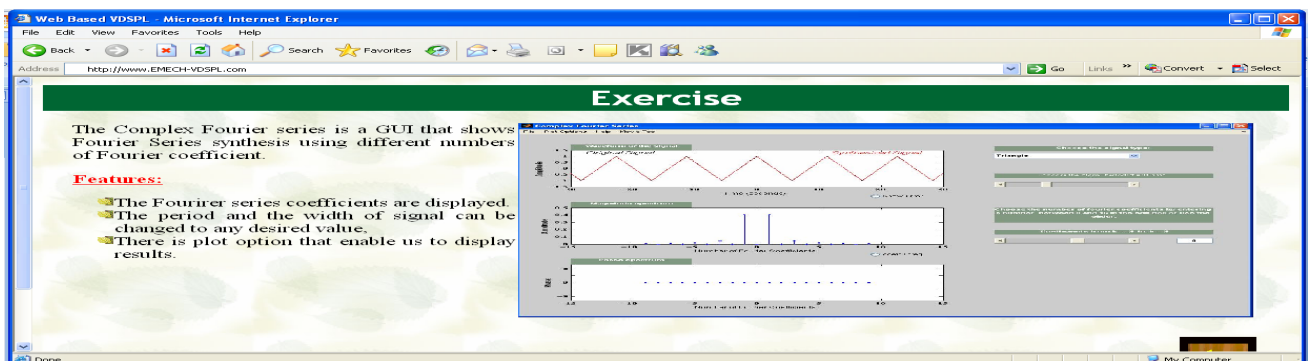


Fig.26 Web page of exercise for experiment (4).

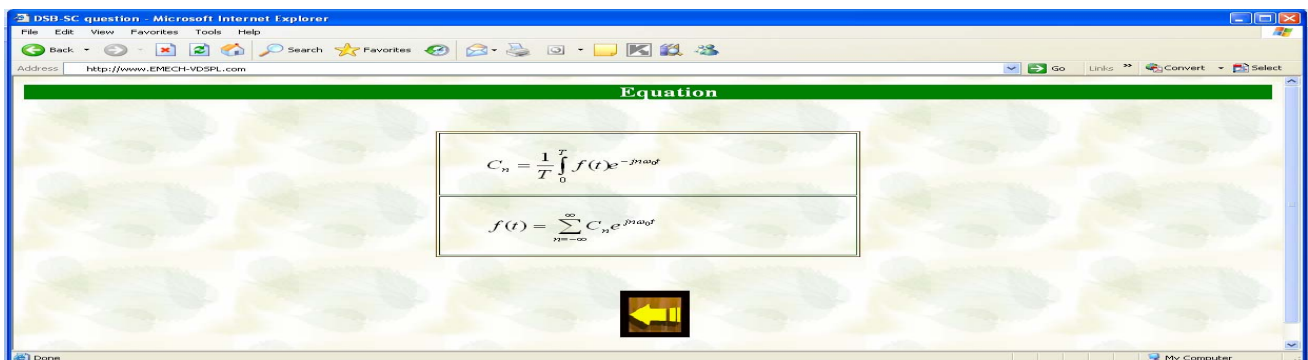


Fig.27 Web page of equations used in experiment (4).

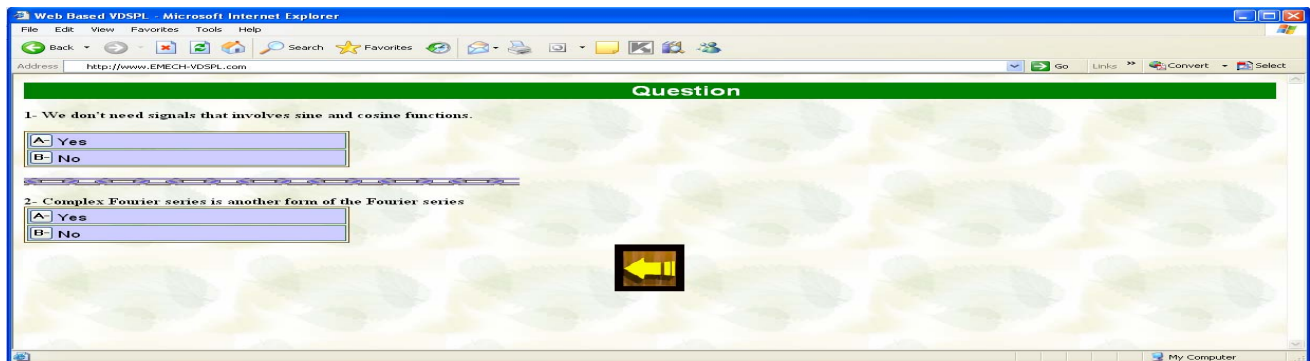


Fig.28 Web page of self test questions applied in experiment (4).

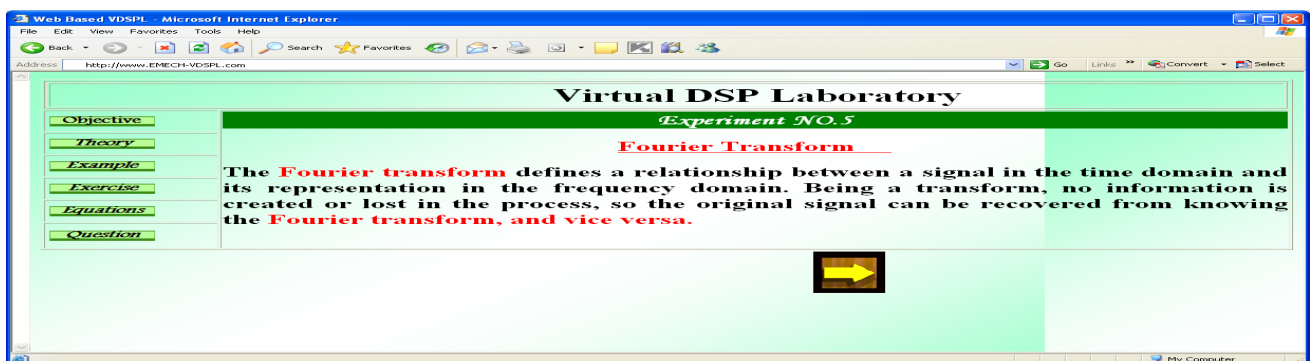


Fig.29 Web page of experiment (5).

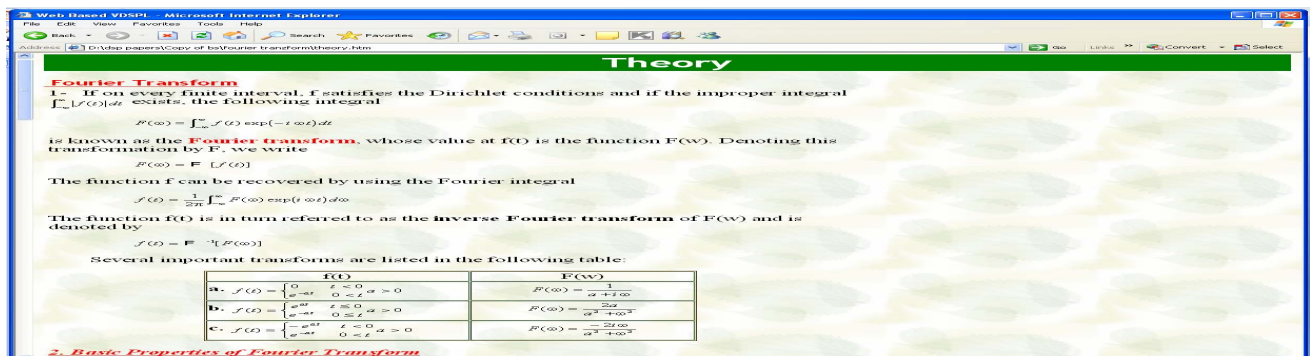


Fig.30 Web page of theory bases for experiment (5).

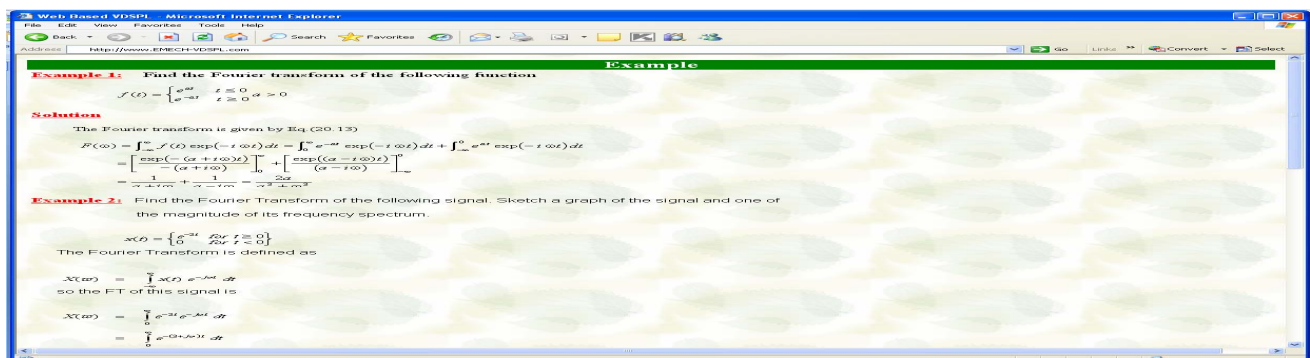


Fig.31 Web page of solved example used in experiment (5).

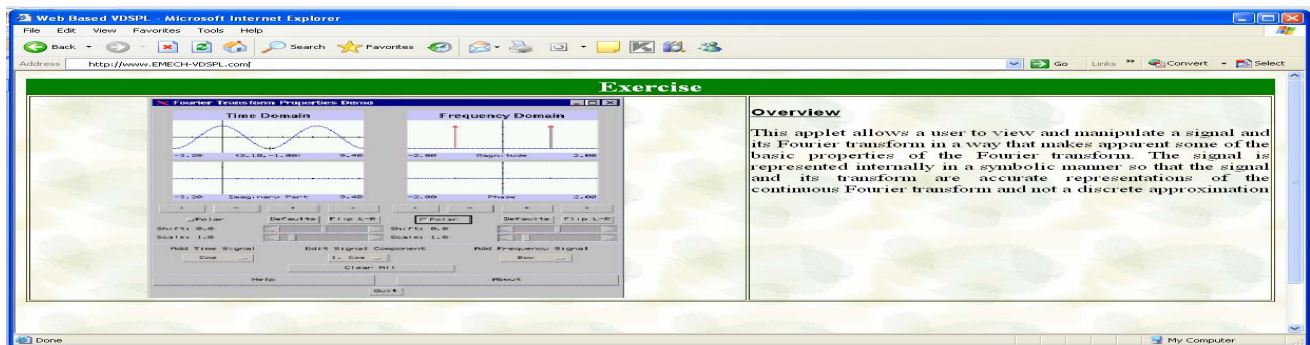


Fig.32. Web page of exercise for experiment (5).

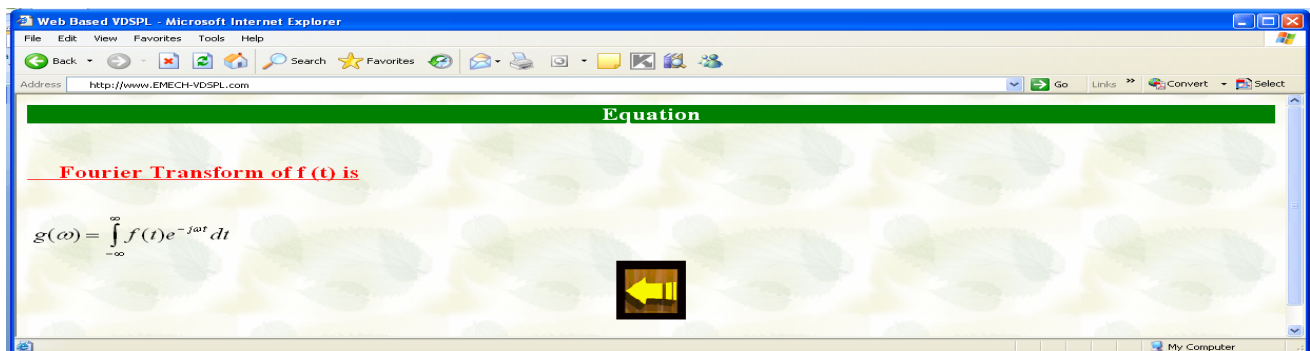


Fig.33 Web page of equations used in experiment (5).

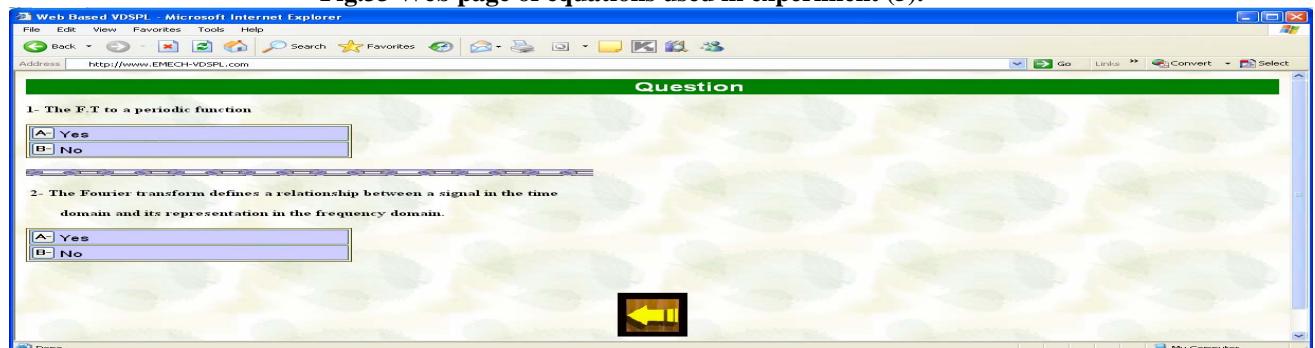


Fig.34 Web page of self test questions applied in experiment (5).

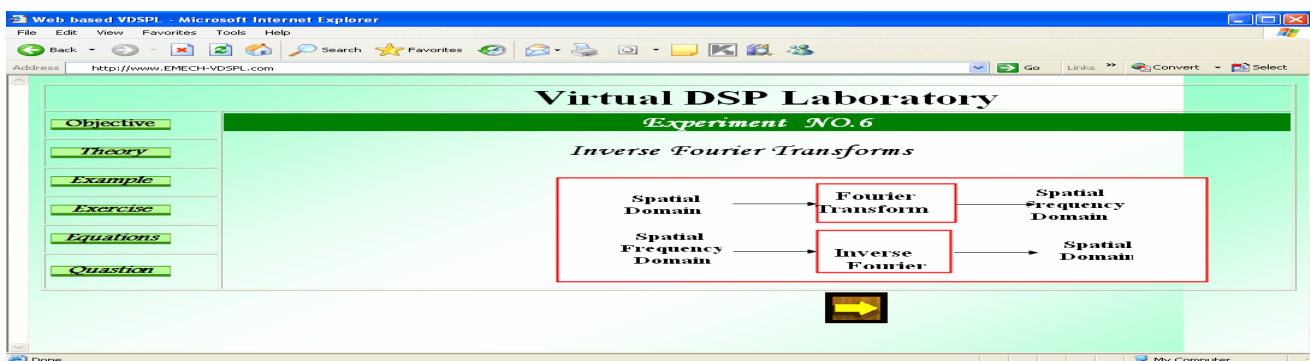


Fig.35 Web page of experiment (6).

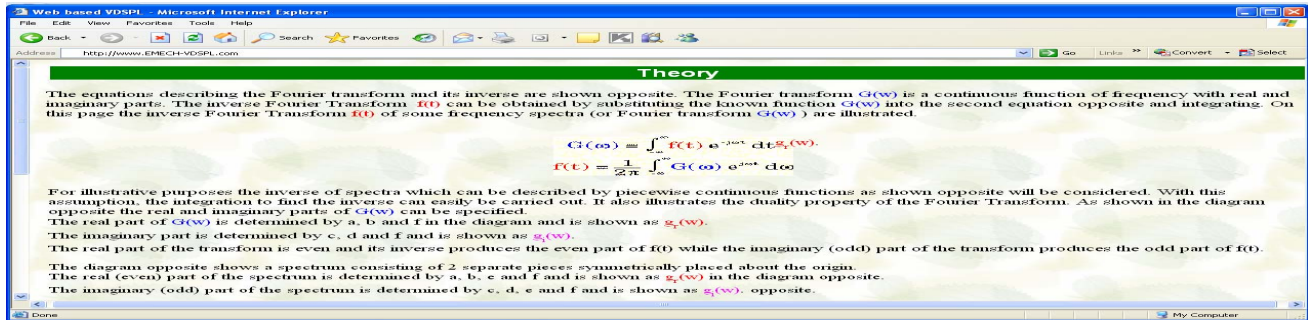


Fig.36 Web page of theory bases for experiment (6).

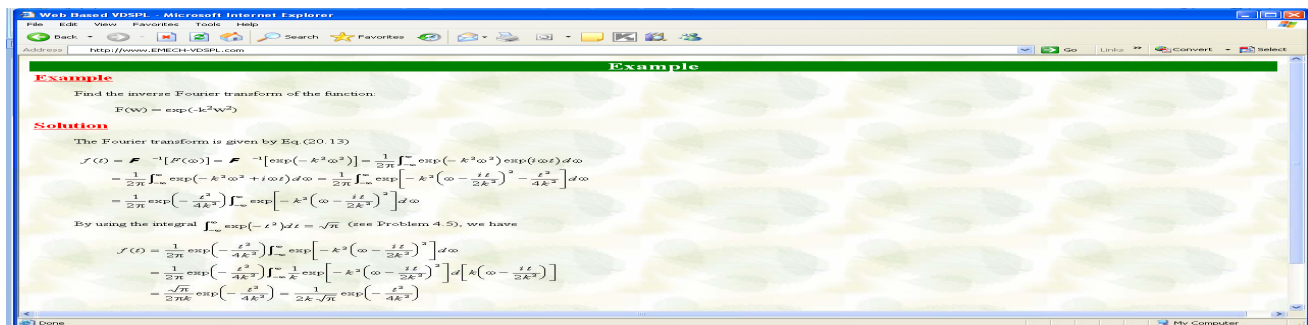


Fig.37 Web page of solved example used in experiment (6).

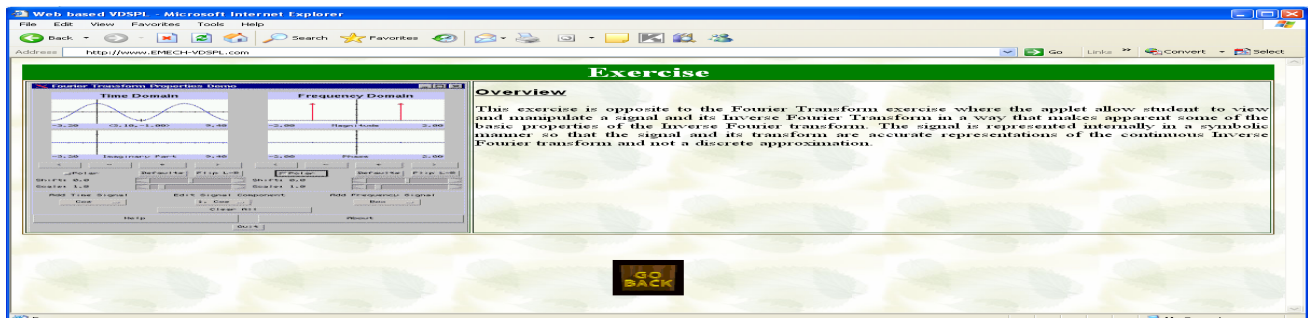


Fig.38 Web page of exercise for experiment (6).

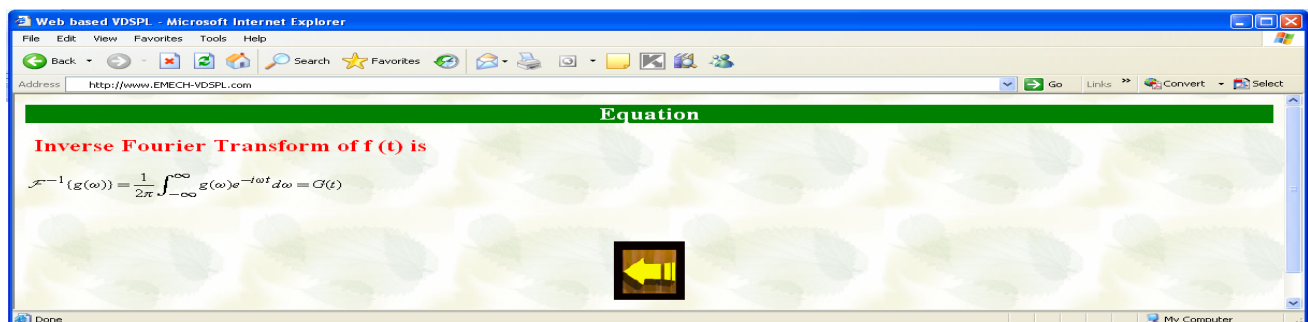


Fig.39 Web page of equations used in experiment (6).

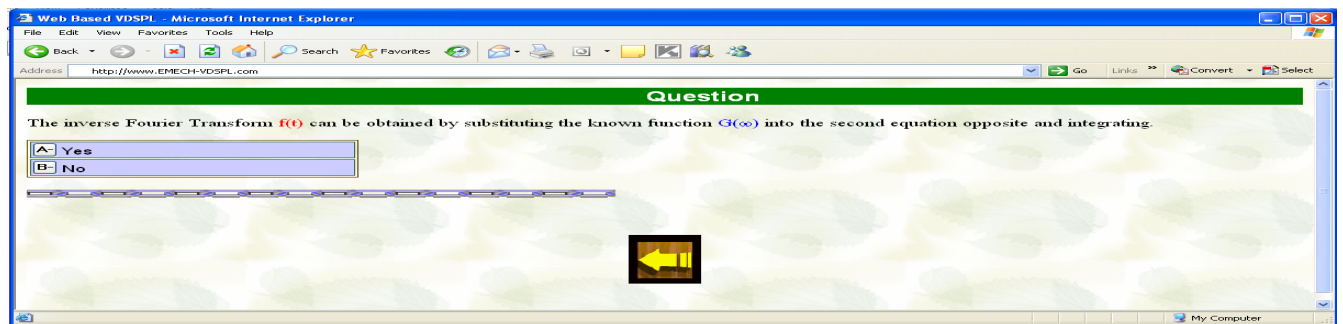


Fig.40 Web page of self test questions applied in experiment (6).

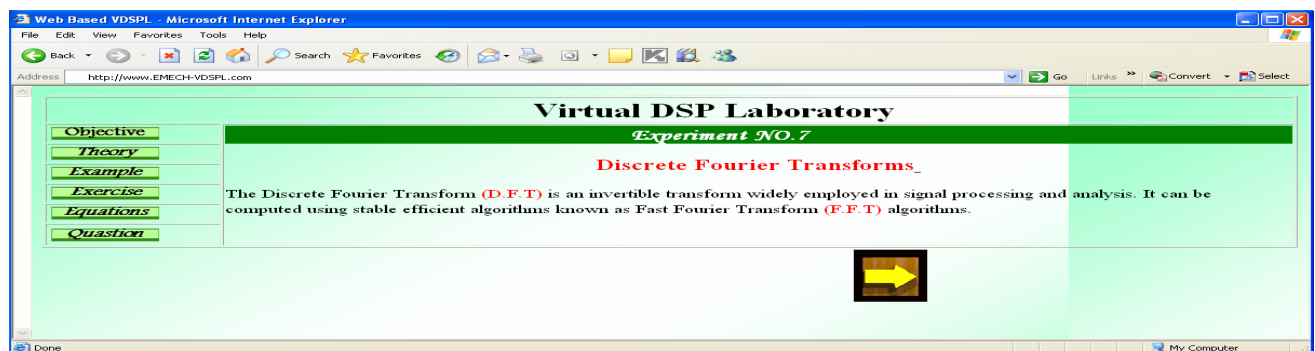


Fig.41 Web page of experiment (7).

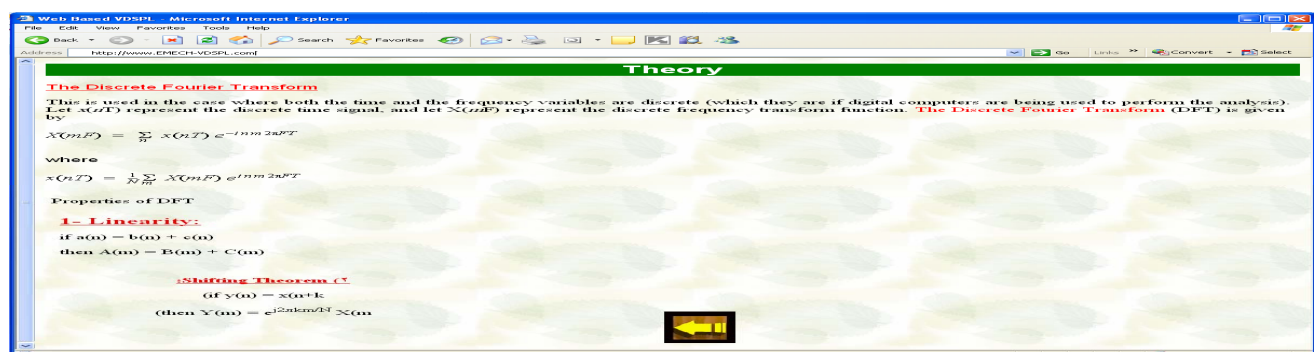


Fig.42 Web page of theory bases for experiment (7).

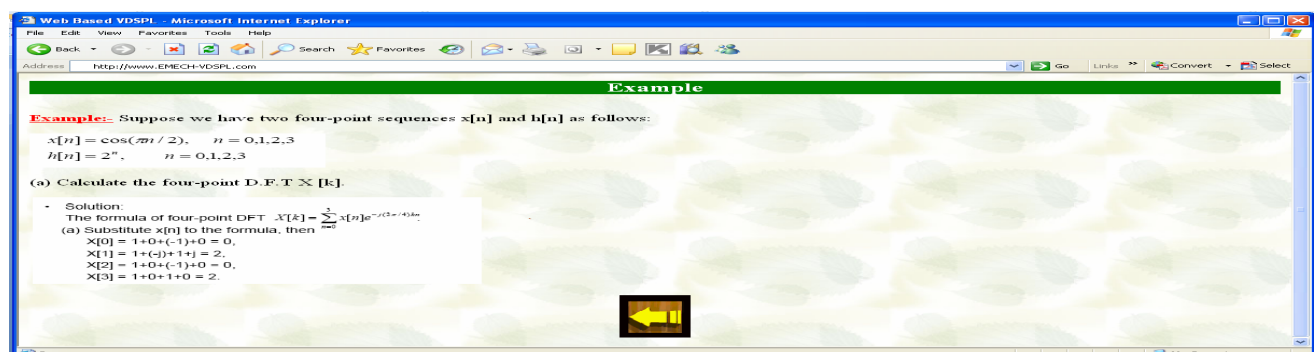


Fig.43 Web page of solved example used in experiment (7).

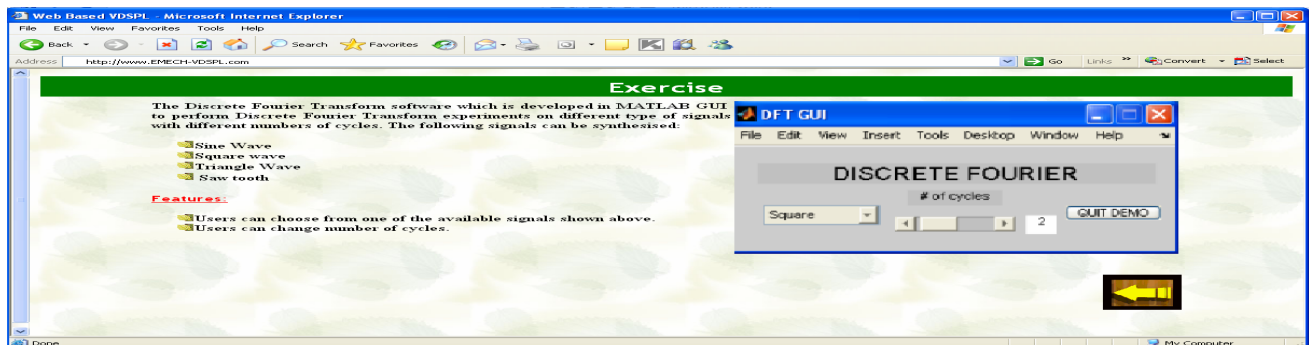


Fig.44 Web page of exercise for experiment (7).

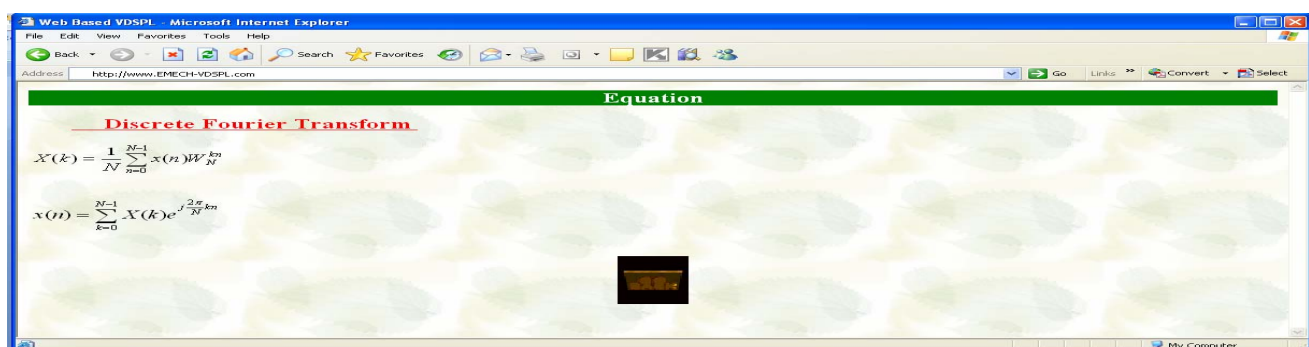


Fig.45 Web page of equations used in experiment (7).

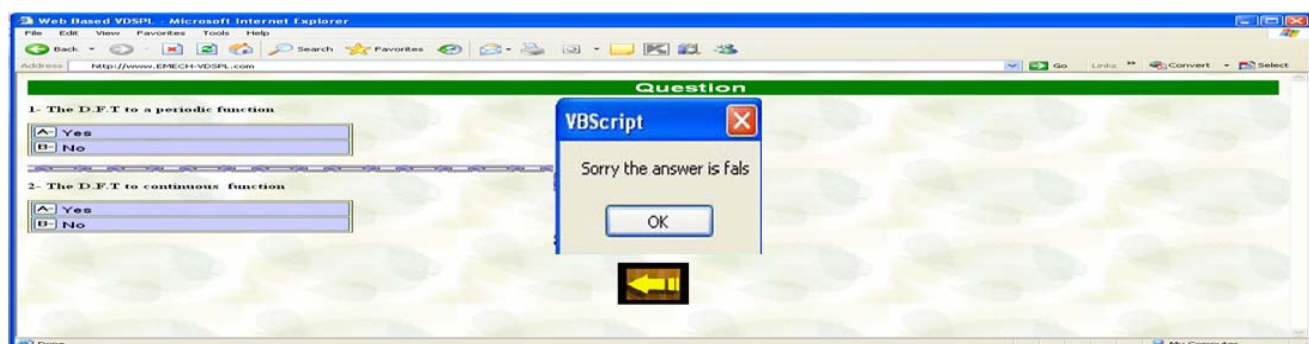


Fig.46 Web page of self test questions applied in experiment (7).

on the FFT button.



Fig.47 Web page of experiment (8).

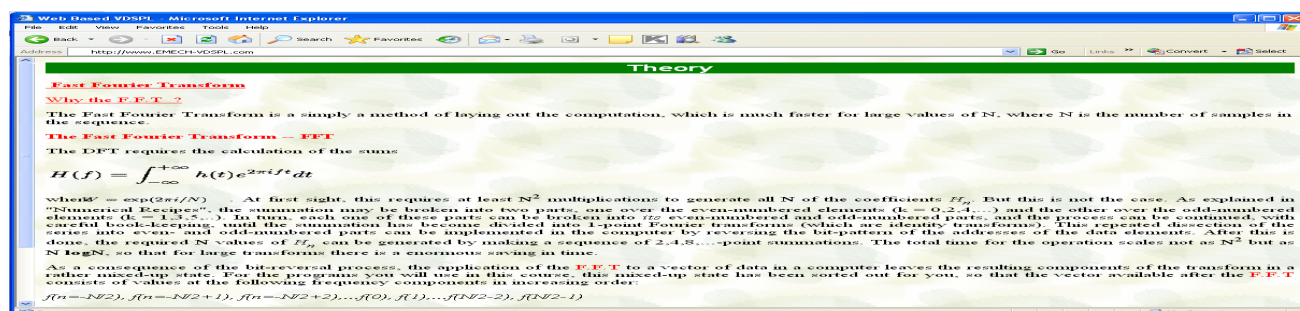


Fig.48 Web page of theory bases for experiment (8).

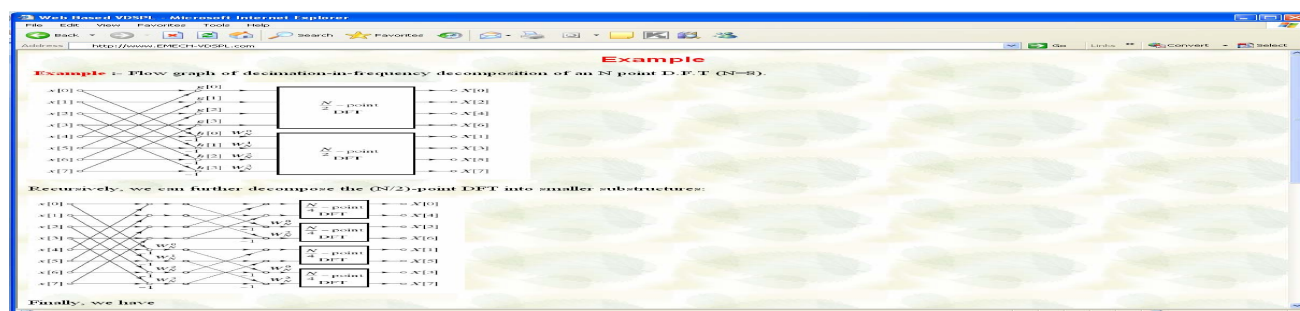


Fig.49 Web page of solved example used in experiment (8).



Fig.50 Web page of exercise for experiment (8).

Equation

$$X(k) = G(k) + W_N^k H(k)$$

Fig.51 Web page of equations used in experiment (8).

Question

1-

The F.F.T is a faster version of the Discrete Fourier Transform (DFT).

☐ A- Yes

☐ B- NO

Fig.52 Web page of self test questions applied in experiment (8).

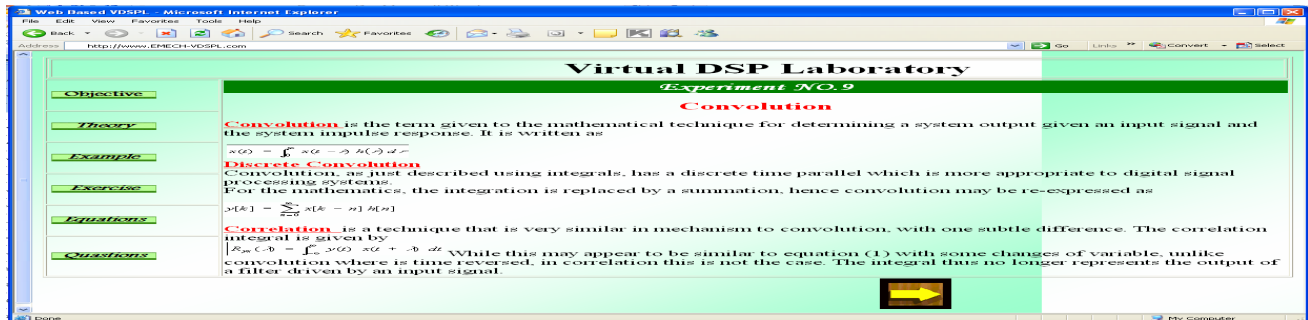


Fig.53 Web page of experiment (9).

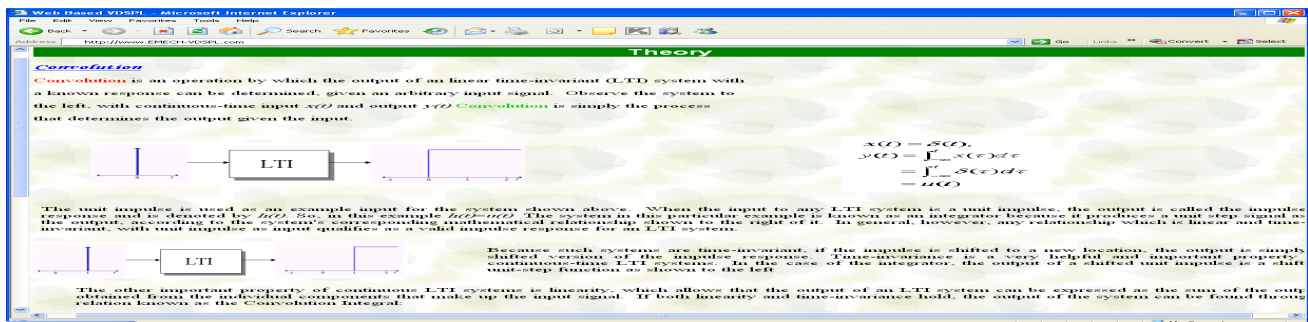


Fig.54 Web page of theory bases for experiment (9).

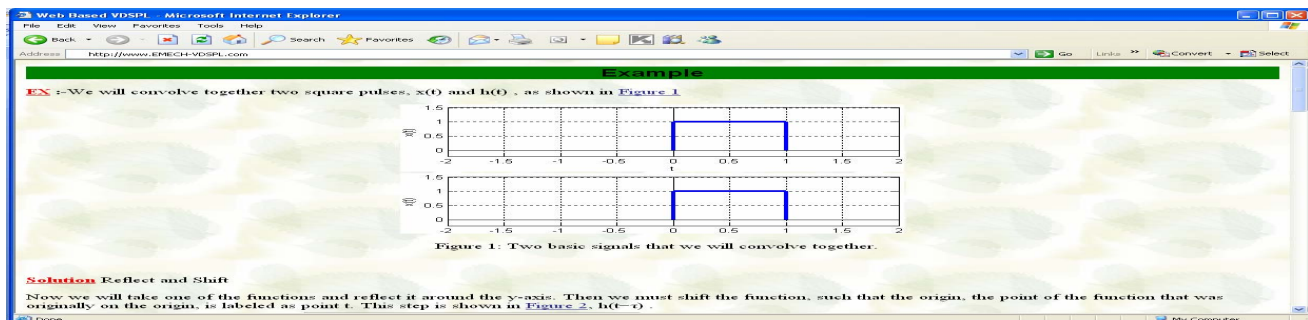


Fig.55 Web page of solved example used in experiment (9).

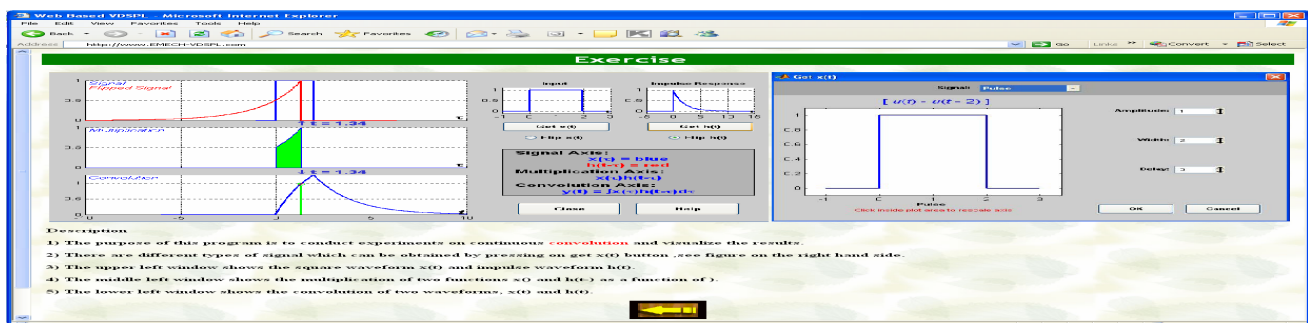


Fig.56 Web page of exercise for experiment (9).

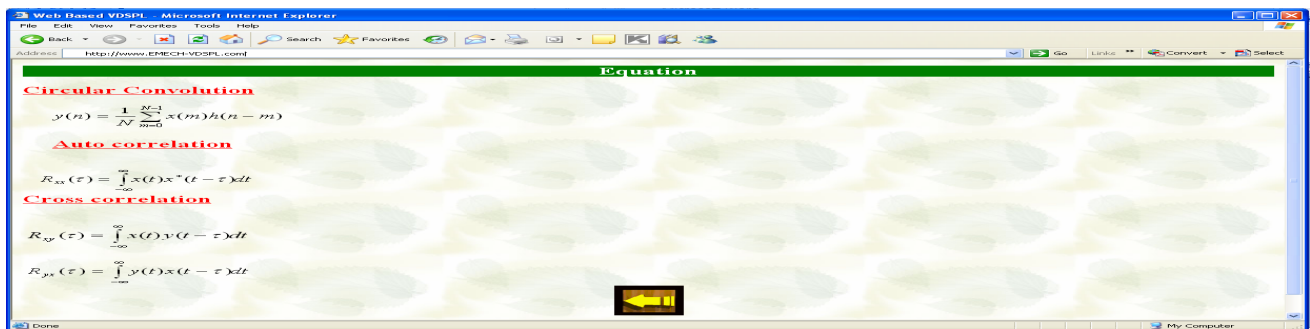


Fig.57 Web page of equations used in experiment (9).

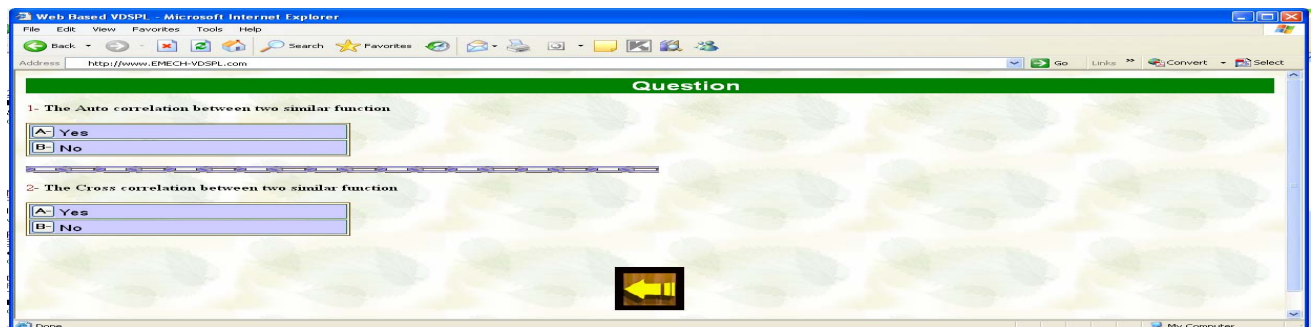


Fig.58 Web page of self test questions applied in experiment (9).

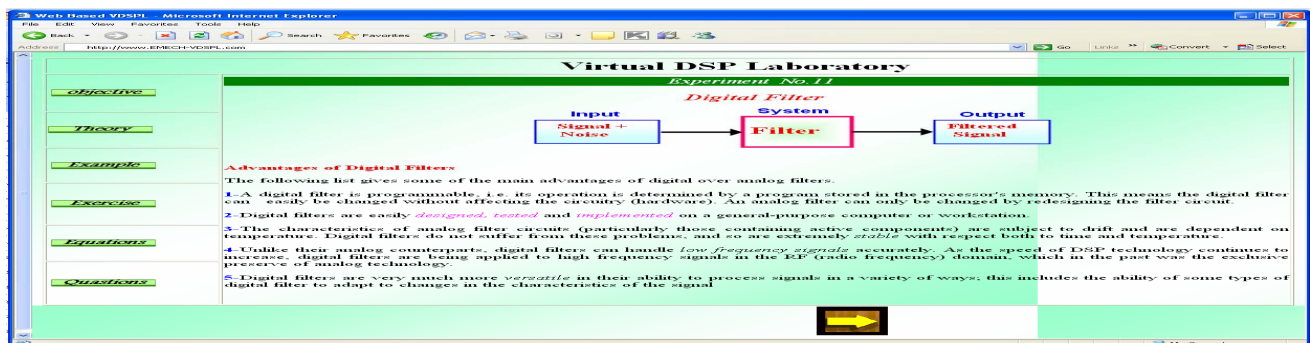


Fig.59 Web page of experiment (11).

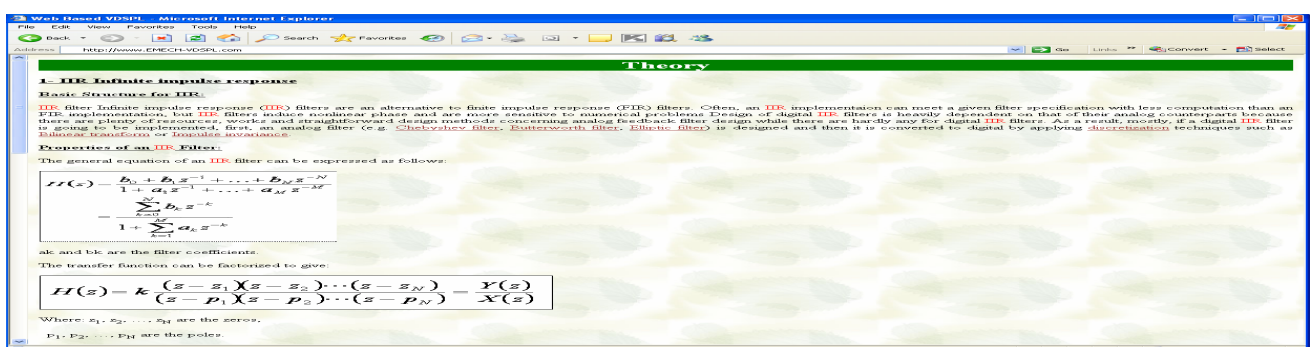


Fig60 Web page of theory bases for experiment (11).

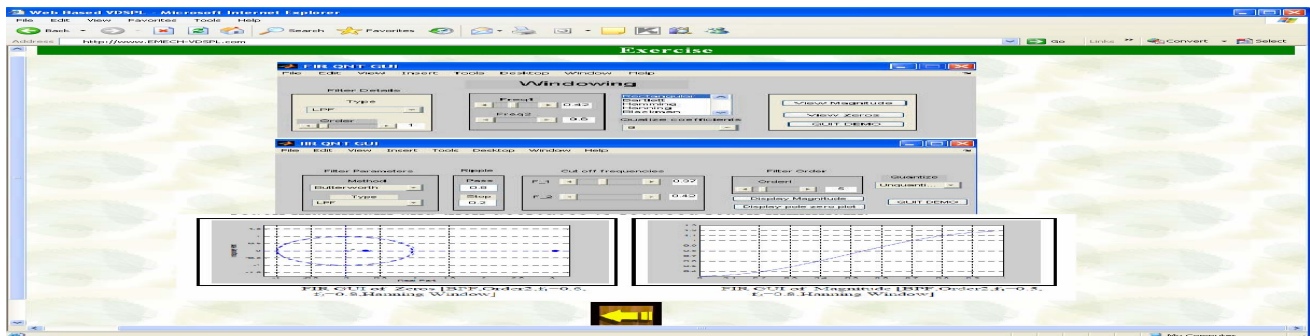


Fig.61 Web page of exercise for experiment (11).

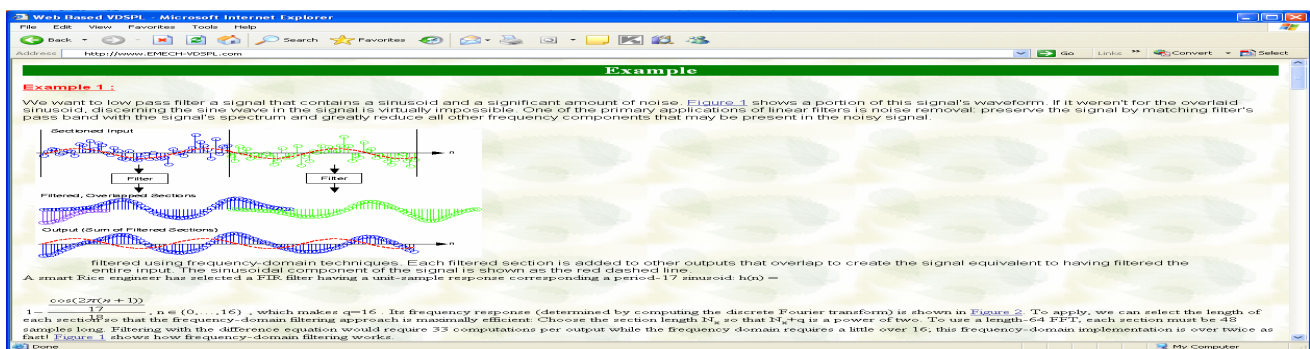


Fig.62 Web page of solved example used in experiment (11).

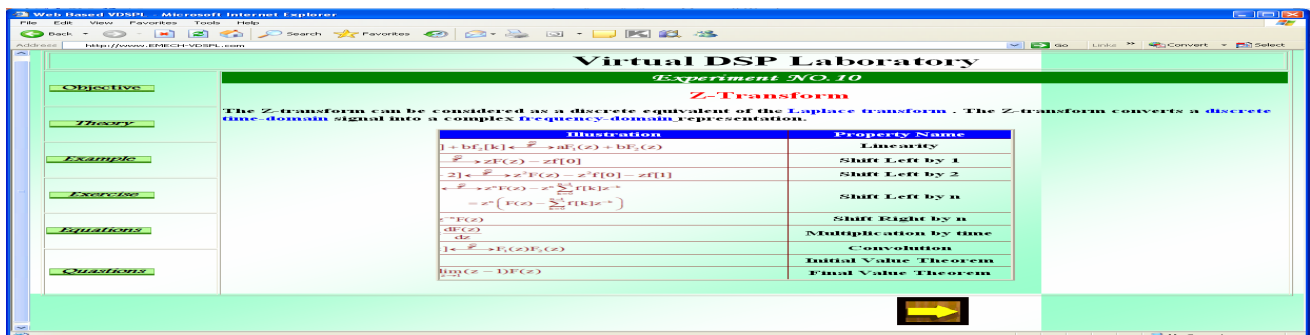


Fig.63 Web page of experiment (10).

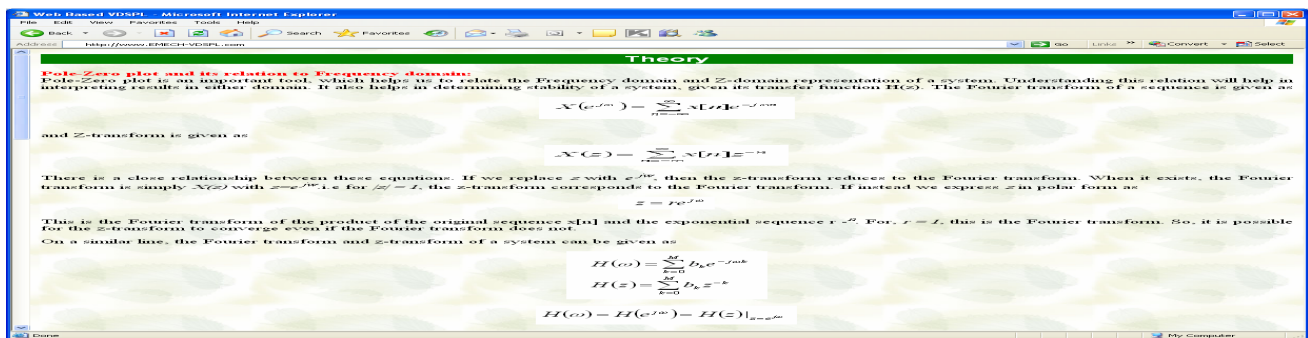


Fig.64 Web page of theory bases for experiment (10).

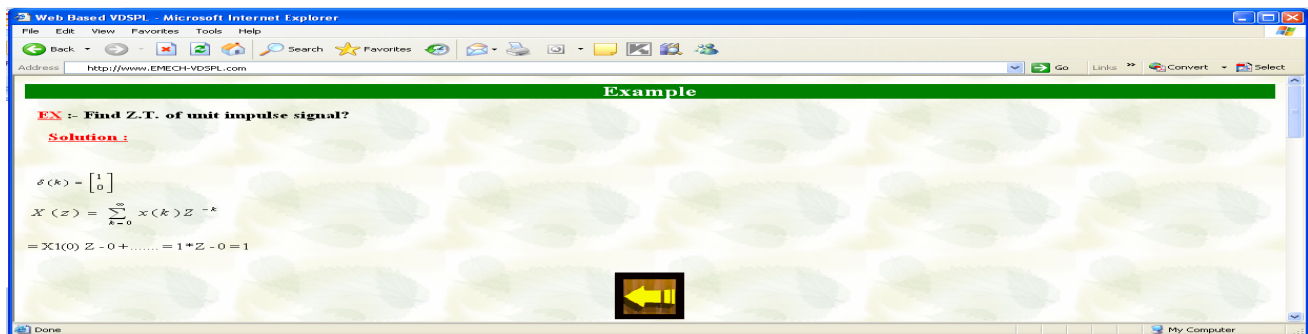


Fig.65 Web page of solved example used in experiment (10).

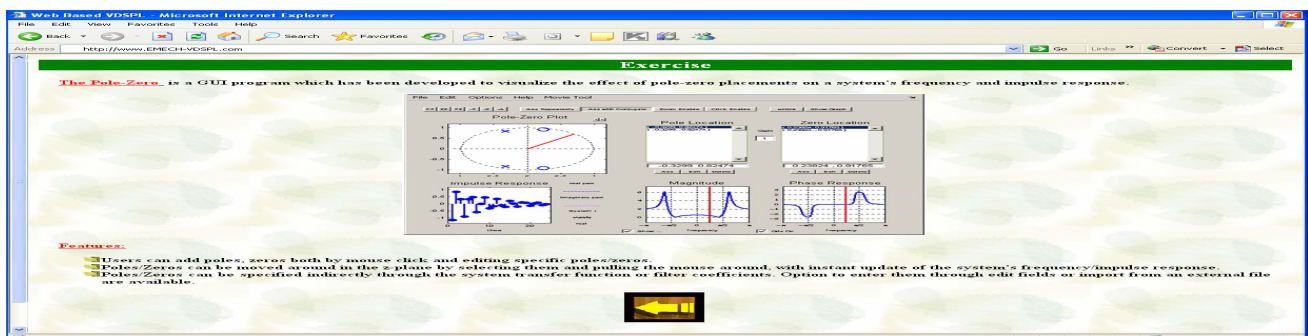


Fig.66 Web page of exercise for experiment (10).

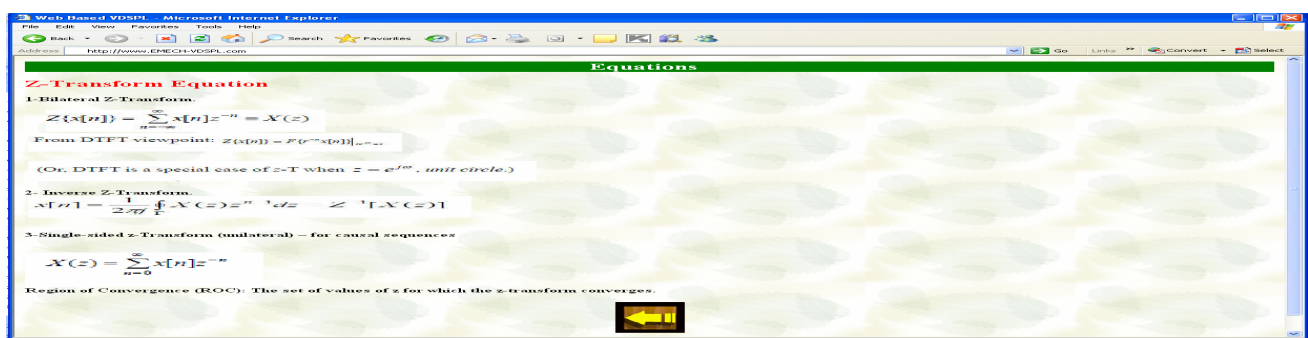


Fig.67 Web page of equations used in experiment (10).

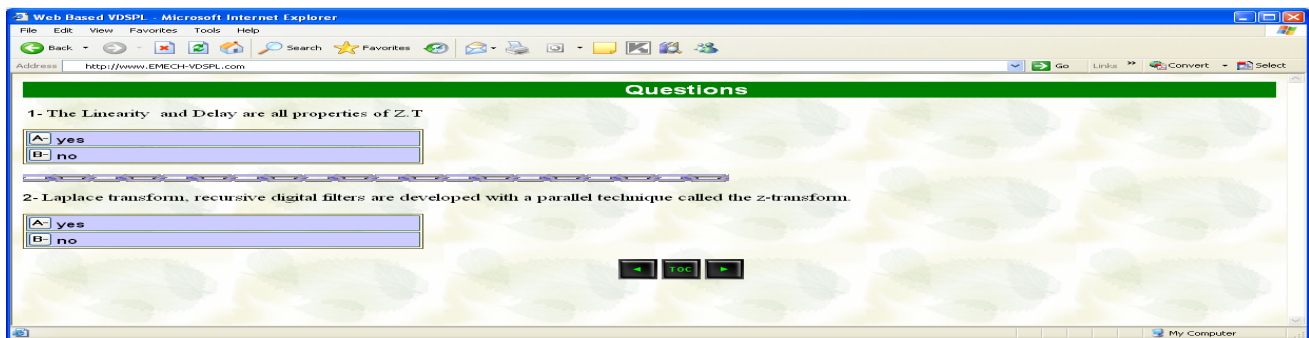


Fig.68 Web page of self test questions applied in experiment (10).

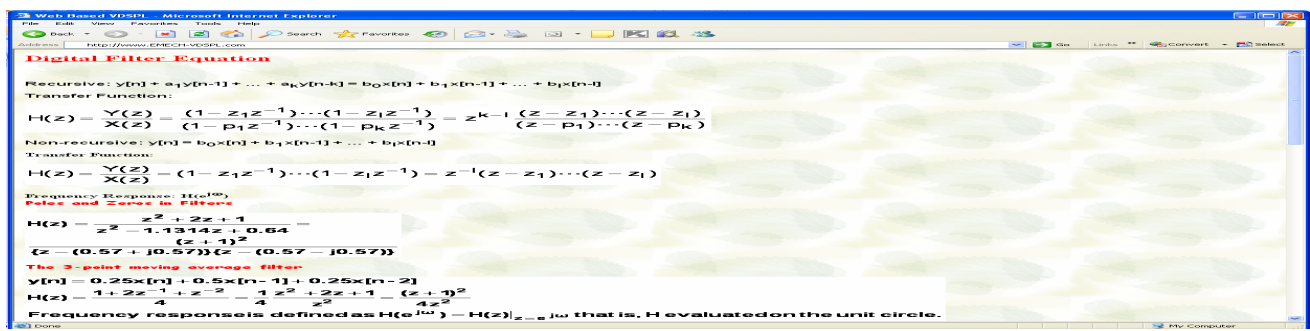


Fig.69 Web page of equations used in experiment (11).

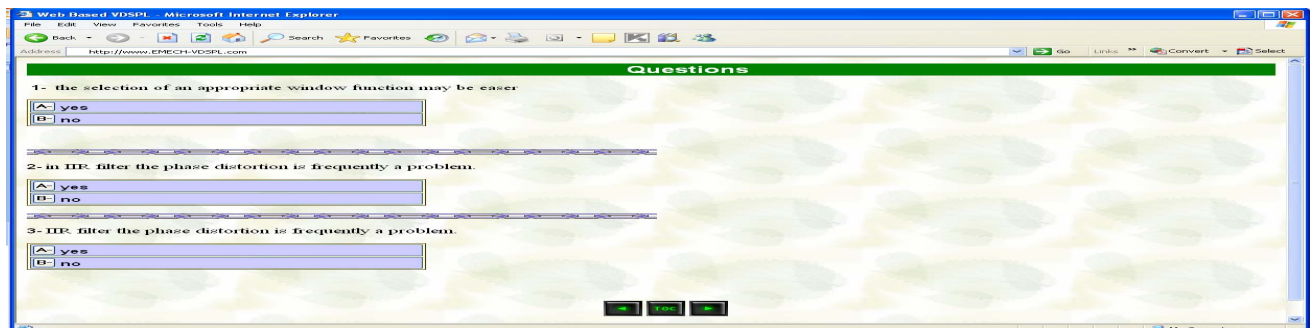


Fig.70 Web page of self test questions applied in experiment (11).

Table 1 Survey results

Survey Questions		Responses						
		1	2	3	4	5	Mean	Standard Deviations
Q1-	Was the virtual laboratory well organized?	0	0	0	2	13	4.86	2.22
Q2-	Were the learning outcomes clearly defined?	0	0	0	4	11	4.73	1.62
Q3-	Ran well on my computer?	0	0	0	1	14	4.93	2.99
Q4-	Loaded in a reasonable amount of time?	0	0	1	1	13	4.8	1.96
Q5-	Was virtual laboratory easy to navigate?	0	0	0	2	13	4.86	2.22

Q6-	There were enough figures and solved examples?	0	0	0	6	9	4.6	1.19
Q7-	Is the virtual laboratory material of high quality?	0	0	0	5	10	4.67	1.37
Q8-	There were enough exercises?	0	0	0	2	13	4.86	2.22
Q9-	Was virtual laboratory easy to understand?	0	0	0	4	11	4.73	1.62
Q10-	Would be helpful in preparing for the hands on laboratory?	0	0	0	7	8	4.53	1.33
Q11-	Have you learned with this virtual laboratory?	0	0	0	2	13	4.86	2.22
Q12-	Would you recommend this laboratory to other students?	0	0	0	5	10	4.67	1.37
Q13-	Overall, how would you rate this virtual laboratory?	0	0	0	1	14	4.93	2.99
Q14-	Should have more images/text demonstrations?	7	5	0	3	0	1.93	1.5
Q15-	Helped me to feel more confident about the procedures?	0	0	0	4	11	4.73	1.62



ESTIMATION OF RUNOFF FOR GOIZHA-DABASHAN WATERSHED WITH AID OF REMOTE SENSING TECHNIQUES

Ahmed A.M. Ali*
Hayder A. Al-Thamiry**
Saddam Qahtan Alazawi

*Professor in Water Resources Engineering Department/Baghdad University.

**Assistant Professor in Water Resources Engineering Department/Baghdad University

ABSTRACT.

Estimation of runoff volume and peak runoff is necessary for designing and operating the dams. One of the accepted models for estimating the runoff is HEC-1 model. Two methods were used in this study to estimate the runoff in Goizha-Dabashan watershed, 2.02 km², Rational method and Soil Conservation Service curve number method (SCS-CN). Satellite image from Landsat-7 (ETM+) was used to develop land use and soil type maps. Watershed was delineated from DEM (<http://www.emrl.byu.edu/gsdu>) with resolution 10 m with aid of WMS 7.1 software. Runoff coefficient was calculated by inverse the Rational equation. Manual calibration was performed until the Nash-Sutcliffe coefficient gives the best results. Results showed that the runoff coefficient is 0.05 and the curve number value for conditions II and III are 75 and 80.5 respectively after calibration. Also, curve number method is better than Rational method for estimating the peak runoff discharge.

الخلاصة.

تقدير حجم السيلح السطحي وذروته ضروري لتصميم وتشغيل السدود. احد اهم النماذج المقبولة لتقدير السيلح السطحي هو نموذج (HEC-1). في هذه الدراسة استخدمت طريقتان لتقدير السيلح السطحي في حوض كويظة-دباشان، 2,02 كم²، وهما طريقة (Rational) وطريقة (SCS-CN). تم استخدام صورة القمر الصناعي (Landsat-7 ETM+) لانشاء خرائط استخدام الارض و نوع التربة. تم تحديد حوض النهر بواسطة نموذج الارتفاعات الرقمي (DEM) (<http://www.emrl.byu.edu/gsdu>) وبدقة 10 م وبمساعدة برنامج (WMS 7.1). عامل السيلح السطحي تم حسابه بعكس معادلة (Rational). وتم استخدام معايرة يدوية للمعادلات بواسطة معادلة (Nash-Sutcliffe) للحصول على افضل النتائج. نتائج هذه الدراسة اوضحت ان مقدار السيلح السطحي لهذا الحوض هو 0,05 و مقدار رقم المنحني (CN) للحالة الثانية والثالثة هو 75 و 80,5 على التوالي. وكذلك، تبين ان طريقة رقم المنحني (CN) هي افضل من طريقة (Rational) في تقدير ذروة السيلح السطحي.

INTRODUCTION.

The Estimation of runoff from rainfall is critical for water resource management and hydraulic design. In the recent years, the use of remote sensing and Geographic Information System (GIS) technologies in runoff estimation from watersheds has gained increasing attention, because of a good runoff model has to include spatially variable geomorphologic parameters such as rainfall, soil characteristics, and land use change.

In hydrologic analysis and design, it is often necessary to develop relations between precipitation and runoff, possibly using some of the factors affecting runoff as parameters. The relations between precipitation and runoff differ with the type of precipitation, the considering of the volume or peak or runoff, or the time distribution of runoff (*Chow, 1964*). Hydrologic systems are generally analyzed by using mathematical models. These models may be empirical or statistical, or founded by known physical laws. In this study, SCS curve number model and Rational method were used to estimation the runoff in Goizha-Dabashan watershed.

The purpose of this research is to demonstrate and evaluate the use of satellite imagery for obtaining the watershed and soil parameters, and to comparison these parameters with the measured values. Also, comparison the calculated runoff from SCS curve number with post results calculated by Deterministic optimization model and Artificial NEURAL Network model, and estimated the runoff coefficient value for Goizha-Dabashan watershed.

PREVIOUS STUDIES.

Barzinji, 2003 studied the hydrology, climate, and watershed management for 11 watersheds in Al-Sulymaniah region, namely; Zalim, Chaqan, Chaq-Chaq, Dewana, Basara, Goizha-Dabashan, Smaquli, Halsho, Tanjaro, Shiranish, and Mawakan. He was focused in his study on Goizha-Dabashan watershed. He described it soils by excavated 16 ponds, and he measured the infiltration rate in 15 ponds. Also, he was constructed a gaging station in it to measure the runoff.

Barzinji, 2007 developed a mathematical model (Deterministic Optimization model) to calculate the runoff during 2002 and 2006 for Goizha-Dabashan watershed. His model is based on water balance principles in which, the main input are precipitation, evaporation, base flow, and other requirement to run the optimization program. He was showed a good relation between calculated and observed runoff (correlation factor= 0.91).

Al-Hamawandi, 2009 studied the rainfall-runoff relationship by using Artificial Neural Network, ANN. He built different ANN watershed models (simple and complex) and tried using Walnut Gulch watershed. The instantaneous ANN model was applied also for Goizha-Dabashan. The results indicate the capability of the model to simulate the runoff-rainfall relationship with correlation coefficient 0.95.

3. GOIZHA-DABASHAN WATERSHED.



Goizha-Dabashan watershed located in the north east of Iraq, in the north of Al-Sulymaniah city between 45°27'00" - 45°28'30" E (Longitude) and 35°35'00" - 35°36'00" N (Latitude) as shown in **Fig 1**. The watershed area is about (2.02km²); and its perimeter is 8.436 km. It was selected due to availability of its data such as; rainfall and runoff storms (10 storms), soil properties data, land use data, location of soil samples, location of infiltrometers, and other data.

THEORITICAL BACKGROUND.

SCS curve number model.

The curve number, CN, method for estimating direct runoff response from rainstorms was developed to fill a technological niche in the 1950. Its popularity is rooted in its convenience, its simplicity, its authoritative origins, and its responsiveness to four readily grasped catchment properties: soil type, land use, treatment, surface condition, and antecedent condition (*Ponce and Hawkins, 1996*). Watersheds have a certain group of soil and fair pasture cover can be classified by various curve numbers. These curves are the relationship obtained between rainfall and runoff, as follows:

$$F/S = Q/P \quad \dots\dots\dots (1)$$

Where $F = P - Q$: is actual retention.

S: is potential retention.

Q: is actual runoff, and

P: is potential runoff that is total rainfall.

The initial abstraction, I_a , is all losses before runoff begins. It included water retention in surface depression and intercepted by vegetation, infiltration,

and evaporation. I_a was approximated by the following equation:

$$I_a = 0.2 S \quad \dots\dots\dots (2)$$

By subtracted I_a from rainfall P in equating (1) and solving for Q, yields:

$$Q = \frac{P - 0.2S}{P + 0.8S} \quad \dots\dots\dots (3)$$

Curve number value range from 0 to 100 and determined from the SCS tables, according to land-cover, hydrologic soil group, treatment, and antecedent moisture condition (AMC). Hydrologic soil group is expressed as four groups (A, B, C, and D) according to the soil's minimum infiltration rate (*ASCE, 1996*). AMC is expressed as three levels, according to rainfall limits for dormant and growing seasons (*Viessman and Lewis, 2003*). For application the curve number model, the watershed is divided to some areas principally by land-cover based area-weighting of curve numbers.

Rational Method.

The rational method dates from the 1850 in Ireland and called the Lloyd-Davies method in Great Britain. It represents the relation between rainfall and peak runoff. This formula is called rational because the units of the quantities involving are numerical consistent approximately (*Suresh, 2005*). The Rational formula is:

$$Q_p = 0.277 C I A \quad \dots\dots\dots (4)$$

Where Q_p : is the peak flow in m³/s.

C: is the runoff coefficient varies from 0 to 1.

I: is the rainfall intensity in mm/hr.

A: is the watershed area in km².

Estimates of the runoff coefficient are based on very limited data, but several studies have shown that it depends on the infiltration rate, surface cover, channel and surface storage and intensity of rainfall (*Schwab, et al, 1966*). The coefficient of runoff varies for different storms on the same catchment, and thus, using an average value C , only a crude estimate of Q_p is obtained, that may have wide margins of error (*Shaw, 1983*).

WMS 7.1 Software.

Watershed Modeling System, WMS, is a comprehensive environment for hydrologic analysis. It was developed by the Environmental Modeling Research Laboratory of Brigham Young University in cooperation with the U.S. Army Corps of Engineers Waterways Experiment Station. The current version, 7.1, is built at March 10 2005. The distinguishing difference between WMS and other applications designed for setting up hydrologic models like HEC-1 and TR-20 is its unique ability to take advantage of digital terrain data for hydrologic model development. WMS uses three primary data sources for model development: Geographic Information Systems (GIS) Vector Data, Digital Elevation Models (DEM), and Triangulated Irregular Networks (TIN).

HEC-1 Model.

The HEC-1, Flood Hydrograph Package, computer program was designed to simulate the surface runoff response of a watershed to precipitation by representing the basin as an interconnected system of hydrologic and hydraulic components. Each component models an aspect of

the precipitation-runoff process within a portion of the basin, commonly referred to as a subbasin.

The model components function based on simple mathematical relationships which are intended to represent individual meteorologic, hydrologic and hydraulic processes that comprise the precipitation-runoff process. These processes are separated into precipitation, interception and infiltration, transformation of precipitation excess to subbasin outflow, addition of base flow and flood hydrograph routing.

WATERSHED DELINEATING.

WMS software provides a powerful tool to delineate the boundary of any watershed. DEM file represents the base layer to delineate the watershed. It was obtained from website (<http://www.emrl.byu.edu/gsdu>) with resolution (10m) and treated with aid of Global Mapper 8 program. The first step to delineate the Goizha-Dabashan watershed is pinpointing the location of the outlet, thus; the Global Position System tool, GPS, was used to obtain the coordinates of the watershed outlet and its boundary. After that, the direction of water entering through the watershed was determined. This step was accomplished by creating a flow direction file, with aid of WMS Software. This software examines each cell in the DEM file and determines the direction of flow for that particular cell based on the elevations of the eight neighboring cells. The watershed was delineated by assigning the outlet cell in the stream flow file. The WMS Software examines the flow direction file to determine which cells will eventually flow through the outlet cell, as shown in **fig. 2**.



The watershed characteristics such as basin area, basin perimeter, basin slope, max flow distance, basin shape factor, elongation ratio, and etc. were calculated from the DEM file and with aid of WMS Software after delineating the watershed boundary. However, the time of concentration was computed by using Kirpich equation and as follows:

$$T_c = 0.02 L^{0.77} Y^{-0.385} \dots\dots\dots (5)$$

Where T_c : is the time of concentration in min.

L : is the maximum length of flow in m, and

Y : is the watershed gradient in meter per meters, or the difference in elevation between the outlet and the most remote point divided by the length, L .

REMOTE SENSING WORKS.

Generally, the remote sensing works can be summarized as follows:

- Selecting the satellite image.
- Layer stack.
- Image subset.
- Image classifying.

The satellite image for Al-Sulymaniah city was obtained from sensors Landsat-7 Enhanced Thematic Mapper Plus (ETM+). It contained nine bands with resolution equal to 14.25m. Layer stack is combining the bands together of an image to obtain a combination image and to facilitate the analyzing it. The satellite image for al-Sulymaniah city was very large and includes area outside the Goizha-Dabashan watershed. Therefore, the subset operation was used to reduce the image size file.

The process of categorizing pixels into broader groups is known as Image classification. The

advantage of classification is to allow cost-effective mapping of the spatial distribution of similar objects (i.e. tree types in forest scenes); a subsequent statistical analysis can then follow (Walsh, 2003).

IMPLEMENTATION OF SCS MODEL PARAMETERS.

SCS Curve number model depends only on one parameter, because the other parameters, initial abstraction and potential maximum retention, are related directly with the curve number. To determine the curve number values, information about the soil types, land use, land treatment, and hydrologic condition must be known. Soil types were determined according to its basic infiltration rates which result from the infiltrometers. Musgrave (1955) was given the following values of basic infiltration in cm per hour for the four hydrologic soil groups: A, more than 0.76; B, 0.38 to 0.76; C, 0.13 to 0.38; D, 0.13 or less. Land use description, treatment, and the hydrologic condition were taken from Barzinji study in 2003. The study area was divided to 15 regions utilizing remote sensing results. Each region has individual curve number value, the composite curve number was calculating as:

$$CN_c = \sum CN_j A_j' \dots\dots\dots (6)$$

Where CN_c : is the composite curve number.

CN_j : is the curve number value for region j , and

A_j' : is the weighted area for the same region.

COMPUTATION OF RUNOFF.

Rainfall distribution is representing the first step for HEC-1 model to identifying the rainfall as hyetograph. Rainfall distribution was constructed for

each rainfall storm by plotting accumulative rainfall depth against time and dividing it by the total depth. Land surface interception, depression storage and infiltration are referred to in the HEC-1 model as precipitation losses. The precipitation loss calculation can be used with either the unit hydrograph method or kinematic wave method. In this study, the unit hydrograph method was used. The average precipitation loss was determined for each time interval and subtracted from the rainfall hyetograph as. The resulting precipitation excess was used to compute an outflow hydrograph for the watershed. The required parameters for SCS curve number methods in HEC-1 mode are:

- I_a : Initial rainfall abstraction. If value is 0, then it will be computed as $5080/CN - 50.8$.
- CN: SCS curve number value for overall watershed (composite value).
- RTIMP - Percentage of drainage basin that is impervious. In the study area, there is no impervious area.

The volume of runoff which calculated in the previous step was transformed to hydrograph by using the unit hydrograph method. SCS dimensionless unit hydrograph method was used in this study. HEC-1 model automatically sets the duration of unit excess equal to the computation interval selected for watershed simulation. Input data for the SCS dimensionless unit hydrograph method in HEC-1 Model consists of a single parameter, T_{PEAK} , which is equal to the lag between the beginning of runoff and the peak of the unit hydrograph. Peak flow is computed as:

$$Q_P = 2.08 \times A / T_{PEAK} \dots\dots\dots (7)$$

Where, T_{PEAK} is the time to peak of unit hydrograph in hours, Q_P is the peak flow of unit hydrograph in $m^3/s/cm$, and A is the watershed area in km^2 .

ESTIMATION OF RUNOFF COEFFICIENT.

The default procedure for calculating the runoff coefficient cannot be used, because there are only 10 storms, and its return period is unknown and cannot be calculated. Therefore, the runoff coefficient was calculated by inverse the Rational method, where the maximum intensity was used in this formula with duration equal or greater than time of concentration. This procedure was used to calculate the runoff coefficient for 20 storms; each storm has an individual value according to its return period. The average value of it was obtained, and supposed as the runoff coefficient for the Goizha-Dabashan watershed.

VERIFICATION AND VALIDATION

Model validation includes initial data collection and subsequent model calibration. Sufficient data must be collected and analyzed to define the characteristics of the model domain (e.g., flows, pressures, precipitation, runoff coefficients, etc.). Model validation includes the comparison of the model results with a data set different from the calibration data set and, if the comparison is not satisfactory, the recalibration of the model using both sets of data (*Adrien, 2004*). For SCS curve number model, it was used for the curve number value to



obtain the best fit of the calculated hydrograph as comparison with observed hydrograph. The curve number value (composite value) for the conditions II and III were changed to give the best results. For Rational method, this process was used to verifying the runoff coefficient. The storms number nine and two was neglected in the verifying because it was assumed as extreme value. Nash model was used to test the fitting of the results as follows:

$$\text{Nash} = \sqrt{1 - \frac{\sum(Q_c - Q_o)^2}{\sum(Q_o - Q'_o)^2}} \quad \dots (8)$$

Where Q_c : is the calculated value.

Q_o : is the observed value, and

Q'_o : is the mean of observed values.

RESULTS AND DISCUSSION.

Watershed properties (watershed characteristics) involved area, shape, slope, etc. and the watershed morphology which consists of elongation ration, circulation ratio, etc. These parameters were computed to comparison the DEM results and field results (Barzinji, 2003) which calculated by taken GPS coordinates and measuring the area by the planimeter, while he was measured the perimeter and channels length by chartometer, as shown in **table 1**. It is notice from this table; all error is not excess 10%, excepted the average watershed slope and centroid stream distance. So, the DEM with resolution 5 m gives accepted results by comparison with field results.

On the other hand, supervised classification was used to classify the land use and soil type of the study area, as shown in figures (3) and (4). It is notice from figures (3); the range land is covering

most the watershed (44%) as opposite of the vine grape land (16%). However, figure (5) shows the comparison between Remote sensing results and field (Barzinji, 2003) results. It is obvious from this figure; there is no high difference in the two results for land use and soil texture excepted in range land (10.1%).

Table 2 shows the value of curve number for the 15 regions. The value of curve number depends on four factors; hydrologic soil group, treatment, land use, and hydrologic condition. The distribution of land used and soil type was obtained from the satellite image by using supervised classification as shown in **Fig. 3** and **Fig. 4**. The soil type was computed according to its basic infiltration rate. So the watershed area was divided to 15 regions which equal the number of infiltrometers.

Runoff Hydrograph and Runoff Coefficient.

Runoff of Goizha-Dabashan watershed was computed with aid of HEC-1 model. The data required to the model are, distribution and depth of rainfall, base flow, loss method parameters, and unit hydrograph parameters. Figures (1 to 10) in Appendix A show the runoff hydrograph for storm number 1 to storm 10. However, Runoff coefficient was calculated for 10 storms by inversed the rational formula. Each model has individual runoff coefficient due to the return period of the storm, as shown in table 3.

The calculated runoff by using SCS-CN method showed an error in it; also, runoff coefficient resulted from Rational method showed there is a

fluctuation in values of runoff coefficient for the ten storms, so optimization process is used to reduce this error.

CALIBRATION AND VERIFICATION.

Calibration process was used to one parameter in each model trial and error method. For SCS curve number model, the optimum value for condition II and condition III were obtained from the first 6 storms and verified for the last 4 storms. Condition III was used if the last storm not exceeded ten days. The value of runoff coefficient is 0.05 after calibration and verification. Storm number nine was neglected from the verification process because it was assumed as extreme value or its return period is high (runoff coefficient increase with increasing the return period and vice versa).

CONCLUSIONS.

- In the light of this study, the following steps can be concluded:
- The difference between DEM results (with 10m resolution) and field results for the watershed properties are not excess 10%, excepted average watershed slope (14.03 %) and centroid stream distance (19.10%).
- There is no high difference between remote sensing results and field results for land use, excepted in range land (the difference is 10.1%).
- The calculated composite values of curve numbers for Goizha-Dabashan watershed are 50.2, 69.5, and 83.3 for conditions I, II, and

III respectively. While, the optimum values for conditions II and III are 75 and 80.5 respectively. Also, the optimum runoff coefficient is 0.05.

- If the SCS curve number model is used without optimized its parameters values, it may cause some error in runoff.
- SCS curve number model is better than Rational method in estimation of peak runoff discharge.
- The Values of Nash model for SCS-CN, Barzinji (2007), and ANN models are 0.909, 0.907 and 0.964 respectively, therefore; ANN is the best with 1 storm failed. And SCS-CN model is better than Barzinji model.

REFERENCES

- Adrien, Nicolas G., 2004, "Computational Hydraulics and Hydrology: An Illustrated Dictionary", CRC Press LLC, New York.
- ASCE, American Society of Civil Engineering, 1996, "Hydrology Handbook", 2nd, Manuals and Reports on Engineering Practice No.28, American Society of Civil Engineers Publications.
- Al-Hamawandi, Saman H. H., 2009, "Watershed Modeling Using Artificial Neural Networks", Ph.D. Dissertation, Water Resources Engineering, University of Baghdad.
- Barzinji, Khalid T. M., 2003, "Hydrologic Studies for Goizha-Dabashan and Other watersheds in



Sulymaniah Governorate", M.Sc. Thesis, College of Agricultural, University of Sulymaniah.

Barzinji, Khalid T. M., 2007, "Deterministic Optimization for Goizha-Dabashan watershed ", Ph.D. Dissertation, College of Agricultural, University of Sulymaniah.

Chow, Ven Te, 1964, Handbook of Applied Hydrology, McGraw-Hill Company, New York.

[Http: //www.emrl.byu.edu/gsdu](http://www.emrl.byu.edu/gsdu).

Musgrave, G. W., 1955, "How Much Rain Enters the Soil", US Department of Agriculture, Yearbook of Agriculture; 151-159.

Nash, J.E. and Sutcliffe, J.V., 1970, "River Flow Forecasting Through Conceptual Models, Part I: A Discussion of Principles", Journal of Hydrology, 10: 282-290.

Ponce, Victor M. and Richard H. Hawkins, 1996, "Runoff Curve Number: Has it Reached Maturity?", Journal of Hydrologic Engineering; 11-19.

Schwab, Glenn O., Richard K. Frevert, Tallcot W. Edminster, and Kenneth K. Barnes, 1966, "Soil and Water Conservation Engineering", 2nd, John Wiley and Sons, Incorporation, New York.

Shaw, Elizabeth M, 1983, "Hydrology in Practice", Van Nostrand Reinhold Company, UK.

Suresh, R., 2005, "Watershed Hydrology", 2nd, Standard Published Distributed, Nai Sarak, Delhi.

Viessman, Warren, Jr. and Gary L. Lewis, 2003, "Introduction to Hydrology", 5th, Parson Education, Incorporation, Delhi.

Walsh, Michael J., 2003, "Remote Sensing: Engineering and Design", US. Army Corps of Engineering.

WMS, Watershed Modeling System, 2004, "WMS v7.1 Tutorial", Brigham Young University, Environmental Modeling Research Laboratory.

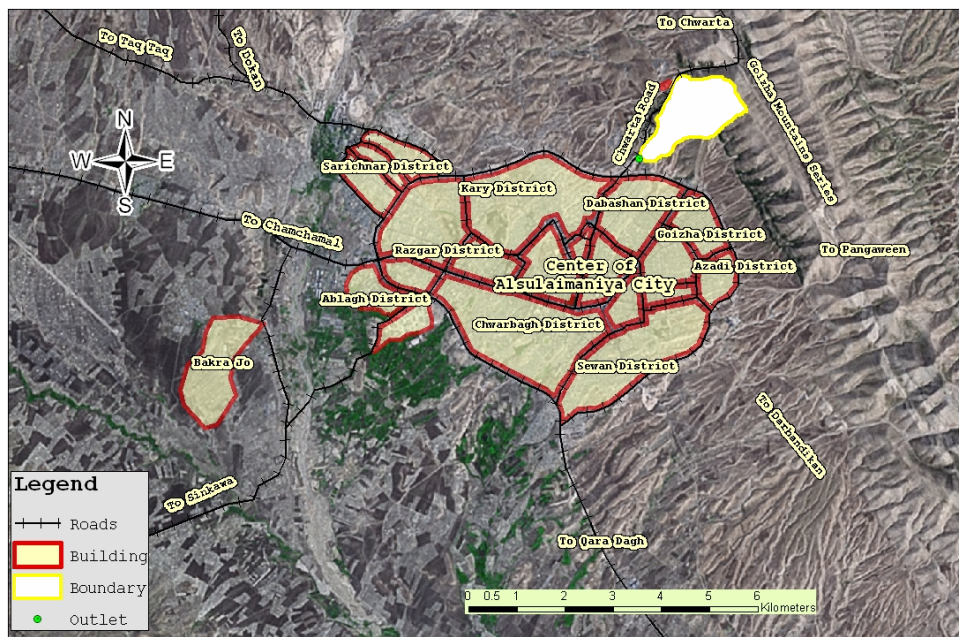


Fig. 1: Location of Goizha-Dabashan watershed in Al-Sulymaniah city.

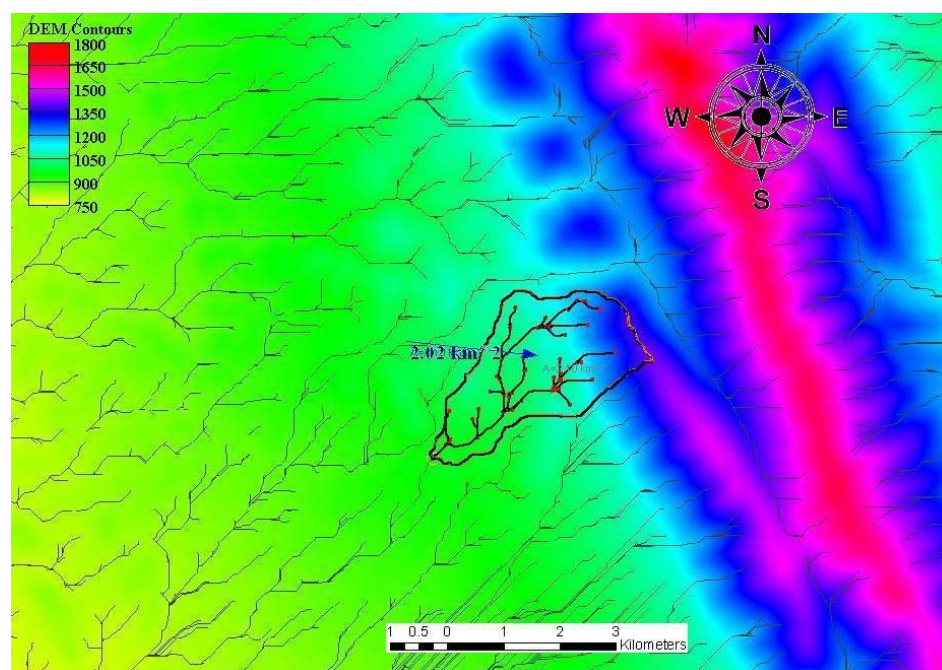


Fig. 2: Streams flow and boundary of the watershed.



Table 1: Comparison for the watershed properties results.

Parameter Name	DEM Results	Field Results	Unit	Percent of Error	Equation
Area	2.02	2.014	km ²	0.3	-
Average Basin Slope	0.126	0.11	m/m	14.03	-
Max Flow Distance	3.2	3	km	6.67	-
Centroid Stream Distance	1.44	1.78	km	19.1	-
Watershed Length	2.47	2.43	km	1.89	-
Watershed Perimeter	6.75	6.63	km	1.81	-
Elongation ratio	0.65	0.65	-	0	$= (4 A / \pi)^{0.5} / L$
Circulation ratio	0.55	0.56	-	1.79	$= A / A_c$
Compactness ratio	1.34	1.31	-	2.29	$= P_b / (2 \sqrt{\pi A})$
Form factor	0.32	0.34	-	3.52	$= A / L^2$
Maximum Elevation Difference	452	482	m	6.22	-
Relief ratio	0.182	0.198	-	8.08	$\Delta H / L$
Time of Concentration	21.6	24	min	10	$= 0.02 L^{0.77} Y^{-0.385}$

* Percent error = $|R_{DEM} - R_{Barjinji}| / R_{Barjinji} \times 100 \%$

* A: watershed area.

* L: the maximum watershed length.

* A_c : the area of a circle has the same perimeter.

* P_b : is the perimeter of the watershed.

* Y: is the watershed gradient.

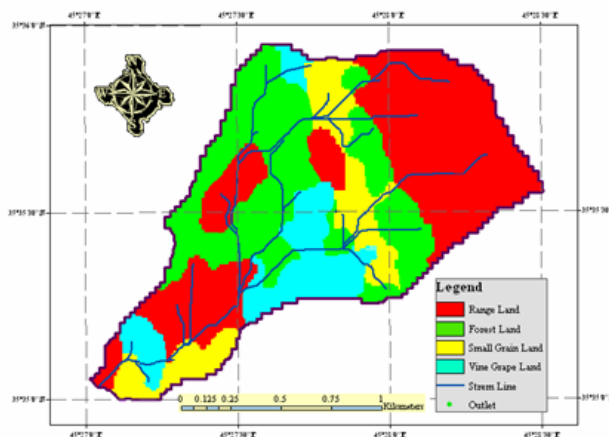


Fig. 3: Land use map.

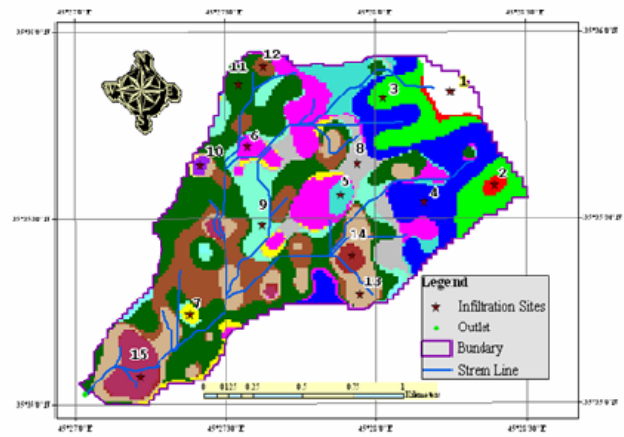


Fig. 4: Soil type map.

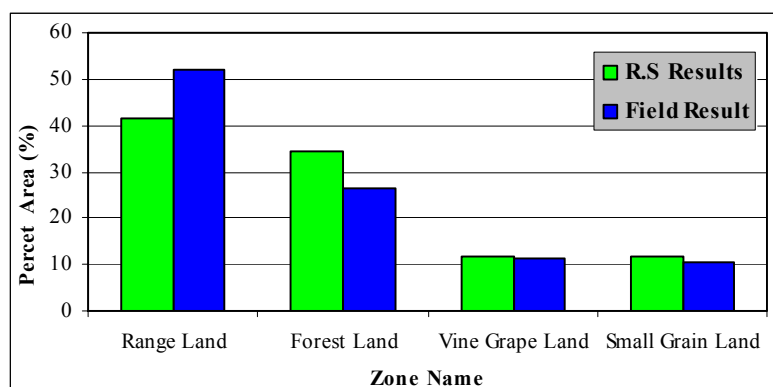


Fig. 5: Percent and total area of land use for Goizha-Dabashan watershed.

Table 2: Curve number values for the study area.

Zone No.	Land use	Area (ha.)	Weighted Area	Soil Type	Condition	Treatment	CN II	CN I	CN III
1	Range	6.158	0.03	D	Good	-	71	50.7	84.9
2	Range	2.803	0.014	D	Good	-	71	50.7	84.9
3	Range	14.151	0.07	D	Good	-	71	50.7	84.9
4	Range	29.881	0.148	D	Good	-	71	50.7	84.9
5	Range	11.486	0.057	D	Good	-	71	50.7	84.9
6	Range	18.217	0.09	C	Fair	-	73	53.2	86.1
7	Range	6.276	0.031	D	Poor	-	89	77.3	94.9
8	Forest	6.434	0.032	B	Good	Contoured	58	36.7	76.1
9	Forest	9.927	0.049	A	Good	Contoured	32	16.5	52
10	Forest	4.993	0.025	C	Good	Contoured	72	51.9	85.5
11	Forest	24.651	0.122	B	Good	Contoured	58	36.7	76.1
12	Small Grain	12.532	0.062	B	Poor	Contoured	74	54.4	86.7
13	Small Grain	21.848	0.108	C	Poor	Contoured	82	65.7	91.3
14	Vine Grape	7.401	0.037	B	Poor	Contoured	73	53.2	86.1
15	Vine Grape	25.243	0.125	B	Poor	Contoured	73	53.2	86.1

Table 3: Nash model Values for the three models, and rainfall depth for each storm.

Storm No	1	2	3	4	5	6	7	8	9	10	Mean
CN Model	0.918	0.95	0.958	0.93	0.7	0.88	0.98	0.988	0.83	0.957	0.909
Barzinji, 2007 Model	0.786	0.702	0.954	0.911	0.936	0.964	0.927	0.982	0.951	0.964	0.907
ANN Model	0.938	0.968	0.95	0.985	0.844	0.994	1	1	1	Failed	0.964
Rainfall Depth (mm)	21.4	18.9	19.65	13.9	16.4	22	14.8	30.3	40	18	

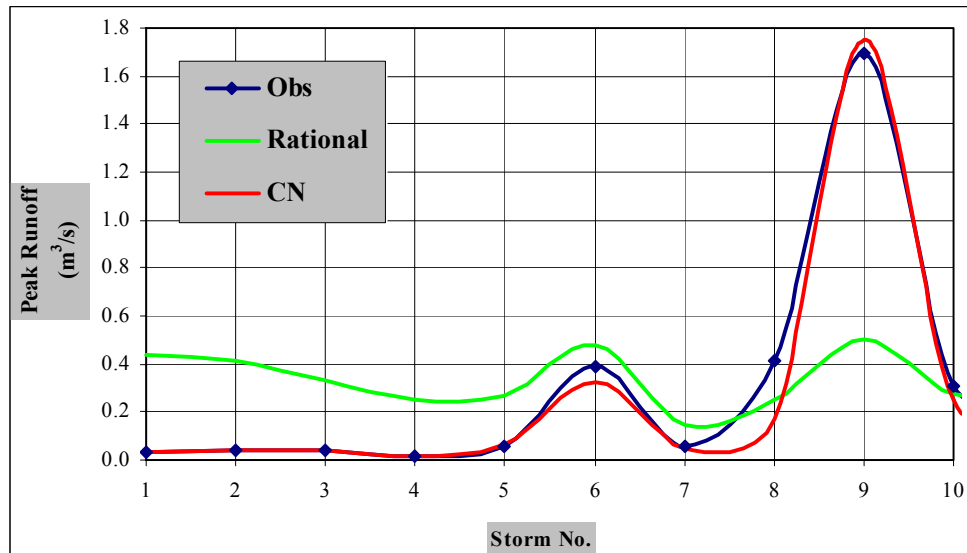


Fig. 6: Observed and calculated peak runoff.

APPENDIX A: RUNOFF HYDROGRAPHS.

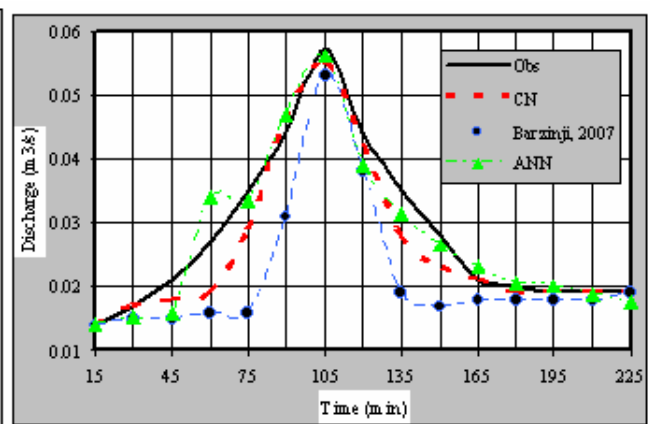
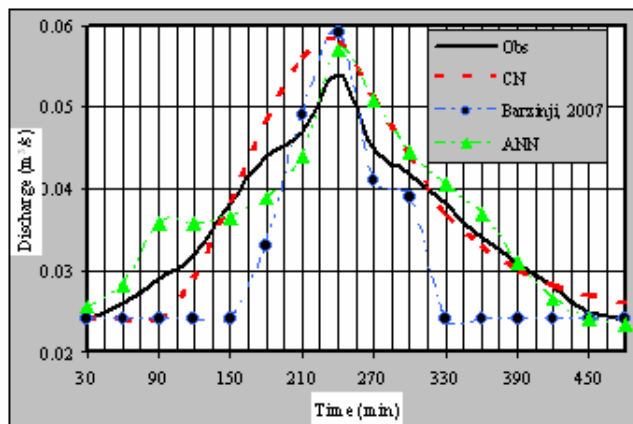


Fig. 1: Observed and calculated runoff for storm Fig. 2: Observed and calculated runoff for storm 2

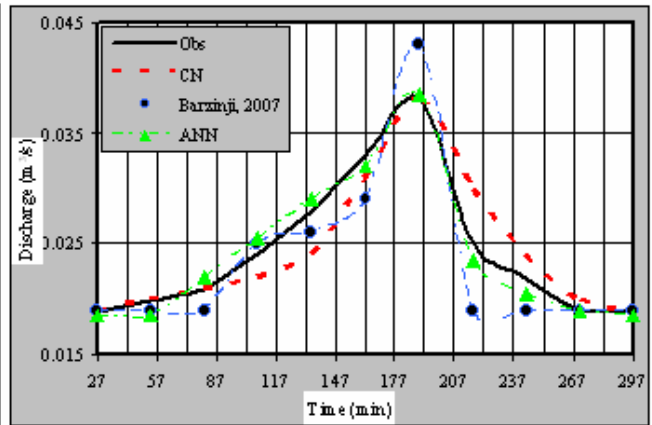
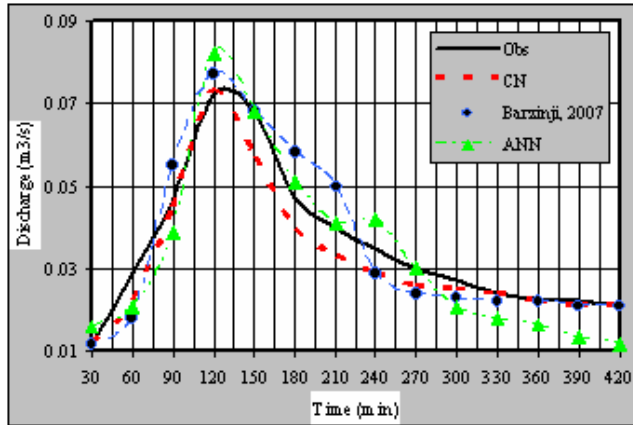


Fig. 3: Observed and calculated runoff for storm 3

Fig. 4: Observed and calculated runoff for storm 4

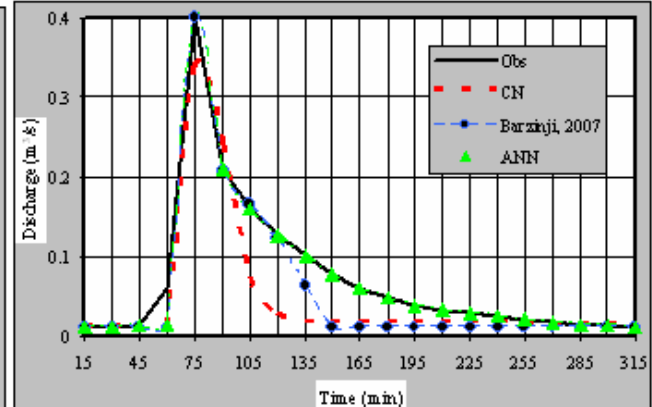
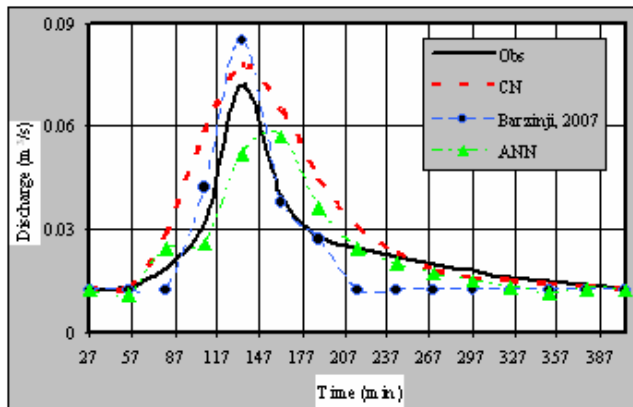


Fig. 5: Observed and calculated runoff for storm 5

Fig. 6: Observed and calculated runoff for storm 6

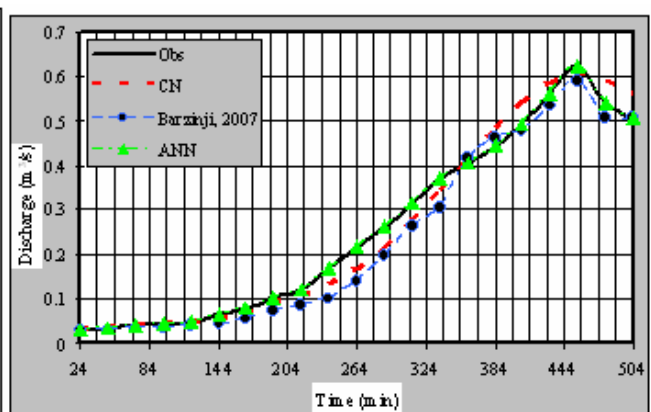
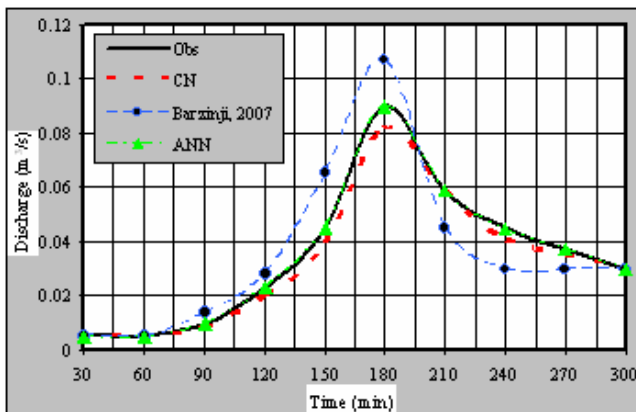


Fig. 7: Observed and calculated runoff for storm 7

Fig. 8: Observed and calculated runoff for storm 8

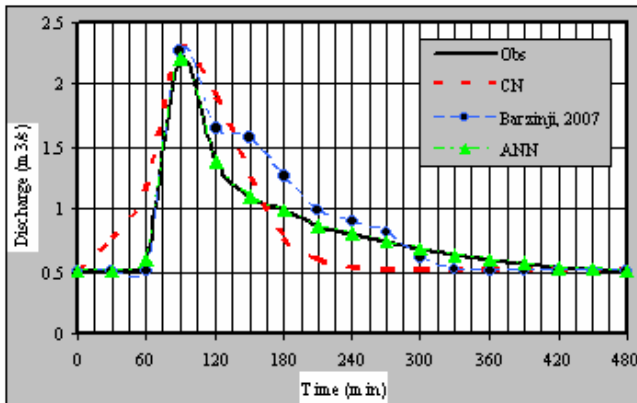


Fig. 9: Observed and calculated runoff for storm 9

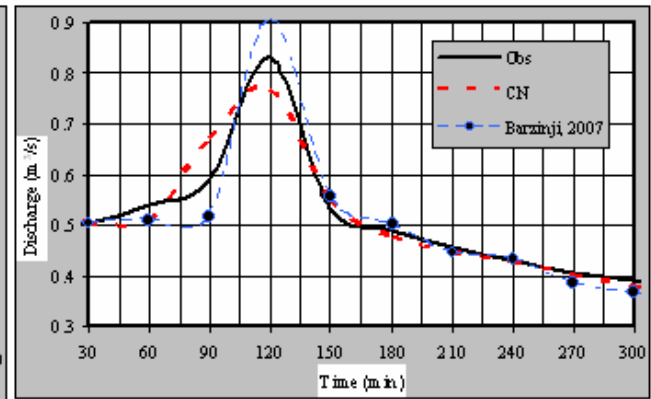


Fig. 10: Observed and calculated runoff for storm 10

MODELING A PROCESS FOR THE REMOVAL OF CADMIUM FROM SIMULATED WASTEWATERS BY ELECTRO-DEPOSITION ON STAINLESS STEEL TUBES BUNDLE

Prof. Dr. Abbas Hamid Sulaymon / PhD Chemical Engineering

Prof. Dr. Adel Obaid Sharif / PhD Chemical Engineering

Dr. Thana Kamil Al-Shalchi / PhD Environmental Engineering

ABSTRACT

Electrochemical processes can provide valuable contributions to the protection of the environment through implementation of effluent treatment and production-integrated processes for the minimization of waste and toxic compounds.

The performance of a novel pilot scale, batch re-cycled, flow-through cell, with stainless steel tubes bundle cathode in the removal of cadmium was investigated utilizing the potential results obtained from a batch mode. The studied electrochemical reaction was the cathodic reduction of Cd^{+2} using 0.5 M sodium sulphate as supporting electrolyte. The analyzed parameters were different initial Cd^{+2} concentrations (50, 100, 200, 300, 400 ppm) and different electrolyte flow-rates (100, 200, 250, 300, 350 L/hr), the tubes number was 920 of 0.6 cm diameters.

The overall empirical mass transfer correlation was found to be:

$$Sh = 0.051 Re^{0.859} Sc^{1/3}$$

$$\text{For } 5 < Re < 20 \text{ and } Sc = 649$$

Experimental results, analysis and correlations showed good performance of the cell and proved its adequacy in the removal of Cd^{+2} from simulated effluents.

الخلاصة

تحقق العمليات الكهروكيميائية مشاركة فاعلة في الحفاظ على البيئة من خلال معالجة المياه العادمة و عمليات الانتاج المتكاملة الهادفة الى تقليل المخلفات و المركبات السامة.

تمت دراسة كفاءة اداء منظومة ريادية مستحدثة، تعمل بنظام شبه الدفعات المستمر وخلية جريان متوازية، قطبها السالب عبارة عن حزمة من الانابيب الفولاذية، في ازالة الكاديوم، وباستخدام الجهد الكهربائي الذي تم الحصول عليه من نظام الدفعات. التفاعل الكهروكيميائي الذي تمت دراسته هو الاختزال الكاثودي لايونات الكاديوم الثنائية باستخدام محلول سلفات الصوديوم (0.5 مولار) كالكتروليت مساعد. المؤشرات التي تم اعتمادها للتحليل هي تراكيز مختلفة لايونات الكاديوم (50، 100، 200، 300، 400 جزء في المليون) و محاليل بمعدلات جريان مختلفة (100، 200، 250، 300، 350 لتر/ساعة)، انابيب الكاثود كانت بعدد 920 و باقطار 0.6 سم. تم ايجاد علاقة ارتباط تجريبية لخواص انتقال الكتلة للخلية الكهروكيميائية و كما يلي:

$$Sh = 0.051 Re^{0.859} Sc^{1/3}$$

$$\text{للمدى التالي: } 5 < Re < 20 \text{ و } Sc = 649$$

اظهرت نتائج التجارب والتحليل المختبرية، اضافة الى علاقات الارتباط التجريبية، اداء جيد للخلية المستخدمة وملاءمتها لازالة الكاديوم من المياه العادمة المختلفة.

KEYWORDS: Electrochemical, Flow-through cell, Cadmium, Tubes bundle.

INTRODUCTION

With a rapidly growing world population and an increasing number of reports on detrimental effects on the environment, its protection has become a major issue and a crucial factor for future technological progress, which will have to meet the requirements for sustainable development. The strategies for environmental protection in industry generally include processes or products which have no or less harmful effects on the environment. Electrochemistry has important roles to play in these strategies; industrial electrochemistry has undergone developments towards cleaner processes and more environmentally friendly products. [Simonsson, (1997)].

Cadmium is a toxic and bio-persistent element and, once absorbed by an organism, remains resident for many years although it is eventually excreted. In humans, long-term exposure is associated with renal dysfunctions. High exposure can lead to obstructive lung disease and has been linked to lung cancer. [Lenntech, (2009)].

The electrolytic method for the removal of heavy metals from aqueous media by using porous electrodes of various geometric shapes and materials, with flowing solutions, represents a successful reactor which presents high mass-transfer conditions. [Tramontina, (2002)].

EXPERIMENTAL WORK

The performance of a novel pilot scale flow-through cell, with stainless steel tubes bundle cathode was studied. Potential values over which cadmium is controlled by mass transfer, was obtained from a rotating disc electrode from previous experiments [Al-Shalchi, (2010)], a value of -1 V was applied for the removal of cadmium from a synthetic solution in the batch re-circulation mode.

The catholyte solution used was a 0.5 M sodium sulphate with different concentrations of cadmium sulphate. Electrolytes with cadmium concentrations of (50, 100, 200, 300 and 400 mg/L) were prepared in the 0.5 M sodium sulphate used as supporting electrolyte. The bulk pH was adjusted to a value of 4.8. The anolyte used had the same composition as the catholyte, but without the presence of cadmium.

The catholyte and anolyte flow-rates used were (100, 200, 250, 300, 350 L/hr).

The novel pilot scale electrochemical reactor used had an overall dimension of (25×25×17) cm; it was made from four Teflon discs. A silicon rubber layer of (1 mm) thickness was placed between each two disks to prevent the electrolyte leakage. The main cell compartments are the cathode chamber and the anode chamber.

The cathode was a configuration of tubes bundle consisting of 920 stainless steel tubes of 0.6 cm outer diameters and 0.4 cm inner diameters arranged on a fixed perforated stainless steel plate inside a disc of 20 cm diameter in triangular pitch arrangement; and the anode was made of a graphite disc of 14 cm diameter and 2 cm thickness. **Figure (1)** illustrates a sectional sketch of the tubes bundle electrode.

The pilot flow system used, operating under batch re-circulating conditions, consisted in addition to the electrochemical cell, the catholyte and anolyte porcelain reservoirs, two recirculation pumps, and two sets of flow meters for measuring the catholyte and anolyte flow rates. **Figure (2)** illustrates the schematic diagram of the pilot plant flow system.

At time intervals of 15 minutes, catholyte samples were taken from the catholyte reservoir in order to be analyzed for Cd^{+2} concentrations by using Atomic Absorption.

RESULTS AND DISCUSSION

The performance of a novel pilot scale, batch re-cycled, flow-through cell, with stainless steel tubes bundle cathode in the removal of cadmium was examined by utilizing the potential results obtained from previous batch mode experiments, it was equal to -1 V.

Effect of Initial Concentration

Experiments were carried out to study the removal rate of Cd^{+2} from solutions of different Cd^{+2} initial concentrations with catholyte and anolyte flow rate of 250 L/hr.

Figure (3) shows the curves of normalized Cd^{+2} concentration ($c(t)/c_o$) as a function of time for different cadmium initial concentrations (50, 100, 200, 300, 400 ppm). As expected, cadmium concentration decays exponentially with time. It can be seen the trends and behaviors of the curves for the different Cd^{+2} concentrations are the same.

Plotting the logarithmic normalized concentration $\ln(c(t)/c_o)$ as a function of time, **Figure (4)**, gives linear relationships; the slopes of the straight lines were used to estimate the mass transfer coefficients by using eq. (1). This

equation is for a batch-recycle mode electrolysis process carried out under mass transfer control: [Bertazzoli, (1998)].

$$\ln\left(\frac{c(t)}{c_0}\right) = -\frac{V_e k_m A_e}{V_T} t \quad (1)$$

Where:

k_m = mass transport coefficient cm s^{-1}
 V_T = volume of electrolyte cm^3
 V_e = overall electrode volume cm^3
 A_e = electrode area per unit electrode volume cm^{-1}
 t = time s
 c_0 = initial concentration ppm
 $c(t)$ = concentration at time (t) ppm

Since (V_e) and (V_T) are known parameters and (A_e) is calculated; then (k_m) can be estimated from the above equation.

The estimated values of (k_m) were plotted against the bulk Cd^{+2} concentrations; **Figure (5)**. It can be seen that the mass transfer coefficient is inversely proportional to the Cd^{+2} concentrations.

Figure (5) shows higher values of mass transfer coefficient with lower values of bulk Cd^{+2} concentrations, this is attributed to the hydrogen evolution, which is the predominant cathodic reaction at low values of the inlet cadmium concentration.

In order to find the mass of Cd^{+2} deposited with time, a mass balance was conducted on three different initial concentrations of cadmium solutions (50, 200, 400 ppm). **Figure (6)** illustrates the mass deposition of cadmium as a function of time. The resulted curves are also exponential with time.

Effect of Electrolytes Flow Rate

Experiments were carried out to study the influence of flow rate of catholyte on the removal rate of Cd^{+2} from solutions with initial concentration of 200 ppm.

Figure (7) shows the curves of normalized Cd^{+2} concentration ($c(t)/c_0$) as a function of time for different catholyte flow rates (100, 200, 250, 300, 350 L/hr). As expected, cadmium concentration decays exponentially with time. It can be seen that higher flow rates enhance the removal of Cd^{+2} . This behavior is attributed to greater rates of mass transport of Cd^{+2} with increased electrolytes flow rates, which reduce the thickness of the boundary layer for mass transfer.

Plotting the logarithmic normalized concentration $\ln(c(t)/c_0)$ as a function of time, **Figure (8)**, gives linear relationships. Following the same previous procedures, values of (k_m) were calculated for each flow rate.

Mass Transfer Correlations

Mass transfer coefficients estimated from the series of experiments on different flow rates were fitted to find an empirical correlation of dimensionless Sherwood number for the tubes bundle cathode under the medium and conditions of the experiments.

Starting from the typical mathematical relationship for dimensionless Sherwood number, which is suitable for electrolytic reactors design:

$$Sh = m Re^n Sc^{1/3} \quad (2)$$

And the so called j_D factor correlation:

$$j_D = Sh Re^{-1} Sc^{-1/3} \quad (3)$$

Where:

$Sh = k_m d_e / D$ Sherwood number
 $Re = u_e d_e / \nu$ Reynolds number
 $Sc = \nu / D$ Schmidt number
 $u_e = u / \varepsilon$ characteristic flow velocity
 D diffusion coefficient $\text{cm}^2 \text{s}^{-1}$
 ε porosity
 d_e equivalent diameter (a characteristic length)
 ν kinematic viscosity $\text{m}^2 \text{s}^{-1}$
 m and n empirical constants dependent on the geometry of the system

[Pletcher, (1991)].

The following correlation is obtained:

$$Sh = 0.051 Re^{0.859} Sc^{1/3} \quad (4)$$

for $5 < Re < 20$ and $Sc = 649$ (calculated from batch mode)

This obtained correlation is of good agreement with [Pickett, (1979)] :

$$Sh_{av} = 0.023 Re^{0.8} Sc^{1/3}$$

It can be used for different reactor geometries providing that the relevant equivalent diameter is correctly formulated:

Table (1) lists the data used for the analysis.

Figures (9) and (10) summarize the Sherwood – Schmidt – Reynolds and j_D correlations, with (CR=0.996) and (CR=0.95) respectively.

CONCLUSIONS

Conclusions

- The performance of the stainless steel tubes bundle electrode, operating in the batch re-circulated mode, was successful in the removal of Cd^{+2} from simulated wastewater.
- The mass transfer coefficient increased with lower values of bulk Cd^{+2} concentration, due to hydrogen evolution; the mass transfer coefficient was correlated with the bulk concentration of Cd^{+2} in sodium sulphate.
- The mass transfer coefficient increased with higher flow rates, due to the reduction in the boundary layer thickness; the mass transfer coefficient was correlated with the electrolyte velocity.
- The overall empirical mass transfer correlation was found to be:

$$Sh = 0.051 Re^{0.859} Sc^{1/3}$$

for $5 < Re < 20$ and $Sc = 649$

Which is in good agreement with literature.

REFERENCES

- Al-Shalchi, T. K. (2010), “Removal of Cadmium from Simulated Wastewaters by Electro-Deposition on Stainless Steel Tubes

Bundle ”, PhD Thesis, College of Engineering, University of Baghdad.

- Bertazzoli, R., Rodrigues, C. A., Dallan, E., J., Fukunaga, M. T., Lanza, M. R. V., Leme, R. R., Widner, R. C. (1998), “Mass Transport Properties of a Flow-Through Electrolytic Reactor Using a Porous Electrode: Performance and Figures of Merit for Pb II Removal”, Braz. J. Chem. Eng. Vol. 15 No. 4.
- Lenntech, Water Treatment & Purification Holding BV (2009), “Heavy Metals”, <http://www.lenntech.com>.
- Pickett, D. J. (1979), “Electrochemical Reactor Design”, Elsevier Scientific Publishing Company.
- Pletcher, D., White, I., Walsh, F. C., Millington, J. P. (1991), “Reticulated Vitreous Carbon Cathodes for Metal Ion Removal from Process Streams; Part I: Mass Transport Studies”, Journal of Applied Electrochemistry 21.
- Simonsson, D. (1997), “Electrochemistry for a Cleaner Environment”, Chemical Society Review Vol. 26.
- Tramontina, J., Azambuja, D. S., Piatnicki, M. S. (2002), “Removal of Cd^{+2} Ion from Diluted Aqueous Solutions by Electrodeposition on Reticulated Vitreous Carbon Electrodes”, Mat. Res., Vol. 4, No. 3.

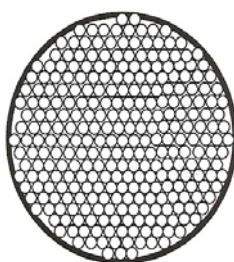


Figure (1) Sectional sketch of the tubes bundle electrode

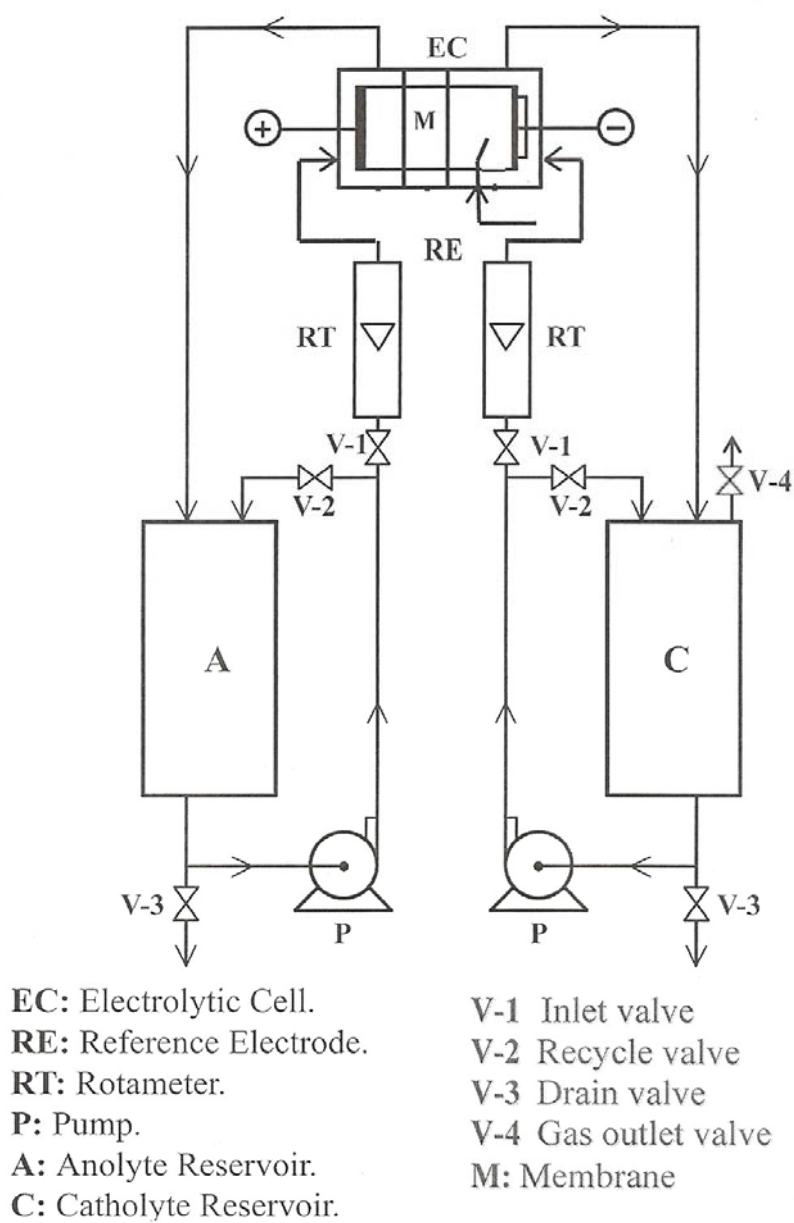


Figure (2) Schematic Diagram of the Pilot Plant Flow System

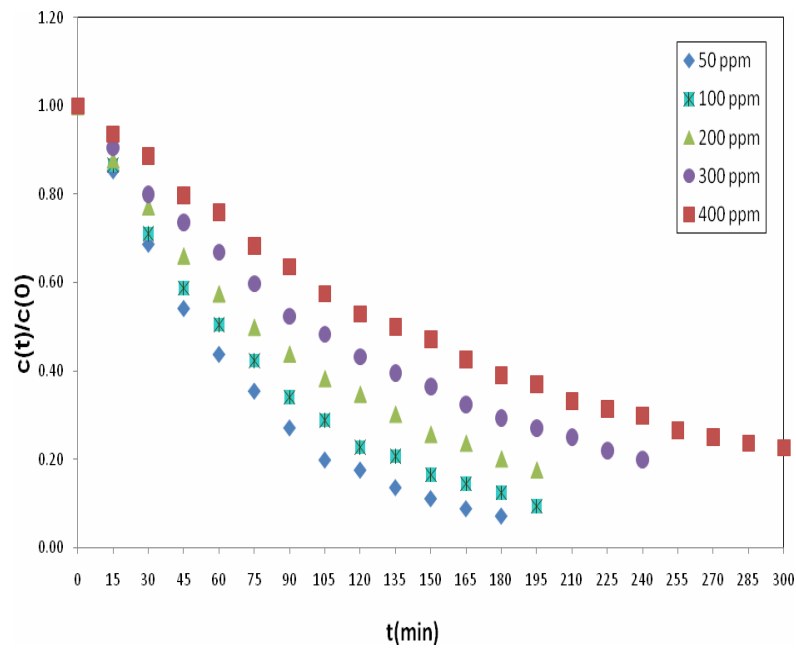


Figure (3) Normalized concentration ($c(t)/c_0$) as a function of time for removal of different Cd^{+2} concentrations and flow rates 250 L/hr

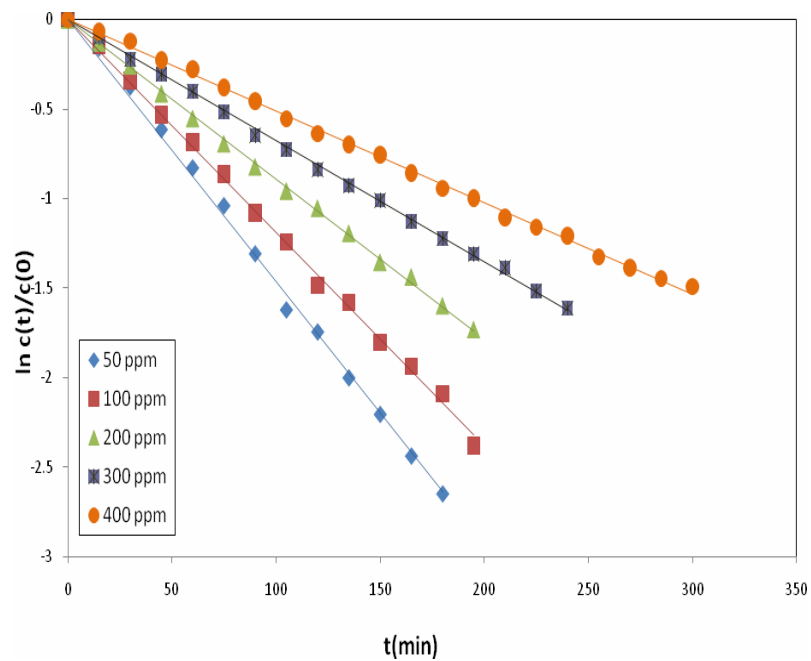


Figure (4) Linearization of normalized concentration as a function of time for different Cd^{+2} concentrations and flow rate of 250 L/hr

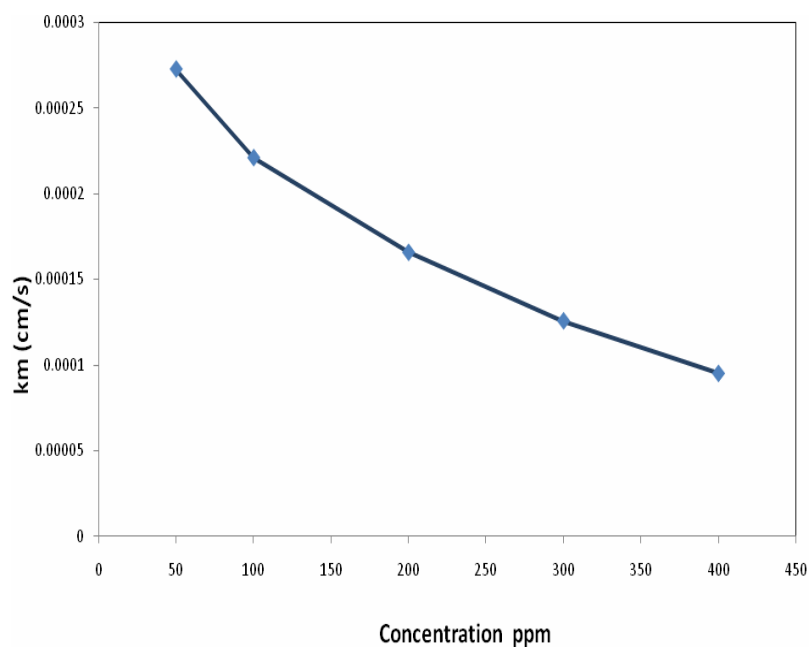


Figure (5) Variation of mass transfer with bulk Cd^{+2} concentrations

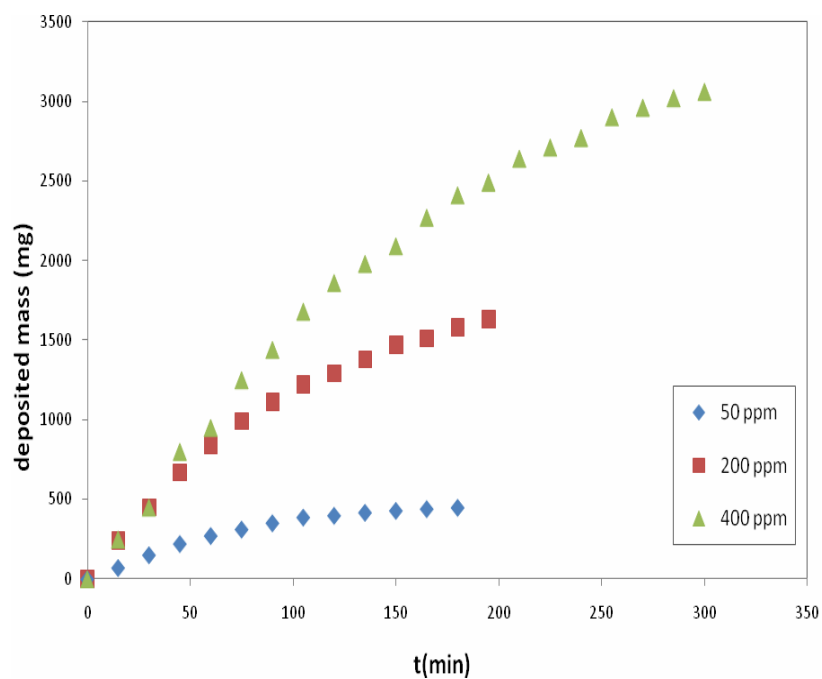


Figure (6) Mass deposited of cadmium with time for different Cd^{+2} concentrations and at flow rate of 250 L/hr

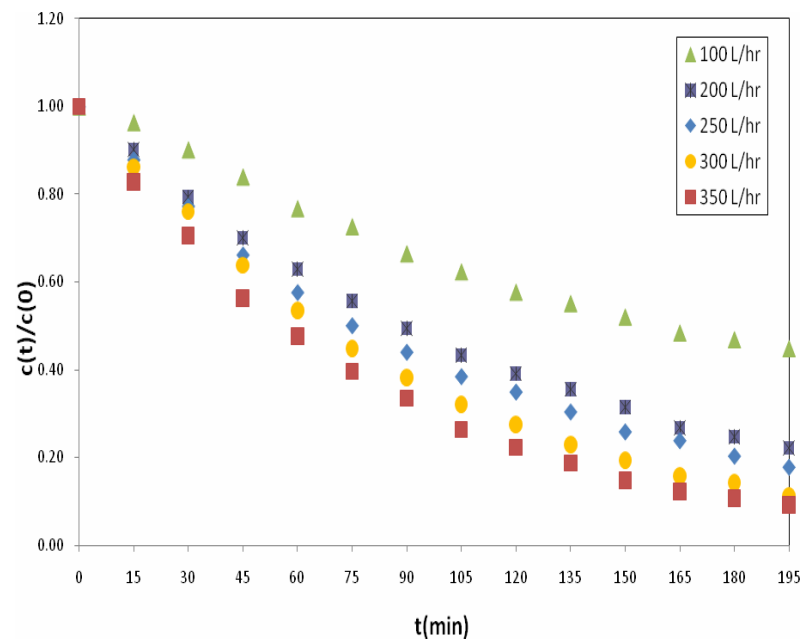


Figure (7) Normalized concentration ($c(t)/c_0$) as a function of time for Cd^{+2} removal for different flow rates and Cd^{+2} concentration of 200 ppm

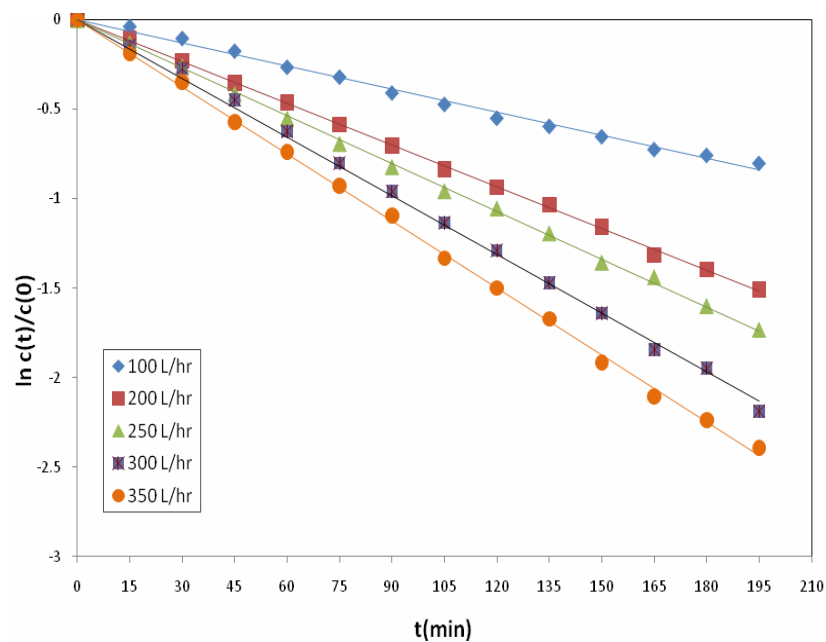


Figure (8) Linearization of normalized concentration as a function of time for different flow rates and Cd^{+2} concentration of 200 ppm



Table (1) Data used for calculations of dimensionless numbers and Cd^{+2} concentration of 200 ppm

Parameters		Flow Rates (L/hr)
$10^5 D \text{ (cm}^2 \text{ s}^{-1}\text{)}$	1.127	100
$10^2 v \text{ (cm}^2 \text{ s}^{-1}\text{)}$	0.731	200
Schmidt number	649	250
Porosity	0.583	300
Equivalent diameter (d_e) (cm)	0.27	350

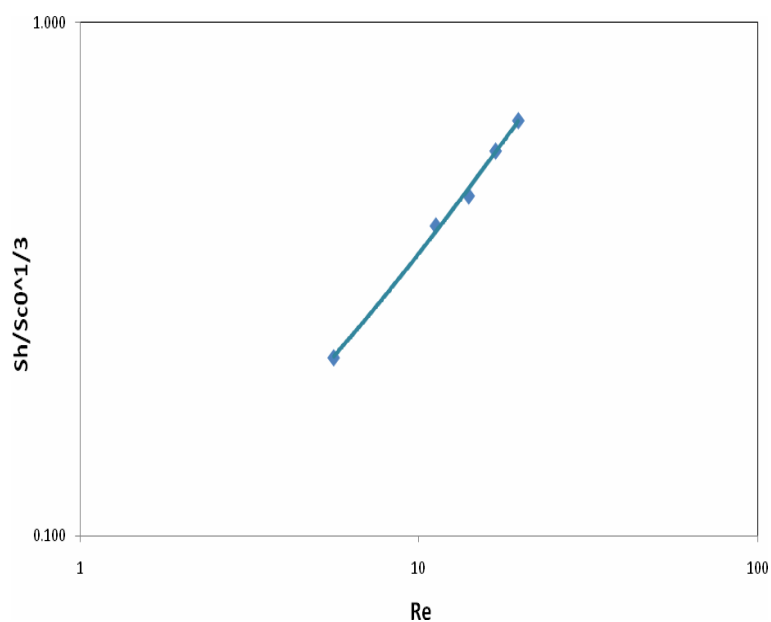


Figure (9) Sherwood-Reynolds correlation for Cd^{+2} concentration of 200 ppm

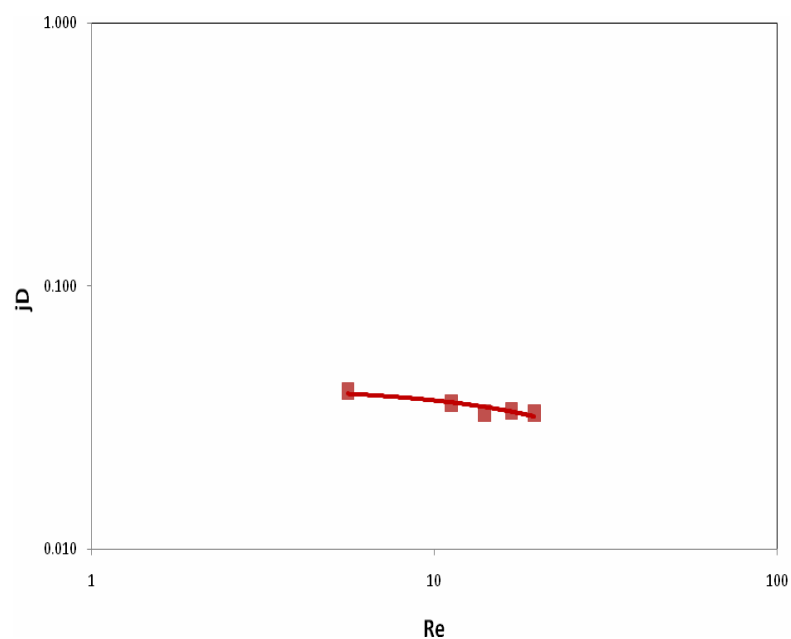


Figure (10) j_D factor-Reynolds correlation for Cd^{+2} concentration of 200 ppm



NEURAL NETWORK APPLICATION FOR BUILDING PROJECTS COST ESTIMATION

Ass. Prof. Dr. Zouhair Al-Daoud

Ali Mohamed Humod

University of Baghdad, College of Engineering, Mechanical Engineering Department

ABSTRACT

This work presents a neural network based cost estimating method, developed for the generation of conceptual cost estimates for total building and electromechanical systems in building project, by using eight parameters available at the early design phase. This model establishes a methodology that can provide an economical and rapid means of cost estimating. Eighteen High rise building projects, built between 1996 and 2009 in Middle East countries used in this study. The performance of developed cost models was tested against costs incurred by projects not used in training of those models. Results show the mean absolute percentage errors (MAPE) are between 1.51% and 4.771% for the five networks, and the maximum/minimum deviation of the cost estimation is 10.2/0.17. These figures considered good cost estimation at the early design stage.

الخلاصة

تقدم هذه الرسالة نموذجا عمليا لتخمين الكلفة اعتمادا على تقنية غير تقليدية و هي الشبكات العصبية الاصطناعية. التي تتضمن الكلفة الكلية لبناء الأبراج السكنية و الفندقية بالإضافة لكلف المنظومات الميكانيكية و الكهربائية، و بالإعتماد على ثمانية عناصر تصف حجم المشروع و خصائصه متوفرة في أوائل مراحل التصميم، و قد أستخدم لغرض تدريب و اختبار هذه الشبكات ثمانية عشر مشروعا حقيقيا مبنية كلها في دول الشرق الأوسط في الفترة ما بين 1996 و 2009. تعتبر الشبكات العصبية الاصطناعية فرع من الذكاء الصناعي و تطبيقات علوم الحاسبات الحديثة، وقد استخدمت في هذا البحث لكفاءتها في إدارة الكلف و المعلومات للتطبيقات الهندسية و لأنها تعتمد في بنائها و تدريبها على معلومات واقعية لمشاريع حقيقية، مما أعطاها إمكانية تعميمها لتخمين كلف مشاريع جديدة. و من المعلوم إن تخمين كلف المشاريع في الأطوار الابتدائية (التخطيط و التصميم) أصبح هو العنصر المحدد و الأساسي في اتخاذ القرارات الحاسمة في الوقت المناسب و خصوصا في ظل التنافس العالمي بين الشركات و المؤسسات العالمية و المحلية و كذلك تقليل من نسب الأرباح المجنبة من هذه المشاريع. إن كفاءة النموذج المقدم اختبرت من خلال تطبيق معلومات لمشاريع لم تدخل في عملية تدريب الشبكات، و قد أظهرت نتائج الاختبارات للشبكات الخمسة ما بين (1.51- 4.77)% كمعدل المطلق للنسبة المئوية للخطأ ، كما إن أعلى و أقل خطأ لكل حالة على إنفراد كان (0.17 و 10.2)% على التوالي، و هي تعتبر نتائج جيدة إذا ما قورنت بالطرق التقليدية.

KEYWORDS: Neural Network, Cost Estimation, Project Management, Functional Analysis, Artificial Intelligence.

INTRODUCTION

Cost is one of the major criteria in decision making at the early stages of a project design process. In today's globally competitive world, diminishing profit margins and decreasing market shares, cost control plays a major role for being competitive while maintaining high quality levels. The cost of a project has a significant effects by decisions made at the design phase. While this influence decreases through all phases of the building project, the committed costs increase. Increasing project costs render effective and efficient decision making on cost issues a necessary for designers. To this end, designers use a number of cost estimating techniques and intuitive judgments by utilizing both their experience and data from previous projects [Duncan, 1996], [US. Department of Defense, 1995] & [CII, 1998].

The most important thing you can do to enhance a project's value is to include the right professionals for a project as early in the design process as possible. If you look at the following Cost Influence Curve **Fig.1**, you will notice that the time to achieve significant cost savings is before construction begins [Kellogg & Kimsey, 2008].

Several cost estimating methods for the different phases of a project like; Preliminary cost estimate, Elemental (functional analysis) estimate, Unit price estimate, Detailed cost estimate, Parametric cost estimates and others [R.S. Means, 1997], [Ayed, 1997] & [Evans, 2007].

Traditional cost estimating procedures follow a quantity take off, while comparative cost estimating relies on parameters such as type, size, and capacity of project. While traditional cost estimating makes use of plans and specifications, comparative cost estimating assumes a relationship between the final cost and the

basic design variables of the project [Evans, 2007].

Developments in computer and software technology have facilitated novel approaches for cost estimation. By the emergence of Artificial Intelligence (AI) tools (i.e., neural networks), possible multi- and non-linear relationships can now be investigated. Methods involving the new technology yield results that are both more realistic and accurate vis-à-vis real life conditions.

ARTIFICIAL NEURAL NETWORK

Neural network is an artificial intelligence model originally designed to replicate the human brain's learning process. The model consists of three main layers: input data layer (example the property attributes), hidden layer(s) (commonly referred as "black box"), and output layer (results), see **Fig.2** Neural network is an interconnected network of artificial neurons with a rule to adjust the strength or weight of the connections between the units in response to externally supplied data [Flood, 1994].

Fig. 3 and eq. (1) show the neural network structure and training equation of the feed-forward neural network.

$$Y_k = g \left(\sum_{j=1}^m w_{jk} f_j \left(\sum_{i=1}^n w_{ij} * x_i - S_i \right) - S_j \right) \quad (1)$$

Where Y_k : network output

f & g : transfer function of the hidden and output layer, respectively.

X_i : network input

i : input layer

j : w_{ij} : weight to layer j from layer i
hidden layer

k : w_{jk} : weight to layer k from layer j
output layer

S_i : bias from layer i to layer j

S_j : bias from layer j to layer k



NEURAL NETWORK MODEL

Current practice indicates the generation of five types of cost estimates:

- Total cost of the project;
- Cost of plumbing system;
- Cost of heating, ventilation and air conditioning system (HVAC);
- Cost of fire protection system;
- Cost of electrical system.

Accordingly, five neural network models were developed. Each network has the same inputs shown in table (1).

APPLICATIONS

a) Data

Eighteen High-rise building projects, built between 1996 and 2009, were collected over a four-month period, from Dar Al-Handasah – Shair and partners- for consultant engineering, the second rated international design firms in hotels and general building in 2006 according to ENR [ENR,2006]. Sample of projects data shown in table (2).

b) Training and testing of the neural network model

The data sample (eighteen projects) divided into two subsets: training, and test. These sets contained, respectively, 78%, and 22%, of the project cases considered in the data sample. The data extraction performed randomly. The training set used for training of each network. The test set used to check the performance of the learning process, during the network's training.

The network had not seen those cases during its training. Performance primarily measured against the accuracy observed in the production set. Once the networks were performing with an acceptable percentage of error, they considered trained and ready to assist the user in generating cost estimates. For the problem at hand, Matlab-NN tool box employed for its ease of use, Speed of training, and for its host of Neural Network

architectures including back propagation, with flexible user-optimization of training parameters. NN tool box includes a simplified set of procedures for building and executing a complete, powerful Neural Networks application. The user has the flexibility to specify own learning rate, activation functions, and initial weight range on a layer basis in the design module, Fig. 4 show the flow chart for developing new network, this procedure was applied for the five networks.

c) Application Results

Data from four projects used for testing purposes. Results of the five networks shown in table (3):

The accuracy of the cost estimates can be close to an expert system developed by Mohamed and Celik [Mohamed,2002], where estimated total costs were found to be between the range of 2% and 4% of the actual cost. While the FIDIC (international federation of consultant engineer), where the bidding of any contract in infrastructure not to exceed 13% of the estimated value, and the bidding of contract in building not to exceed 6% of the estimated value [FIDIC,2007].

These results compare favorably with past research that has shown that traditional methods of cost estimation are less accurate, as evidenced by reported values of MAPE between 20.8% [Skitmore,1990] and 27.9% [Lowe,1996].

DISCUSSION OF THE RESULTS

In present work, neural networks used to model the relationship between inputs (location, date and design variables) and outputs (cost of total building and electromechanical systems).

Performance of the training many algorithms were tested and the Scaled conjugate gradient backpropagation (trainscg), showed the best accuracy results.

The simulated annealing technique used to capture the best solution (weights and biases) among several local minima.

One of methods for improving network generalization is to use a network that is just large enough (number of hidden layers and number of neurons in each) to provide an adequate fit. The larger the network, the more complex the functions the network can create. If we use a small network, it will not have enough power over fit the data.

Unfortunately, it is difficult to know beforehand how large a network should be for a specific application.

Therefore, change architecture by raising the no. of neuron in hidden layer is used starting from 8 neurons to optimize network architecture and to improve the generalization. Adding more hidden layers is tried but it increased the error in test set.

CONCLUSIONS

- The using a neural network for cost estimation shown to be capable of providing accurate estimates of building and electromechanical systems cost per square meter by using eight parameters available at the early design phase. This model establishes a methodology that can provide an economical and rapid means of cost estimating for the total building and electromechanical systems of future building design processes.
- When increase the number of neuron in hidden layer, it is not always increase the result accuracy, because when the number of hidden neurons is too large the network overfit the training data, in which the network perform well for training data only and cannot generalize its knowledge to unseen (new) operating conditions and when the number of hidden neurons is too small, the network suffers underfitting problem, in which the

network cannot learn the relationship distributed among training data set.

REFERENCES

- Amr S. Ayed "Parametric Cost Estimating of Highway Projects using Neural Networks". M.Sc. Thesis, Newfoundland, Canada. 1997
- CII. "Improving Early Estimates". Construction industry Institute, University of Texas at Austin. Austin, TX, USA. 1998
- D.K. Evans¹, Dr J.D. Lanham¹, Dr R. Marsh "Cost estimation method selection: matching user requirement and knowledge availability to methods". University of West of England, Bristol, UK. 2007
- ENR Engineering News-Record. "2006 global construction sourcebook." 2006.
- FIDIC (international federation of consultant engineer), www.fidic.org/, 2007.
- Flood, I., and Kartam N. "Neural networks in civil engineering. 1: Principles and Understanding, and II: Systems and application." Journal of Computing in Civil Engineering. ASCE. 8(Z), 131 -162. 1994
- Kellogg & Kimsey, Inc website, www.kelloggkimsey.com/2008.
- Lowe, D. J. Experiential learning in design cost estimating. Ph.D. thesis, UMIST. 1996

- Mohamed A, Celik T. "Knowledge based-system for alternative design cost estimating and scheduling." Knowledge Based Systems, USA. 2002
- R.S. Means "Building Construction Cost Data". R.S. Means Company Inc., Kingston, MA. 1997
- Skitmore, M., Stradling, S., Tuohy, A. and Mkwezalamba, H. "The Accuracy of Construction Price Forecasts," University of Salford, Manchester. 1990
- US. Department of Defense. "Parametric Cost Estimating Handbook." Department of Defense, United States of America. Arlington, VA, USA. 1995
- William R. Duncan. "A guide to the project management body of knowledge", Project Management Institution, USA. 1996

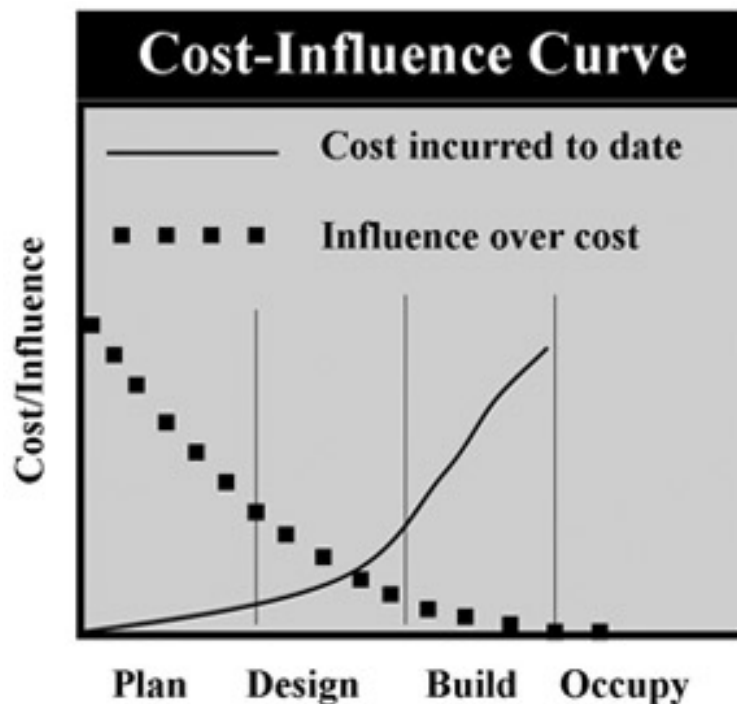


Fig. 1: Cost-Influence Curve

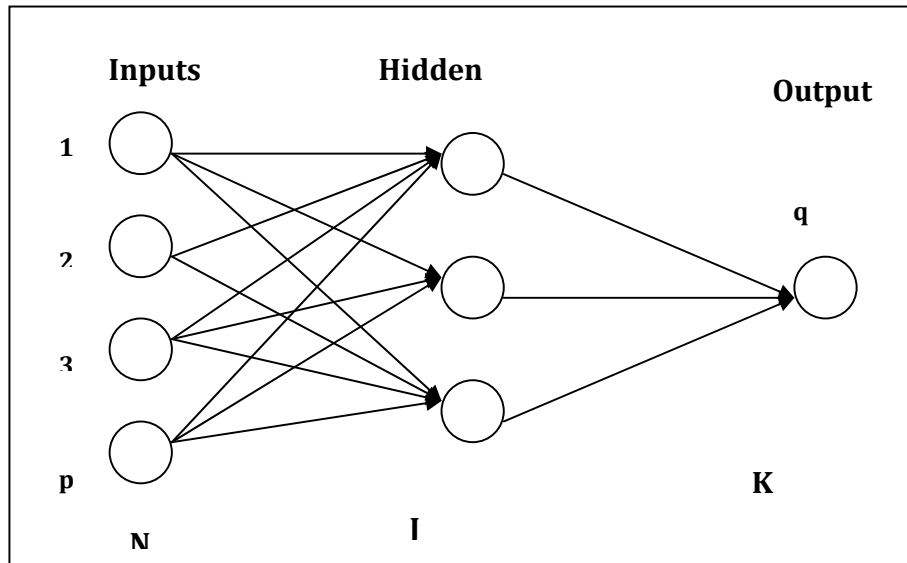


Fig. 2: Feed-Forward neural network

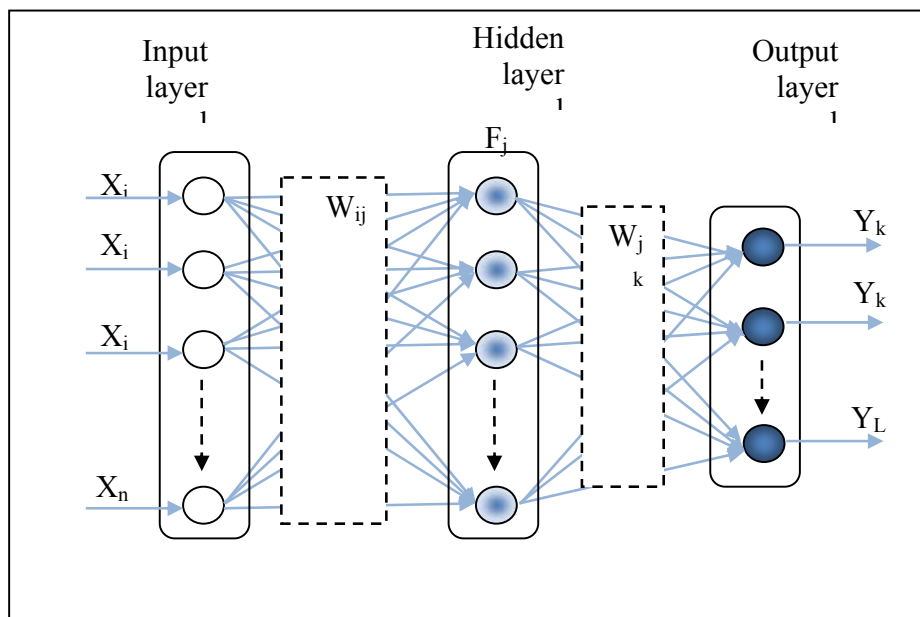


Fig. 3: Neural network structure



Table 1: 8-key parameters for network input layer

Design Parameter	Definition	Range
X1	Country	Iraq, Lebanon, KSA, Egypt, Qatar and Others
X2	Date	1996-2016
X3	Type of Building	HRAP (0), Hotel (1)
X4	Gross Floor Area	8500-113000 m ²
X5	No. of Floors in Basement	1-5
X6	No. of Floors in Podium	1-3
X7	No. of Floors Upper level	5-40
X8	Total No. of Rooms or Apartments	24-1735

Table: 2 Sample of projects data

	Project Name	Location	Date	GFA m2	Basement floors	Podium Floors	Tower Floors	No. of Rooms
1	Grand Hyatt Hotel Beirut	Lebanon	2009	54,541	5	3	8	402
2	Al Khojah Tower Jaddah	Saudi Arabia	2001	21,741	1	2	12	24
3	Doha Intercontinental Hotel	Qatar	1999	27,000	2	3	6	300
4	Hilton International Hotel Hurghada	Egypt	1996	22,152	2	3	12	225

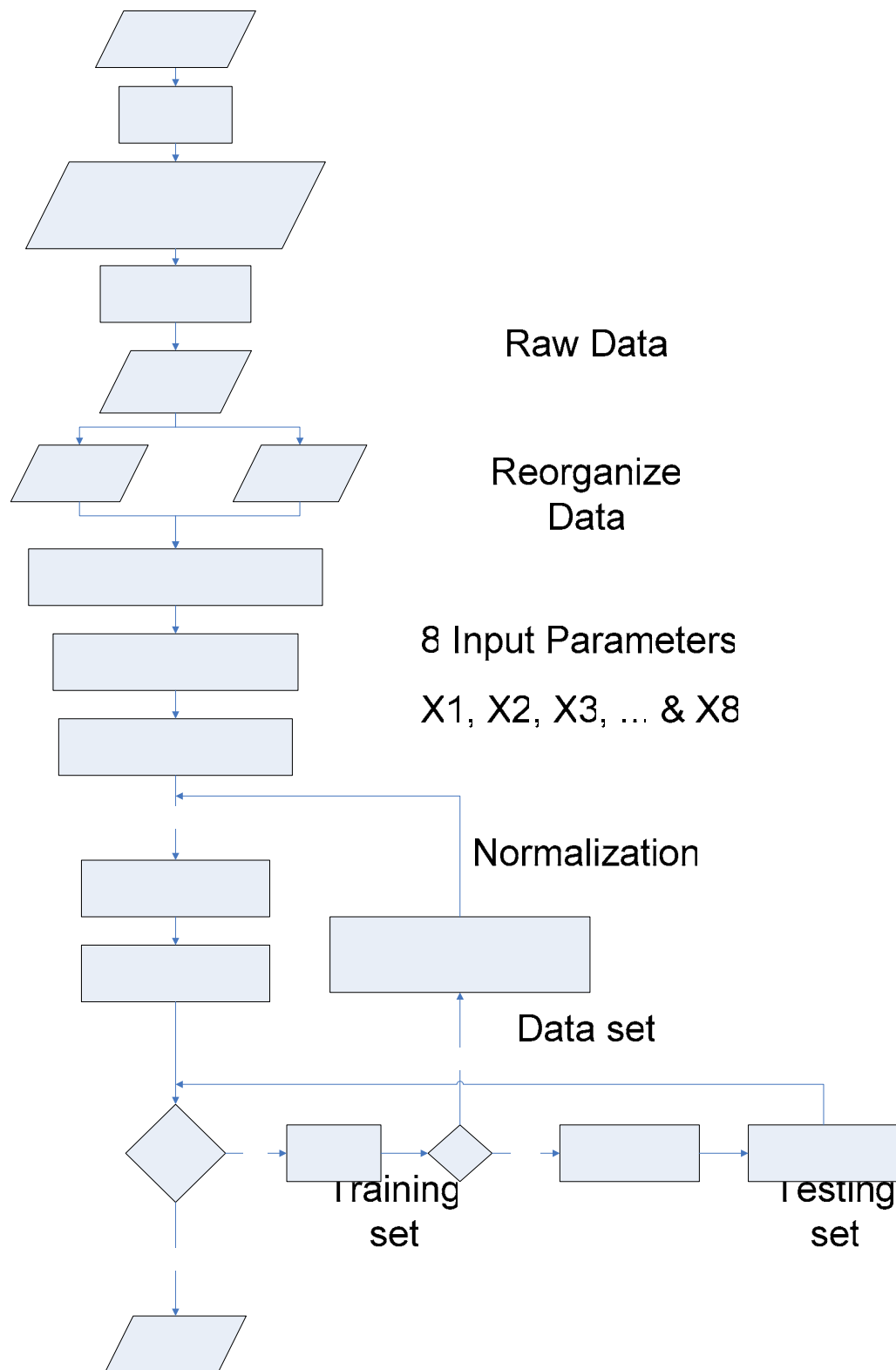


Fig. (4): Flow chart for developing new network
Upload data to Matlab Software

**Table 3: Results of the five network**

Network	No. of neuron in Input(N): Hidden(J): Output(K)	MAPE %
Total building	8:14:1	1.51
Plumbing	8:18:1	4.627
Hvac	8:10:1	3.604
Fire protection	8:12:1	4.771
Electrical	8:8:1	2.99



EXPERIMENTAL STUDY OF FRICTION STIR SPOT WELDING FOR BRASS ALLOY(426/1CUZN10)

Qasim M. Doos

Department of Mechanical engineering, College of Engineering ,University of Baghdad

Harith H. Abdullah

NASSER Company ,Ministry of Industry and mineral.

ABSTRACT

Friction stir spot welding (FSSW) is a promising solid state joining process and is widely being considered for automotive industry. In this work mechanical properties of friction stir spot welded joints were investigated for ISO(426/1CuZn10) copper alloy. The effect of main welding parameters were studied including, welding tool rotational speed, preheat time (15, 30)s , plunging time (10,30)s , dwell time 10 s ,plunging depth (0.7,0.8) mm. Group of matrices of welding parameters were used to study the effect of each parameter on properties of welded joints. Series of (FSSW) experiments were conducted using manual drilling machine.

Effect of welding parameters on mechanical properties of welded joints were investigated using tensile shear test. Micro-hardness test used to indicate the changes in hardness across welding region. Based on the welding experiments conducted in this study, the results show that copper alloy (426/1CuZn10) was easy weldable using (FSSW) process with maximum failure load (420 N) at (2000 rpm) rotating speed and (70 s) total time for (0.5 mm) sheet thickness.

دراسة تجريبية لطريقة اللحام بالاحتكاك والخلط الموقعي لسبيكة براس (246/1CuZn10)

الخلاصة

اللحام بالاحتكاك والخلط الموقعي من طرق لحام الحالة الصلبة الواعدة التي تستخدم بشكل واسع في صناعة السيارات. في هذا العمل تم دراسة وتحري الخواص الميكانيكية للحام الاحتكاك والخلط الموقعي لسبيكة النحاس (426/1CuZn10). تم دراسة تأثير العوامل الرئيسية للحام المتضمنة سرعة الدوران وزمن التسخين الابتدائي (15، 30) ثانية وزمن سرعة الاختراق (10، 30) ثانية وزمن الانتظار 10 ثانية وعمق الاختراق (0.7، 0.8) ملم.

تم دراسة مجموعات من المصفوفات المتضمنة عوامل اللحام ودراسة تأثير كل من هذه العوامل على خواص اللحام. تم تصنيع عدة خاصة باللحام وتم اجراء هذه التجارب بواسطة ماكينة تنقيب يدوي.

تأثير عوامل اللحام على الخواص الميكانيكية تمت دراستها بواسطة اختبار الشد القصي. اختبار الصلادة تم اجراءه لملاحظة التغير في الصلادة عبر منطقة اللحام. بناء على تجارب اللحام في هذه الدراسة ظهر ان سبيكة النحاس (426/1CuZn10) قابلة للحام باستعمال هذه الطريقة (اللحام بالخلط والاحتكاك الموقعي) مع اكبر حمل للفشل بلغ 420 نيوتن عند سرعة 2000 دورة/دقيقة وزمن كلي 70 ثانية لصفائح سمكها 0.5 ملم.

KEYWORDS: Friction, Stir, Spot, Welding, Brass, 426/1CuZn10, Qasim, Doos, Harith, FSSW.

INTRODUCTION

The FSSW process consists of three phases; plunging, stirring, and retraction. The process starts with spinning the tool and slowly plunging it into a weld spot until the shoulder contacts the top surface of work piece. Then, the stirring phase enable the materials of two work pieces mix together. Lastly, once a predetermined penetration is reached, the process stops and the tool retract from the work piece. The resulting weld has a characteristic hole in the middle of the joint [Scheme et al 2005]. Show Fig.1.

Tools consist of a shoulder and a probe which can be integral with the shoulder or as a separate insert possibly of a different material. The design of the shoulder and of the probe is very important for the quality of the weld. The probe of the tool generates the heat and stirs the material being welded but the shoulder also plays an important part by providing additional frictional treatment as well as preventing the plasticised material from escaping from the weld region. The plasticized material is extruded from the leading to the trailing side of the tool but is trapped by the shoulder which moves along the weld to produce a smooth surface finish [Cemal, 2005].

Welding of brass is usually difficult by conventional fusion welding processes because the brass has the high thermal diffusivity, which is about 10–100 times higher than in many steels and nickel alloys. Brass materials, as known, are copper (Cu) and zinc (Zn) alloys. The welding temperature, for example in the TIG welding, reaches almost 4200 °C in the electrode (cathode) and nearly 3200 °C in the work piece (anode) during welding. These temperatures exceed both the melting and boiling temperatures of both copper (1083 °C) and zinc (419 °C). In addition, the melting temperature of zinc oxide occurs as a result of zinc evaporation is 1907 °C. For this reason, during welding it is possible for zinc and copper to evaporate from the work piece [Cemal, 2005].

Weldability varies inversely with electrical and thermal conductivities. Welds of moderate quality can be obtained on very thin metal, but it is generally not practicable to attempt the spot welding of copper. The high conductivity of copper dissipates power input throughout the work, instead

of concentrating it to produce useful heat [L. Phillis, 1960].

The main objective of present work is Study caplibility of friction stir spot welding process to weld poor weldability materials such as brass (by conventional welding process), obtain the best procedures for this process and study the effect of welding parameters (rotating speed rate, plunging rate, dwell time and plunging depth) in the weld strength.

EXPERIMENTAL WORK

The experimental work involves the procedures for friction stir spot welding of brass alloy. Drilling machine was used to get these joints by using steel tool with different welding parameters. Tensile shear tests are carried out to evaluate the maximum shear force (i.e. strength) of weld joints. The material used in this work was copper alloy (90% Cu 10% Zn), its chemical composition as shown in **Table (1)**. Properties of metal measured by tensile test and their as shown in **Table (2)**. This alloy is difficulty in welding by conventional spot welding processes. Sheets cut as rectangular shape; their long and width according to ASTM [T.B. JEFFERSON, 1951], standard dimensions of spot weld test specimens. 0.5 mm thickness sheet used and it was useful because the available machine has small power capacity which cannot use for high thickness. Single sheet have dimension 16 x 76 mm comparing with steel and aluminum alloy show Fig. 2. Machine used in this work was drill which has variable speed range (500 to 3000 rev/min). Tool was made from tool steel, tool dimension as shown in Fig. 3.

Many experiments had been done before set good procedure for welding a brass. Procedures involved the following step: Preheat Step :This step not recorded in literatures, but many experiments in this study showed preheat step is essential step. A tool dwells many seconds to heat sheets by friction. We can call this time "Preheat time". To carry out FSSW process, two brass plates, 0.5 mm in thickness, 76 mm length and 16 mm in width. These two brass plates were then placed one on another and clamped with a vice so that they would not separate during welding process. During the



experiments it had been used a drill machine which has high rotation speed to rotate stirrer tip. The stirrer was made by special hot working steel. Length of stirrer tip had been chosen 0.8 % from total thickness of material to obtain better stirring effect. The welds were made on one side using three combinations of tools rotation speed; preheat time and plunging time where each test result was obtained from the average of three tests. Considering previous works the welding process was carried out by rotating the stirrer at rang from 1000 to 2000 rpm and by plunging the plates at various speeds under a constant friction force. Two values used for each parameter (only rotating speed 3 values taken) to experiments its effect on welding force due to values of tensile test for samples were very near and testing devices not have high accurate. By using the predetermined welding parameters, three different samples were welded for mechanical tests. Tension and hardness measurements were made as mechanical tests. Other specimens welded for study effect of plunging depth. Two various depths (0.7, 0.8 mm) are used. Tensile specimens were preparation according to ASTM. Tensile shear test was used to measure tensile shear force (or strength) which used for spot welding. Microhardness testing for spot welded joint was carried out across welding region. The type of microhardness tester was "Micromet" in mechanical department.

RESULT AND DISCUSSION

From experiments, welds joints failed when rotating speed was 600 rpm or less. When rotating speed less than appointed value, the generating heat will be not enough to stir and mix operation. Welding occur when temperature of metal reach 0.8 of melting temperature of welding metal. Results show direct relation between rotating speed rate with welds joint force, show Fig.4.

Use low rotating speed rate and more preheat time and plunging time allow to generating more heat, and metal mixing, results are shown in Fig. 5. Preheat time allow to rise temperature of brass where ductility increase too ,so recrystallian of grain occur at this state mixing operation became ready at stir step.

At plunging time equal to 30 second welding process passes as shown in Fig. 6 at three values of

rotating speed. 420 N force occur at 30 second preheat while 340 N force at 15 second. Weld shear force increases with plunging time, show Fig. 7. Weld shear force increases from 160 N at 10 second to 340 N at 30 second. Long plunging time allows to efficient mixing of metal.

Decrease in shear force at rotating speed 2000 rpm with dwell time 20 s may be occur due to enlarge of grain size, force decreases with grain size. Plunging depth increases 0.1 mm from 0.7 to 0.8 as shown in Fig. 8.

That cause rise in welding force from 180 to 250 N. Increasing plunging depth improve weld force by increase volume of mixing metal in welding region ,show Fig. 9. Welding process failed at 15 s preheat time with 10 s plunging time while welding joint done at 15 s preheat and 15 s plunging time for same rotating speed. That is mean a last parameters represent critical point for welding operation. Microhardness test was done on top surface of spot weld joint according points 0,1,2,3 as shown in Fig. 10. Results of Microhardness test is shown in fig. 11.

CONCLUSION

According to results of the present study for FSSW process on selected copper alloy, several conclusions can be written regarding alloy weldability and mechanical properties.

- Poor weldability alloys by conventional spot welding process as copper alloy (426/1CuZn 10) can be welded using different (FSSW) parameters giving different welding results.
- Preheat dwell time is very effective parameter on the welding process for high thermal conductivity alloys and small thickness.
- Main welding parameters affected joints strength are tool rotating speed and plunging depth of tool.
- It was found that there is direct relation between above parameters and strength of joints. Total time for welding process is more effective parameter than other.

- The maximum weld force obtained was (420N) for sheet thickness (0.5 mm) with rotating speed 2000 rpm and total time 70 s.
- The microhardness in welding region was 97 HV higher than shoulder region 76 HV and base metal 67 HV.

REFERENCES

- Cemal Meran , The joint properties of brass plates by friction stir welding, ,Mechanical Engineering Department, Engineering Faculty, Pamukkale University, Turkey ,5 May 2005.
- L. Phillis, welding handbook, fourth edition, section four ,metals and their

weldability, AMERICAN WELDING SOCIETY.,671.52,a512 1960.

- Scheme M. Awang, V. H. Mucino et al ,Thermo-Mechanical Modeling of Friction Stir Spot Welding (FSSW) Process, West Virginia University, Copyright © SAE International (2005).

- T.B. JEFFERSON. et al, the welding encyclopedia, thirteenth edition, McGRAW-HILL 1951.

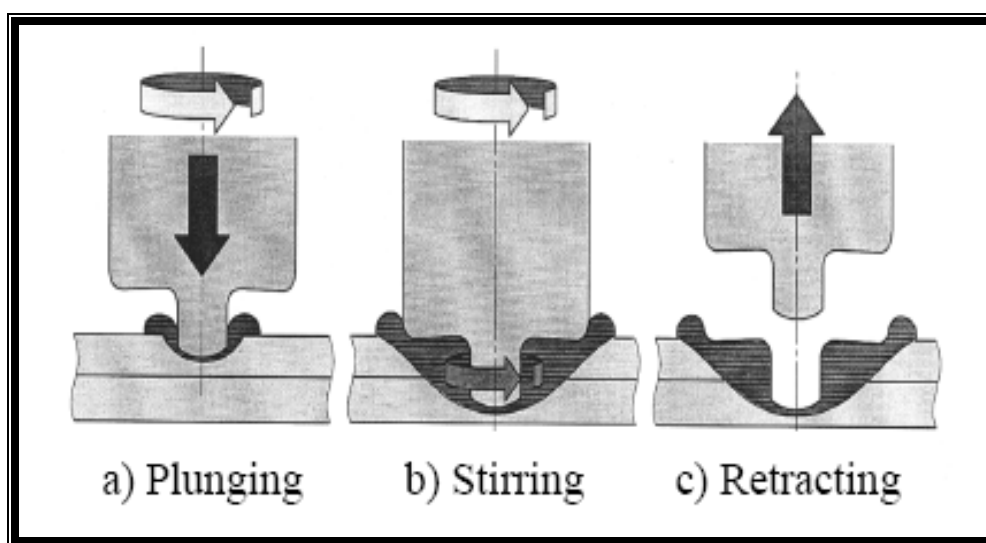


Fig. (1): Three stages of friction stir spot welding process [Cemal, 2005].

Table (1): Chemical Composition for Brass Alloy.

Material type	426/1CuZn 10
Chemical composition	90% Cu 10% Zn



Table (2): Mechanical Properties of Brass Alloy

Ultimate strength	290 N/ mm²
Elongation	46 %
Hardness	67 HV

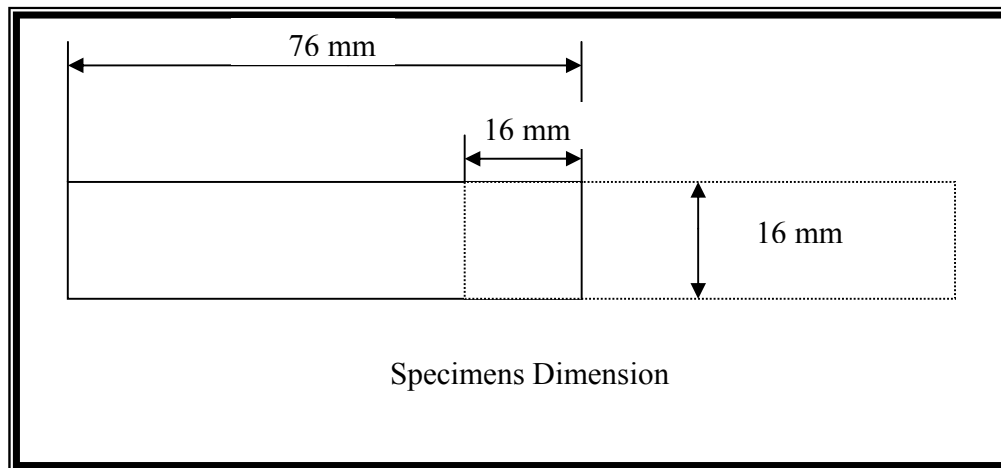


Fig.(2) : Specimen Dimensions

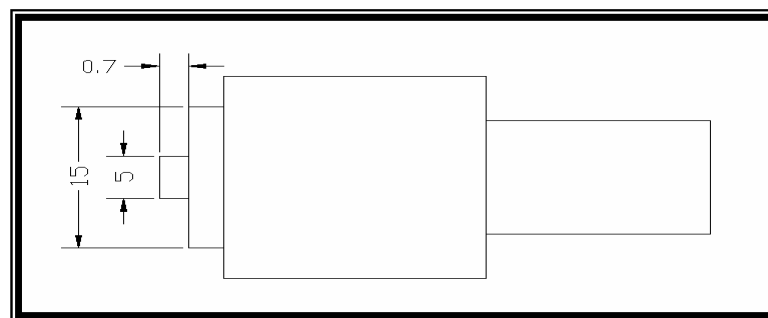


Fig.(3) : Tool Dimensions (mm).

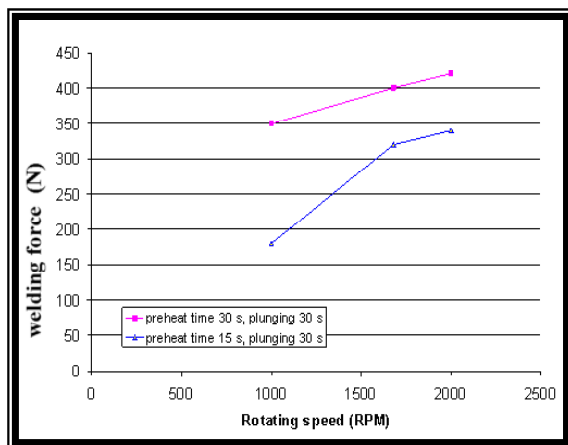


Fig. (4): Effect of Rotating Speed on Weld Shear Force at Constant Plunging

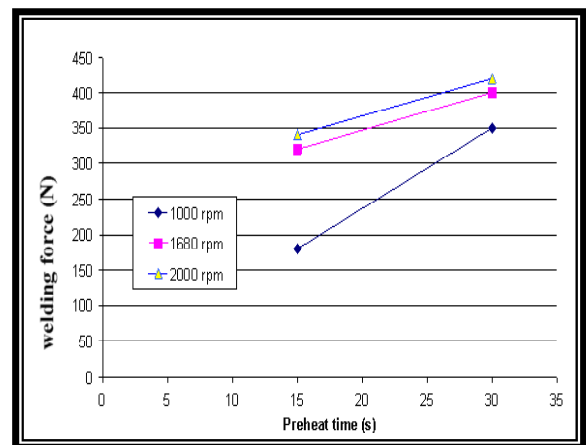


Fig. (5): Effect of Preheat Time on Welds Forces with Constant Plunging Time Equal to 30 Second.

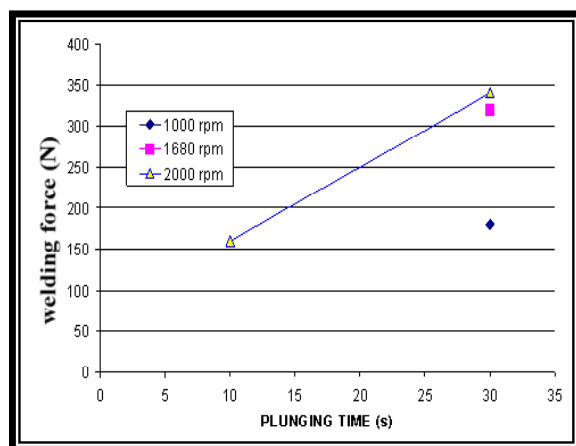


Fig. (6): Weld Force vs. Plunging Time at Constant Preheat Time 15 Second.

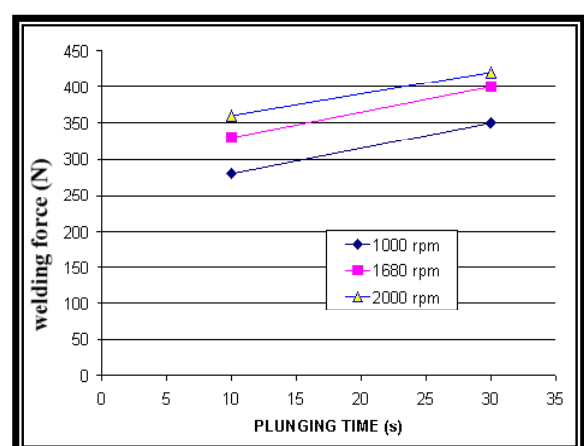


Fig. (7): Weld Forces vs. Plunging Time at Constant Preheat Time 30 Second.

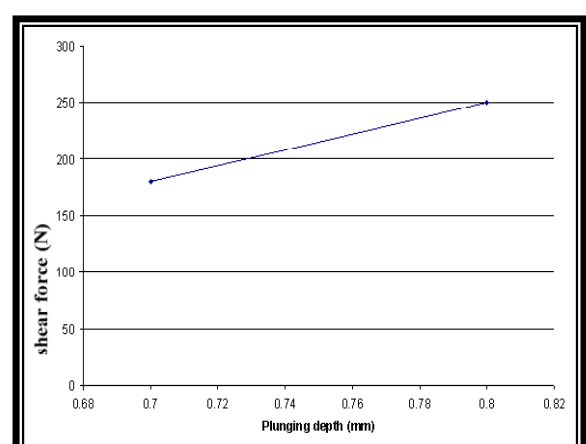
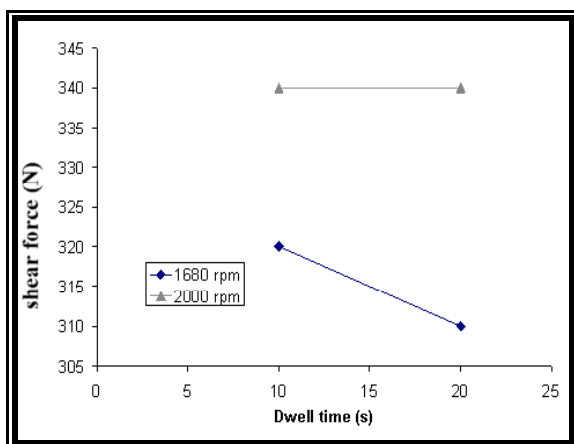


Fig. (8): Effect of Dwell Time on Shear Force of Welds.

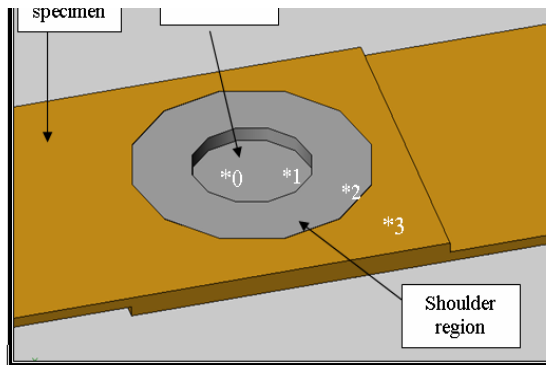


Fig. (10): Points measured by microhardness test

Fig. (9): Effect of Plunging Depth on Shear Force of Welds.

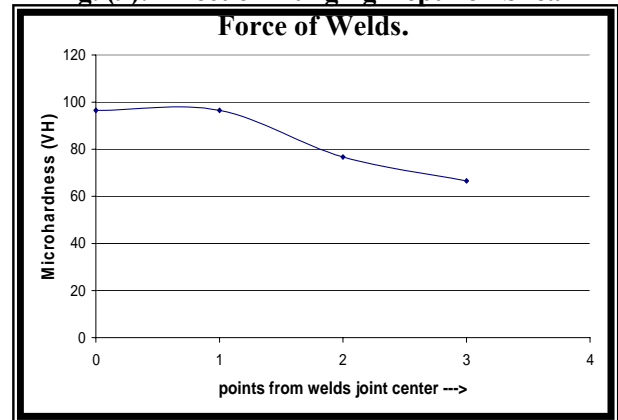


Fig. (11): Microhardness values across welds joint area.



NATURAL CONVECTION IN CONFINED CYLINDRICAL ENCLOSURE OF POROUS MEDIA WITH CONSTANT AND PERIODIC WALL TEMPERATURE BOUNDARY CONDITIONS

Prof.Dr. Ihsan Y. Hussain
Mech. Engr. Dept.
College of Engineering
University of Baghdad
Baghdad-Iraq.

Mohammad Mahdie Saleh
M.Sc. Student
Mech. Eng. Dept.

ABSTRACT

Numerical investigations of unsteady natural convection heat transfer through a fluid-saturated porous media in inclined cylindrical enclosure are studied by solving the governing (3-D) Darcy-Boussinesq equations using finite difference method. The momentum equation of flow was solved by Relaxation method and the energy equation by using Alternating Direction Implicit (ADI) method. The problem is analyzed for modified Rayleigh number with range of (50-300), angles of inclination ($0^\circ, 25^\circ, 45^\circ, 60^\circ, 90^\circ$), amplitude of sinusoidal temperature (0.2, 0.4, 0.8) and period (0.005, 0.01, 0.02). Results indicate an increase in the heat transfer with increasing of Rayleigh number, time, amplitude, angle of inclination and period. Also average and local Nusselt number were calculated and it is found that Maximum temperature and velocity occur at angle $\alpha=45$ and this indicate a strong buoyancy force effect on convective flow.

(Darcy-Boussinesq equation)

(300-50)

.(ADI)

.(0.02 0.01 0.005)

(0.8 0.4 0.2)

($90^\circ 60^\circ 45^\circ 25^\circ 0^\circ$)

(45)

KEYWORD(S): Natural Convection; Cylindrical Enclosure; Porous Media; Sinusoidal Temperature Variation.

INTRODUCTION

Natural convection heat transfer in fluid-saturated porous media is a research topic of practical importance due to the many practical applications which can be modeled or approximated as transport phenomena in porous media, these flows appear in a wide variety of industrial application, as well as in many natural

circumstances such as ground water flows, oil recovery processes, thermal insulation engineering, food processing, casting and welding of manufacturing processes, etc. Representative reviews of these applications and others convective heat transfer applications in porous media may be found in the recent books by

(Ingham and Pop 1998), (Nield and Bejan 1999), and (Vafai and Hadim 2000), (Mohammad and Nawaf, 2005). Many studies were reported which deals with porous media, (Wang and Zhang, 1990) studied three-dimensional steady natural convection in an inclined liquid-saturated porous concentric cylinders for different variables. (Shivakumara et.al., 2002) studied numerically transient free convection in a vertical cylindrical annulus filled with a fluid saturated porous medium with $T_i > T_o$ while the top and bottom boundaries are adiabatic, a finite difference ADI and Successive Line Overrelaxation are used to solve the governing equations. (Iyer and Vafai, 1999) analyzed numerically free convection fluid flow and heat transfer in a horizontal cylindrical annulus in the presence of a porous geometric perturbation, the flow in the porous region is modeled using Brinkman-Forchheimer-Darcy model and the governing equations is modeled as (3-D) and solved numerically using Galerkin method of the finite element formulation. (Mohammad, 2008) studied natural convection in cylindrical enclosure of porous medium with constant and periodic wall temperature boundary conditions, the flow is modeled using Darcy model and the governing equations is solved numerically using finite difference method. Also there are studies for Cartesian enclosures such as (Wajeih, 2006) who studied transient 3-D natural convection in confined porous media with periodic boundary conditions numerically and experimentally, the effect of the oscillating surface temperature on the fluid flow and heat transfer within the enclosure were determined. The purpose of the present paper is to study the natural convection flow behavior and its effects on the heat transfer and temperature distribution within a cylindrical enclosure filled with saturated porous medium and which is inclined by angle α from the horizontal, also velocity distribution and Nusselt number will be explained.

MATHEMATICAL MODEL

A schematic representation of the system under investigation is shown in Fig.(1). The cylindrical system of coordinates (r, ϕ, z) is represented. The system is inclined with angle (α) from the horizontal so, the gravitational acceleration (g) acts in the negative (r, z) directions and positive (ϕ) direction as shown in Fig.(1)

The (3-D) cylindrical space contains a porous material of permeability (K) and porosity (\mathcal{E}) which is saturated with a Boussinesq fluid of viscosity (ν) and coefficient of thermal expansion (β) .

From Fig.(1) the components of gravity can be written as follows;

$$\vec{g} = g_r \vec{i} + g_\phi \vec{j} + g_z \vec{k} \quad (1)$$

$$\left. \begin{aligned} g_r &= -g \sin(\alpha) \cos(\phi) \\ g_\phi &= g \sin(\alpha) \sin(\phi) \\ g_z &= -g \cos(\alpha) \end{aligned} \right\} \quad (2)$$

By substituting the three components in eqs.(1)

$$\vec{g} = -g \sin(\alpha) \cos(\phi) \vec{i} + g \sin(\alpha) \sin(\phi) \vec{j} - g \cos(\alpha) \vec{k} \quad (3)$$

The equations which describe the problem of natural convection in cylindrical enclosure are mass, momentum, and energy equations (Bejan, 1984);

$$\text{C.E} \quad \frac{1}{r} \frac{\partial}{\partial r}(ru) + \frac{1}{r} \frac{\partial v}{\partial \phi} + \frac{\partial w}{\partial z} = 0 \quad (4)$$

And from Darcy law for momentum the three components (r, ϕ, z) with the effect of gravity are as follows;

r -component

$$u = \frac{K}{\mu_f} \left(-\frac{\partial p}{\partial r} + \rho_f g_r \right) = \frac{K}{\mu_f} \left(-\frac{\partial p}{\partial r} - \sin(\alpha) \cos(\phi) \rho_f g \right) \quad (5)$$

ϕ -component

$$v = \frac{K}{\mu_f} \left(-\frac{1}{r} \frac{\partial p}{\partial \phi} + \rho_f g_\phi \right) = \frac{K}{\mu_f} \left(-\frac{1}{r} \frac{\partial p}{\partial \phi} + \sin(\alpha) \sin(\phi) \rho_f g \right) \quad (6)$$

z -component

$$w = \frac{K}{\mu_f} \left(-\frac{\partial p}{\partial z} + \rho_f g_z \right) = \frac{K}{\mu_f} \left(-\frac{\partial p}{\partial z} - \cos(\alpha) \rho_f g \right) \quad (7)$$

E.E

$$(\rho c_p)_m \frac{\partial T}{\partial t} + (\rho c_p)_f \left[u \frac{\partial T}{\partial r} + \frac{v}{r} \frac{\partial T}{\partial \phi} + w \frac{\partial T}{\partial z} \right] = K_m^* \left(\frac{1}{r} \frac{\partial}{\partial r} \left(r \frac{\partial T}{\partial r} \right) + \frac{1}{r^2} \frac{\partial^2 T}{\partial \phi^2} + \frac{\partial^2 T}{\partial z^2} \right) \quad (8)$$

In order to write the basic equations and variables in dimensionless form, the following factors and scales are introduced.

D : Diameter, α_m / D : velocity, ΔT_o : temperature, amplitude

$$\frac{(\rho c_p)_m D^2}{K_m^*}: \text{time}, \quad \frac{\alpha_m \mu_f}{K}: \text{pressure}, \quad \frac{D^2}{\left(\frac{K_m^*}{(\rho c_p)_m} \right)}:$$

period

Now we shall define the new dimensionless variables as;

$$R = \frac{r}{D}, Z = \frac{z}{D}, U = \frac{uD}{\alpha_m}, V = \frac{vD}{\alpha_m}, W = \frac{wD}{\alpha_m}, \tau = \frac{t}{(\rho c_p)_m D^2 / K_m^*}, P = \frac{p}{\alpha_m \mu_f / K}, a = \frac{A}{\Delta T_o}, \theta = \frac{T - T_o}{\Delta T_o}, \eta = \frac{\text{per}}{D^2 / \left(\frac{K_m^*}{(\rho c_p)_m} \right)} \quad (9)$$

The dimensionless form for the basic equations is obtained by substituting the above factors in eqs.(4-8) and the corresponding form of the governing equations in vector form will be as follows;

$$\nabla \cdot \vec{V} = 0 \quad (10)$$

$$\vec{V} = -\nabla \vec{P} + \frac{KDg}{v_f \alpha_m} \begin{bmatrix} -\sin(\alpha)\cos(\phi) \\ \sin(\alpha)\sin(\phi) \\ -\cos(\alpha) \end{bmatrix} + \quad (11)$$

$$R_a \theta \begin{bmatrix} \sin(\alpha)\cos(\phi) \\ -\sin(\alpha)\sin(\phi) \\ \cos(\alpha) \end{bmatrix}$$

$$\frac{\partial \theta}{\partial \tau} + \vec{V} \cdot \nabla \theta = \nabla^2 \theta \quad (12)$$

Where: $R_a = \frac{g\beta K \Delta T_o D}{v_f \alpha_m}$ = Modified Rayleigh number for porous medium

Since $\frac{KDg}{v_f \alpha_m} = c = \text{constant}$ so, eqs.(11) will be

$$\vec{V} = -\nabla \vec{P} + c \begin{bmatrix} -\sin(\alpha)\cos(\phi) \\ \sin(\alpha)\sin(\phi) \\ -\cos(\alpha) \end{bmatrix} + \quad (13)$$

$$R_a \theta \begin{bmatrix} \sin(\alpha)\cos(\phi) \\ -\sin(\alpha)\sin(\phi) \\ \cos(\alpha) \end{bmatrix}$$

Now by introducing a vector potential (Φ) of the form

$$\vec{V} = \nabla \times \Phi \quad (14)$$

Into the formulation, the resulting equations may be solved numerically faster and more accurately. This vector potential satisfies identically the continuity equation. The potential is also solenoidal since the velocity is solenoidal (incompressible flow) (Wajeeth, 2006).

$$\nabla \cdot \vec{V} = \nabla \cdot (\nabla \times \Phi) = 0 \quad (15)$$

$$\text{So, } \nabla \cdot \Phi = 0 \quad (16)$$

$$\frac{1}{R} \frac{\partial (R\Phi_R)}{\partial R} + \frac{1}{R} \frac{\partial \Phi_\phi}{\partial \phi} + \frac{\partial \Phi_Z}{\partial Z} = 0 \quad (17)$$

Taking the curl of eqs.(13);

$$\nabla \times \vec{V} = \nabla \times (-\nabla \vec{P}) + \nabla \times (ca) + \nabla \times (R_a \theta b) \quad (18)$$

Where:

$$a = \begin{bmatrix} -\sin(\alpha)\cos(\phi) \\ \sin(\alpha)\sin(\phi) \\ -\cos(\alpha) \end{bmatrix}, \quad b = \begin{bmatrix} \sin(\alpha)\cos(\phi) \\ -\sin(\alpha)\sin(\phi) \\ \cos(\alpha) \end{bmatrix}$$

And introducing eqs.(14) and (16) and by solving the resulting equations, this yield the following set of equations;

$$\nabla^2 \Phi_R = \left(\frac{1}{R} \frac{\partial \theta}{\partial \phi} \cos(\alpha) + \frac{\partial \theta}{\partial Z} \sin(\alpha) \sin(\phi) \right) R_a \quad (19)$$

$$\nabla^2 \Phi_\phi = \left(\frac{\partial \theta}{\partial Z} \sin(\alpha) \cos(\phi) - \frac{\partial \theta}{\partial R} \cos(\alpha) \right) R_a \quad (20)$$

$$\nabla^2 \Phi_Z = \left(-\frac{1}{R} \frac{\partial R \theta}{\partial R} \sin(\alpha) \sin(\phi) - \frac{1}{R} \frac{\partial \theta}{\partial \phi} \sin(\alpha) \cos \phi \right) R_a \quad (21)$$

The left hand side of the above three equations can be obtained as follows (**Hiroiyuki 1981**)

$$\vec{\Omega} = \nabla \times \vec{V} = \nabla \times (\nabla \times \vec{\Phi}) = \nabla (\nabla \cdot \vec{\Phi}) - \nabla^2 \vec{\Phi} = -\nabla^2 \vec{\Phi} \quad (22)$$

Where $\vec{\Omega}$ represents vorticity

$$\text{Thus, } -\vec{\Omega} = \nabla^2 \vec{\Phi} \quad (23)$$

$$-\nabla^2 \Phi_Z = \frac{\partial^2 \Phi_Z}{\partial R^2} + \frac{1}{R} \frac{\partial \Phi_Z}{\partial R} + \frac{1}{R^2} \frac{\partial^2 \Phi_Z}{\partial \phi^2} + \frac{\partial^2 \Phi_Z}{\partial Z^2} \quad (24)$$

$$-\nabla^2 \Phi_R = \frac{\partial^2 \Phi_R}{\partial R^2} + \frac{1}{R^2} \frac{\partial (R \Phi_R)}{\partial R} + \frac{2}{R} \frac{\partial \Phi_R}{\partial R} + \frac{1}{R^2} \frac{\partial^2 \Phi_R}{\partial \phi^2} + \frac{\partial^2 \Phi_R}{\partial Z^2} + \frac{2}{R} \frac{\partial \Phi_Z}{\partial Z} \quad (25)$$

$$-\nabla^2 \Phi_\phi = \frac{\partial^2 \Phi_\phi}{\partial R^2} + \frac{1}{R} \frac{\partial \Phi_\phi}{\partial R} - \frac{\Phi_\phi}{R^2} + \frac{1}{R^2} \frac{\partial^2 \Phi_\phi}{\partial \phi^2} + \frac{\partial^2 \Phi_\phi}{\partial Z^2} + \frac{2}{R^2} \frac{\partial \Phi_R}{\partial \phi}$$

The hydrodynamic and thermal boundary conditions for the problem are;

$$\Phi_R = \Phi_Z = \frac{\partial \Phi_\phi}{\partial \phi} = 0 \quad \text{at } \phi = 0, \pi \quad (26)$$

$$\Phi_R = \Phi_\phi = \frac{\partial \Phi_Z}{\partial Z} = 0 \quad \text{at } Z = 0, L \quad (27)$$

$$\Phi_Z = \Phi_\phi = \frac{\partial (R \Phi_R)}{\partial R} = 0$$

$$\text{at } R = R(\text{wall}) \quad (28)$$

And due to symmetry

$$\frac{\partial \Phi_R}{\partial R} = \frac{\partial \Phi_\phi}{\partial R} = \frac{\partial \Phi_Z}{\partial R} = 0 \quad \text{at } R = 0 \quad (29)$$

For the temperature field, the non-dimensional thermal boundary conditions are

$$\frac{\partial \theta}{\partial \phi} = 0 \quad \text{at } \phi = 0, \pi \quad (30)$$

$$\frac{\partial \theta}{\partial Z} = 0 \quad \text{at } Z = 0, L \quad (31)$$

And due to symmetry

$$\frac{\partial \theta}{\partial R} = 0 \quad \text{at } R = 0 \quad (32)$$

For the wall boundary, two cases for the cylinder temperature will be considered:

Case (1): constant wall temperature

$$\theta = 1 \quad \text{at } R = R(\text{wall}) \quad (33)$$

Case (2): the temperature of the side wall varies sinusoidally with time about a mean value ($\bar{\theta}$) with amplitude (A) and period (per), as graphically depicted in **Fig.(2)**

$$\theta = 1 + a \sin\left(\frac{2\pi\tau}{\eta}\right) \quad \text{at } R = R(\text{wall}) \quad (34)$$

The initial conditions for the problem are;

Case (1): The flow is started at time ($\tau = 0$) so,

$$\theta = U = V = W = \Phi_R = \Phi_\phi = \Phi_Z = 0 \quad \text{everywhere} \quad (35)$$

Case (2): To minimize the number of cycles that are necessary for the solution to become periodic, we began all the simulations starting from an initial temperature and flow field, and applying equation (34) with known period and amplitude we will obtain on the periodic solution (**Mohammad, 2008**).

The local and average Nusselt number for the cylinder surfaces are defined respectively as;

$$Nu = -\frac{\partial \theta}{\partial R} \Big|_{R=R(\text{wall})} \quad (36)$$

$$Nu = -\frac{2D}{\pi L} \int_0^\pi \int_0^L \frac{\partial \theta}{\partial R} \Big|_{R=R(\text{wall})} dZ R d\phi \quad (37)$$

The components of the dimensionless velocity are related to the components of the dimensionless vector potential as follows;

$$\left. \begin{aligned} U &= \frac{1}{R} \frac{\partial \Phi_Z}{\partial \phi} - \frac{\partial \Phi_\phi}{\partial Z} \\ V &= \frac{\partial \Phi_R}{\partial Z} - \frac{\partial \Phi_Z}{\partial R} \\ W &= \frac{1}{R} \frac{\partial (R \Phi_\phi)}{\partial R} - \frac{1}{R} \frac{\partial \Phi_R}{\partial \phi} \end{aligned} \right\} \quad (38)$$

NUMERICAL FORMULATION

The above equations were approximated by finite-difference methods, the parabolic equations (energy equation) solved using the Alternating Direction Implicit (ADI) method, the Relaxation method were used for solving of elliptic equations (momentum equations). The numerical solution is obtained by dividing the domain of interest into a grid network of several nodes the position of a node on the grid is defined by the indices (i), (j), and (k) which will be used for indicating the points along (r, ϕ , z) directions respectively and the index (n) will be used for indicating the time step. A mesh of (21 x 21 x 21) grid size seemed reasonable and was be used in the present study.

Applying the (ADI) method on the energy equations yields;

i-implicit

$$a_i \theta_{i-1,j,k}^{n+1} + b_i \theta_{i,j,k}^{n+1} + c_i \theta_{i+1,j,k}^{n+1} = d_i f(\theta^n) \quad (39)$$

j-implicit

$$a_j \theta_{i,j-1,k}^{n+2} + b_j \theta_{i,j,k}^{n+2} + c_j \theta_{i,j+1,k}^{n+2} = d_j f(\theta^{n+1}) \quad (40)$$

k-implicit

$$a_k \theta_{i,j,k-1}^{n+3} + b_k \theta_{i,j,k}^{n+3} + c_k \theta_{i,j,k+1}^{n+3} = d_k f(\theta^{n+2}) \quad (41)$$

Applying the Relaxation method on the momentum equations yields;

M.E. in R-component

$$\begin{aligned} & \left(\frac{\theta_{i,j+1,k} - \theta_{i,j-1,k}}{2R_i \Delta \phi} \right) \cos(\alpha) Ra + \left(\frac{\theta_{i,j,k+1} - \theta_{i,j,k-1}}{2\Delta Z} \right) \sin(\alpha) \sin(\phi) Ra \\ & + \left(\frac{\Phi_{R(i+1,j,k)} - 2\Phi_{R(i,j,k)} + \Phi_{R(i-1,j,k)}}{\Delta R^2} \right) + \\ & 3 \left(\frac{\Phi_{R(i+1,j,k)} - \Phi_{R(i-1,j,k)}}{R_i \Delta R} \right) + \frac{\Phi_{R(i,j,k)}}{R_i^2} \\ & + \left(\frac{\Phi_{R(i,j+1,k)} - 2\Phi_{R(i,j,k)} + \Phi_{R(i,j-1,k)}}{R_i^2 \Delta \phi^2} \right) + \\ & \left(\frac{\Phi_{R(i,j,k+1)} - 2\Phi_{R(i,j,k)} + \Phi_{R(i,j,k-1)}}{\Delta Z^2} \right) \\ & + 2 \left(\frac{\Phi_{Z(i,j,k+1)} - \Phi_{Z(i,j,k-1)}}{2R_i \Delta Z} \right) = Error = 0 \end{aligned} \quad (42)$$

M.E. in ϕ -component

$$\begin{aligned} & \left(\frac{\theta_{i,j,k+1} - \theta_{i,j,k-1}}{2\Delta Z} \right) \sin(\alpha) \cos(\phi) Ra \\ & - \left(\frac{\theta_{i+1,j,k} - \theta_{i-1,j,k}}{\Delta R} \right) \cos(\alpha) Ra + \\ & \left(\frac{\Phi_{\phi(i+1,j,k)} - 2\Phi_{\phi(i,j,k)} + \Phi_{\phi(i-1,j,k)}}{\Delta R^2} \right) - \frac{\Phi_{\phi(i,j,k)}}{R_i^2} + \\ & \left(\frac{\Phi_{\phi(i+1,j,k)} - \Phi_{\phi(i-1,j,k)}}{R_i \Delta R} \right) + \left(\frac{\Phi_{\phi(i,j+1,k)} - 2\Phi_{\phi(i,j,k)} + \Phi_{\phi(i,j-1,k)}}{R_i^2 \Delta \phi^2} \right) + \\ & 2 \left(\frac{\Phi_{R(i,j+1,k)} - \Phi_{R(i,j-1,k)}}{2R_i^2 \Delta \phi} \right) + \left(\frac{\Phi_{\phi(i,j,k+1)} - 2\Phi_{\phi(i,j,k)} + \Phi_{\phi(i,j,k-1)}}{\Delta Z^2} \right) = Error = 0 \end{aligned} \quad (43)$$

M.E. in Z-component

$$\begin{aligned} & - \left(\frac{\theta_{i,j+1,k} - \theta_{i,j-1,k}}{2R_i \Delta \phi} \right) \sin(\alpha) \cos(\phi) Ra \\ & - \left(\frac{\theta_{i+1,j,k} - \theta_{i-1,j,k}}{\Delta R} \right) \sin(\alpha) \sin(\phi) Ra - \\ & \frac{\theta_{i,j,k}}{R_i} \sin(\alpha) \sin(\phi) Ra^* + \left(\frac{\Phi_{Z(i+1,j,k)} - 2\Phi_{Z(i,j,k)} + \Phi_{Z(i-1,j,k)}}{\Delta R^2} \right) + \\ & \left(\frac{\Phi_{Z(i,j+1,k)} - 2\Phi_{Z(i,j,k)} + \Phi_{Z(i,j-1,k)}}{R_i^2 \Delta \phi^2} \right) + \\ & \left(\frac{\Phi_{Z(i,j,k+1)} - 2\Phi_{Z(i,j,k)} + \Phi_{Z(i,j,k-1)}}{\Delta Z^2} \right) \\ & + \left(\frac{\Phi_{Z(i+1,j,k)} - \Phi_{Z(i-1,j,k)}}{R_i \Delta R} \right) = Error = 0 \end{aligned} \quad (44)$$

A computer program was developed in Fortran 90 language to perform the numerical solution. The program consists of main program and two-subroutines, in the main program, the first step is input of data then after specifying the initial and boundary conditions of the problem, the vector potential ($\Phi_R, \Phi_\phi, \Phi_Z$) at every grid point in the domain are calculated from an iterative process, then calculate velocities (U, V, W) from ($\Phi_R, \Phi_\phi, \Phi_Z$), after this calculate i,j,k-implicit coefficients (a, b, c, d) for the tridiagonal systems of equations. Then calculate T at every grid point in the domain. After this the local and average Nusselt number will be calculated then printing the results in the last part of the main program. The first subroutine solves the tridiagonal system of equations formed in the calculating of the temperature field while the second subroutine calculates the average Nusselt number. The time implementation of program is between 15 to 70 minutes depending on the studied case and time intervals. The following is the numerical equations which solved by the program.

RESULTS AND DISCUSSION

Numerical results have been obtained for radius $R=0.5$ and length $L=1$, the computations were carried out for only one half of the computational domain due to symmetry about central vertical line. For the first case (constant wall temperature boundary conditions), **Figs.(3 and 4)** shows the isothermal lines and velocity vectors for different Rayleigh number and angle of inclination. It is clear that $\vec{V} = 0$ at both ends and so the velocity and temperature distributions will differ with different cross-sections. Here we choose $Z=1$, for temperature and 0.75 for velocity, as shown an increase in temperature and heat transfer with increase of Ra number and α and the maximum value of temperature and velocity is at $\alpha = 45$ since the gravity vector aligned with the flow and the density imbalance helps the circulation of the fluid inside the enclosure. The ascending and descending flows will causes the movement of convective fluid, this processes caused velocity vectors movement. **Fig.(5)** shows the variation of average Nusselt number with different Ra number and angle of inclination, it is found that as Ra number increase the Nu number increase this indicate a strong buoyancy force and more heat transferred and circulated in the enclosure. **Fig.(6)** shows the distribution of local Nusselt number and as shown the maximum value of local Nu at vertical position, its value increase with increasing Ra number and decrease with increase of (Z) due to effect of boundary layer. For the second case (periodic wall temperature boundary conditions), **Fig.(7)** shows the temperature distribution (isothermal lines) at $Ra = 125$, $Z=1$, different simulations and angle of inclination (**Table 1**) show the values of amplitude and period which will be used in this study. During the first three simulations at fixed period heat transferred to enclosure is very high and increase with increasing amplitude and angle of inclination also the isothermal lines began to deform with increase of amplitude and angle, this deforming in the right side is greater than that in the left side. Hot regions formed in the height right corners and this hot regions increase with increasing amplitude, cross section, Ra , and angle of inclination. At simulation (4) a different behavior appears, the cold layer surrounding the wall, the hot layer confined in the center of enclosure, a regions of high temperature appear and began to move to right side with increase of (α, Z) . at simulations (5) also the behavior

changed, the cold layer surrounding the wall, the hot layer occupies the center of cylinder, thickness of thermal boundary with increase of (Z) and decrease with increase of (α) , the lines of thermal boundary becomes curvilinear with increase of (α) . **Fig.(8)** shows the variation of average Nusselt number with dimensionless time, it is found that that the average Nusselt number along the hot wall varies sinusoidally according to the variation of the hot wall temperature and it increases with increase of amplitude and decrease with increase of period. The value of the Nusselt number at the hot wall fluctuates at the most, from maximum periodic value of $Nu = 1.7$ at $\tau = 0.0015$ to a minimum value of $Nu = -1.99$ at $\tau = 0.00625$, this is for simulation (1), the hot wall Nusselt number is negative over a short duration of the cycle $0.0037 \geq \tau \leq 0.0087$, stating that over this time period there is an overall energy loss or a net heat transfer exiting the enclosure through the hot wall. **Fig.(9)** shows the variation of Nusselt number with time at $Ra (125, 200)$ and $\alpha=45$, there is an increase in Nusselt value with increase Ra number. By comparing the average Nusselt number in this case with the case of constant wall temperature. We found in case one the average Nusselt number decreases with time until reach steady state in a curvilinear behavior and all heat is transferred to enclosure but in case two the value of average Nusselt number at hot wall is fluctuates from maximum to minimum value in a sinusoidal profile and heat is transferred to enclosure then to outside, this is the effect of period and amplitude.

A comparison was made for the case one to validate the results by convert the problem to a concentric cylinder like the study by (**Khalid, 2002**) and using his boundary conditions in the present study, choosing the Nusselt number as a comparison parameter because it gives a clear picture to heat transfer into computational domain, so, a plots gives the relation between average Nusselt number and Ra number for aspect ratio ($S=1$) and radius ratio ($Y = 2, 5, 10$) are presented in **Fig.(10)** as a comparison between results of (Khalid) and present work. It is found that the same behavior of increasing in Nu number with increase of Ra is obtained, and a small difference between results is detected. Results difference is caused by difference in model, difference in grid size.

In order to describe the relation between the dependent variable (Nusselt number) and the independent variables (Raylieh number and angle



of inclination), a correlation have been made to describe the heat transfer data as in the form of ;

$$Nu=B (Ra^c.(1/(1+\cos\alpha))^n) \quad (45)$$

This correlation work for all range of Ra number and angles of inclination, the values of constants are;

$$Nu=0.605324899*Ra^{0.389673014} (1/(1+\cos\alpha))^{-0.07051460} \quad (46)$$

α in rad

CONCLUSIONS

Numerical results obtained for natural convection in an inclined liquid-saturated porous enclosure can be summarized as follows. Average Nusselt number increase with increase of Ra number, and increase very slightly or decrease with increase angle of inclination but in periodic case average Nusselt number increase with increase of amplitude and decrease with increase of period and increase very small with increase of Ra number and its variation is a sinusoidal profile with the time from maximum value in positive direction to a minimum in negative direction. Maximum temperature and velocity occur at $\alpha = 45$ and this is increase with increase Ra number. Local Nusselt number increase with increase Ra number and decrease with increase Z and maximum value of it at vertical position $\alpha = 0$.

REFERENCES

- Bejan, A.; "Convective Heat Transfer", Wiley, New York, 1984.
- Hiroyuki O., and Tsutomu S., 1981 "Natural Convection in Inclined Circular Cylindrical Annulus Heated and Cooled on its End Plates",

Int. J. Heat Mass Transfer, Vol.24, No. 4, pp.727-737.

- Iyer, S. V. and Vafai, K.; "Passive Heat Transfer Augmentation in a Cylindrical Annulus Utilizing a Porous Perturbation", Numerical Heat Transfer, Part A, 36, PP.115-128, 1999.
- Mohammad, A. A. and Saeid, N. H.; "Natural Convection in a Porous Cavity with Spatial Sidewall Temperature Variation", Int. J. of Numerical Methods for Heat and Fluid Flow, Vol.15, No.6, PP.555-566, 2005.
- Mohammad, M. S.; "Natural Convection in Confined Cylindrical Enclosure of Porous Media with Constant and Periodic Wall Temperature Boundary conditions", M.Sc. Thesis, University of Baghdad, 2008.
- Shivakumara, I. S., Prasanna, B. M. R. Rudraiah, N. and Venkatachalappa, M.; "Numerical Study of Natural Convection in a Vertical Cylindrical Annulus Using Non-Darcy Equation", J. of Porous Media, Vol.5, No.2, PP.87-102, 2002.
- Wang, B. X. and Zhang; "Natural Convection in Liquid-Saturated Porous Media between Concentric Inclined cylinder", Int. J. Heat Mass Transfer, Vol.33, PP.827-833, 1990.
- Wajeeth, K. H.; "Transient Three-Dimensional Natural Convection in Confined Porous Media with Periodic Boundary Conditions", PhD. Thesis, University of Technology, 2006.

NOMENCLATURE

Symbol	Description
a	Dimensionless amplitude
A	Amplitude
B	Constant in equation (45)
c_p	Specific heat at constant pressure
D	Diameter of cylinder
g	Acceleration due to gravity
K	Permeability
K_m^*	Effective thermal conductivity of porous media
L	Length of cylinder
Nu	Nusselt number

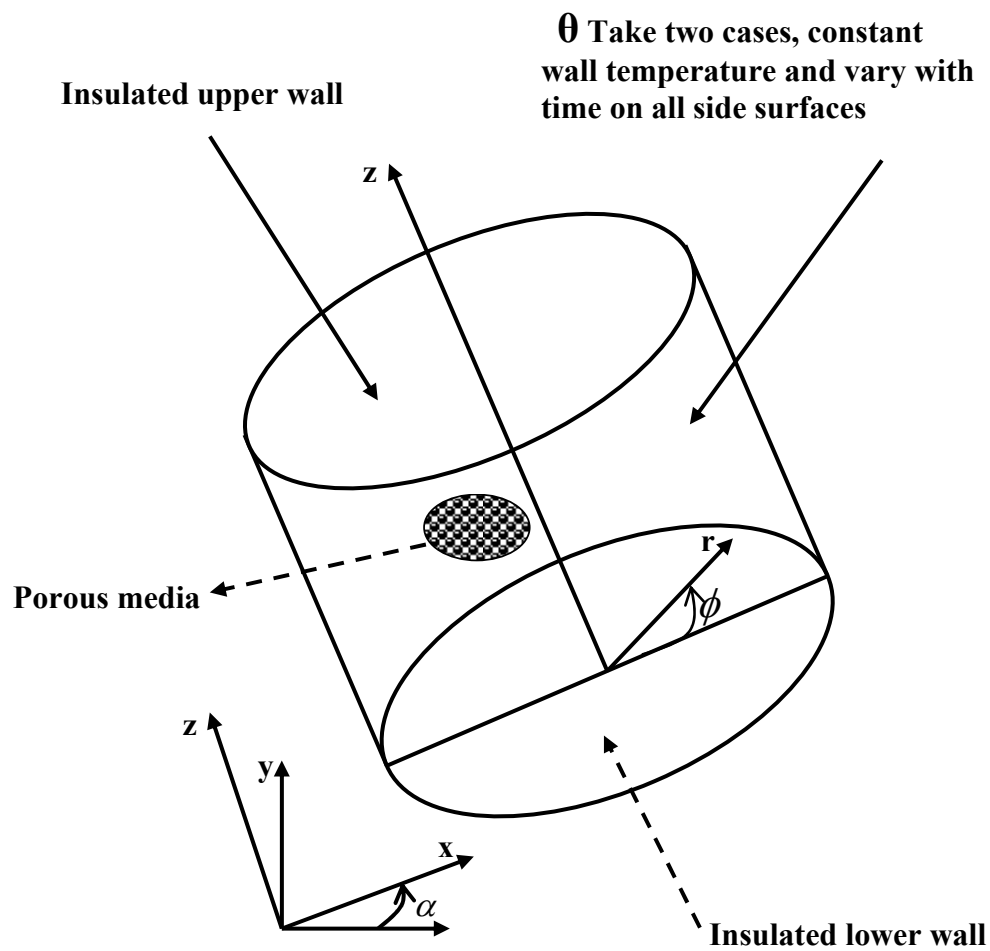
P	Dimensionless pressure
p	Pressure
R	Dimensionless radial coordinate
r	Radial coordinate
Ra	Raylieh number
T_o	Reference temperature
\bar{T}_h	Mean hot wall temperature
T_h	Hot wall temperature
t	Time
U	Dimensionless component of velocity in R-direction
u	Velocity component in R-direction
V	Dimensionless component of velocity in ϕ -direction
v	Velocity component in ϕ -direction
W	Dimensionless component of velocity in Z-direction
w	Velocity component in Z-direction
Z	Dimensionless axial coordinate
z	Axial coordinate

Greek symbols	
α	Angle of inclination
α_m	Effective thermal diffusivity of porous medium
β	Volumetric thermal expansion coefficient
θ	Dimensionless temperature
ϕ	Angular coordinate
Φ	Vector potential
$\Phi_R, \Phi_\phi, \Phi_Z$	Vector potential components in R, ϕ and Z directions
ρ_o	Reference density at T_o
τ	Dimensionless time
per	period
η	Dimensionless period
μ	Dynamic viscosity
ν_f	Kinematic viscosity of the fluid
$\Delta R, \Delta \phi, \Delta Z$	Distance between the grid points in R, ϕ and Z direction
$\Delta \tau$	Interval between two time steps
∇	Del operator

Subscript	
Symbol	Description
f	Fluid
i, j, k	Grid points location in R, ϕ and Z directions
h	Hot
m	Solid
c,n	Constants in equation (45)
o	Reference

Table (1): Input Data for the Simulations

Simulation number	Ra	a	η
1	125	0.2	0.01
2	125	0.4	0.01
3	125	0.8	0.01
4	125	0.4	0.005
5	125	0.4	0.02


Fig.(1): Geometrical Shape of the Problem

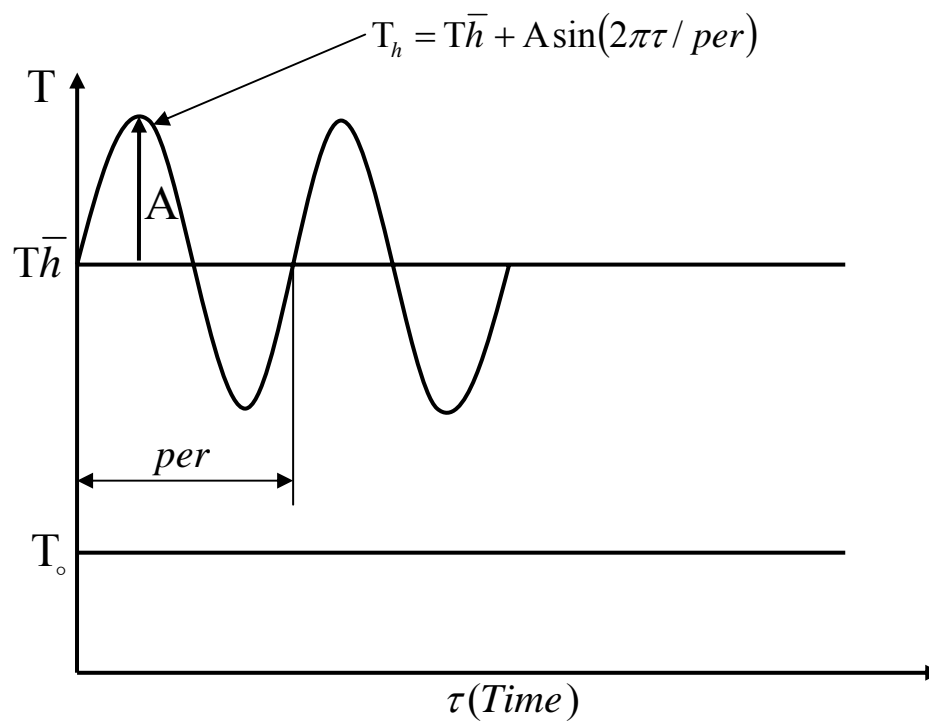
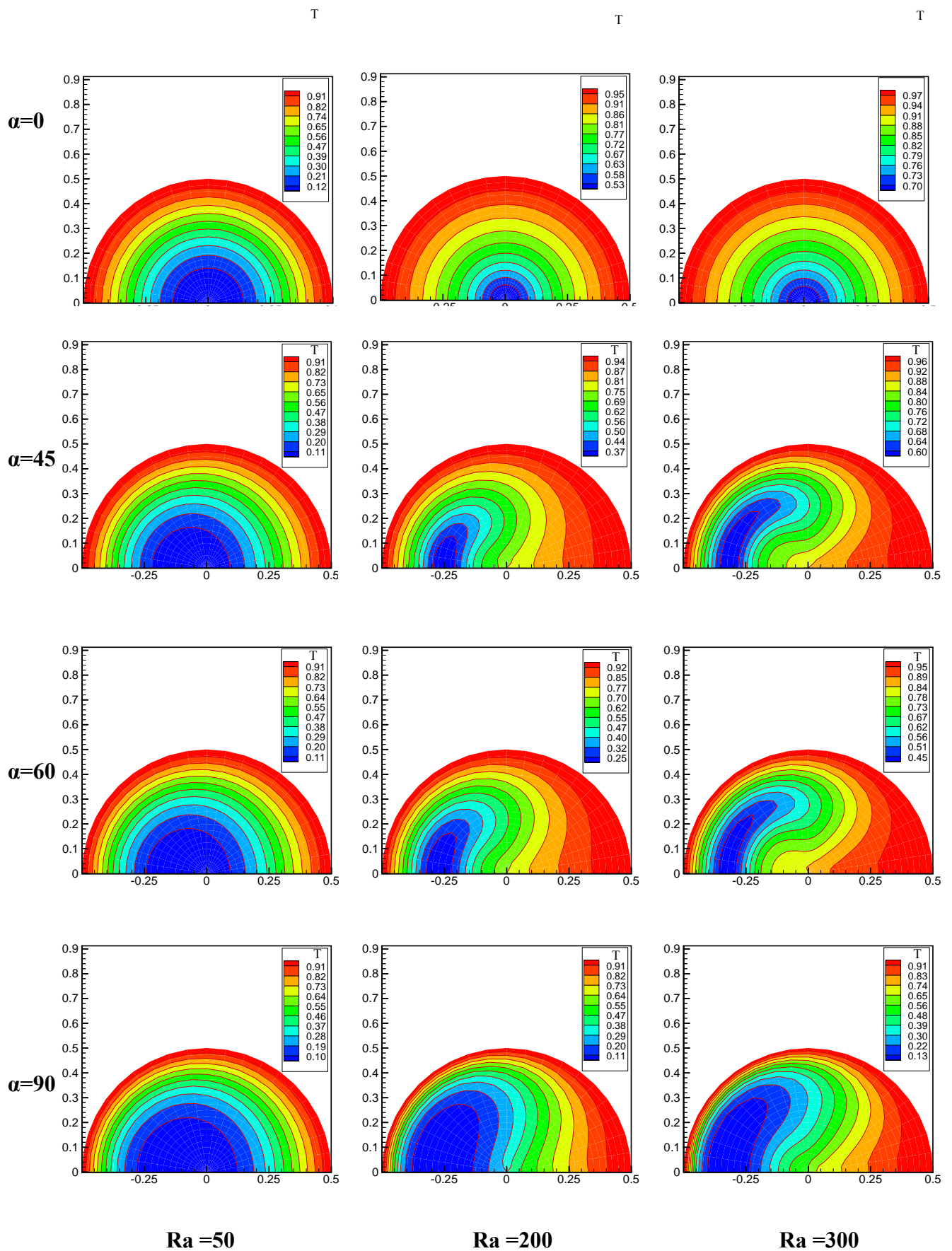


Fig.(2): The Hot Wall Time-Dependent Boundary Condition

Fig.(3): Transient Temperature Distribution for $Z=1$

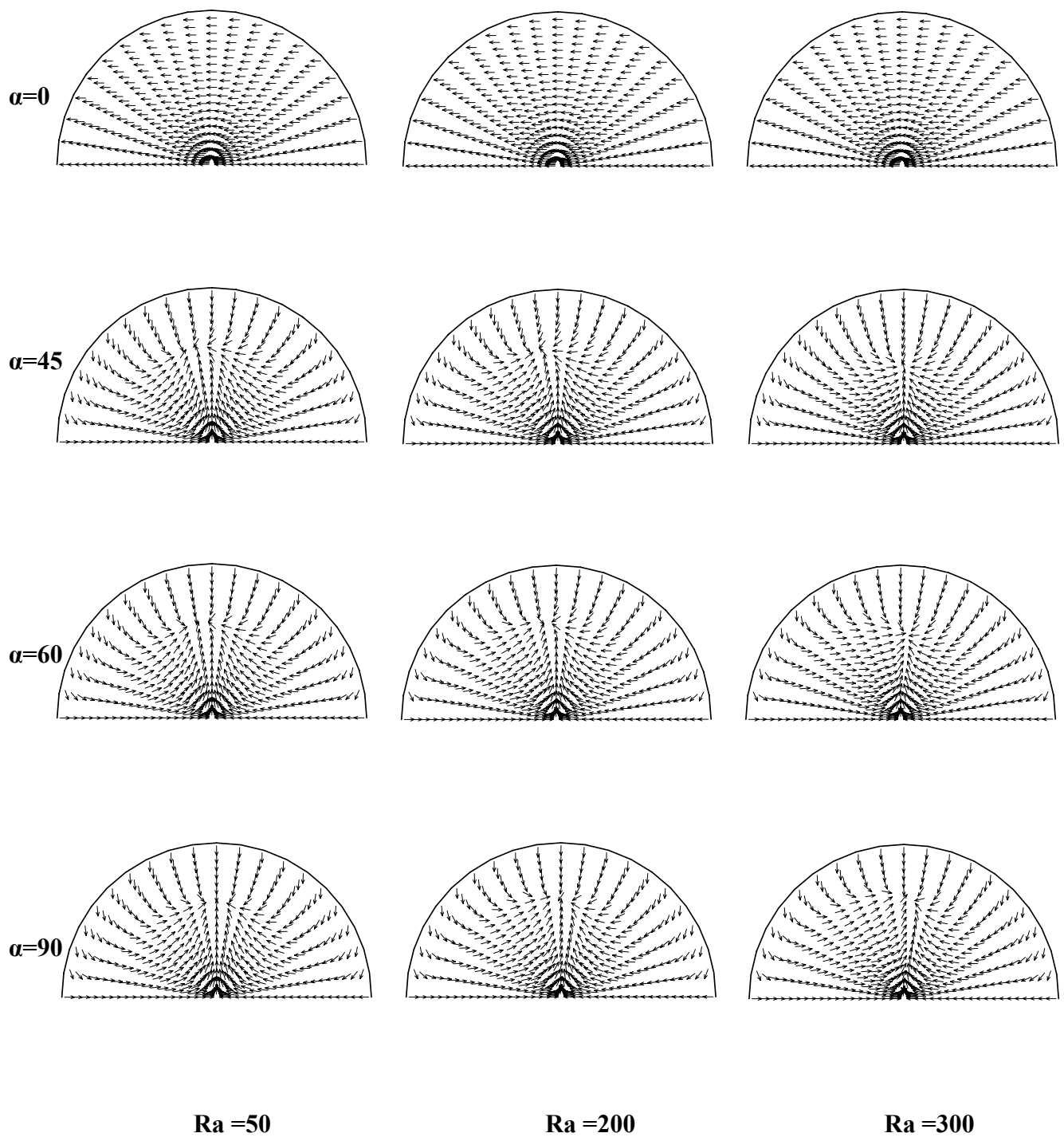
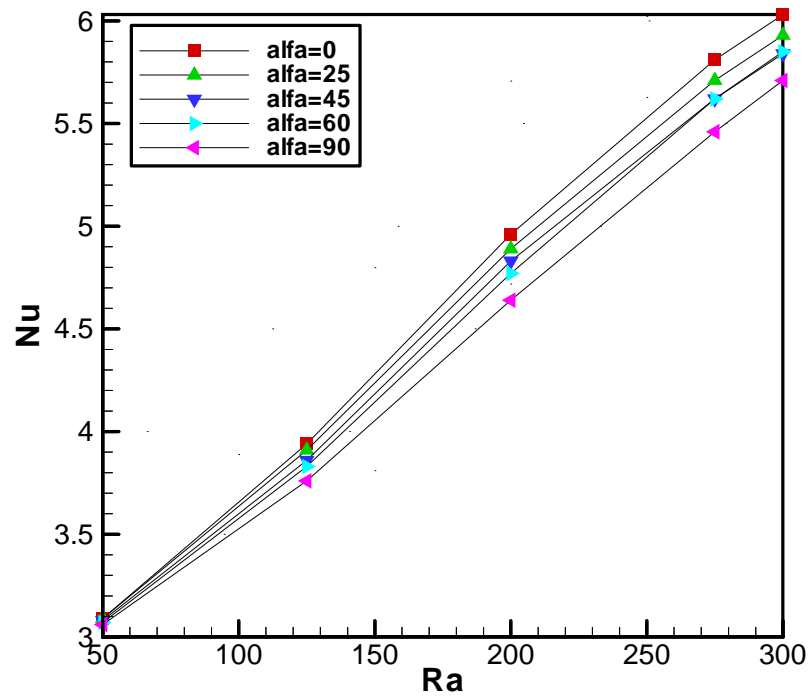
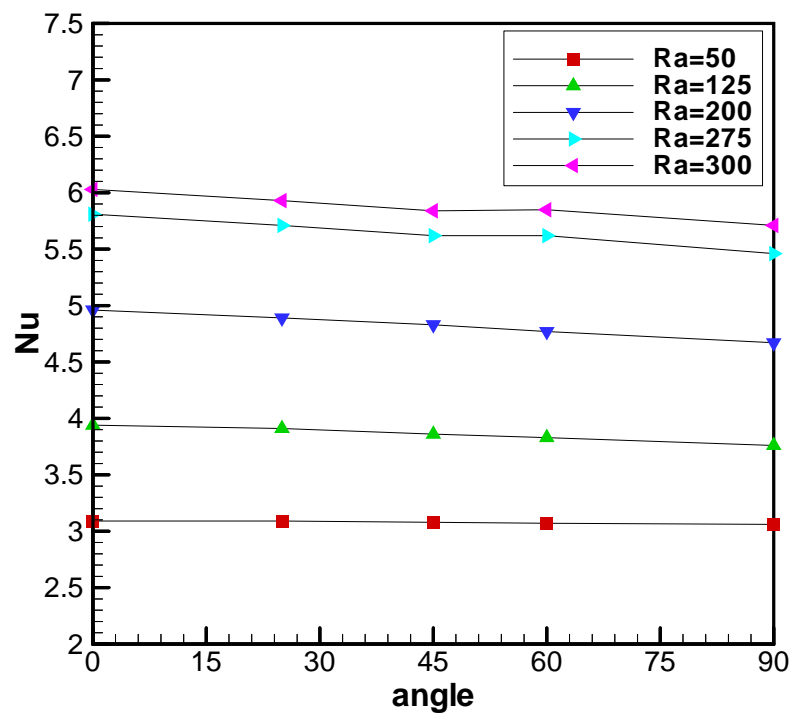


Fig.(4): Velocity vectors for $Z = 0.75$



a



b

Fig.(5): Variation of Nusselt number, **a with Ra number, **b** with angle of inclination**

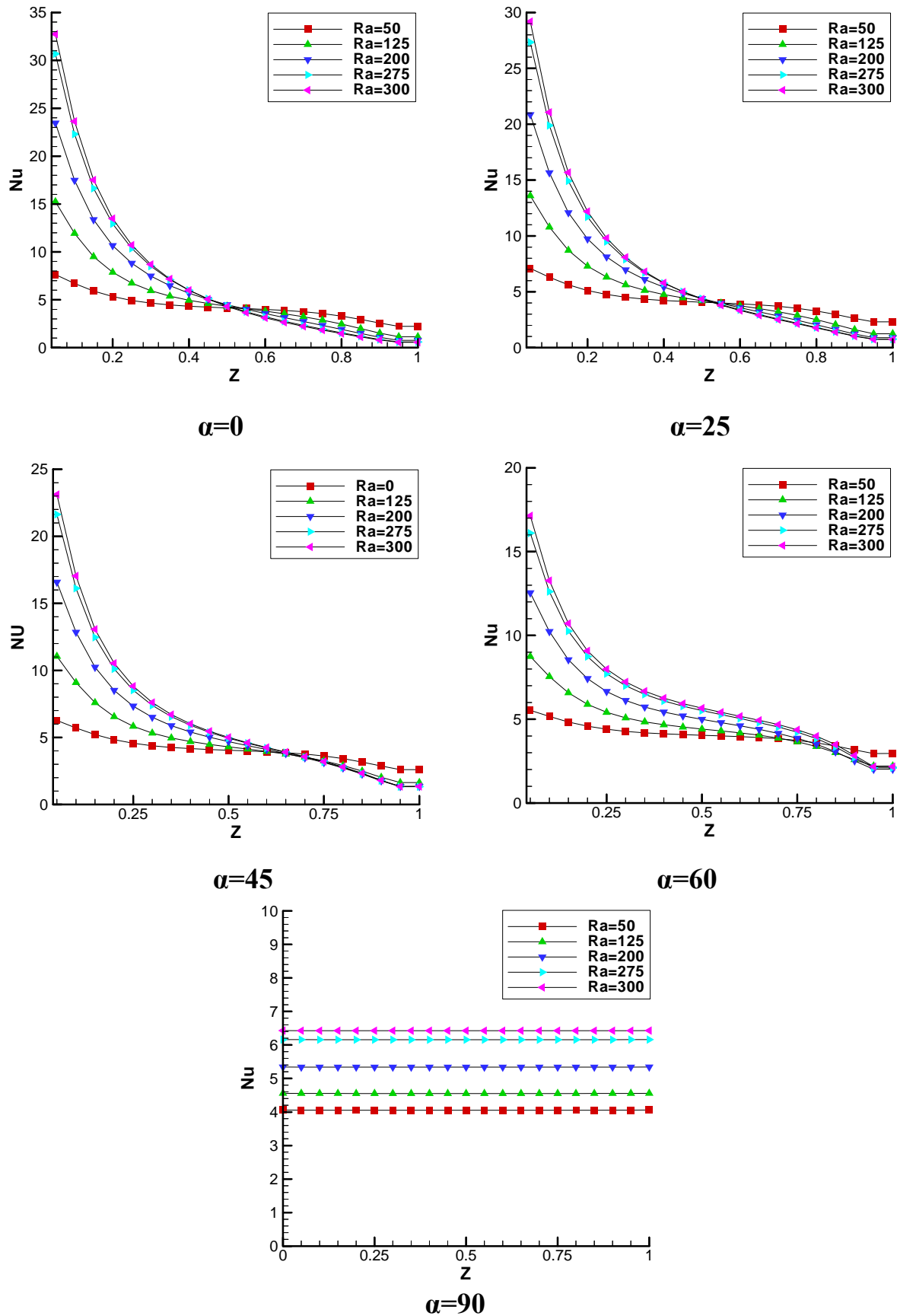


Fig.(6): Variation of Local Nusselt Number with (Z) for Different Ra Number

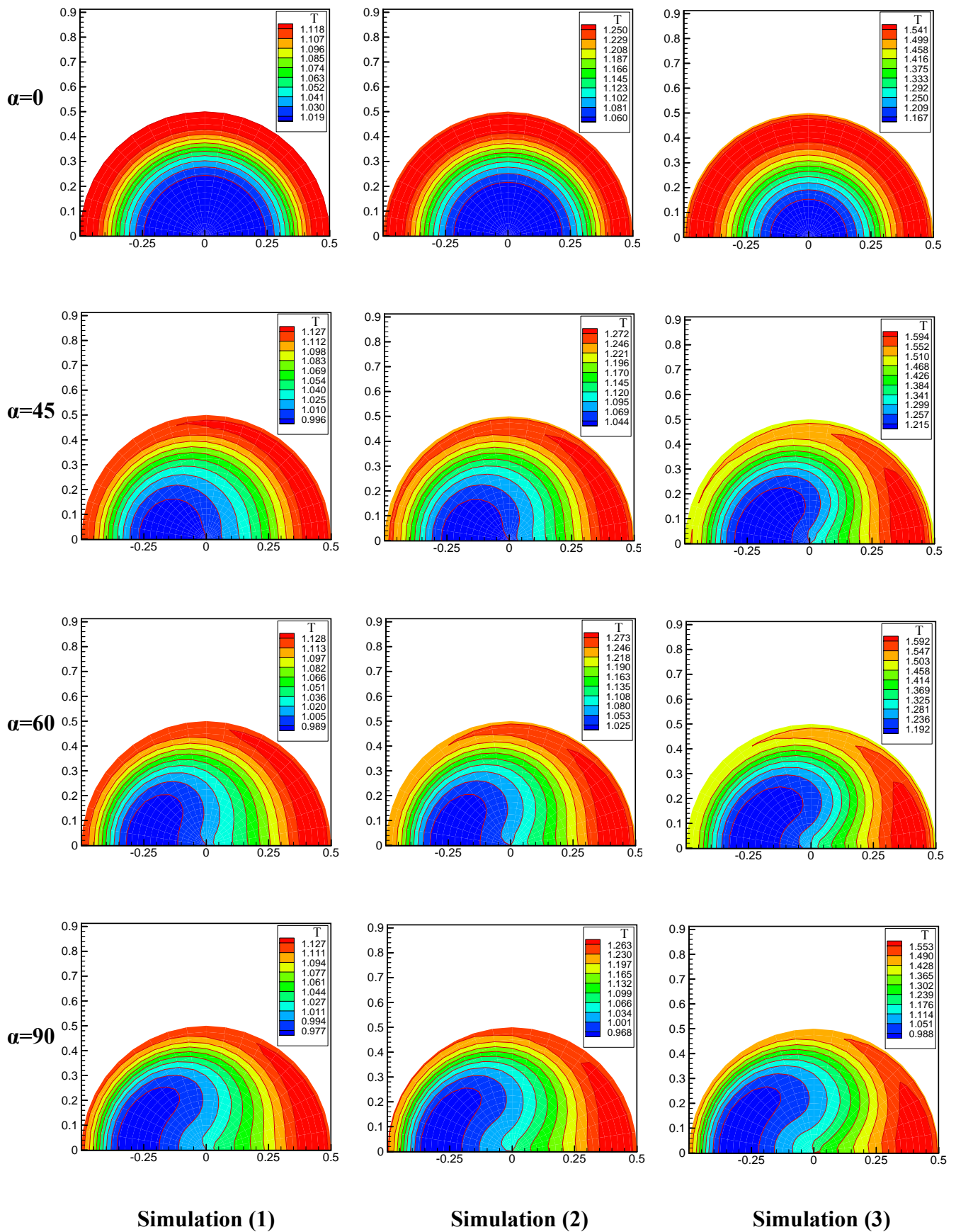
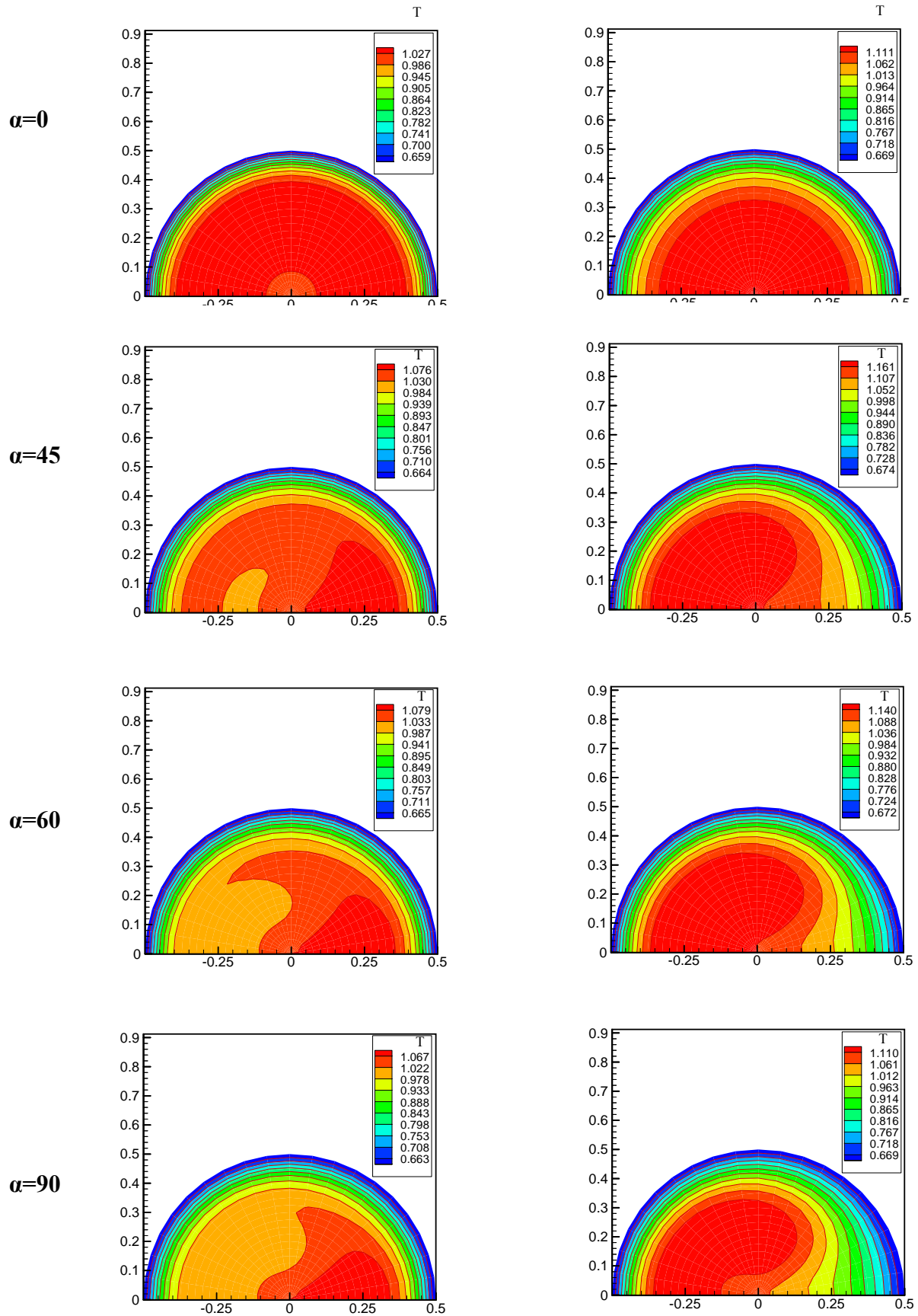


Fig.(7):Transient Temperature Distribution at $Ra = 125$



Simulation (4)

Simulation (5)

Fig.(7): Continued

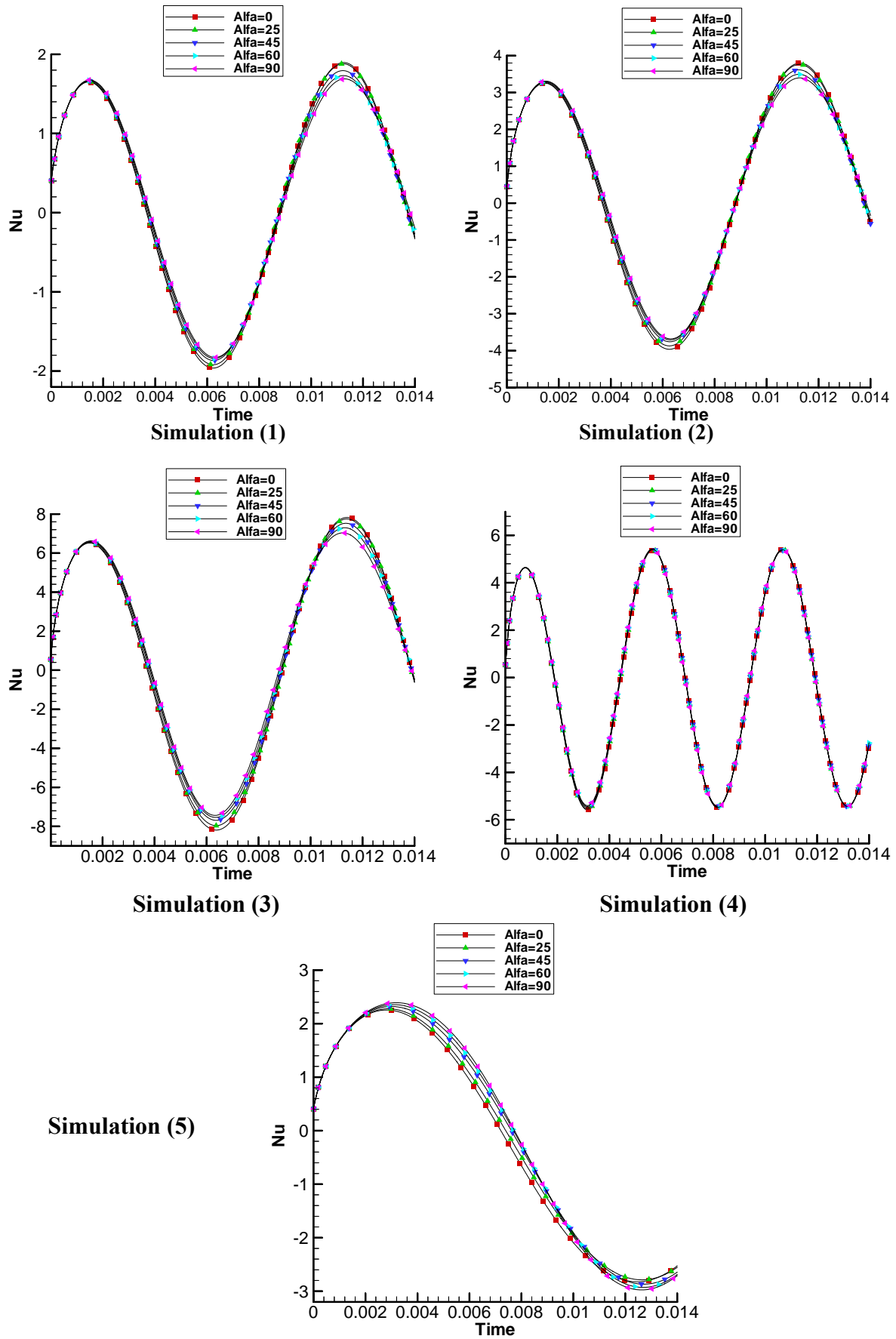
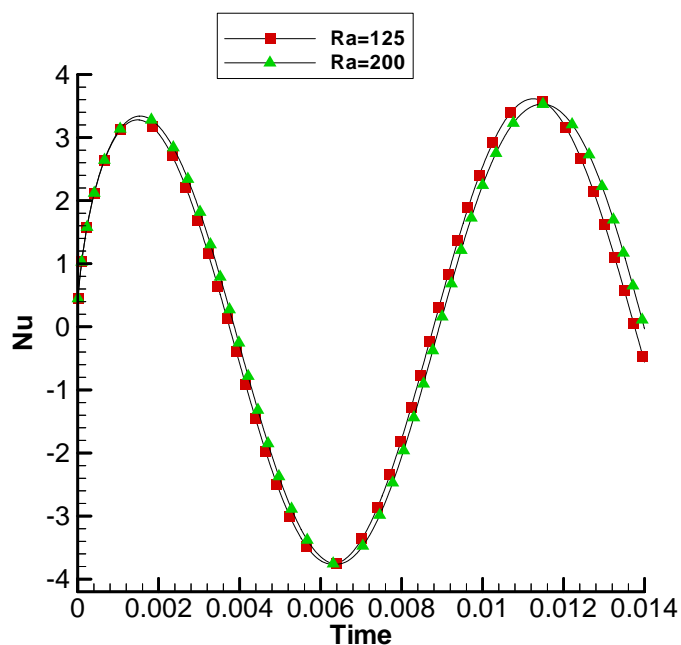
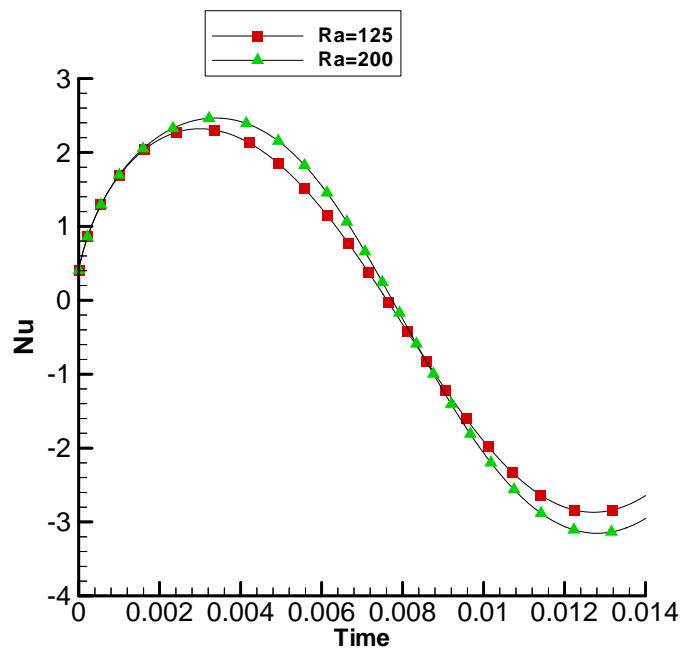


Fig.(8): Transient Nusselt Number for Different Simulations, $Ra = 125$



Simulation (1)



Simulation (5)

Fig.(9) Transient Nusselt Number for $\alpha = 45$

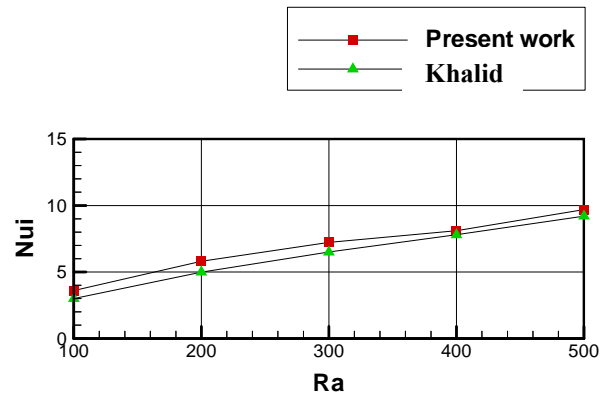
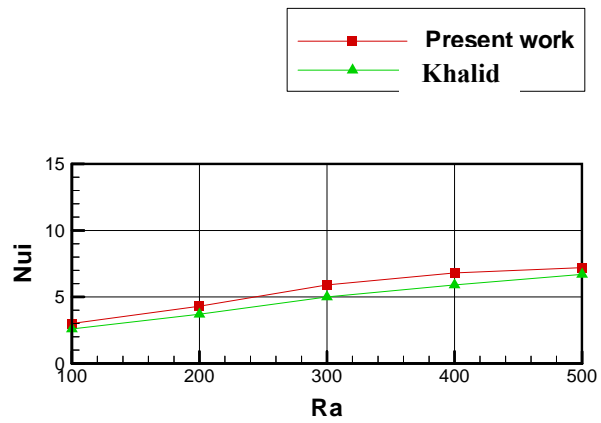
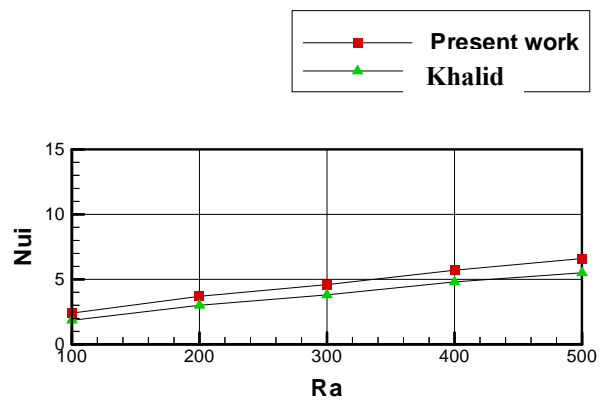
 $Y=2$  $Y=5$  $Y=10$ 

Fig.(10): Comparison of the Results



CORROSION OF AMALGAMS IN ORAL CAVITY

Ghassan L.Yusif
Mechanical department
University of Baghdad

ABSTRACT

This paper is a study of the effect of natural saliva (oral cavity) and a fluoride mouthwash on dental amalgams. Two types electrodes were made the first was of a high copper amalgam while the second was made from a low copper amalgam. They were immersed in two types of electrolytes for twelve hours and the whole galvanic cell was connected to a computer via a potentiostat. Their corrosion currents, corrosion voltage and corrosion resistance was recorded and compared to find which medium that is usually has the most severe effect on the amalgams corrosion.

الخلاصة

تم في هذا البحث دراسة تأثير محلول الفلورايد واللغاب الطبيعي على سبيكة حشوه السن الزئبقية حيث تم صناعة نوعين من الحشوات الزئبقية الأولى عالي النحاس والثاني واطئ النحاس. تم غرسهما في محلولين المذكورين قابلين للتوصيل الكهربائي لفترة اثنا عشر ساعة وتم إيجاد مقاومتهما للتآكل والتيار المقاوم للتآكل وفولتية التآكل مع المقارنة بينهما وإيجاد إي المحلولين له التأثير الأسوء في عملية التآكل للحشوات الزئبقيتين.

KEYWORDS:

amalgam, dental materials, corrosion of teeth fillings, saliva effect on amalgams

The beneficial effect is that Zinc makes the amalgam mixture more plastic and easy to handle.

The Electrolytes:

The electrolytes used in the experiment were two types:

The 1st electrolyte was natural saliva accumulated in a sucker obtained from a dental clinic. The composition of the saliva was shown in Table2.

The second electrolyte was a mouthwash used for dental hygiene (pH=3.9), which had the composition shown in Table3.

The second type of electrolyte used to find the effect of dental mouthwash on dental amalgams, since most mouthwashes and toothpaste contain fluoride.

The Electrochemical Corrosion Apparatus:

The apparatus used in the experiment consisted of a glass container with three openings at the top. The 1st opening was for a rotating disc electrode, the 2nd for platinum electrode and the 3rd was for a standard calomel electrode (SCE). The electrodes used were maintained at body temperature $\pm 2^\circ\text{C}$ to maintain oral conditions. the entire assembly was connected to a computer controlled potentiostat. the electrolyte was circulated inside the container at a speed of 450 rpm, as shown in Fig 1.

Data Collection:

The data collected was from a twelve-hour period. The polarization curves in which the current is a function of electrical potential:

$$I = f(E) \quad (3)$$

were plotted so as to determine the corrosion resistance of the amalgams in the electrolytes. the polarization curves & Stern – Geary relationship were used to find the current density for the corrosion current (I_c) and the polarization resistance R_p (Milton 2007).

$$R_p = B/I_{\text{corr}} \quad (4)$$

While all laboratory corrosion tests require accelerating corrosion processes, only electrochemical tests can directly amplify the impact corrosion process. this is because all electrode kinetics associated with corrosion process to qualify corrosion rates. The amplification of the electrical signals generated during these tests has permitted very precise and sensitive measurement. For this reason this part was conducted in the UAE since Iraq lacks such devices.

$$B = \frac{b_a \cdot b_c}{2.3(b_a + b_c)} \quad (5)$$

B: Can be calculated from (b_a) & (b_c) which are the slopes of anodic and cathodic Tafel slopes respectively.

Corrosion Rate Determination

The rate of corrosion was gained by

- Plotting the obtained data from the current-potential curves that were obtained, and then extrapolating the cathodic and anodic Tafel lines to current potation so as to obtain the slope at that point.
- The Tafel slops of the anodic and cathodic curve can be used in the stern-Geary eg. to determine the corrosion rate.

THE RESULTS:

The corrosion resistance of the two different amalgams that were immersed in the two different electrolytes was measured after 12 hr's and their results are shown in table 4 & 5. Their corrosion curves are given in figures 2 & 3.

Low Copper Amalgams.

In the natural saliva the low copper amalgam started with a very high corrosion resistance but after 3 hr's started to drop and at the end of the 12 hr period it had reached (200) mV/SCE, whereas it went much more severe corrosion relatively when it was immersed in a fluoride mouthwash (fig 3).it did not start with a very good corrosion resistance and dropped even more at the end of the experiment and stabilized at (-350) mV/SCE.

In addition, the polarization resistance was much higher in the natural saliva in accompany to a lower corrosion current (table 5) than it had in the fluoride solution.

High Copper Amalgam.

For the natural saliva, in the first 4 hrs the high copper amalgam had a lower corrosion resistance (Fig 3) but in due time it increased gradually and stabilized at a higher corrosion resistance of (230) mV/SCE, whereas in the fluoride electrolyte its corrosion resistance dropped severely and stabilized at (-350) mV/SCE. It had a much higher corrosion resistance in natural saliva than in the fluoride solution, showing a higher corrosion current (table 5) in the fluoride mouthwash than in the natural saliva.

DISCUSSION

From the obtained results it is obvious that corrosion occurs within an amalgam which make up a tooth filling the corrosion was much more severe in the fluoride mouth wash than in natural saliva. The purpose of the fluoride substance is to kill bacterial growth, yet while it is doing this it corrode any amalgam fillings in the mouth. This will eventually lead to the failure of the alloy due to It being subjected to alternate stresses from chewing food in addition to its corrosion

Early dental amalgams contained less than 5% copper had limited corrosion resistance (Stephen) as it was proven in the experiment. The higher copper amalgam had a much higher corrosion resistance in natural saliva then in the fluoride mouthwash.

In a high copper amalgam the Ag-Sn-Zn irregular particles are mixed with the Ag-Cu to produce the amalgam alloy. Mixed with Mercury (Hg), Ag-Hg and Sn-Hg phases form almost as quickly as Sn-Hg forms, and then the released Hg reacts with more Ag-Sn to produce predominately Ag-Hg. Therefore little or no Sn-Hg resides in the set amalgam.

Of special interest is the actual geometry in the phases involved. The Ag-Hg (γ_1) crystals are relatively equi-axed. Contrary to these grains Sn-Hg (γ_2) crystals are elongated and look like tongue depressor blades. This has a major consequence for corrosion. While the Sn-Hg crystals represent little volume of the mixture they tend to touch

(connected) through the entire dental amalgam allowing penetrating corrosion to take place.

Shifting to high copper amalgam has both the advantage that Cu-Sn is less corrosion prove and the grains do not routinely touch each other so that only superficial corrosion occurs (Stephen).

All amalgams leak mercury into the mouth to some extent. (R.C House 1980).

In addition to Sn-rich corrosion products of high copper amalgams, Cu-rich amalgams also form Cu- containing corrosion product. Two products were identified Cu_2O a red product and $\text{CuCl}_2 \cdot 3\text{Cu}(\text{OH})_2$ a green product.

As soon as an amalgam is filled into the moth it starts corroding. This is one reason why amalgam fillings have to be replaced when they became in our mouths we also have the chemical corrosion that can be caused by electrical activity previously discussed. We have both these factors increasing the corrosion of the amalgam, which is process of releasing metal ions into our saliva.

In addition to the weakening of the amalgam strength due to corrosion the mercury into the body have disastrous health effects. Research show that mercury is associated with disorder such as multiple sclerosis, Alzheimer's disease depression and reduced immune functioning Mercury exposure also presents a risk to fetuses in mothers who have amalgam fillings and may cause birth defects.(N.K. Sarkar 2000)

CONCLUSION

- Each and every person who has an amalgam filling has a battery constantly working in his/her mouth releasing metallic toxic ion into the body.
- Both high and low copper amalgam under corrosion, but high copper amalgam has more corrosion resistance.
- While fluoride solution are for oral hygiene. They are more useful to people with healthy teeth. Where as any one who has fillings made from amalgam, the will corrode much faster when using fluoride dental products Fluoride may act bacterial growth on teeth yet it also corrodes amalgam a much faster rate.

REFERENCES



- Edgar W.M and O'Mullane, D.M. (ed) (1996). Saliva and oral health, (2nd edn), British Dental Association, London.
- Gilbert H. Jackson, III, B.S. chem., J.D. Law, Quantitative Analysis of Hg, Ag, Sn, Cu, Zn and Trace Elements in Amalgam Removal From Au abutment Tooth underneath A Gold Alloy Bridge That had been in Vivo for Nine plus Years.
- Gláucia Maria Oliveira de Queiroz, Leando Freitas Silava, Jose Tarcisio Lima Ferreira, Jose Antonio da Cunha P. Gomes and Lucio Sather Jan 29, 2007, "Electrochemical behavior and PH stability of artificial Saliva for Corrosion tests.
- M. Karthega, S. Tamiselvi and N. Rajendran Trends Biomater. Artif. Organs vol. 20(1), pp31-34 (2006), Effect of PH on the corrosion Behavior of Ti-6Al-4V alloy for Dental implant application in Fluoride Media.
- Millon Stern & A.L. Geary (Journal of electro chemical Society, vol. 104, No.1, 56-63, (1957) "Electrochemical Polarization: I. A Theoretical Analysis of the shape of Polarization Curves"
- N. K. Sarkar and J.R. Park (2000), Department of Dentistry, New Orleans 70119.
- R.C. House, M.w. Patterson, G.B. Pellen and R.B. McCoy. J prosthet Dent. (1980) Oct; 44:423-5.
- Raymon A. Higgins, (1973) Engineering Metallurgy part 1 4th edition P.418.
- S. J Marshall, J.H. Lin and G.W. Marshall. J. Biomed Mater. Res. (1982) Jan; 16:81-5
- CuO₂ and CuCl₂.3Cu(OH)₂ corrosion products on copper rich dental amalgams
- Stephen C. Bayne, department of operative dentistry school of dentistry, University of North Carolina.

NOMENCLATURE

Ag: Silver
 Cu: copper
 H₂: Hydrogen
 Sn: tin
 Zn: zinc
 Hg: mercury
 O₂: oxygen
 I_c: corrosion current in mA/cm²
 R_p: polarization resistance in Kohm.cm²
 E_{corr}: voltage corrosion in volts
 b_a: anodic slope
 b_c: cathodic slope
 γ: gamma phase

Table 1: electro potential of the elements that make up a typical amalgam (Raymon 1973)

Silver (Ag)	+0.80
Copper (Cu)	+0.52
Hydrogen (H ₂)	0.00
Tin (Sn)	-0.14
Zinc (Zn)	-0.76

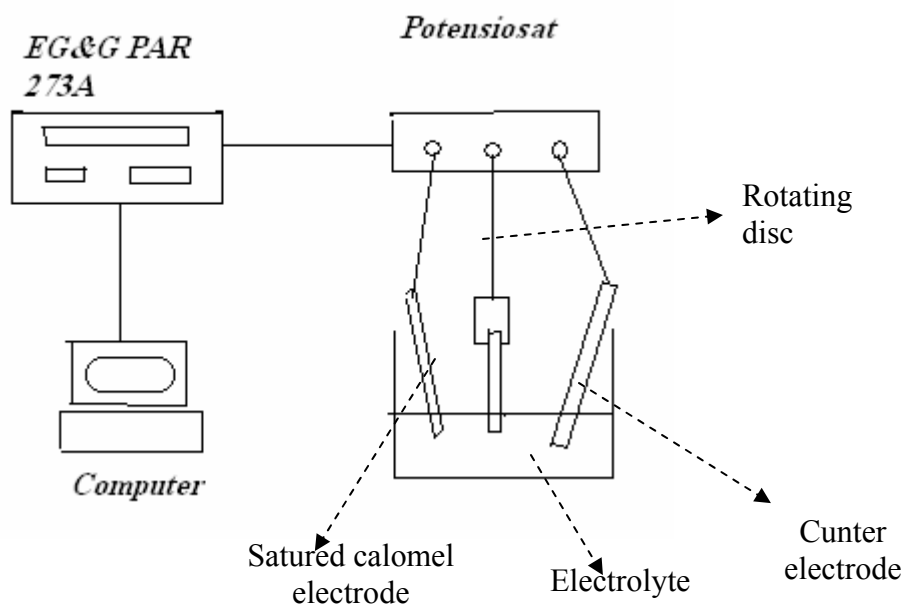
Table 2: composition and concentration of elements for natural saliva

Element	Concentration mmol/L
sodium	2-2
potassium	36
calcium	2.8

magnesium	0.5
chloride	40
bicarbonate	25
phosphate	39

Table 3: composition and concentration of mouth wash

Compound	Concentration ppm
Amine Fluoride Dafour	95
Sodium Fluoride	150

**Fig 1: Apparatus setup****Table (4): Corrosion potential (E_{corr}) of the specimens in different electrolytes after a period of 12 hr's**

Electrolytes	E_{corr} (mv/sce)	
	Low Cu Amalgam	High Cu Amalgam
1. Natural Saliva	200	230
2. Fluoride Mouthwash	-370	-350

Table (5): Corrosion current densities i_{corr} (mA/cm²) and polarization resistance R_p (Kohm.cm²)



Amalgam	Natural Saliva		Fluoride Mouthwash	
	i_{corr}	R_p	i_{corr}	R_p
1.Low Cu Amalgam	1.36	500	2.8	160
2.High Cu Amalgam	2.2	550	3.0	165

Polarization Cures for Natural Saliva

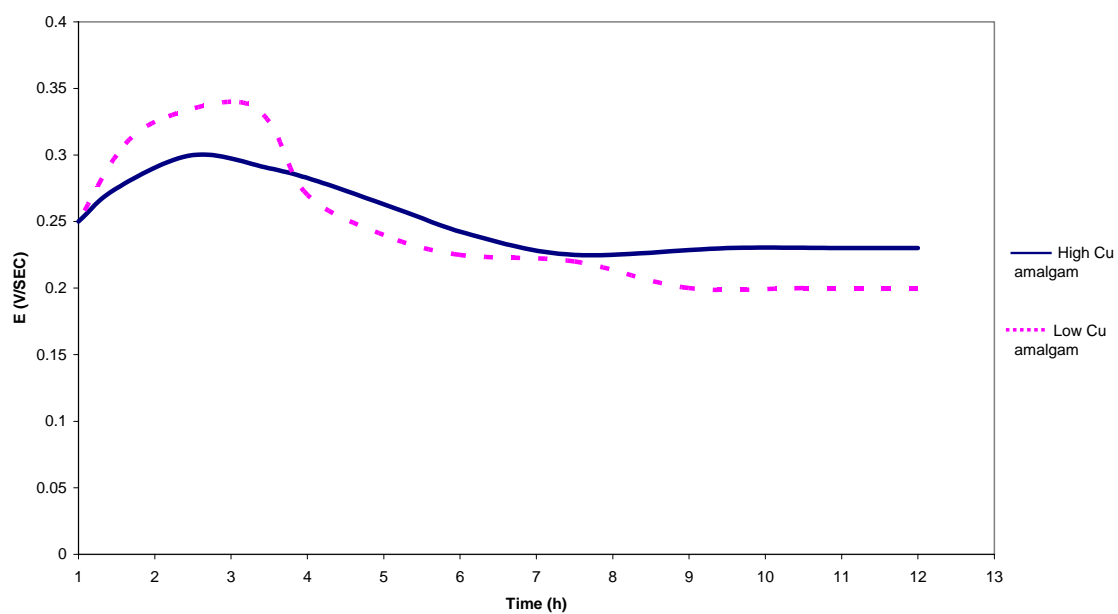


Fig 2

Time Polarization curve for Fluoride Mouth wash

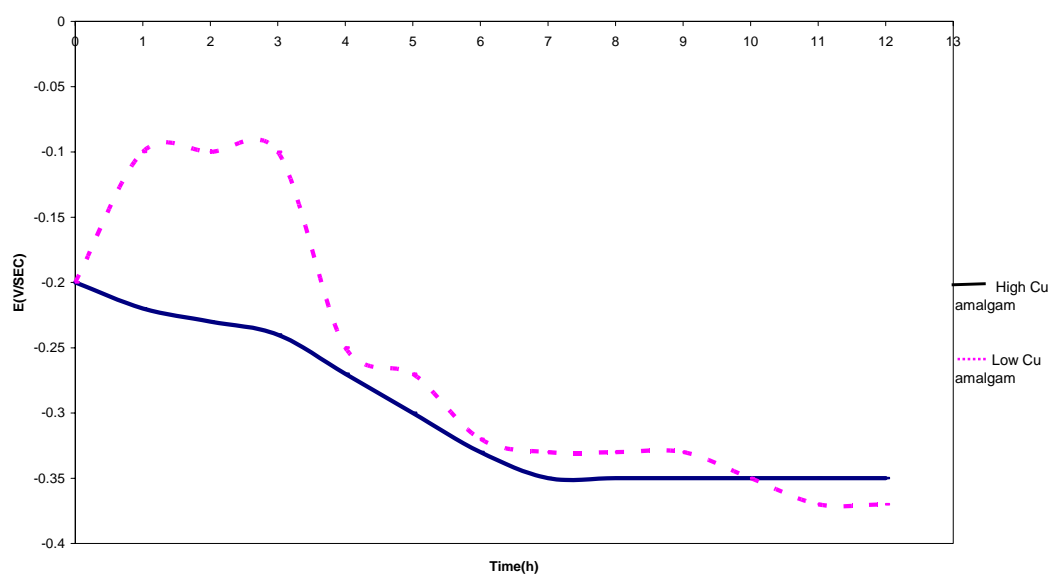


Fig 3

FORCED CONVECTION THERMAL BOUNDARY LAYER DEVELOPMENT IN A POROUS MEDIA NEAR A WALL WITH VARIABLE TEMPERATURE BOUNDARY CONDITION

Mrs. Luma F. Ali
Mech. Engr. Dept.
College of Engr.
University of Baghdad
Baghdad-Iraq

ABSTRACT

The behavior of forced convection heat transfer characteristics through and over porous layer near a heated flat plate at variable temperature has been investigated numerically. Two cases of variable wall temperature boundary condition are studied. The first case is of linear temperature variation with position along the flat plate and the second case is of sinusoidal temperature variation with time of heating. The flow field in the porous region is governed by the Darcy-Brinkman-Forchheimer equation, the thermal field in the porous region by the energy equation and the part over the porous matrix includes flow and heat transfer equations. Solutions of the problem have been carried out using a finite difference method through the use of a stream function-vorticity transformation. The effects of various governing dimensionless parameters, Darcy number, Reynolds number, Prandtl number as well as the inertia parameter are thoroughly explored. The variation of the non-dimensional period and amplitude values of the sinusoidal temperature distinction with time was also studied. Good results were obtained and reported graphically. It was found that the local Nusselt number on the flat plate increases with the increasing of the increasing non-dimensional values of period and amplitude individually.

الخلاصة:

يتناول البحث دراسة خصائص انتقال الحرارة بالحمل القسري خلال و فوق طبقة وسط مسامي موضوعة فوق صفيحة ذات درجة حرارة متغيرة باستخدام الطريقة العددية للفروقات المحددة. لقد تضمنت الدراسة حالتان من تغير درجة الحرارة كشرط حدي للجزء السفلي من الطبقة المسامية. ان الحالة الاولى كانت لتغير درجات الحرارة خطيا مع البعد على طول الصفيحة. اما الحالة الثانية فان التغير كان بشكل موجي مع الزمن. تضمن النموذج الرياضي للجريان خلال الوسط المسامي معادلة الجريان بالاعتماد على صياغة (Brinkman-) Forchheimer المستمدة من قانون دارسي و معادلة الطاقة خلال الوسط المسامي و الجزء الاخر للجريان فوق الوسط المسامي. تم حل المعادلات الحاكمة عدديا باستخدام طريقة الفروق المحددة. و قد استخدمت طريقة (الدوامية-دالة الانسياب). خلال البحث تم دراسة تأثير عدد من المجاميع اللابعدية مثل رقم دارسي، رقم رينولدز، رقم برانتل كذلك تأثير القصور الذاتي. بالاضافة الى ذلك تم دراسة تأثير التغير في طول و ارتفاع الموجة اللابعدية لتغير درجة الحرارة الموجي مع الزمن. لقد ذكرت النتائج بشكل تخطيطي و تم الحصول على النتائج الجيدة. و قد وُجد من هذه النتائج ان رقم نسلت الموضعي على طول الصفيحة يزداد بزيادة طول و ارتفاع الموجة اللابعدية كل على حدة.

KEYWORDS: Porous Media, Forced Convection, Heat Transfer, Numerical Solution.

INTRODUCTION

Forced convection heat transfer through porous media has a major topic for various studies during the past decades due to many engineering applications such as thermal insulation engineering, water movements in geothermal reservoirs, underground spreading of chemical waste, thermal insulation, direct-contact heat exchangers, nuclear waste repository, grain storage, and enhanced recovery of petroleum reservoir. The heat transfer with forced convection in porous media is an interesting and challenging physical problem; therefore a considerable attention was given to this type of problems by accomplishing theoretical and experimental studies.

The problem of forced convection flow and heat transfer along a flat plate in a porous medium was examined by Beckermann & Viskanta [1987] including both, the inertia and boundary effects, while porosity variations close to the wall are not considered. They derived the velocity and temperature profiles for the fully-developed momentum boundary layer and from the results they determined the wall shear stress and the Nusselt number as functions of modified Reynolds and Prandtl numbers. In addition, Vafai and Thiyagaraja [1987] analytically studied the fluid flow and heat transfer for three types of interfaces, namely, the interface between two different porous media, the interface separating a porous medium from a fluid region and the interface between a porous medium and an impermeable medium. Another related problem is that of Poulikakos and Kazmierczak [1987]. In that work a fully developed forced convection in a channel filled with a porous matrix was investigated and the existence of a critical thickness of the porous layer at which the value of Nusselt number reaches a minimum was demonstrated.

A fundamental investigation on the effects of employing intermittently porous cavities for regulating and modifying the flow and temperature fields was done by Vafai & Huang [1994]. They used a general flow model that accounts for the effects of the impermeable boundary and inertial effects to describe the flow inside the porous region and the solution of the problem has been carried out using finite difference method through the use of a stream function-vorticity transformation. Also the effects

of various governing dimensionless parameters, such as the Darcy number, Reynolds number, Prandtl number and the inertia parameter were thoroughly explored. Then Huang & Vafai [1994] presented an analytical solution for forced convection boundary layer flow and heat transfer through a composite porous/fluid system by considering a layer of porous media over a flat plate with constant temperature boundary condition. The details of the interaction phenomena occurring in the porous medium and the fluid layer were systematically analyzed, revealing the effects of various parameters governing the physics of the problem. Their results presented a comprehensive yet easy comparative base for numerical solutions addressing this type of interfacial transport and their analysis provided a rather accurate simulation of the interfacial transport.

Furthermore a finite-volume computational model had been developed by Vadakkan [2001] to analyze the steady performance of a pin fin array experiencing forced convection in a duct. This pin fin array was considered using transport equations of porous media. The analysis had been done utilizing two different approaches in solving the temperature fields in the porous structure and indicated that there is a significant difference between the solid and fluid temperature at higher values of porosity and lower values of the interstitial heat transfer coefficient.

For an unsteady forced convection on a flat plate embedded in the fluid-saturated porous medium with inertia effect and thermal dispersion, Cheng & Lin [2002] presented a precise and rigorous method to obtain the entire solution from one-dimensional transient conduction to steady forced convection in porous medium under conditions of uniform wall temperature and uniform heat flux, respectively. In addition, the aim of their work is to quantify the effect of inertia force on the intermediate regime of unsteady forced convection in a porous medium. Huang et al. [2005] carried out a numerical study for enhanced heat transfer from multiple heated blocks in a channel by porous covers. The flow field was governed by the Navier-Stokes equation in the fluid region, the Darcy-Brinkman-Forchheimer equation in the porous region, and the thermal field by the energy equation. Solution of the coupled governing equations was obtained

using a stream function-vorticity analysis. This study details the effects of variations in the Darcy number, Reynolds number, inertial parameter, and two pertinent geometric parameters, to illustrate important fundamental and practical results.

In order to study the development of the forced convection thermal boundary layer in a definite layer of porous media near a wall with two types of temperature boundary condition, a flat plate of specified length and covered with definite height of porous media and a fluid with ambient velocity and temperature flowing over and through the porous matrix is taken into account in the present paper. Two cases for the lower boundary temperature condition are used; one is linear temperature variation with the length of the plate and the other is the temperature boundary condition that varies sinusoidally with time.

MATHEMATICAL FORMULATION

The configuration of the problem under investigation is depicted in **Fig. 1**. It includes a flat plate of length L covered with a porous media layer of height H . A fluid with constant temperature T_∞ and velocity u_∞ is flowing through and over this porous medium layer. In this study, it is assumed that the flow is laminar, incompressible, and two dimensional. In addition, the thermo-physical properties of the fluid and the porous matrix are assumed to be constant and the fluid-saturated porous medium is considered homogenous and isotropic and in local thermodynamic equilibrium with the fluid. For the fluid region the conservation equations for mass, momentum, and energy are [Vafai & Huang 1994]:

$$\frac{\partial \rho_f}{\partial t} + \nabla V_f = 0 \quad (1)$$

$$\frac{\partial V_f}{\partial t} + V_f \cdot \nabla V_f = -\frac{1}{\rho_f} \nabla P_f + \nu_f \nabla^2 V_f \quad (2)$$

$$\frac{\partial T_f}{\partial t} + V_f \cdot \nabla T_f = \alpha_f \nabla^2 T_f \quad (3)$$

Based on the Brinkman-Forchheimer-extended Darcy model, which accounts for the effects of the inertial and impermeable boundary, the mass, momentum and energy equations in the porous matrix can be expressed as [Vafai & Huang 1994]:

$$\varepsilon \frac{\partial \rho_p}{\partial t} + \rho_p \cdot \nabla V_p = 0 \quad (4)$$

$$\frac{\rho_p}{\varepsilon^2} \left(\varepsilon \frac{\partial V_p}{\partial t} + V_p \cdot \nabla V_p \right) = -\frac{1}{\rho_p} \nabla P_p \quad (5)$$

$$-\left(\frac{\mu_{eff}}{K} + \frac{F \cdot \varepsilon}{\sqrt{K}} V_m \right) V_p + \frac{\mu_{eff}}{\varepsilon} \nabla^2 V_p$$

$$(\rho C)_f \left(\sigma \frac{\partial T_p}{\partial t} + V_p \cdot \nabla T_p \right) = k_{eff} \nabla^2 T_p \quad (6)$$

In order to express the governing equations in dimensionless form, the following non-dimensional quantities may be defined:

$$Y = \frac{y}{L}, \quad X = \frac{x}{L}, \quad V = \frac{v}{u_\infty}, \quad U = \frac{u}{u_\infty}, \quad P = \frac{p}{\rho u_\infty^2},$$

$$\theta = \frac{T - T_\infty}{T_w - T_\infty}, \quad V_m = \sqrt{\frac{u^2 + v^2}{u_\infty^2}} = \sqrt{U^2 + V^2},$$

$$\text{Re}_L = \frac{\rho u_\infty L}{\mu}, \quad Da_L = \frac{K}{L^2}, \quad \text{Pr}_f = \frac{\mu_f C_p}{k_f},$$

$$\text{Pr}_{eff} = \frac{\mu_f C_p}{k_{eff}}, \quad \sigma = \frac{\varepsilon \rho_f C_p f + (1 - \varepsilon) \rho_s C_s}{\rho_f C_p f},$$

$$t^* = \frac{t u_\infty}{L}, \quad AL = \frac{FL \varepsilon}{\sqrt{K}} \quad (7)$$

After utilizing the above dimensionless groups and canceling the pressure term P from the resulted equations [Qahtan 2005], the vorticity and temperature equations respectively for the fluid region may be expressed as follows:

$$\frac{\partial \omega_f}{\partial t^*} + \frac{\partial (U \omega)_f}{\partial X} + \frac{\partial (V \omega)_f}{\partial Y} = \frac{1}{\text{Re}_L} \left(\frac{\partial^2 \omega_f}{\partial X^2} + \frac{\partial^2 \omega_f}{\partial Y^2} \right) \quad (8)$$

$$\frac{\partial \theta_f}{\partial t^*} + \frac{\partial (U \theta)_f}{\partial X} + \frac{\partial (V \theta)_f}{\partial Y} = \frac{1}{\text{Re}_L \text{Pr}_f} \left(\frac{\partial^2 \theta_f}{\partial X^2} + \frac{\partial^2 \theta_f}{\partial Y^2} \right) \quad (9)$$

Whereas the vorticity and temperature equations for the porous region may be stated as the following two equations [Qahtan 2005]:

$$\varepsilon^* \frac{\partial \omega_p}{\partial t^*} + \frac{\partial (U \omega)_p}{\partial X} + \frac{\partial (V \omega)_p}{\partial Y} = -\frac{\varepsilon^2}{\text{Re}_L Da_L} \omega_p$$

$$- AL \cdot \varepsilon V_m \omega_p - AL \cdot \varepsilon \left(V_p \frac{\partial V_m}{\partial X} - U_p \frac{\partial V_m}{\partial Y} \right) +$$

$$\frac{\varepsilon}{\text{Re}_L} \left(\frac{\partial^2 \omega_p}{\partial X^2} + \frac{\partial^2 \omega_p}{\partial Y^2} \right) \quad (10)$$

$$\sigma \frac{\partial \theta_p}{\partial t^*} + \frac{\partial(U\theta)_p}{\partial X} + \frac{\partial(V\theta)_p}{\partial Y} = \frac{1}{\text{Re}_L \text{Pr}_{eff}} \left(\frac{\partial^2 \theta_p}{\partial X^2} + \frac{\partial^2 \theta_p}{\partial Y^2} \right) \quad (11)$$

The governing equations above are cast in terms of the vorticity-stream formulation. Therefore the stream function and vorticity may be introduced as:

$$U = \frac{\partial \psi}{\partial Y}, \quad V = -\frac{\partial \psi}{\partial X} \quad (12)$$

$$\omega = \frac{\partial V}{\partial X} - \frac{\partial U}{\partial Y} \quad (13)$$

Where (ω) is the vorticity component perpendicular to the flow surface. Also the vorticity may be related to the stream function by using the stream function equation which may be formulated as:

$$-\omega = \frac{\partial^2 \psi}{\partial X^2} + \frac{\partial^2 \psi}{\partial Y^2} = \nabla^2 \psi \quad (14)$$

The applicable boundary conditions necessary to complete the problem formulation are:

$$\left. \begin{array}{ll} X=0 & Y \quad \mathcal{G}=0, U=1, V=0, \psi=Y, \omega=-\frac{\partial^2 \psi}{\partial X^2} \\ X=1 & Y \quad \frac{\partial \mathcal{G}}{\partial X} = \frac{\partial \omega}{\partial X} = \frac{\partial \psi}{\partial X} = \frac{\partial U}{\partial X} = \frac{\partial V}{\partial X} = 0 \\ Y=0 & 0 < X < 1 \quad U=V=\psi=0, \omega=-\frac{\partial^2 \psi}{\partial Y^2} \\ Y \rightarrow \infty & 0 < X < 1 \quad \mathcal{G}=0, U=\frac{\partial \psi}{\partial Y}=1, \omega=-\frac{\partial^2 \psi}{\partial X^2} \end{array} \right\} \quad (15)$$

In the present work two cases of boundary conditions were taken for the temperature condition at the lower boundary $Y = 0$. The first case is taken as temperature boundary condition which varies linearly with X and it is expressed in non-dimensional form as:

$$\mathcal{G} = X \quad (16)$$

While the second case for the lower boundary condition is the temperature that varies sinusoidally with time and formulated in non-dimensional form as follow:

$$\mathcal{G} = 1 + a \sin\left(\frac{2\pi t^*}{\eta}\right) \quad (17)$$

In addition to the above boundary conditions, the two sets of conservation equations

are coupled by the following matching conditions at the porous/fluid interface [Vafai & Huang 1994], [Huang & Vafai 1994]:

$$\left. \begin{array}{l} u|_{y=H^-} = u|_{y=H^+}, v|_{y=H^-} = v|_{y=H^+} \\ p|_{y=H^-} = p|_{y=H^+}, \mu_{eff} \frac{\partial v}{\partial y}|_{y=H^-} = \mu_f \frac{\partial v}{\partial y}|_{y=H^+} \\ \mu_{eff} \left(\frac{\partial u}{\partial y} + \frac{\partial v}{\partial x} \right)|_{y=H^-} = \mu_f \left(\frac{\partial u}{\partial y} + \frac{\partial v}{\partial x} \right)|_{y=H^+} \\ T|_{y=H^-} = T|_{y=H^+}, k_{eff} \frac{\partial T}{\partial y}|_{y=H^-} = k_f \frac{\partial T}{\partial y}|_{y=H^+} \end{array} \right\} \quad (18)$$

and the initial conditions are:

$$\theta = \psi = \omega = 0 \quad \text{for} \quad t^* = 0 \quad (19)$$

In the present work, an explicit finite difference numerical technique is used in order to solve the flow and heat equations. The finite difference form of the fluid and porous media regions and boundary and initial conditions are formulated in the next section.

NUMERICAL SOLUTION

To solve the above partial differential equations, a finite difference numerical technique is employed. A grid of points is first established throughout the calculation domain. However, the uniform rectangular grid system is the same for the fluid and porous media regions.

An explicit finite difference method is utilized for the energy and vorticity equations (equations (8-11)) as recommended by [(Anderson et al. 1984) and (Fletcher 1987)]. In the explicit method, the vorticity and temperature are calculated at future time ($t^* + \Delta t^*$) for any internal grid by using the vorticity and temperature values at time (t^*) for the specified grid and the neighbor grids which are known from the initial conditions of the problem under consideration. By employing this time matching technique the values of the vorticity and temperature for the whole domain will be known for each time step until reaching the steady state condition. This condition is attained when the value of the average Nusselt number for two consecutive runs would become less than 10^{-8} .

On the other hand, after formulating the stream function equation (equation (14)) in finite difference form, the relaxation method is utilized in order to solve the resulted algebraic equations iteratively at each time step by employing Gauss-Seidel iterative technique. In this method, convergence has been achieved when the absolute value of relative error for the whole grid points between two successive iterations, found by trial and error, was equal to 10^{-4} .

A computer program written in FORTRAN was used. Once the above algebraic flow and heat transfer equations is solved, the temperature distribution for internal and boundary grid points is identified. Then, when the steady state condition for the linear variation temperature boundary condition is reached and specified time for the sinusoidal variation with time temperature boundary condition is spend, the local Nusselt number value is found by employing the following formula [Anderson et al. 1984]:

$$Nu_x = -X * \frac{k_{eff}}{k_f} * \frac{-3\theta(i,1) + 4\theta(i,2) - \theta(i,3)}{2\Delta Y} \quad (20)$$

where k_{eff}/k_f is taken equal to one.

While the average Nusselt number is found by integrating the local Nusselt number along the plate length by employing the Simpson numerical integration rule as given in the following expression:

$$\overline{Nu} = \frac{1}{L} \int_0^L Nu_x \, dx \quad (21)$$

RESULTS AND DISCUSSION

In the present paper, the numerical values for the case under consideration was taken for a porous media layer of height $H/L = 0.02$ and porosity equal to 0.92. The metal foams was used as a porous medium and the material was Aluminum (606-T6) with thermal conductivity of 200 W/m.K . Two cases of the temperature boundary condition at the lower boundary of the porous matrix are studied. The first case is the linear temperature variation with position until reaching steady state condition and the second case is the sinusoidal temperature variation with time for a specified period of time. Several values of dimensionless parameters were taken in order

to study their effects on the heat transfer behavior. The Reynolds number values were verified within the laminar and transition regions ($1 \times 10^5 - 5 \times 10^5$), the Prandtl number values were taken for three most utilized fluids (air 0.7, water 7, and engine oil 100), three Darcy number values were considered (8×10^{-6} , 2×10^{-6} , and 9×10^{-7}), and the effect of three inertial parameter values (0.001076, 0.0025, 0.00323) were studied. Finally, the variation effect of the non-dimensional values of the sinusoidal temperature variation with time boundary condition was also investigated. These constant values were the non-dimensional amplitude a (0.2, 0.4, and 0.8) and the non-dimensional period η (0.005, 0.01, and 0.02).

A testing for the optimum distance between grid points in X direction was done and the relation between the average Nusselt number and the number of grid points was sketched in **Fig. 2** for the linear temperature variation with position and sinusoidal temperature variation with time cases. From this figure, it is shown that a 75 grid point in X direction is suitable to choose for the present case study. As well, similar test was made for the number of grid points in Y direction and it was found that the 75 grid point is appropriate.

The propagation of the temperature through and over the porous media for five instances is demonstrated in **Fig. 3** for the linear temperature variation case and in **Fig. 4** for the sinusoidal temperature variation case. It is clear from these figures that the temperature values through the porous matrix are high in the beginning because of the small thermal boundary layer effect. But after a period of time this layer is grown up and then the temperature decreases.

Effect of the Reynolds Number

The variation of the average Nusselt number versus time for three values of Reynolds number for linear temperature variation case is presented in **Fig. 5**. It is clear from this figure that the time required to reach steady state condition decreases with increasing Reynolds number values. The increasing of Reynolds number causes a bigger value of the inertia force with respect to the viscosity force and then increasing in the velocity gradient followed by decreasing of the

time required for steady state condition. The same behavior was obtained for the sinusoidal case for specific non-dimensional time (equal to two) as illustrated in **Fig. 6**. In this figure, only one value of Reynolds number is drawn because, in the sinusoidal temperature case, there is not any significant effect of Reynolds number variation on the average Nusselt number.

By referring to **Fig. 7** and **Fig. 8** it can be observed that the temperature gradient increases with the increasing of the Reynolds number. As a result, this increase in temperature gradient causes an increase in the local Nusselt number value as exposed in **Fig. 9** and **Fig. 10** for the linear and sinusoidal temperature variation respectively. Furthermore, the effect of the Reynolds number on the thermal boundary layer thickness for the two cases under study can be noticed from **Fig. 11** and **Fig. 12**. From these two figures, it can be deduced that the thermal boundary layer is grown inside the porous matrix only because of the solid structure of the porous media which causes a loss in the heat energy. As well, from these two figures it can be noticed that the thermal boundary layer thickness decreases with the Reynolds number increasing. This decreasing of the layer thickness is due to the sharp decreasing in the temperature gradient in the Y -direction because of the diffusion term small value.

Effect of the Darcy Number

Results for the effect of Darcy number variation are presented in several figures. In **Fig. 13** the relation between the average Nusselt number versus time for the linear temperature variation case is sketched. From this figure, it is clear that the time required for steady state condition decreases with the decreasing of the Darcy number values. This behavior is due to the increasing of the velocity gradient in Y -direction with the Darcy number decreasing values. Moreover, the decrease in Darcy number value means an increase in the flow uniformity and reduces vorticity and this leads to the reduction in the time required for steady state condition. Similar figure is presented for the sinusoidal temperature variation case for specific non-dimensional time value in **Fig. 14**. There is no significant change in Nusselt number values when the Darcy number is varied therefore only two cases were sketched in this figure.

The effect of Darcy number variation on the local Nusselt number along the flat plate is presented in **Fig. 15** and **Fig. 16**. From these figures, it is clear that the local Nusselt number increases with the decreasing of the Darcy number. This decrease in Darcy number with constant porosity cause a decreasing in the solid fraction volume and increasing in the heat transfer exposed area. As a result, a rising in the temperature slop in Y -direction is occurred as shown in **Fig. 17** and **Fig. 18** and consequently an increasing in the local and average Nusselt number values. **Fig. 19** and **Fig. 20** is adapted to the non-dimensional temperature distribution and the thermal boundary layer thickness. These two figures show that any reduction in Darcy number yields a decreasing in the thermal boundary thickness because of the enlarging in the velocity slop in Y -direction.

Inertial Effects

In order to study the inertia effect several figures are sketched. In **Fig. 21**, the relation between the average Nusselt number with time is illustrated. From this figure, it is clear that the time required to reach steady state condition decreases with the inertia effect increase. This behavior is due to the increasing in the velocity slop with inertia effect rising and then leads to a reduction in the time required for steady state condition. Similar figure is presented for the sinusoidal temperature variation but for specific value of time in **Fig. 22**. In addition, it can be noticed that the inertia is less effective than the Darcy number on the required time for steady state and this is because of the velocity slop value.

In **Fig. 23** and **Fig. 24**, the inertia effect on the local Nusselt number along the flat plate is illustrated for the linear and sinusoidal temperature variation. From these two figures it is shown that any increase in the inertia effect leads to a small reduction in local Nusselt number. This behavior is because of the small reduction in the temperature slope in Y -direction, as shown in **Fig. 25** and **Fig. 26**, and this slope reduction causes a small decreasing in the local and Average Nusselt number values. For the same reason, the thermal boundary layer thickness decreases with the inertia effect rising as depicted in **Fig. 27** and **Fig. 28**.

Effect of the Prandtle Number

To study the effects of the Prandtl number on the flow and temperature fields, three different Prandtl numbers were chosen such that they will cover a wide range of thermo-physical fluid properties such as the kinematics viscosity. The variation of the average Nusselt number versus time is shown in **Fig. 29** for linear temperature variation. From this figure, it is clear that whenever the kinematics viscosity is lower, the time required for steady state condition is higher. The reason of this trend is that, at specific Reynolds number, lower value of viscosity leads to smaller viscosity force and then smaller inertia and this needs more time to reach steady state. On the other hand, **Fig. 30** is sketched for the sinusoidal temperature variation and for specific time. It can be seen that the time required to reach a complete periodic behavior (vanishing of transient period) raises with the Prandtl number increasing. The reason of this manner is that the inertia force increases with the viscosity force increasing which depends on fluid type.

Obviously, the Prandtl number variations have no effect on the flow field. Whereas, the variation of Prandtl number has significant effect on heat transfer as it is presented in several figures. In **Fig. 31** and **Fig. 32**, it can be observed that the local Nusselt number increases with the increasing of the Prandtl number because of the rate of temperature change with respect to the Y -direction high value. This high rate of change value is clearly shown in **Fig. 35** and **Fig. 36** for linear and sinusoidal temperature variation correspondingly. For the same reason the thermal boundary layer thickness decreases with increasing Prandtl number values as illustrated in **Fig. 33** and **Fig. 34**.

Finally, an attempt was made to study the effect of the non-dimensional period and amplitude variation for the sinusoidal temperature boundary condition at the lower boundary near the flat plate. Results for this attempt are presented in several figures. The effect of the non-dimensional period on the variation of the local Nusselt number at the end of the flat plate is illustrated in **Fig. 37**. From this figure, it is clear that the local Nusselt number increases slightly with the rising of the non-dimensional period increasing. While there is not any difference in the temperature rate of change with respect to Y -direction as it is noticed from **Fig. 38**. Similar figures are sketched in order to demonstrate the effect of the non-

dimensional amplitude. The same trends of curves are obtained when sketching these figures in order to express the effect of non-dimensional amplitude variation in **Fig. 39** and **Fig. 40**. From these two figures, it can be observed that the local Nusselt number increases with increasing amplitude and also there is not any significant change in the temperature rate of change with increasing amplitude. The reason of the increasing in local Nusselt number is due to the direct relation with the temperature.

The heat transfer characteristics of the present issue for the linear temperature variation with position and sinusoidal temperature variation with time cases are sketched in the following two figures. These figures include the heat transfer characteristics of previous work [Qahtan 2005] with constant temperature condition for the lower boundary. In **Fig. 41**, it is found that the temperature gradient in Y -direction for the sinusoidal temperature case is identical to that of Qahtan. However, the temperature gradient for the linear temperature case has a little distinction in magnitudes but the same trend of curves. This behavior leads to a similar trend of curves for the local Nusselt number variation for Qahtan's work and sinusoidal temperature case as shown in **Fig. 42**.

CONCLUSIONS

The main focus of this research is to study the development of forced convection thermal boundary layer development in a porous media near a flat plate with variable temperature boundary condition by using the finite difference numerical technique. It may be concluded that the rate of heat transfer increases with the Reynolds number and Prandtl number increasing. In addition this rate increases with the inertia effect and Darcy number decreasing. Furthermore, the same trend of curves is obtained for the two cases of temperature boundary condition; the first case is of linear temperature variation with X -direction and the second is of sinusoidal temperature variation with time. It can be deduced that the time required vanishing the transient behavior of the sinusoidal temperature variation and reach a complete periodic behavior increases with the Prandtl number rising. Finally, the increasing of the non-dimensional period and amplitude of the sinusoidal temperature variation boundary condition case yields an increase in the local

Nusselt number. This increasing in Nusselt number leads to an increase in the rate of heat transfer.

REFERENCES

- Anderson, A. D., Tannehill, C. J., and Pletcher, H. R., "Computational Fluid Mechanics and Heat Transfer", Hemisphere, New York, (1984). (case of three authors)
- Beckerman, C., and Viskanta, R., "Force Convection Boundary Layer Flow and Heat Transfer along Flat Plate Embedded in a Porous Media ", Int. J. Heat Mass Transfer, Vol. 30, (1987). (case of two authors)
- Cheng, W. T., and Lin H. T., "Unsteady Forced Convection Heat Transfer on a Flat Plate Embedded in the Fluid-Saturated Porous Medium with Inertia Effect and Thermal Dispersion", Int. J. Heat Mass Transfer, Vol. 45, (2002). (case of two authors)
- Fletcher, C.A.J., "Computational Techniques for Fluid Dynamics 2", Springer –Verlag Berlin Heidelberg New York, (1987). (case of one authors)
- Huang, P.C., and Vafai, K., "Analysis of Flow and Heat Transfer over an External Boundary Covered with a Porous Substrate ", ASME, J. Heat Transfer, Vol. 116, (1994). (case of two authors)
- Huang, P.C., Yang C. F., Hwang J. J., and Chiu, M. T., "Enhancement of Forced-Convection Cooling of Multiple Heated Blocks in a Channel Using Porous Covers", Int. J. Heat Mass Transfer, Vol. 48, (2005). (case of four authors)
- Poulikakos, D., and Kazmierczak, M., "Forced Convection in a Duct Partially Filled a Porous Material" J. Heat Transfer, Vol. 109, (1987). (case of two authors)
- Qahtan A. F. Al-Abidy, "Forced Convection Thermal Boundary Layer Development in a Porous Media Near a

Heated Wall", Thesis, University of Technology, (2005). (case of one author)

- Vadakkan U., "Forced Convection through a Duct Containing a Pin Fin Array", ME608 Semester Project, (2001). (case of one author)
- Vafai, K., and Huang, P.C., "Analysis of Heat Transfer Regulation and Modification Employing Intermittently Emplaced Porous Cavities", Trans. ASME, J. Heat Transfer, Vol. 116, (1994). (case of two authors)
- Vafai, K., and Thiyagaraja, R., "Analysis of Flow and Heat Transfer at The Interface Region of Porous Medium ", Int. J. Heat and Mass Transfer, Vol. 30, (1987). (case of two authors)

NOMENCLATURE

Symbols

a : Non-dimensional amplitude.

AL : Inertial parameter for porous medium.

C_p : Specific heat [$J/kg.K$].

Da : Darcy number.

F : A function used in expressing inertia terms.

H : Height of porous medium [m].

k : Thermal conductivity of the porous media.

K : Permeability of the porous medium [m^2].

L : Plate length [m].

Nu : Nusselt number.

p : Pressure N/m^2 .

P : Non-dimensional pressure.

Pr : Prandtl number.

Re : Reynolds number.

t : Time [s].

t^* : Non-dimensional time.

T : Temperature [$^{\circ}C$].

u : x – Component velocity [m/s].

U : X – Component non-dimensional velocity u/u_{∞} .

v : y – Component velocity [m/s].

V : Y – Component non-dimensional velocity v/u_{∞} .

V_m : Mean value of X and Y – velocity components.

x : Horizontal coordinates.

X : Non-dimensional horizontal coordinate.

y : Vertical coordinates.

Y : Non-dimensional vertical coordinate.

Greek Symbols

α : Thermal diffusivity [m^2/s].

\mathcal{E} : Porosity.

η : Non-dimensional period.

ψ : Non-dimensional stream function.

ω : Non-dimensional vorticity.

\mathcal{G} : Non-dimensional temperature.

σ : Thermal capacity ratio.

ρ : Density [kg/m^3].

μ : Dynamic viscosity of fluid [$N.s/m^2$].

Subscript

∞ : Free stream.

f : Fluid.

p : Fluid inside porous media.

eff : Effective.

w : Wall.

s :

Solid.

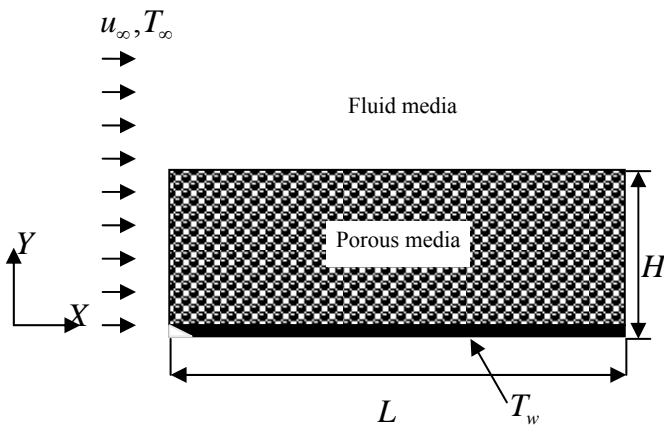


Fig. (1): The Schematic Diagram of the Physical Model.

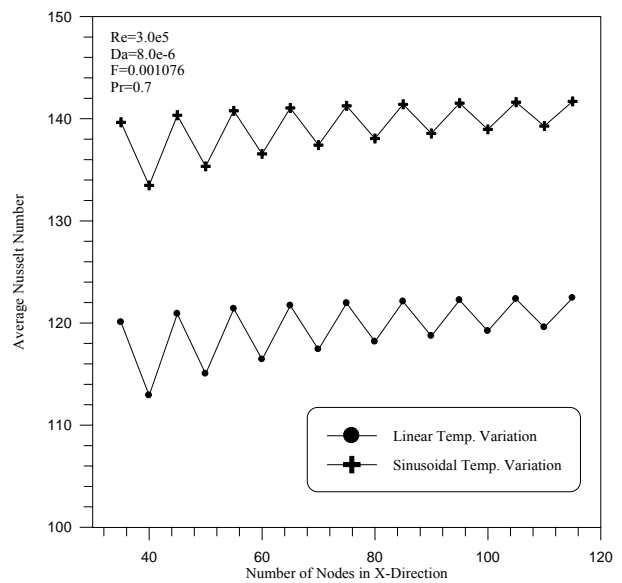


Fig. (2): Average Nusselt Number versus Number of Nodes in X-Direction (Linear and Sinusoidal

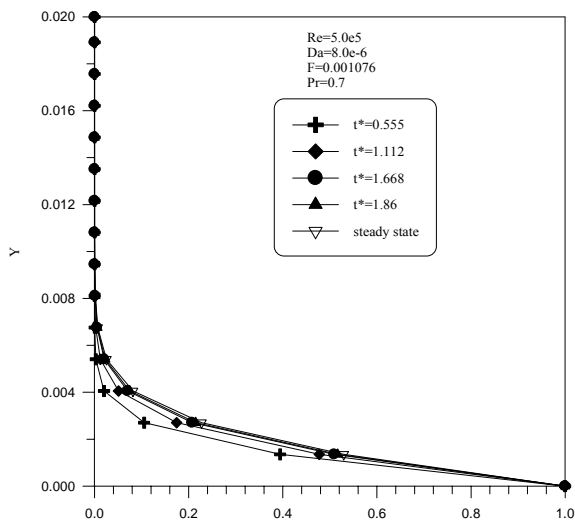


Fig. (3): Propagation of the Non-Dimensional Temperature with Time (Linear).

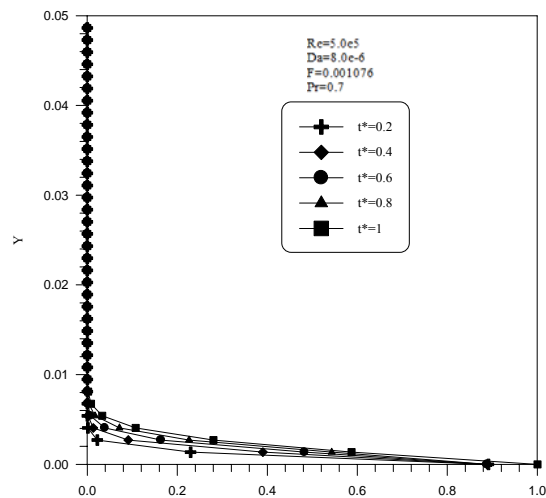


Fig. (4): Propagation of the Non-Dimensional Temperature Time (Sinusoidal).

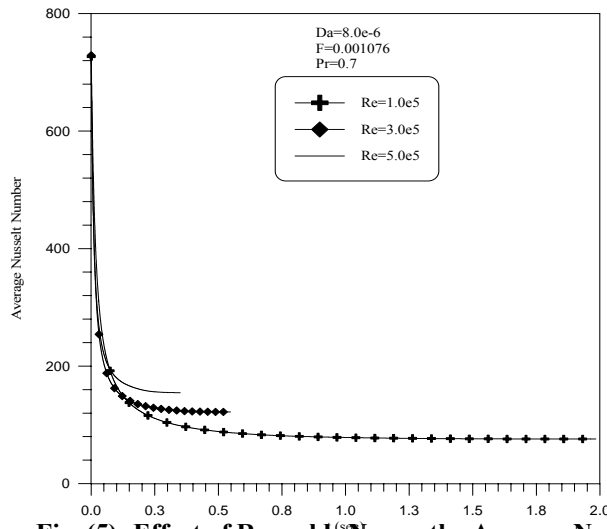


Fig. (5): Effect of Reynolds No. on the Average Nusselt Number Variation with Time (Linear).

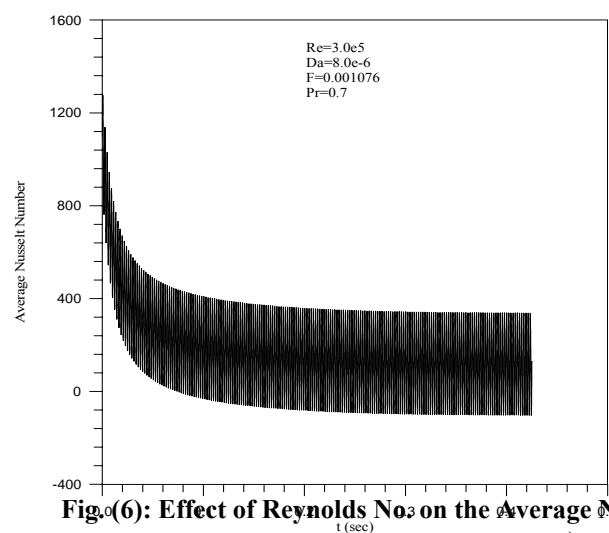


Fig. (6): Effect of Reynolds No. on the Average Nusselt No. Variation with Time (Sinusoidal).

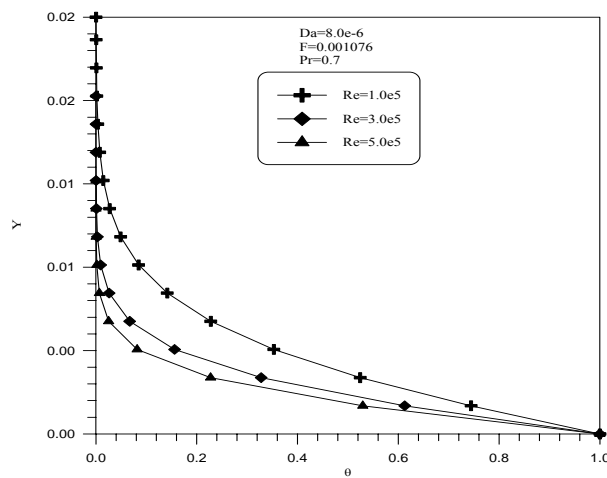


Fig. (7): Effect of Reynolds No. on the Temperature at the Flat Plate End (Linear).

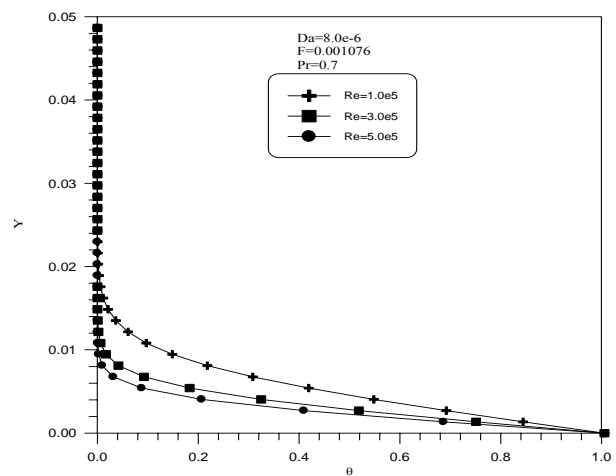


Fig. (8): Effect of Reynolds No. on the Temperature at the End of the Flat Plate (Sinusoidal).

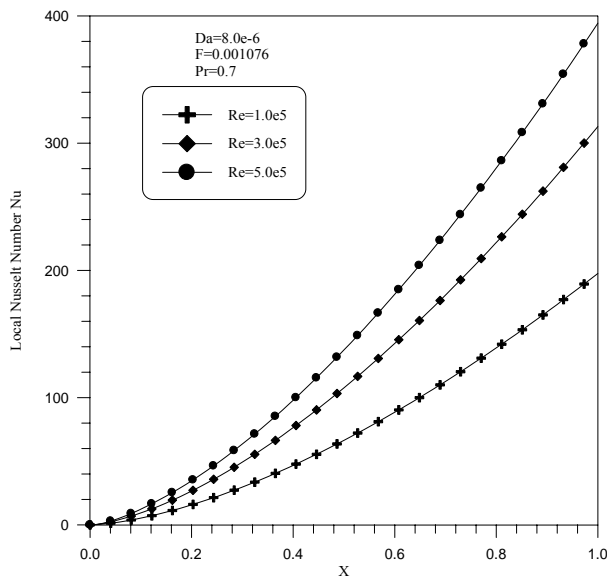


Fig. (9): Effect of the Reynolds Number on the Local Nusselt No. along the Flat Plate (Linear).

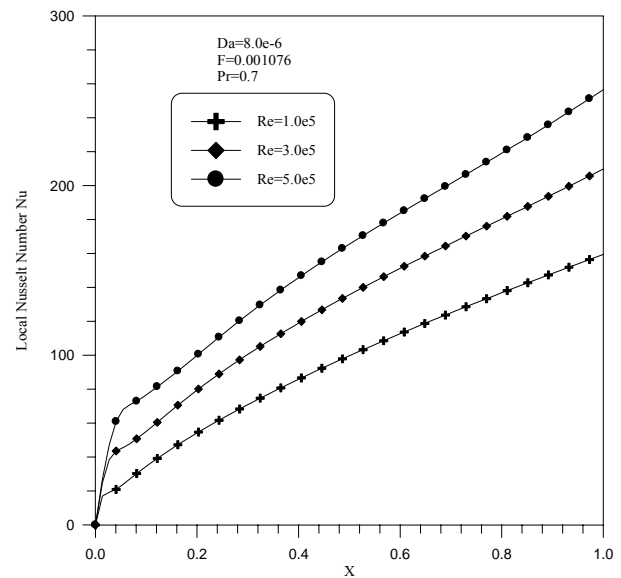


Fig. (10): Effect of the Reynolds Number on the Local Nusselt No. along the Flat Plate (Sinusoidal).

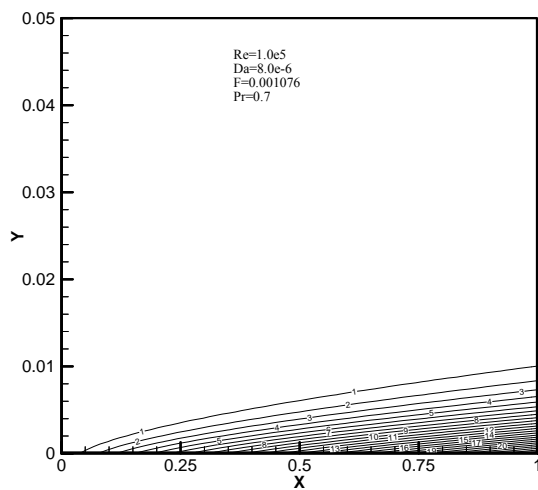


Fig. (11): Distribution of the Non-Dimensional Temp. at Various Reynolds Number (Linear).

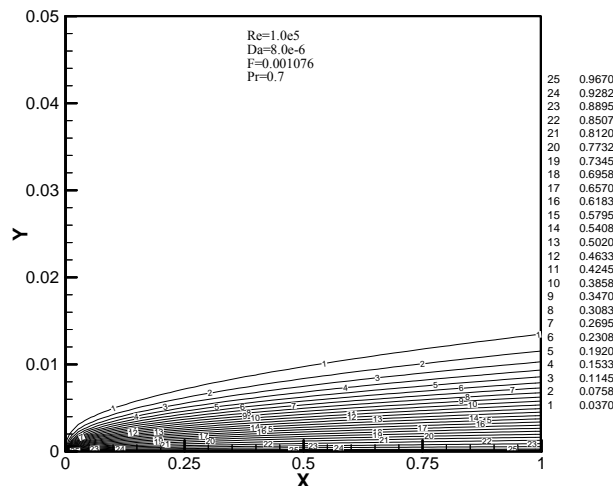
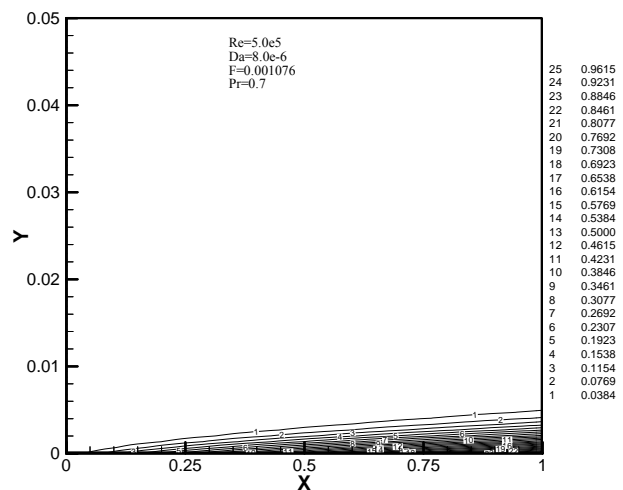


Fig. (12): Distribution of the Non-Dimensional Temp. at Various Reynolds Number (Sinusoidal).

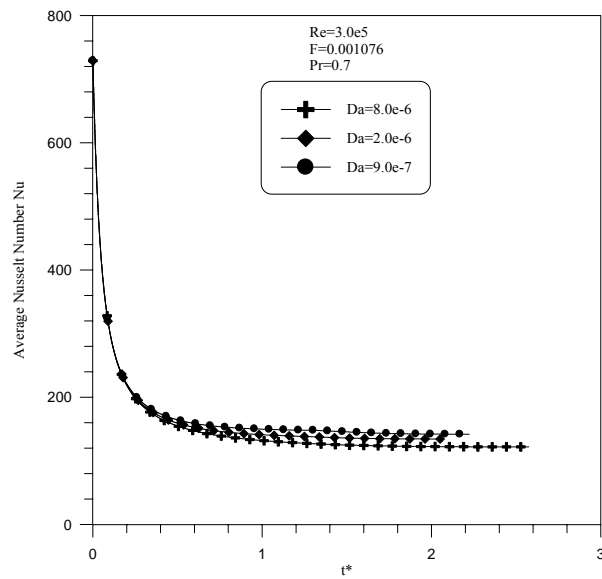


Fig. (13): Effect of Darcy Number on the Average Nusselt Number with Time (Linear).

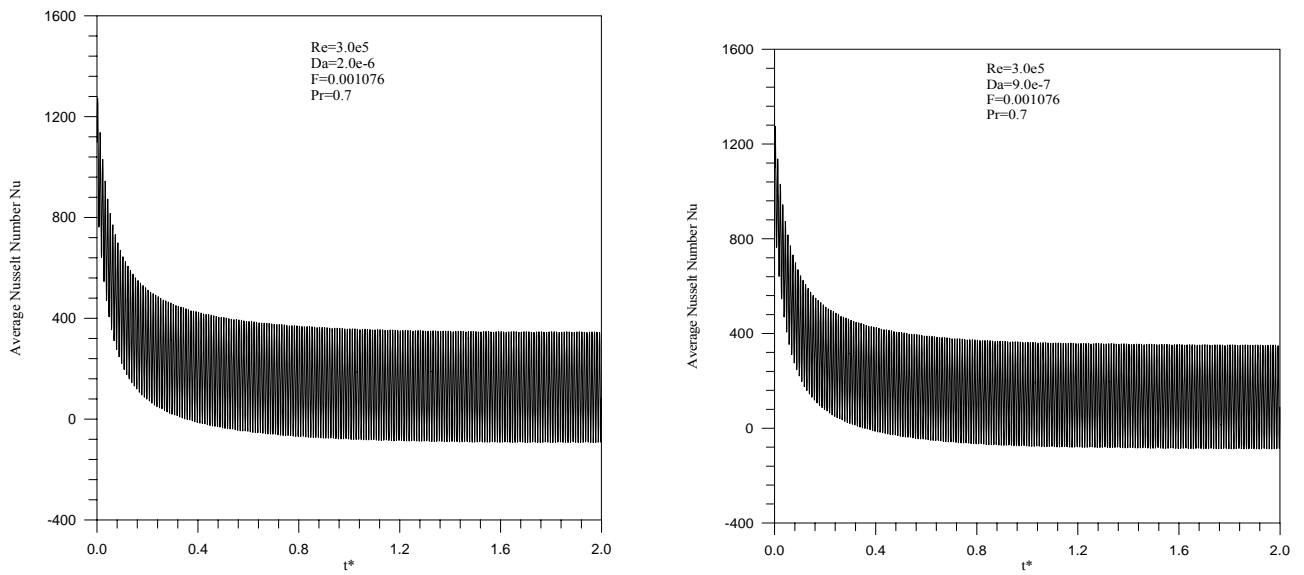


Fig. (14): Effect of Darcy Number on the Average Nusselt Number with Non-Dimensional Time for Specified Reynolds Number (Sinusoidal).

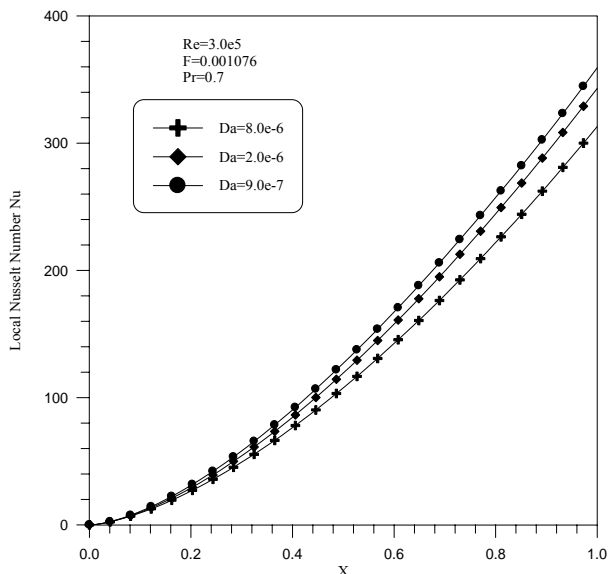


Fig. (15): Effect of Darcy Number on the local Nusselt Number along the Flat Plate (Linear).

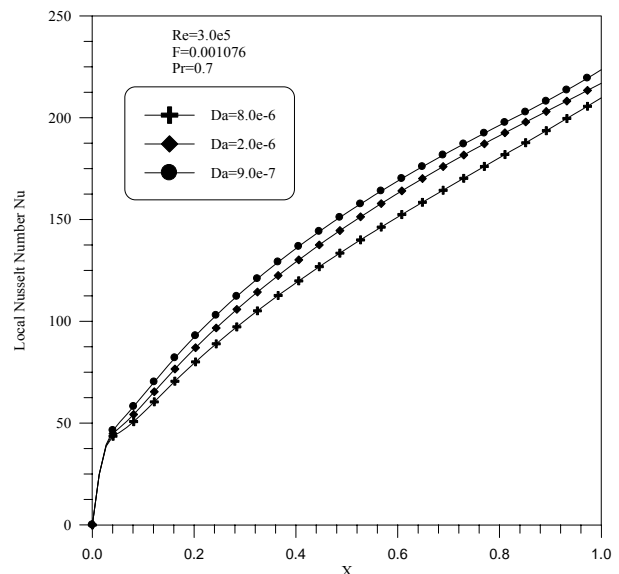


Fig. (16): Effect of Darcy Number on the local Nusselt Number along the Flat Plate (Sinusoidal).

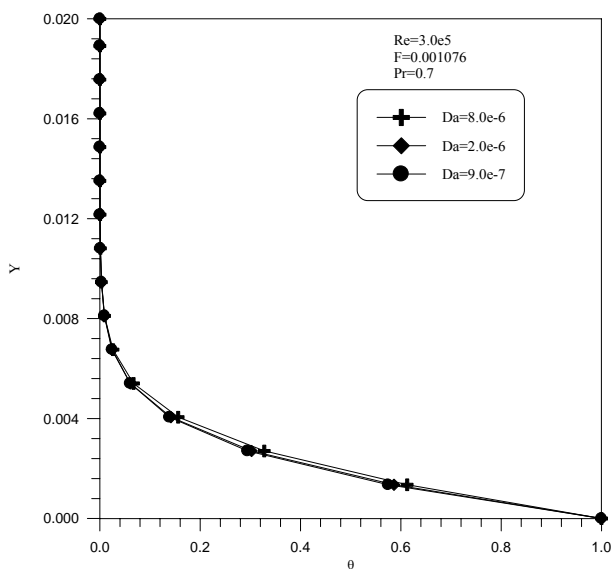


Fig. (17): Effect of Darcy Number on the Non-Dimensional Temp. at the Flat Plate End (Linear).

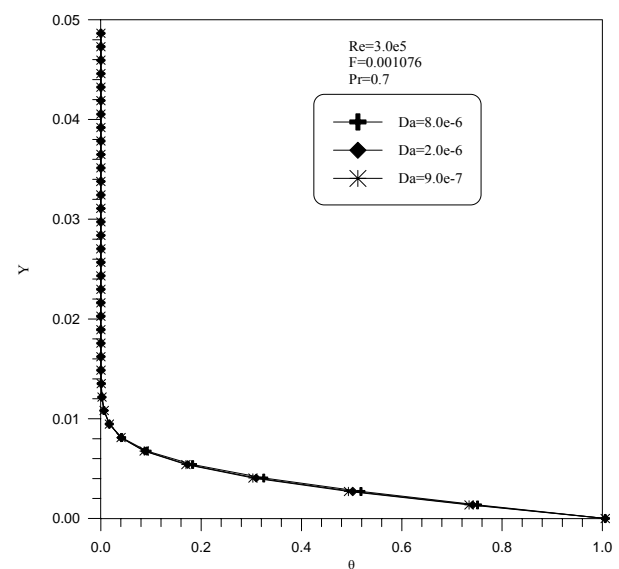


Fig. (18): Effect of Darcy Number on the Non-Dimensional Temp. at the Plate End (Sinusoidal).

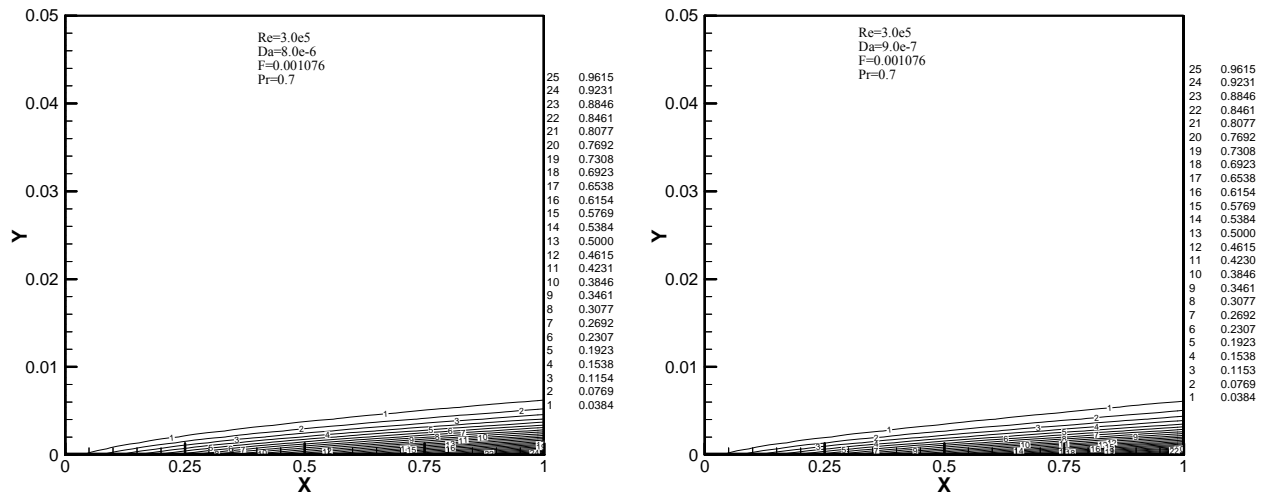


Fig. (19): Distribution of the Non-Dimensional Temp. at Various Darcy Number (Linear)

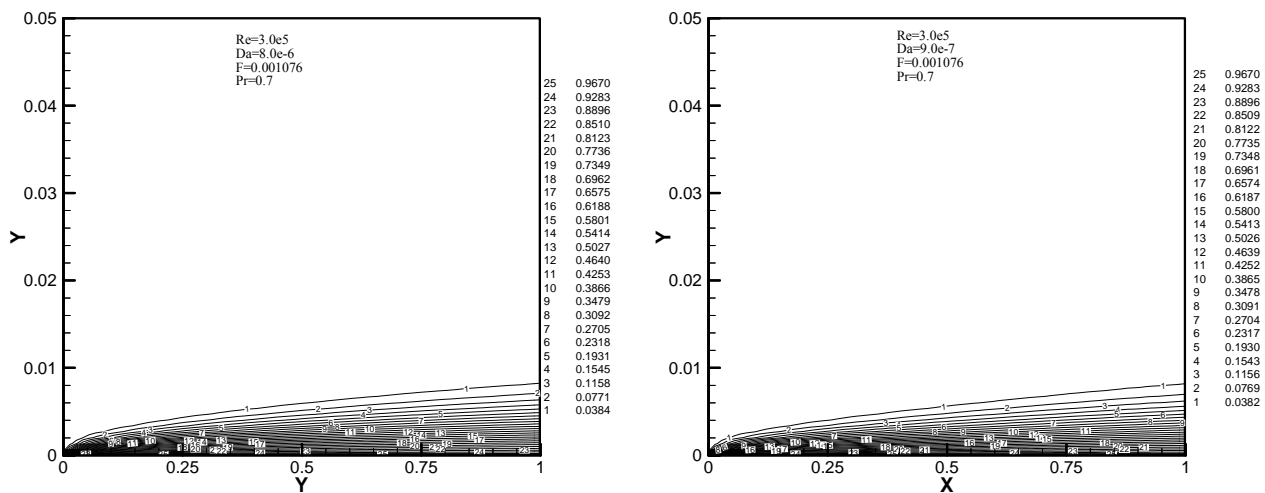


Fig. (20): Distribution of the Non-Dimensional Temp. at Various Darcy Number (Sinusoidal).

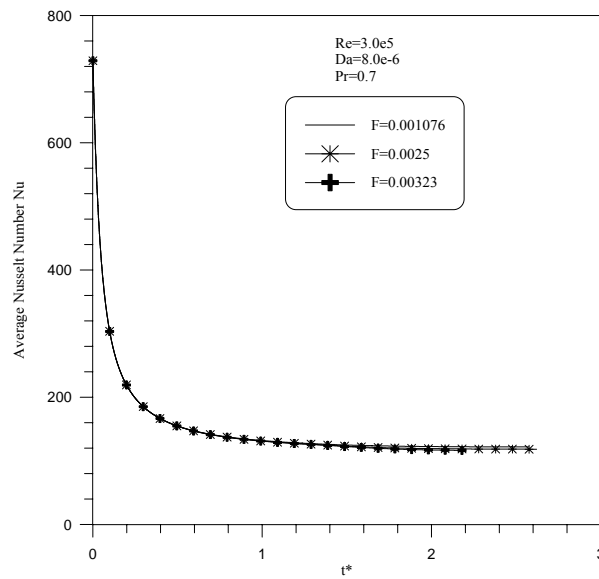


Fig. (21): Effect of Inertia on the Average Nusselt Number with Non-Dimensional Time (Linear).

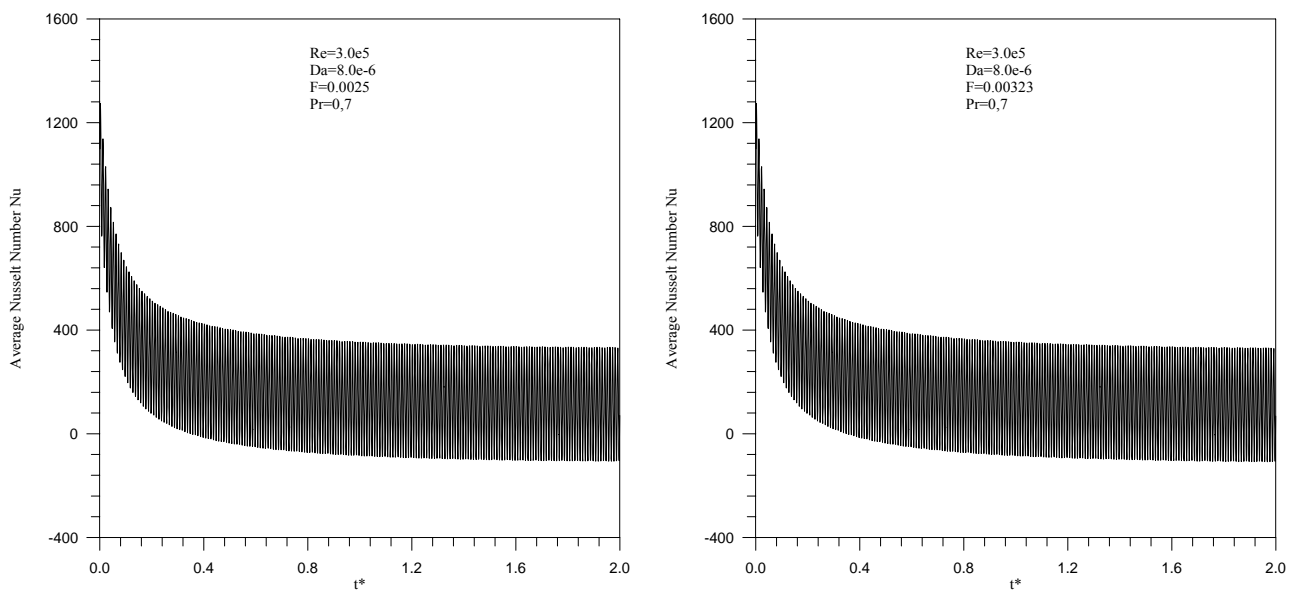


Fig. (22): Effect of Inertia on the Average Nusselt Number with Time (Sinusoidal).

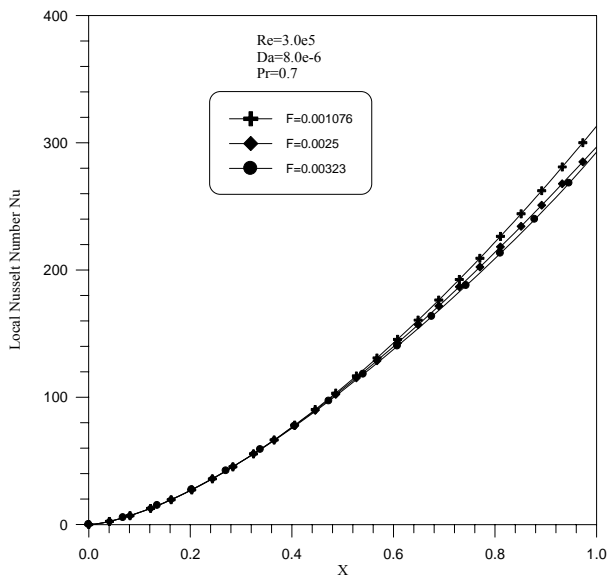


Fig. (23): Effect of Inertia on the local Nusselt Number along the Flat Plate (Linear).

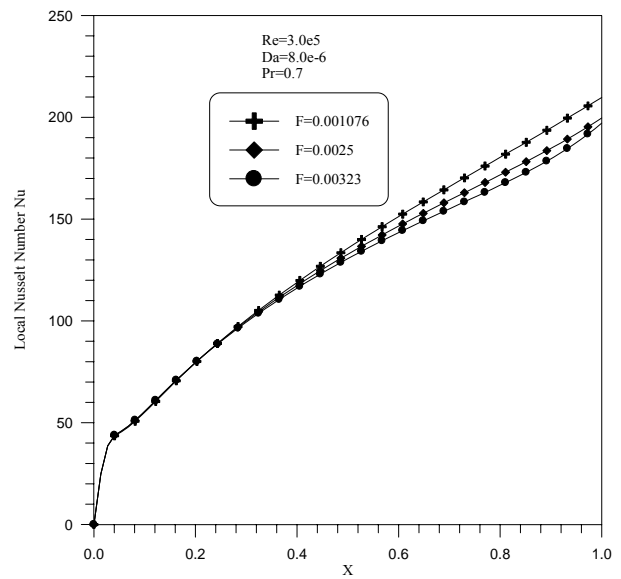


Fig. (24): Effect of Inertia on the local Nusselt Number along the Flat Plate (Sinusoidal).

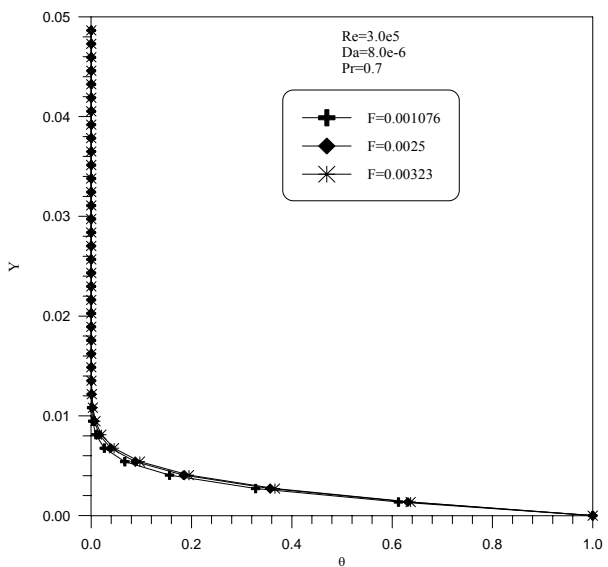


Fig. (25): Effect of Inertia on the Temperature at the Flat Plate End (Linear).

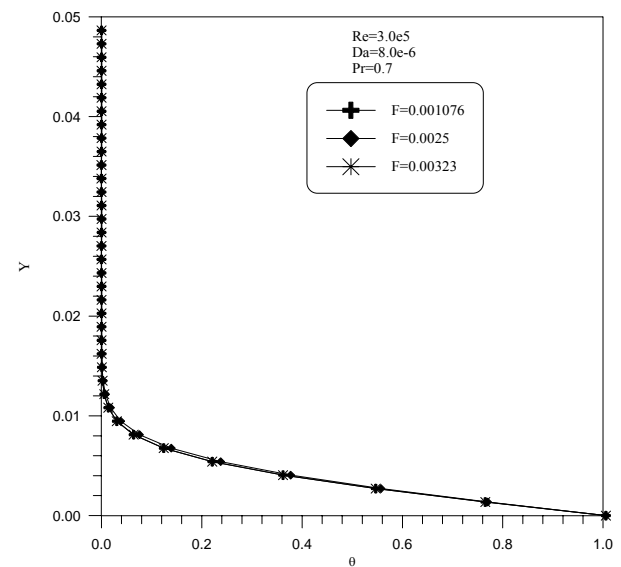


Fig. (26): Effect of Inertia on the Temperature at the End of the Flat Plate (Sinusoidal).

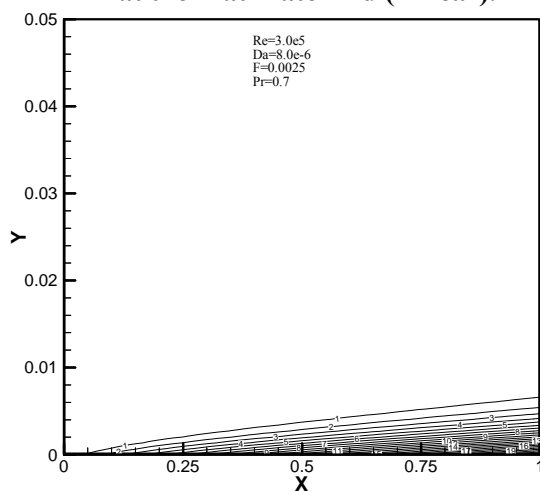
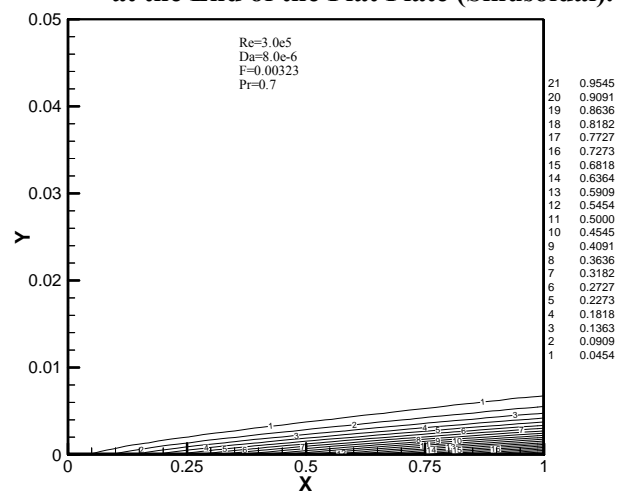


Fig. (27): Effect of Inertia on the Temperature Distribution at Specific Reynolds Number (Linear).



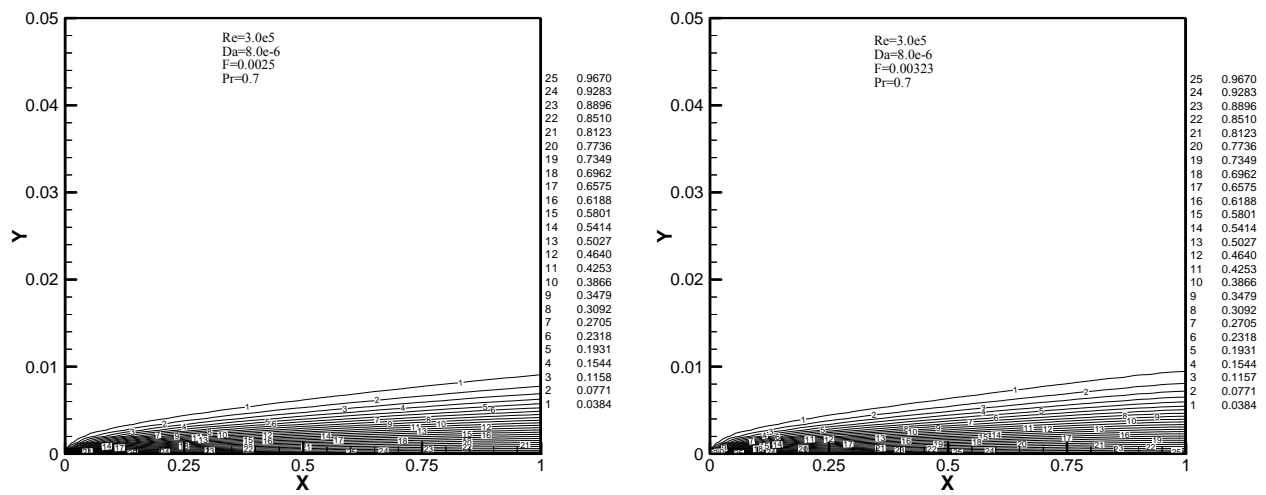


Fig. (28): Effect of Inertia on the Temp. Distribution at Specific Reynolds Number (Sinusoidal).

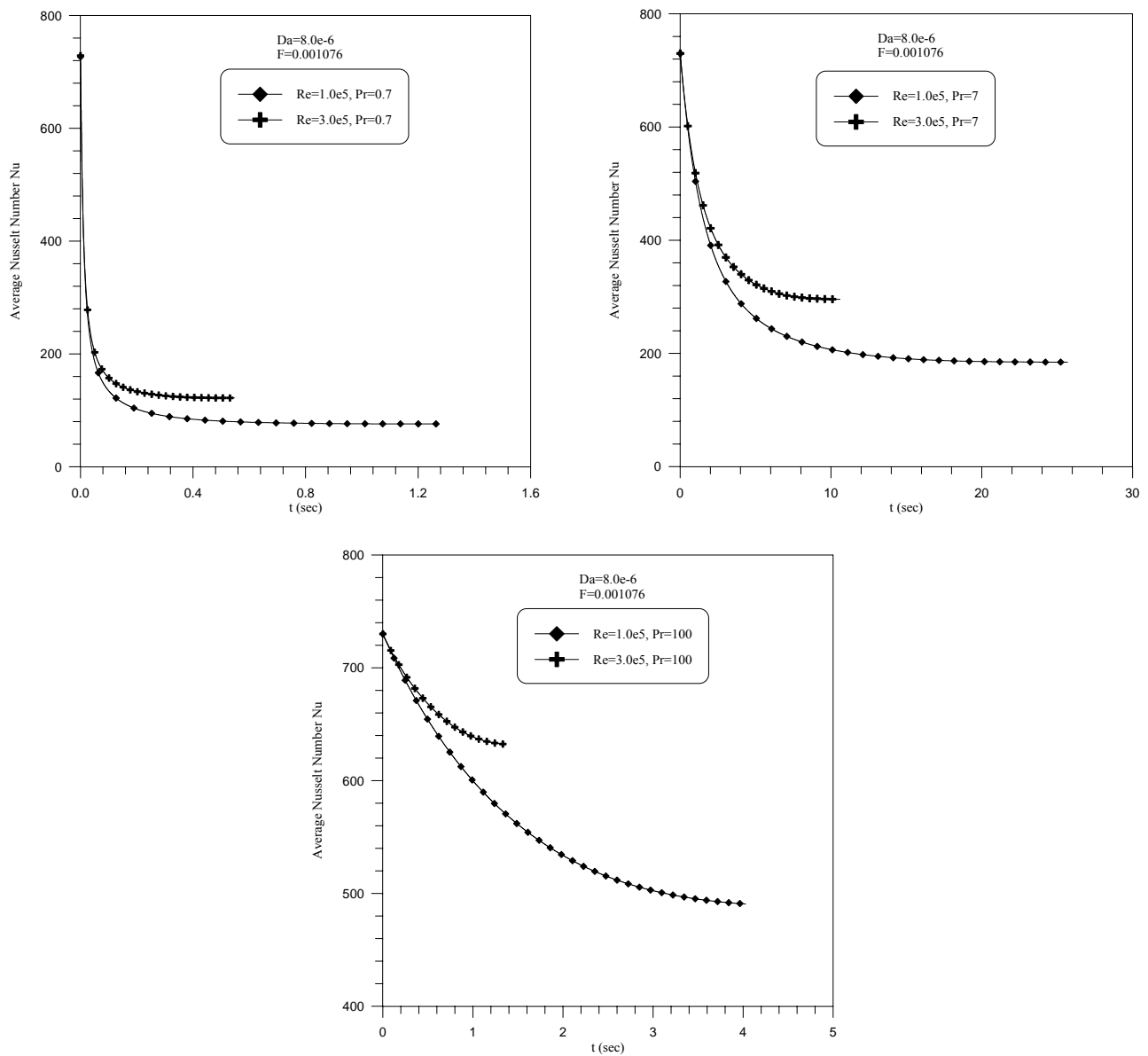


Fig. (29): Effect of Prandtl Number on the Average Nusselt Number Variation with Time at Specific Reynolds Number (Linear).

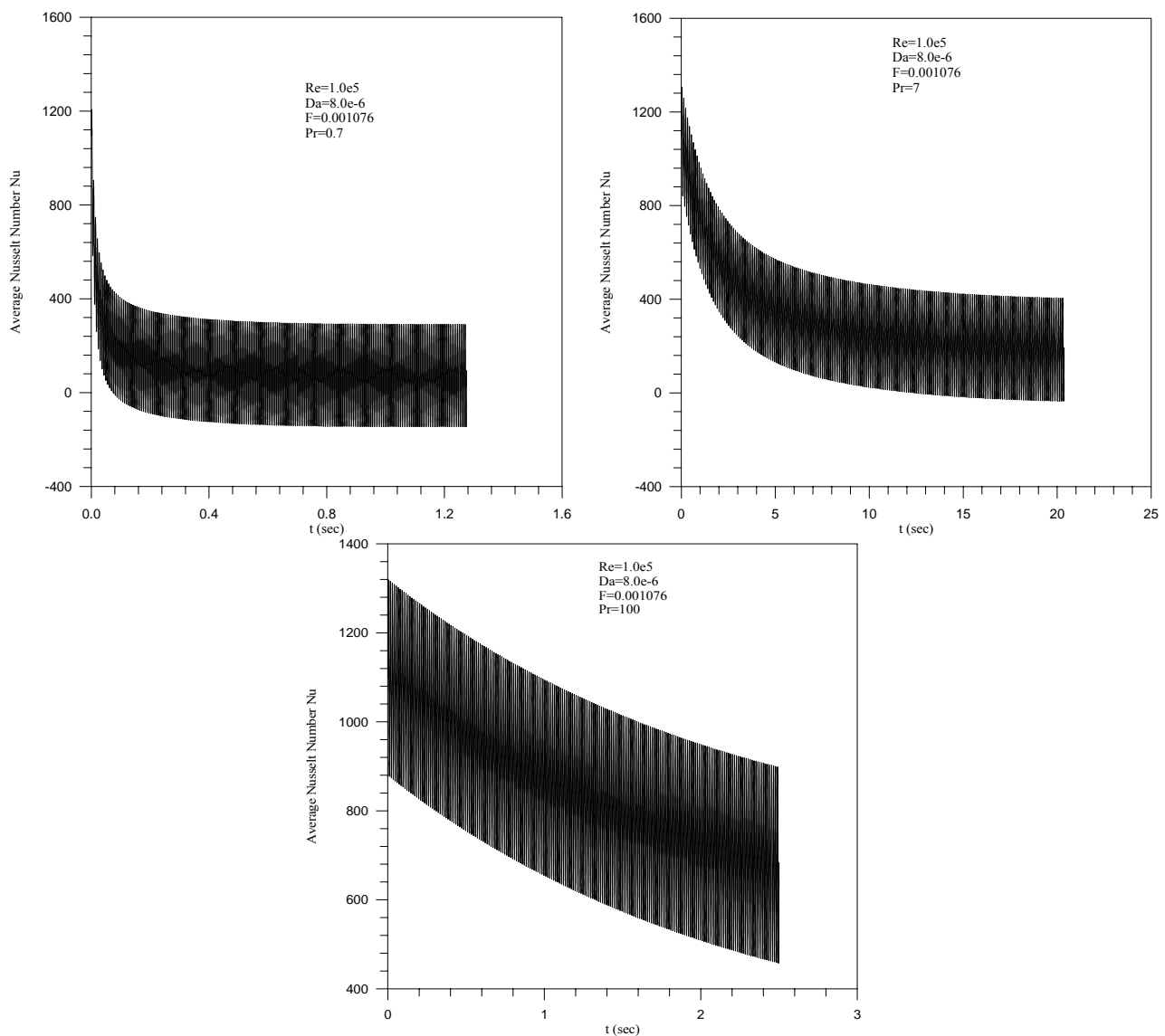


Fig. (30): Effect of Prandtl Number on the Average Nusselt Number Variation with Time at Specific Reynolds Number (Sinusoidal).

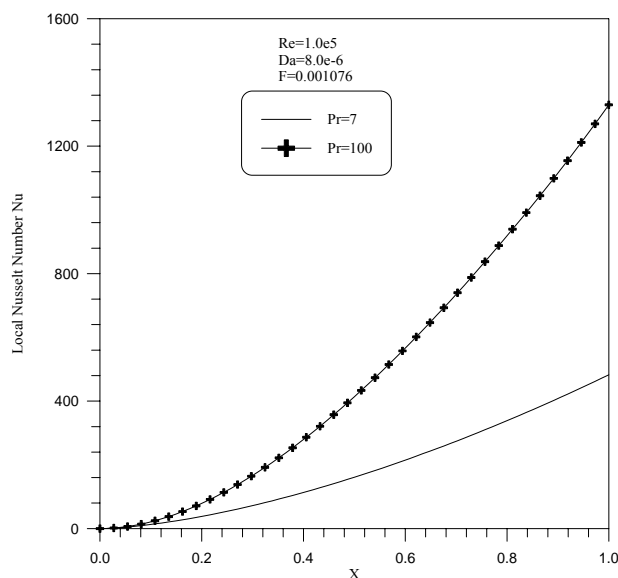


Fig. (31): Effect of Prandtl Number on the Local Nusselt Number Variation with Time (Linear).

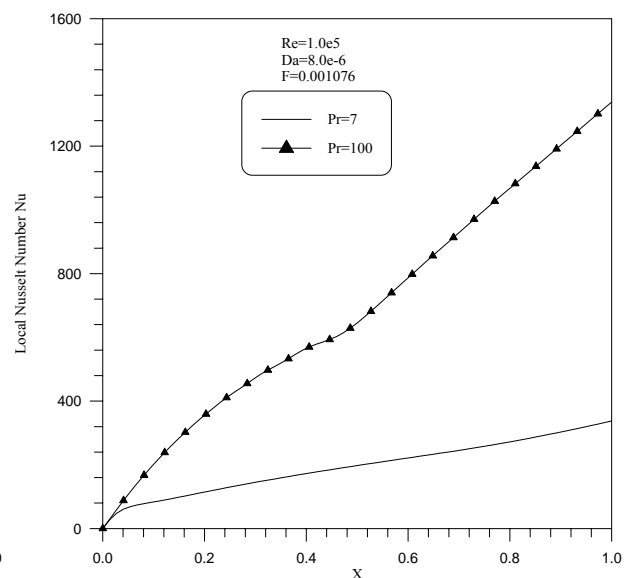


Fig. (32): Effect of Prandtl Number on the Local Nusselt Number Variation with Time (Sinusoidal).

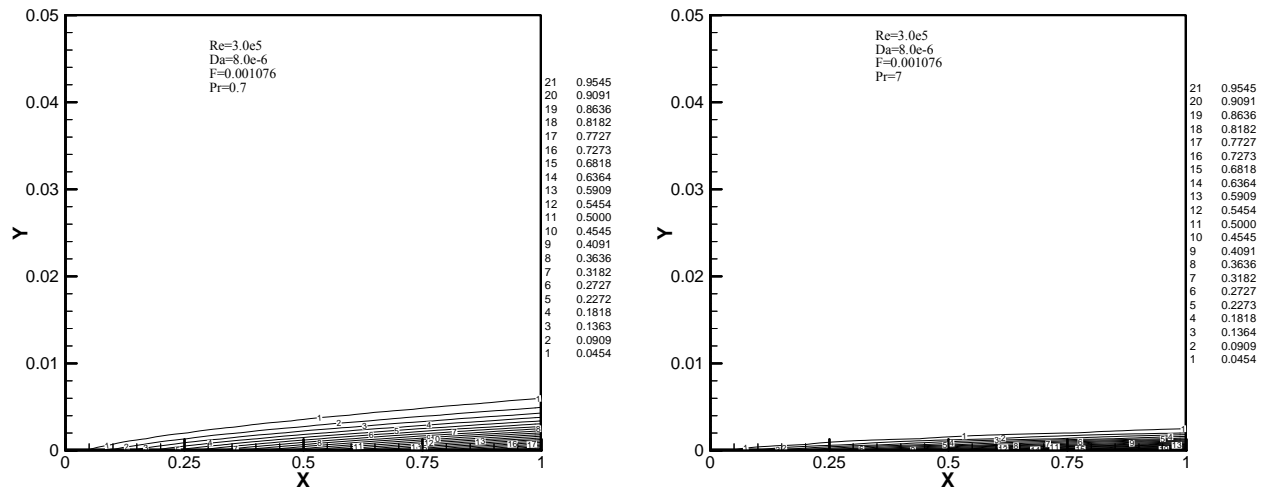


Fig. (33): Effect of Prandtl Number on the Temperature Distribution (Linear).

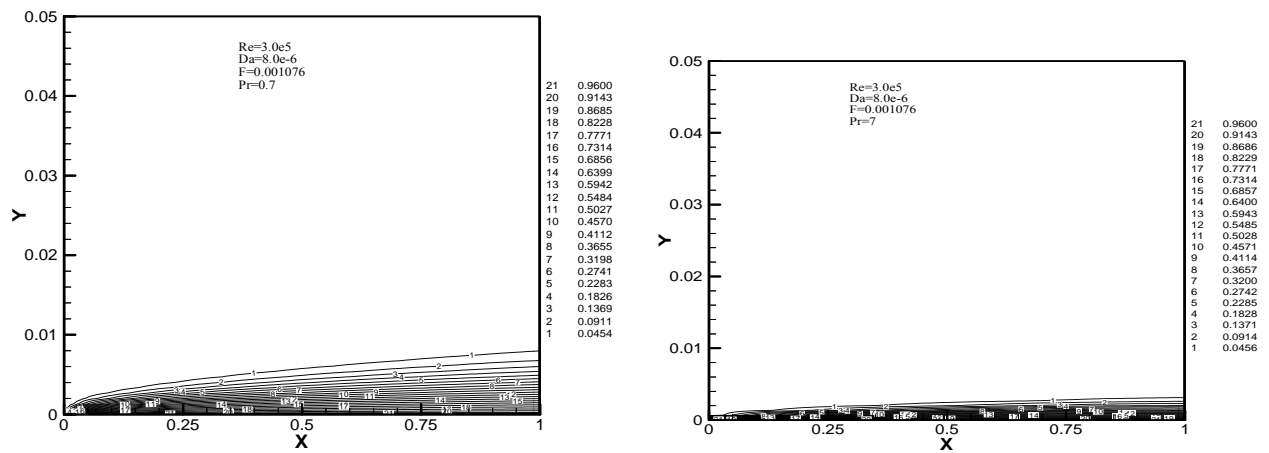


Fig. (34): Effect of Prandtl Number on the Non-Dimensional Temp. Variation (Sinusoidal).

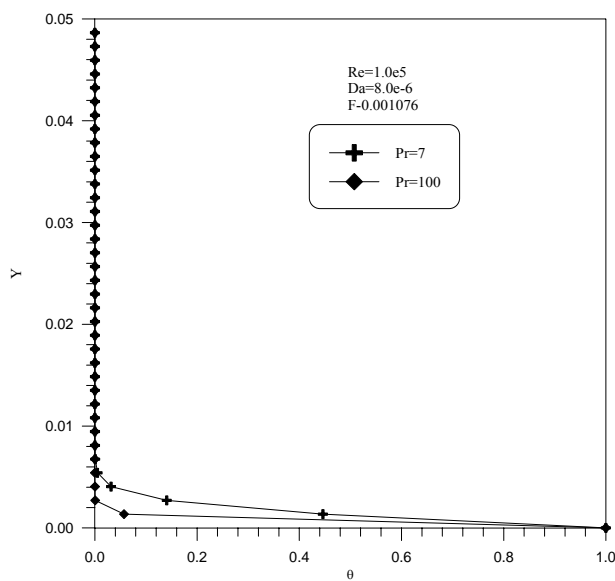


Fig. (35): Effect of Prandtl Number on the Temperature at the Plate End (Linear).

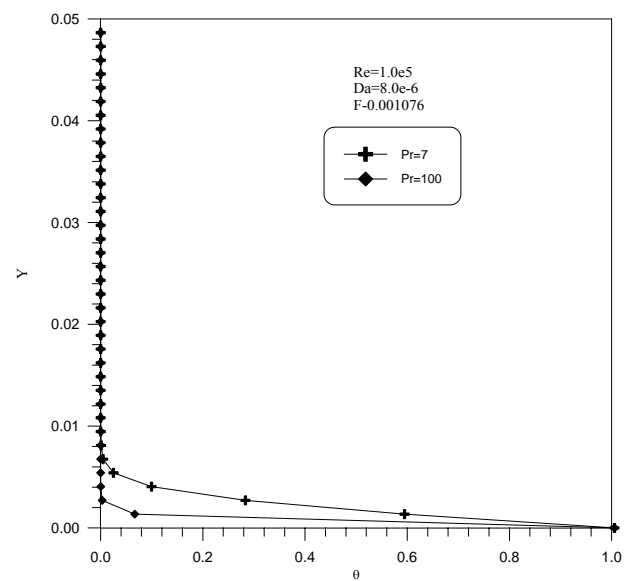


Fig. (36): Effect of Prandtl Number on the Temperature at the Plate End (Sinusoidal).

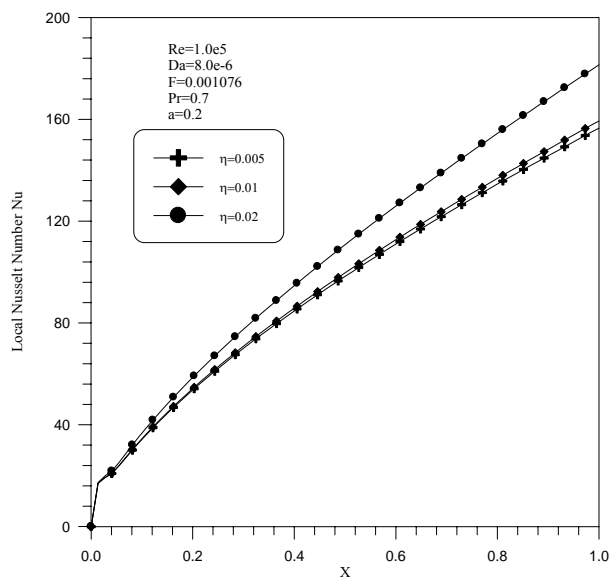


Fig. (37): Effect of Period on the Local Nusselt Number Variation (Sinusoidal).

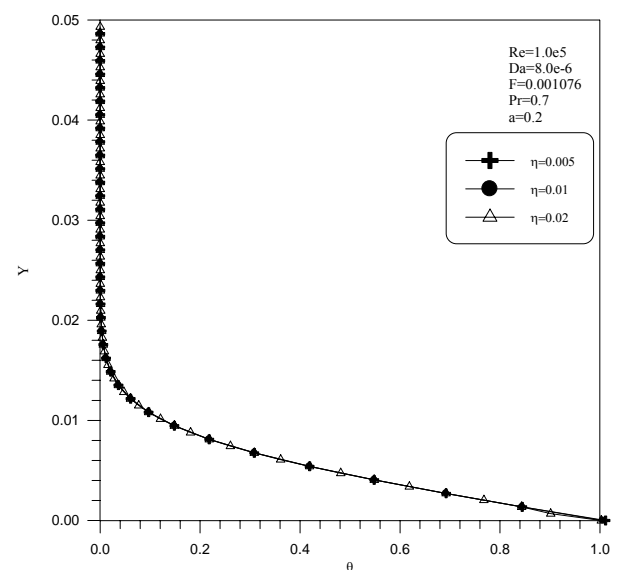


Fig. (38): Effect of Period on the Temperature at the Plate End (Sinusoidal).

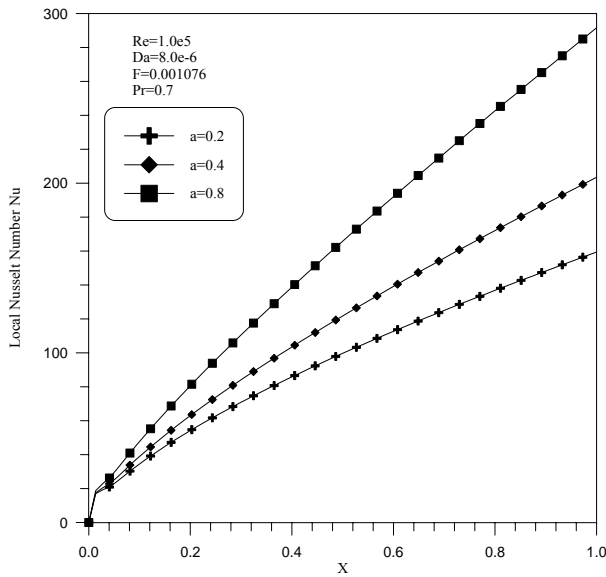


Fig. (39): Effect of Amplitude on the Local Nusselt Number Variation for $\eta = 0.01$ (Sinusoidal).

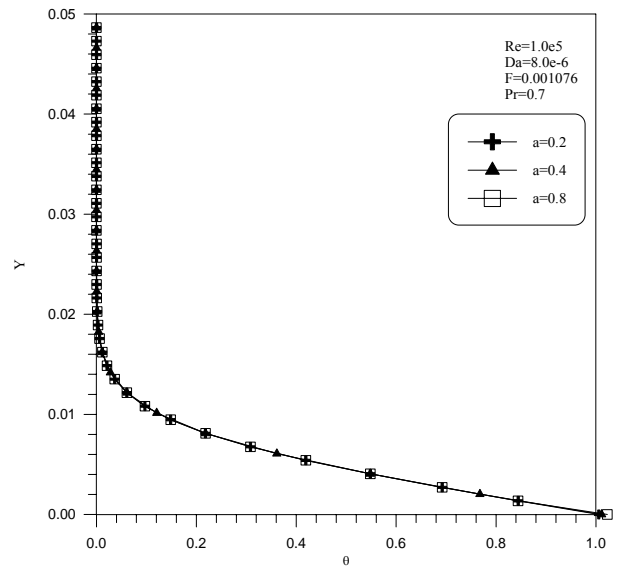


Fig. (40): Effect of Amplitude on the Temperature at the Plate End for $\eta = 0.01$ (Sinusoidal).

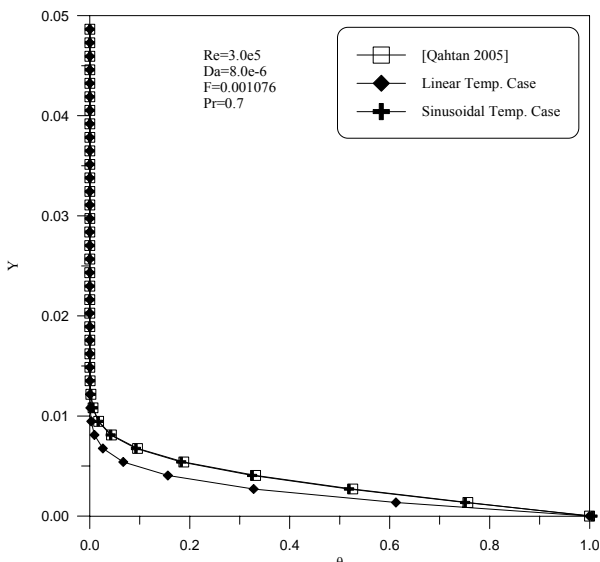


Fig. (41): Comparison of the Temp. at the Plate End for the Two Temp. Cases and Recent Work

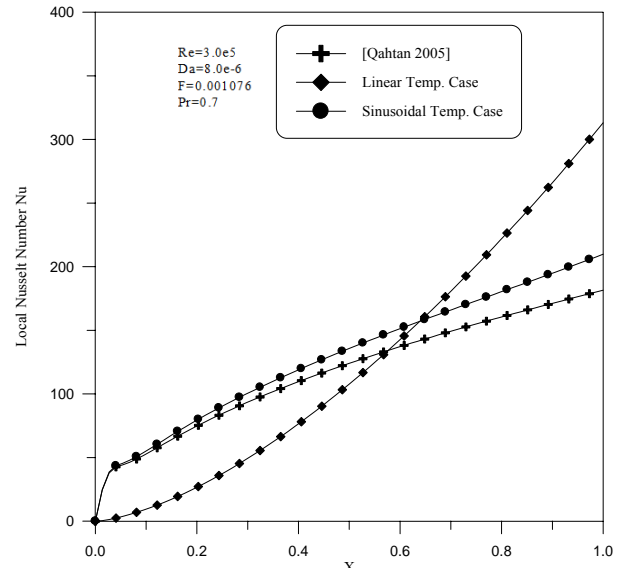


Fig. (42): Comparison of the Local Nusselt Number for the Two Temp. Cases and Recent Work



REMOVAL OF PHOSPHORUS FROM WASTEWATER BY ADSORPTION ONTO NATURAL IRAQI MATERIALS

Ass.Prof.Dr.Majd I. Abdul Wahab* Dr. Awatif Soaded Alsaqqar**Sura Kareem Ali**

*College of Eng./Chemical Eng.Dept.

** College of Eng./Civil Eng.Dept.

ABSTRACT

This study focused on treating wastewater to remove phosphorus by adsorption onto natural and local materials. Burned kaolin, porcelinite, bauxite and limestone were selected to be tested as adsorption materials. The adsorption isotherms were evaluated by batch experiments, studying the effects of pH, temperature and initial phosphorus concentration. The results showed that at pH 6, temperature 20°C and 300 mg/l initial phosphorus concentration; the sorption capacity was 0.61, 9, 10 and 13 mg/g at 10 h contact time, for burned kaolin, porcelanite, limestone and bauxite respectively. As the pH increased from 2 to 10 the removal efficiency for the materials differs in behaviour. The removal efficiency increased from 40 to 90 % for limestone, and decreased from 60 to 30 % for porcelinite. As for bauxite it increased from 60 to 90 % reaching pH 6 then decreased to 30%. Burned kaolin showed the lowest adsorption capacities in these tests. The adsorption isotherms showed that the Langmuir–Freundlich model significantly correlated the experimental data for porcelinite and bauxite, whereby the Freundlich model was best for limestone. The Freundlich and Langmuir–Freundlich models both fit for Burned kaolin. The results show that it is possible to adsorb phosphate from wastewater onto natural Iraqi material and their ability could be ranged as limestone> bauxite> porcelanite> burned kaolin.

KEYWORDS: adsorption, wastewater, phosphorus, bauxite, limestone, porcelanite

الخلاصة

في هذا البحث تمت دراسة طريقة واطئة الكلفة لإزالة الفسفور بالامتزاز وباستعمال مواد طبيعية و محلية. تم اختيار الكاؤولين المحروق، البورسيلينات، البوكسايت و الحجر الكلسي (اللايمستون) كموا محلية في عملية الامتزاز. بدراسة تأثير المتغيرات من الدالة الحامضية، درجة الحرارة، كمية المادة الممتزة، تركيز الفسفور ومدة التماس على عملية الامتزاز. أظهرت النتائج المختبرية، عند الدالة الحامضية 6، درجة الحرارة 20 درجة مئوية و 300 ملغم/ لتر تركيز الفسفور في مياه الفضلات، كانت 0.61، 9، 10 و 13 ملغم/غرام بعد مدة تماس 10 ساعات الكاؤولين للبورسيلينات، الحجر الكلسي و .الكمية الممتزة من الفسفور البوكسايت على التوالي. التجربة وعند زيادة الدالة الحامضية من 2 الى 10 تغيرت نسبة إزالة الفسفور لكل مادة بأسلوب متغاير. زادت نسبة الإزالة من 40 الى 90 %، للحجر الكلسي وانخفضت من 60 الى 30 % للبورسيلينات. اما للبوكسايت زادت من 60 الى 90 % عند الدالة الحامضية 6 ثم انخفضت الى 30 %. مادة الكاؤولين المحروق كانت اضعف المواد لامتزاز الفسفور في هذه التجارب. حللت النتائج المختبرية باستخدام موديلات :

Freundlich and Langmuir–Freundlich

اظهرت النتائج يمكن استخدام هذه المواد في امتزاز الفسفور و كفاءة هذه المواد تترتب بالشكل التالي: الحجر الكلسي < البوكسايت < البورسيلينات < الكاؤولين المحروق.



INTRODUCTION

Discharge of phosphate loaded wastewater is one of the major sources of phosphorus in water bodies, causing environmental problems such as eutrophication and algae bloom. Different types of natural materials have been tested as adsorption media such as minerals, rocks, soils and marine sediments. These materials can be used as substrates with or without pre-treatment in order to optimize the phosphorus sorption capacity. Among the minerals and rock materials are Dolomite and Dolomite sands, Limestone, Opoka, Wollastonite, Bauxites, Zeolites, and soils such as Marl and Spodosols. Marine sediments such as shell sand and maerl have also been investigated (Del et al., 2003; Siddhesh and Robert, 2004; Bernd and Alan, 2006; Benjamin, 2007). A short description of some of these materials is outlined :

Limestone: is a sedimentary rock that has attracted attention as a candidate substrate for phosphorus sorption due to its high content of calcium mainly CaCO_3 . The material has been tested in laboratory as well as in field studies. The main mechanisms for phosphorus sorption were the formation of Ca-complexes and precipitation mechanisms (Johansson, 1999).

Opoka: is marine sediment belonging to a group of silica-calcite sediments, found in the deep strata in the eastern part of Europe it has been suggested suitable for wastewater treatment (Johansson, and Gustafsson, 1998;

Brogowski and Renman, 2004).

Wollastonite: is a calcium metasilicate mineral, which is a by-product from the mining of Wollastonite and garnet (ferrous metasilicate). The material has been investigated with regard to phosphorus sorption capacity by several researchers (Brooks et al., 2000; Hedstrom, 2006).

Natural Zeolite: a group of aluminosilicates and comprise a large number of minerals. Zeolites are characterised by high contents of Si- and Al-oxides, and a three-dimensional structure with channels and pores. Different zeolites have been investigated, and the sorption capacities have been calculated according to the Langmuir equation. When mixing zeolites with natural resources for phosphorus adsorption, they demonstrated to have low sorption capacity which results that it is not recommending for phosphorus removal (Sakadevan and Bavor, 1998; Siddhesh and Robert, 2004; Benjamin, 2007).

ADSORPTION MEDIA

In this work four types of natural local materials supplied by the state company of Geological Survey and Mining were used as adsorption medias for phosphate ions. These materials are Bauxite, Porcelanite, Burned kaolin and limestone, which are obtained from various sites at the western part of Iraq. They are taken from industrial beds in

Tarfawi site the Jandily Vally in Al-Rutba region and the west side of Al-Najaf city. The selected materials have been chosen in this work due to their physical and chemical properties which give their ability to absorb phosphorus on their molecular species from the bulk liquid. Also they are of low cost and are locally available.

The chemical analysis of the adsorption media was achieved by using Atomic Absorption Spectrophotometer type PYE UNICAM SP9 in the state company of Geological Survey and Mining. The composition of each material used in this study is presented in Table 1.

The physical properties of the different adsorption media were analyzed in the Oil Research and Development Center-Ministry of Oil. Table 2 represents the physical properties for the selected materials.

ISOTHERM EXPERIMENTS

Batch experiments were adopted to obtain the equilibrium data. Artificial wastewater was prepared from dissolving KH_2PO_4 at different concentrations, 50, 100, 200 and 300 mg/l. Each adsorbent, ranging in weight 0.1, 1, 5 and 10 g were placed in individual 500 ml plastic bottles. The bottles were placed at fixed positions in a water bath with a shaker (Type: Model BS-11). The bottles

were left for 15min to 120 hrs to permit adsorption to reach equilibrium conditions. The experiments were conducted at 15, 20, 30 and 40°C and the shaker was fixed at a speed of 100 rpm. The experiments were conducted under controlled and uncontrolled pH conditions. Buffer solutions, 0.1M of H_2SO_4 and NaOH were added drop wise to the water to control the pH. In these runs the pH was controlled at 2, 4, 6, 8 and 10. Buffer solutions were not added to the uncontrolled pH experiments. The details of the experimental runs are illustrated in Tables 3 and 4.

SAMPLES ANALYSIS

A spectrophotometer manufactured by Shimadzu Cooperation model UV-160V was used to identify the absorbance or transmittance of each sample at a wavelength of 690 nm. Each sample was filtered with Whatman filter and diluted to appropriate volume using deionized water. One ml of ammonium molybdate solution and 2 drops of stannous chloride were added to the diluted sample. The solution was mixed and the color was allowed to develop for 10 minutes. The resulting blue colored complex was analyzed by visible range colorimetry method on the spectrophotometer and the concentrations of



phosphorus remaining in the solutions were found from the prepared calibration curve

RESULTS AND DISCUSSION

Effect of Initial Phosphate

Concentration

Experiments were undertaken to study the effect of various initial concentrations 50, 100, 200 and 300 mg/l at 20°C on phosphate removal using burned kaolin, porcelanite, bauxite and limestone as adsorbents. The removal efficiency of phosphate from the solution and the sorption capacity (q), were calculated. Figures 1-4 indicate a rapid initial uptake rate of phosphate at the beginning and, thereafter, the adsorption capacity remaining almost constant. The adsorption of phosphate reached equilibrium at variable times according to the initial concentration of phosphate and also to the type of the adsorption media. The higher the initial concentration of phosphate species, the larger is the amount of phosphate species adsorbed. The variation in the extent of adsorption increase is due to the fact that initially, all sites on the surface of sorbent were vacant and the solute concentration gradient was relatively high. Consequently the extent of phosphate species uptake decreases significantly with the increase of contact time, which is dependent on the decrease in the number of vacant sites on the surface of adsorption media. After lapse of

some time, the remaining vacant surface sites are difficult to be occupied due to repulsive forces between the solute molecules on the solid surface and the bulk phase (Mezenner and Bensmaili, 2008; Krishnan and Haridas, 2008; Boujelben et al., 2008, Zhu et al., 2008).

Figures 1 to 4 show that kaolin has a very low adsorption capacity ranging from 0.1 to 0.6 mg/g when increasing the phosphorus concentration from 50 to 300 mg/L. However, the adsorption capacity was high in bauxite 2-13 mg/g, limestone 2-10 mg/g and in porcelanite 2-9 mg/g, showing good adsorption activity in these materials.

It can be observed from Figures 5 to 8 that the percentage of phosphate removal decreased with increasing the initial phosphate concentration. Very low removal was observed using kaolin reaching 6% at 50 and 100 mg/l phosphate and decreased to 4% for 300 mg/l phosphate. High percentage removal ranging from 80-90% was observed with bauxite for the different concentrations of phosphate. As for limestone, 70 to 80% removal was achieved and 50 to 70% for poreclanite.

The lower uptake at higher concentration resulted from an increased ratio of initial number of moles of phosphate to the available surface area hence fractional adsorption becomes dependent on the initial concentration. For a given adsorption dose the total number of available adsorption sites

is fixed thereby adsorbing almost the same amount of adsorbate, thus resulting in a decrease in the percentage removal. Similar conclusions were also observed for the adsorption of phosphate from aqueous solutions onto different materials by Hameed et al., 2007 and Krishnan and Haridas 2008.

EFFECT OF TEMPERATURE

The effect of temperature on the phosphate adsorption rate (q_e) was studied over the temperature range of 15, 20, 30 and 40°C. It can be observed from figures 9-12 that the phosphate adsorption rate on these adsorbents increases with increasing the temperature. This indicates that the adsorption of phosphate ions was favored at higher temperatures. The sorption of phosphate is endothermic, thus the extent of adsorption increased with increasing temperature. Also the difference in the adsorption rate of the studied adsorbents is due to the difference in physical and chemical composition. The maximum adsorption rate was very low in kaolin and increased from about 0.005 to 0.01 mmol/g with increasing the temperature. Bauxite produced the highest adsorption rate 0.14 to 0.15 mmol/g where the rates of porcelanite and limestone were about the same. Similar trend was also observed for phosphate

removal reported by Huang et al., 2008; Krishnan and Haridas 2008; Boujelben et al., 2008 and Zhu et al., 2008.

EFFECT OF PH

To examine the effect of pH on the adsorption of phosphate, batch experiments using phosphate solution with initial concentration of 300 mg/l were conducted. Ten grams of each adsorbent was added to 500 ml of phosphate solution. The pH of the solution increased from 2, 4, 6, 8 and 10. Figure 13 show the effect of pH on the removal efficiency for the selected medias at 10 h contact time and 20°C. A very slight effect of pH on the performance of burned kaolin can be observed where the removal efficiency didn't exceed 4%. For porcelanite and bauxite adsorbents, the removal efficiency increased as the pH increased and reached a maximum value of 65% at pH 4 for porcelanite and 85% at pH 6 for bauxite. As the pH increased to 10, the removal efficiency decreased gradually to about 35% for the two medias. For limestone the situation was different, as the pH increased the removal efficiency increased from 35% to 90%.



MODELING OF SORPTION

EQUILIBRIUM

In order to optimize the design of an adsorption system to remove phosphate from aqueous solutions, it is important to establish the most appropriate correlation for the equilibrium curves. The isotherm data were analyzed using three of the mostly used equilibrium models. Langmuir, Freundlich and Langmuir-Freundlich.

The experiments were conducted at temperatures 15, 20, 30 and 40°C for 10 g adsorbent dose, pH 6, and the initial phosphate concentration ranging 50, 100, 200 and 300 mg/l. The Langmuir model is an ideal model for homogenous monolayer adsorption while the langmuir-Freundlich model is obtained by introducing a power law expression of the Freundlich model into the Langmuir model. The best fit values of the model parameters estimated by linear regression analyses are listed in Tables 5-8 for the different materials. The correlation coefficients (R^2), provides measurement of model fitness. A comparison of the experimental isotherms with the adsorption isotherm models showed that the Langmuir equation represented the poorest fit of the experimental data for burned kaolin as compared to the other isotherm equations. For poreclanite, bauxite and limestone the best fits are Freundlich, Langmuir-Freundlich and Freundlich, repetitively.

CONCLUSIONS

The results of the present study can provide a process for developing a low-cost technology based on adsorption by burned kaolin, porcelanite, bauxite and limestone for phosphate removal from wastewater. The following points can be concluded from the present study:

- Burned kaolin, porcelanite, bauxite and limestone could be employed as adsorbents in the removal of phosphates and their ability could be arranged in the following order: Limestone> Bauxite> Porcelanite> Burned kaolin
- As the initial concentration of phosphate species increases 50 to 300 mg/l, the amount of adsorbed phosphate species on the adsorbent increases. The adsorption capacity in bauxite and limestone and porcelanite ranged 2-13 mg/g with increasing the phosphate concentration in the solution.
- The percent of phosphate removal decreases as the initial concentration of phosphate increases 50 to 300 mg/l. It increased 80-90% in bauxite, 70-80% in limestone and 50-70% in poreclanite. Kaolin showed very low removal efficiency.
- As the temperature increases 15-40°C the adsorption rate increases over the studied adsorbent which indicates that

the adsorption of phosphate was favoured at higher temperature, since the adsorption of phosphate is endothermic. Bauxite showed the highest rate 0.14-0.15 mmol/g where porcelainite and limestone were about the same. Very low rates 0.005-0.01 mmol/g was observed in kaolin.

- The adsorption process is highly dependent on the pH of the solution. For porcelainite and bauxite the removal efficiency increased as the pH increased and reached a maximum value of 65% at pH 4 and 85% at pH 6 for porcelainite and bauxite respectively. Then the removal efficiency decreased. For limestone the situation was different, the removal efficiency increased and reached a maximum value 90% at pH 10.

- The adsorption isotherms of phosphate could be well described by Langmuir-Freundlich models for porcelainite and bauxite, while the Freundlich model for limestone. The two models, Freundlich and Langmuir-Freundlich, could be used for burned kaolin.

REFERENCES

- Benjamin Opoku, 2007, "Suitability of different reactive filter media for onsite wastewater treatment", M.Sc. Thesis, KTH, Architecture and built Environment.

- Bernd Nowacka and Alan T. Stone, 2006, "Competitive adsorption of phosphate and phosphonates onto goethite", water research 40 2201–2209.
- Boujelben N., Bouzid J., Elouear Z., Feki M. and Montiel A., (2008). "Phosphorous removal from aqueous solutions using iron coated natural and engineered sorbents", Journal of Hazardous Materials, 151, 103-110.
- Brogowski, Z. and Renman, G, 2004, "Characterization of Opoka as a Basis for its use in Wastewater Treatment", Polish Journal of Environmental Studies, Vol. 13, No. 1, 15-20.
- Brooks, A.S., Rozenwald, M.N., Geohring, L.D., Lion, L.W., Steenhuis, T.S., 2000, "Phosphorus removal by wollastonite: a constructed wetland substrate", Ecological Engineering 15, 121–132.
- Del M. Bubba, C.A. Arias, H. Brix, 2003, "Phosphorus adsorption maximum of sands for use as media in subsurface flow constructed reed beds as measured by the Langmuir isotherm", Water Research 37, 3390–3400.
- Hameed B.H., Ahmad A.A., N. Aziz, 2007, "Isotherms, kinetics and thermodynamics of acid dye adsorption on activated palm ash", Chemical Engineering Journal 133, 195–203.
- Hedstrom A., 2006, "Wollastonite as reactive filter medium for sorption of wastewater ammonium and phosphorus", Environmental Technology, vol. 27, 7, pp. 801-809.
- Huang W., Wang S., Zhu Z., Li, L., Yao X., Rudolph V. and Haghseresht F., 2008, "Phosphate removal from



wastewater using red mud”, *Journal of Hazardous Materials* 158, 35-42.

- Johansson, L., 1999 “Industrial by-products and natural substrata as phosphorus sorbents”, *Environmental Technology* 20, 309–316.
- Johansson, L., and Gustafsson, J.P., 1998, “Phosphate removal using Blast Furnace Slags and Opoka-mechanisms”, *Water Research*.34: 259-265.
- Krishnan K.A. and Haridas A., 2008. “Removal of phosphate from aqueous solutions and sewage using natural and surface modified coir pitch”, *Journal of Hazardous Materials* 152, 527-535.
- Mezenner N.Y. and Bensmaili A., 2008, “Kinetics and thermodynamics study of phosphate adsorption on iron hydroxide-eggshell waste”, *Chemical Engineering Journal*, Article in press.
- Sakadevan, K., and Bavor, H. J., 1998. Phosphate adsorption characteristic of soils, slags and zeolite to be used as substrates in constructed wetland systems. *Water Resources* 32 (2): 393-399.
- Siddhesh Shevade and Robert G. Ford, 2004, “Use of synthetic zeolites for arsenate removal from pollutant water”, *Water Research* 38, 3197–3204.
- Zhu M. X., Ding K.Y., Xu S.H. and Jiang X., 2008, “Adsorption of phosphate on hydroxyaluminum-and hydroxyiron-montmorillonite complexes”, *Journal of Hazardous Materials*, Article in press.



Table 1 Chemical Composition of Adsorption Media

Material	SiO ₂	Al ₂ O ₃	Fe ₂ O ₃	MgO	CaO	SO ₃	L.O.I
	Wt. %						
Bauxite	30.25	60.59	1.19	2.48	6.45	-	0.14
Porcelanite	59.5	28.25	1.08	<1	<1	-	0.1
Burned Kaolin	53.95	40.49	1.21	0.95	2.46	0.80	0.14
Limestone	5.000	4.000	2.50	2.50	85.3	-	0.7

Table 2 Physical Properties of the Adsorption Media

Material	Surface Area, m ² /g	Pore Volume cm ³ /g	Bulk Density g/cm ³
Bauxite	82.02	0.18	0.78
Porcelanite	16.68	0.25	1.05
Burned Kaolin	0.23	0.03	1.10
Limestone	9.17	0.26	0.83

Table 3 Controlled pH Experiments

Run	Temp. °C	pH	Time hr	Phosphate concentration mg/l	Weight of adsorbent g	Particle mesh no.	Type of adsorbent
1	20	2, 4, 6, 8 and 10	0.25 -120	300	10	(8-16)	Limestone
2	20	2, 4, 6, 8 and 10	0.25 -120	300	10	(8-16)	Kaolin
3	20	2, 4, 6, 8 and 10	0.25 -120	300	10	(8-16)	Bauxite
4	20	2, 4, 6, 8 and 10	0.25 -120	300	10	(8-16)	Porcelanite

Table 4 Uncontrolled pH Experiments

Run	Temp., °C	Time hr	Initial concentration mg/l	Weight of adsorbent g	Particle mesh no.	Type of adsorbent
1	15, 20, 30 and 40	0.25 up to 48	50, 100, 200 and 300	0.1, 1, 5 and 10	(8-16)	Limestone
2	15, 20, 30 and 40	0.25 up to 48	50, 100, 200 and 300	0.1, 1, 5 and 10	(8-16)	Kaolin
3	15, 20, 30 and 40	0.25 up to 48	50, 100, 200 and 300	0.1, 1, 5 and 10	(8-16)	Bauxite
4	15, 20, 30 and 40	0.25 up to 48	50, 100, 200 and 300	0.1, 1, 5 and 10	(8-16)	Porcelanite

Table 5 Isotherm Constants for Phosphate Adsorption onto Burned kaolin

M.I. Abdul Wahab A. S. Alsaqqar S. K. Ali	Removal Of Phosphorus From Wastewater By Adsorption Onto Natural Iraqi Materials
---	---

Parameters	Temperature, °C			
	15	20	30	40
Langmuir				
q_m mmol/g	0.011	0.011	0.012	0.015
b (L/mmol)	0.327	0.482	0.594	0.709
R^2	0.974	0.981	0.966	0.993
Freundlich				
n	1.073	1.584	1.509	1.699
k_f (mmolL ^{-1/n} g ⁻¹ L ^{1/n})	0.003	0.003	0.005	0.520
R^2	0.992	0.998	0.994	0.997
Langmuir-Freundlich				
n	0.998	0.991	0.975	1.010
k (mmol/L)	2.725	2.744	2.780	26.60
R^2	0.994	0.993	0.978	0.994

Table 6 Isotherm Constants for Phosphate Adsorption onto Porcelanite

Parameters	Temperature, °C			
	15	20	30	40
Langmuir				
q_m mmol/g	0.138	0.173	0.176	0.156
b (L/mmol)	0.851	0.736	1.389	3.433
R^2	0.985	0.966	0.975	0.983
Freundlich				
n	1.465	1.361	1.452	1.780
k_f (mmolL ^{-1/n} g ⁻¹ L ^{1/n})	0.061	0.073	0.109	0.139
R^2	0.989	0.986	0.965	0.952
Langmuir-Freundlich				
n	0.998	1.019	1.047	1.018
k (mmol/L)	2.722	2.670	130.1	122.8
R^2	0.989	0.987	0.968	0.955

Table 7 Isotherm Constants for Phosphate Adsorption onto Bauxite

Parameters	Temperature, °C			
	15	20	30	40
Langmuir				
q_m (mmol/g)	0.960	0.260	0.227	0.205
b (L/mmol)	0.332	4.816	3.447	18.88
R^2	0.953	0.961	0.999	0.951
Freundlich				
n	1.073	1.403	1.509	1.699
k_f (mmolL ^{-1/n} g ⁻¹ L ^{1/n})	0.264	0.404	0.248	0.520
R^2	0.999	0.998	0.991	0.878
Langmuir-Freundlich				
n	1.003	0.999	1.039	0.987
k (mmol/L)	283.7	19.82	25.00	4.953
R^2	0.999	0.999	0.992	0.954



Table 8 Isotherm Constants for Phosphate Adsorption onto Limestone

Parameters	Temperature, °C			
	15	20	30	40
Langmuir				
q_m mmol/g	0.227	0.185	0.134	0.133
b (L/mmol)	0.829	1.336	6.713	16.29
R^2	0.988	0.956	0.989	0.987
Freundlich				
n	1.313	1.505	2.286	3.142
k_f (mmolL ^{-1/n} g ⁻¹ L ^{1/n})	0.107	0.109	0.131	0.142
R^2	0.993	0.998	0.996	0.991
Langmuir-Freundlich				
n	0.997	1.037	1.081	1.304
k (mmol/L)	115.9	62.56	11.25	3.098
R^2	0.998	0.999	0.973	0.902

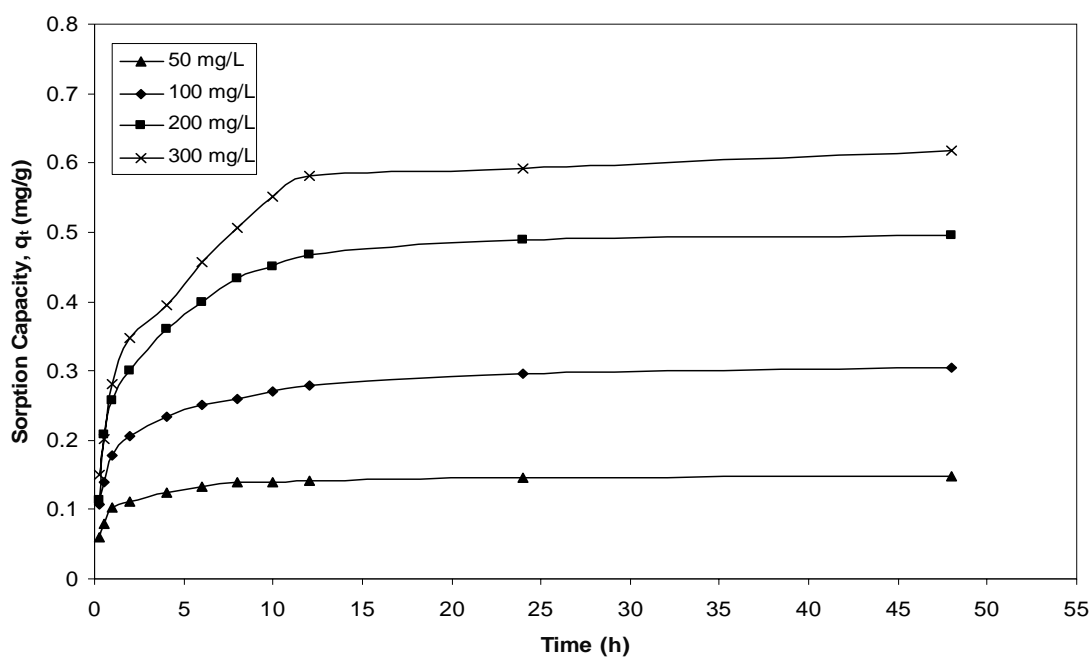


Figure 1 Variation of Sorption Capacity for burned kaolin at several initial phosphate concentrations at 20°C and pH 6.

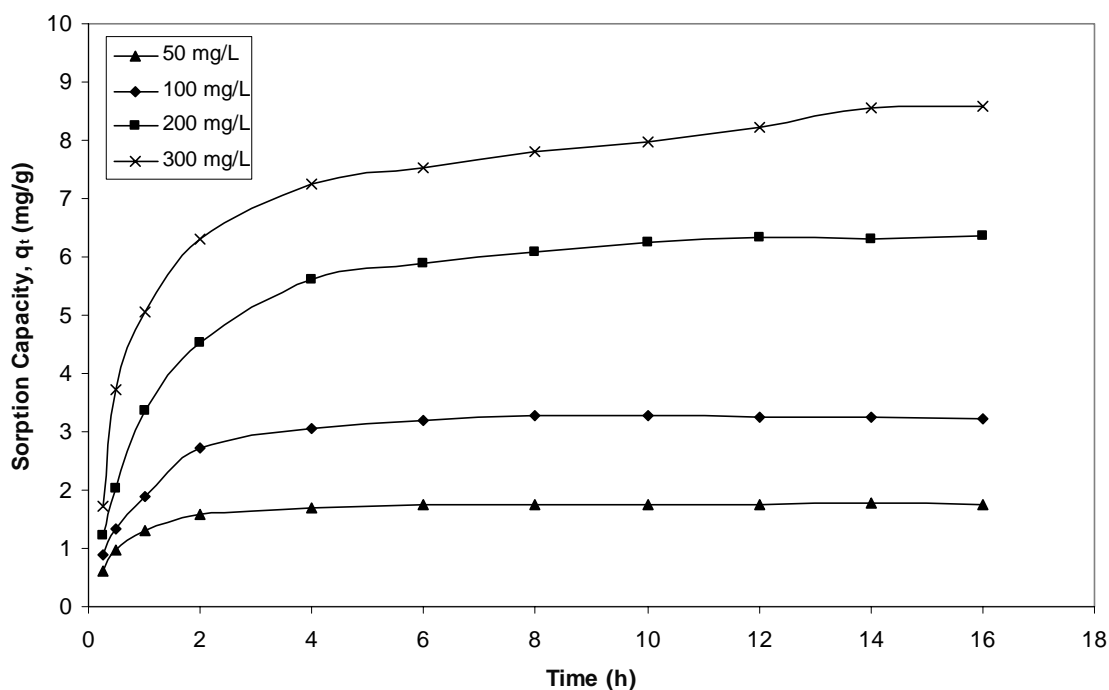


Figure 2 Variation of Sorption Capacity for Porcelanite at several initial phosphate concentrations at 20°C and pH 6.

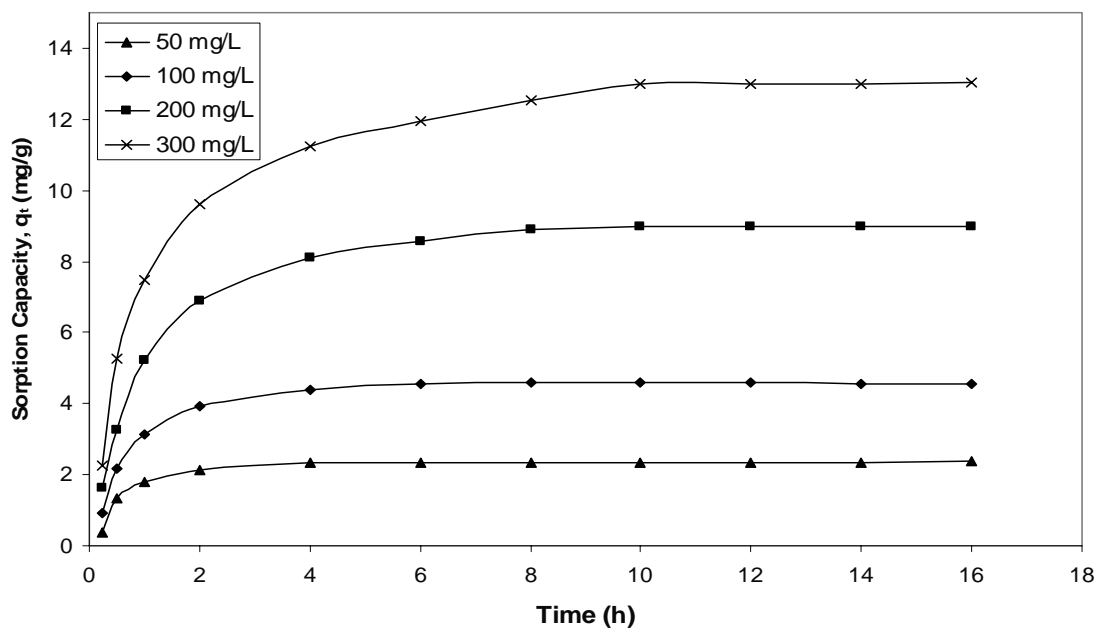


Figure 3 Variation of Sorption Capacity for Bauxite at several initial phosphate concentrations at 20°C and pH 6.

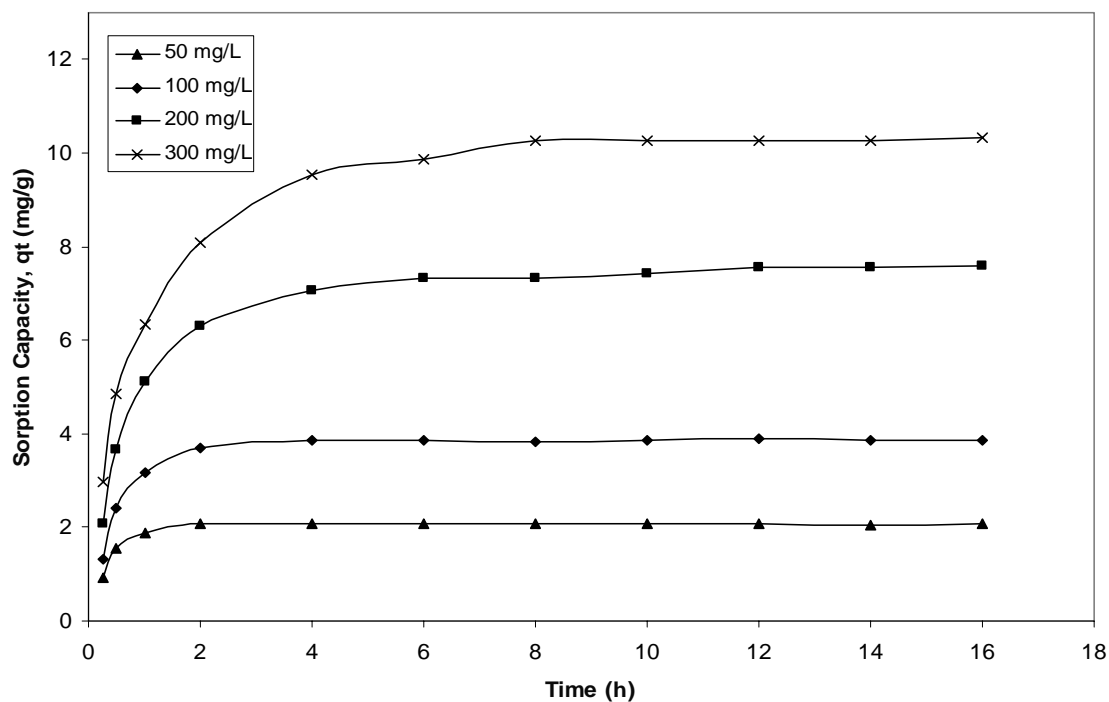


Figure 4 Variation of Sorption Capacity for Limestone at several initial phosphate concentrations at 20°C and pH 6.

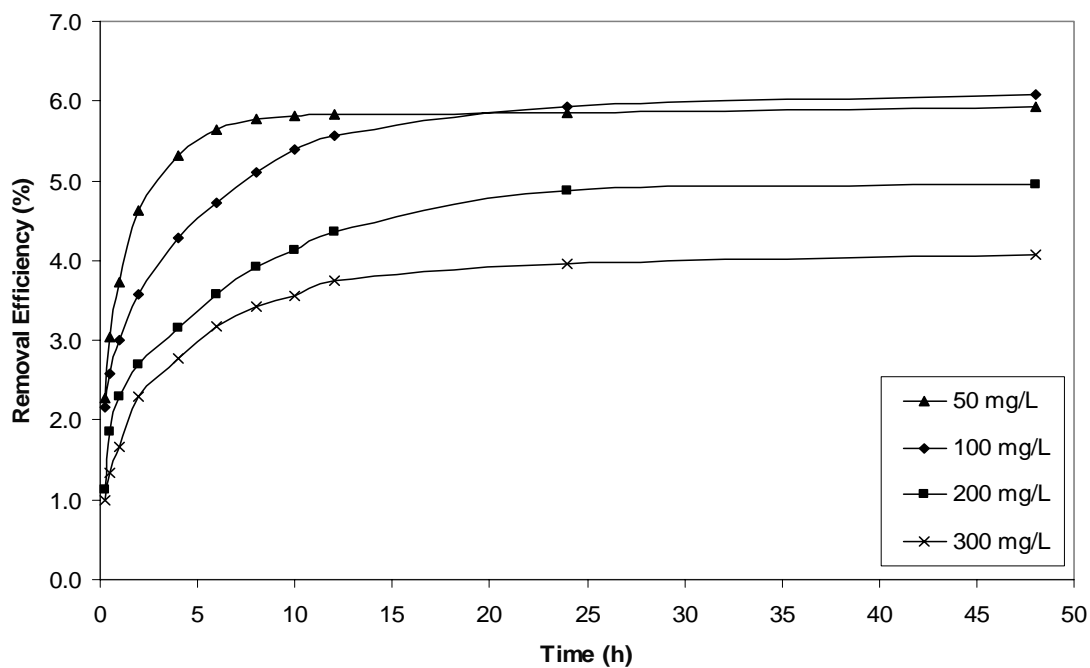


Figure 5 Effect of initial concentration of phosphate ions in the solution on removal efficiency onto Burned kaolin at 20°C, pH 6.

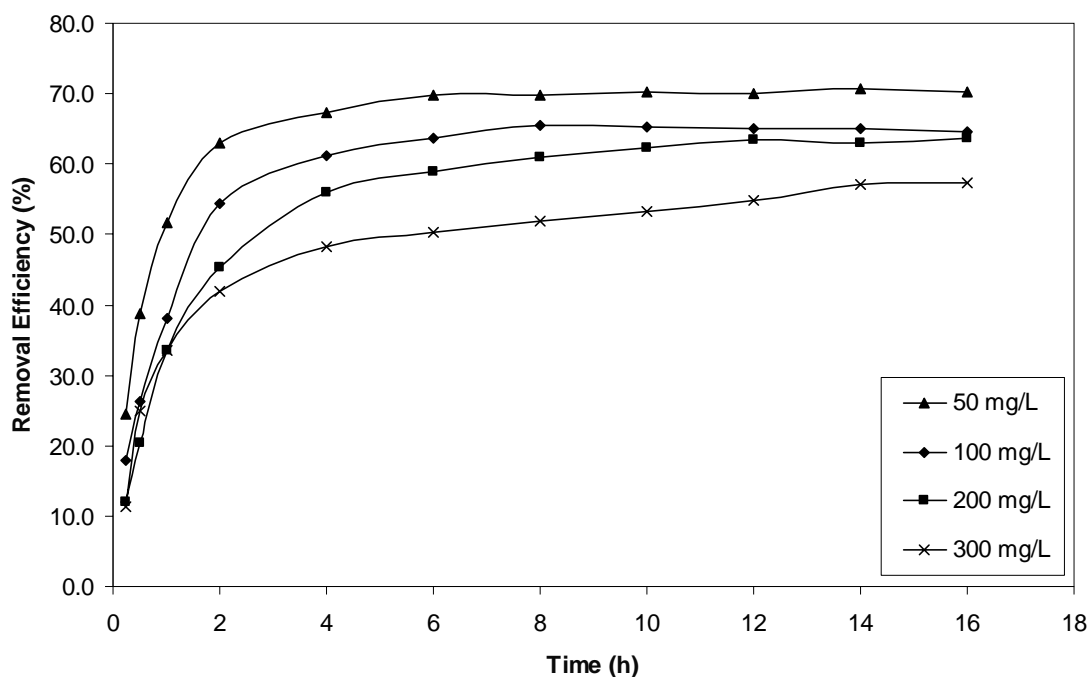


Figure 6 Effect of initial concentration of phosphate ions in the solution on removal efficiency onto Porcelanite at 20°C, pH 6.

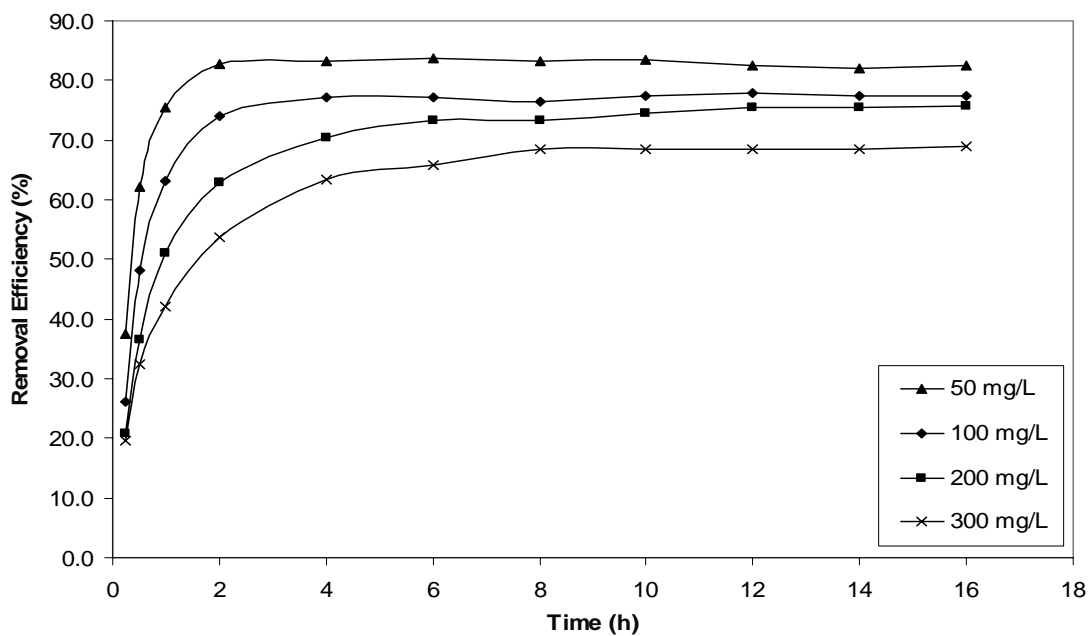


Figure 7 Effect of initial concentration of phosphate ions in the solution on removal efficiency onto Bauxite at 20°C, pH 6.

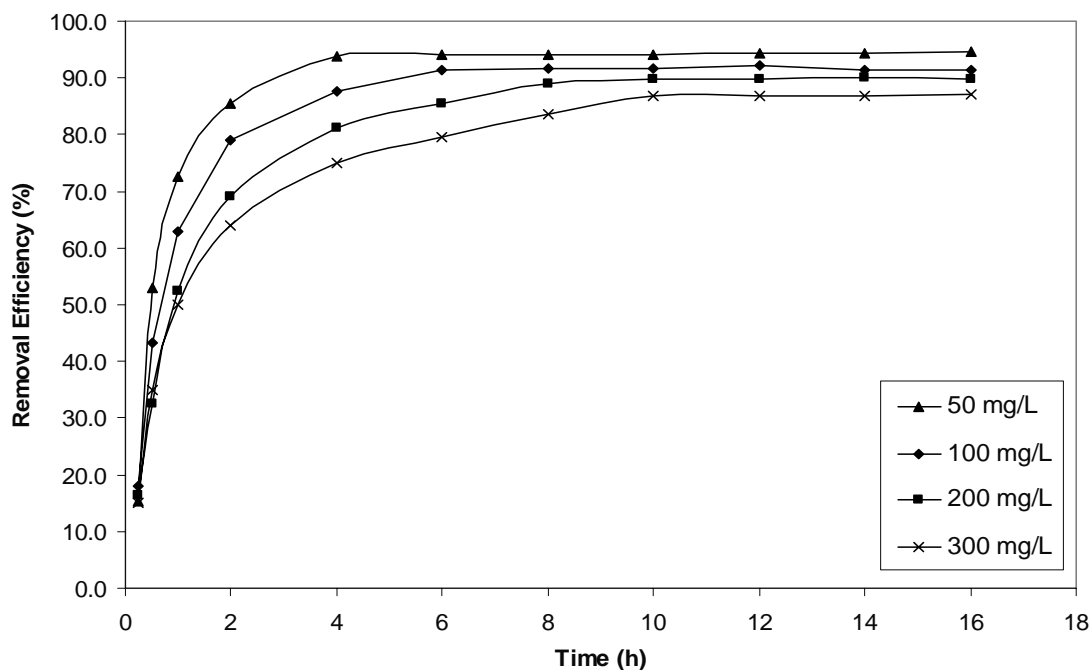


Figure 8 Effect of initial concentration of phosphate ions in the solution on removal efficiency onto Limestone at 20°C, pH 6.

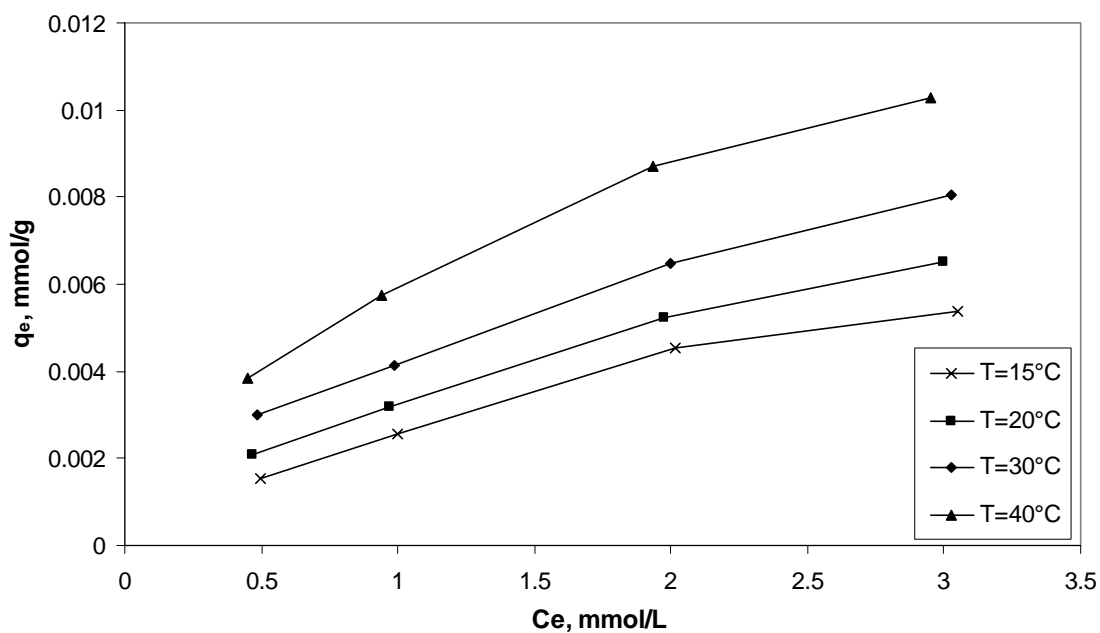


Figure 9 Phosphate adsorption rate at various temperatures using Burned kaolin as adsorbent. (Contact time 10h, dose 10g and pH 6).

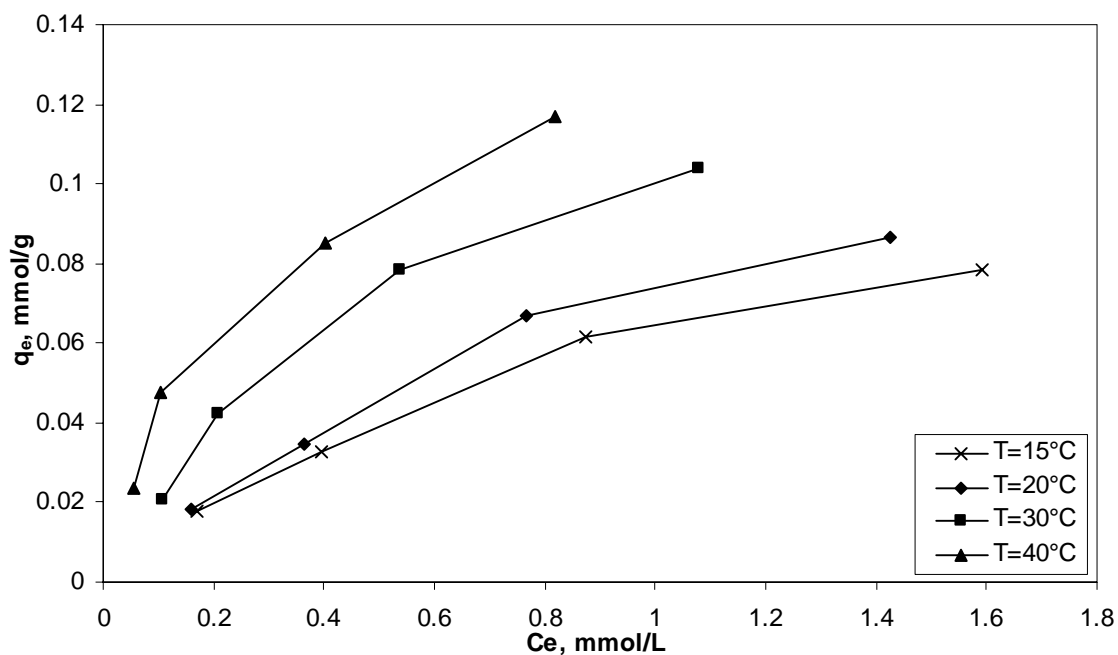


Figure 10 Phosphate adsorption rate at various temperatures using Porcelanite as adsorbent. (Contact time 10h, dose 10g and pH 6).

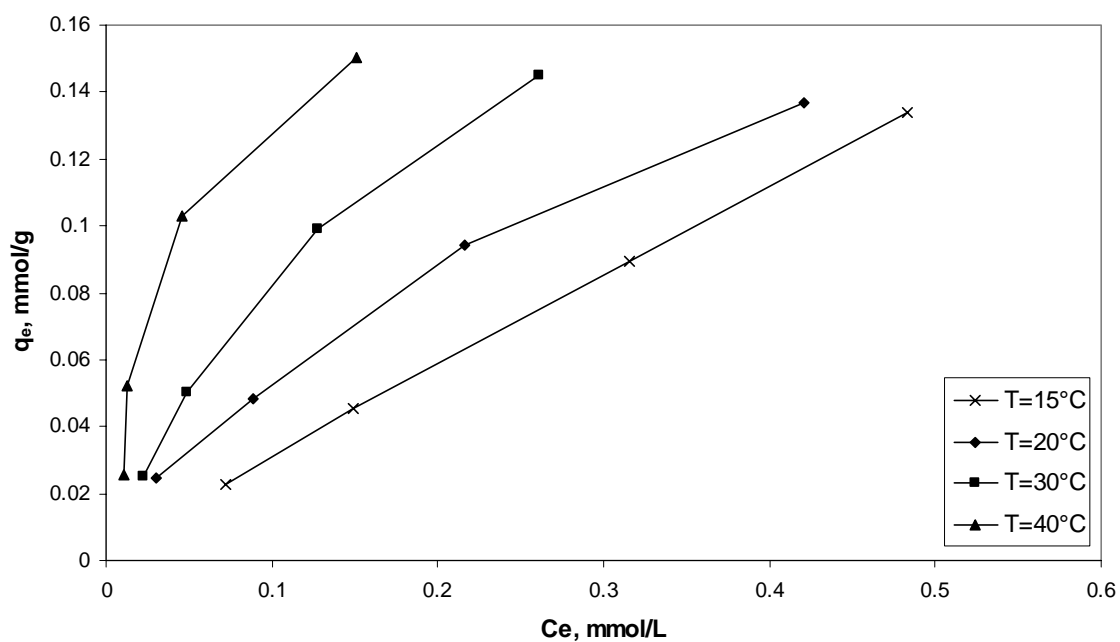


Figure 11 Phosphate adsorption rate at various temperatures using Bauxite as adsorbent. (Contact time 10h, dose 10g and pH 6).

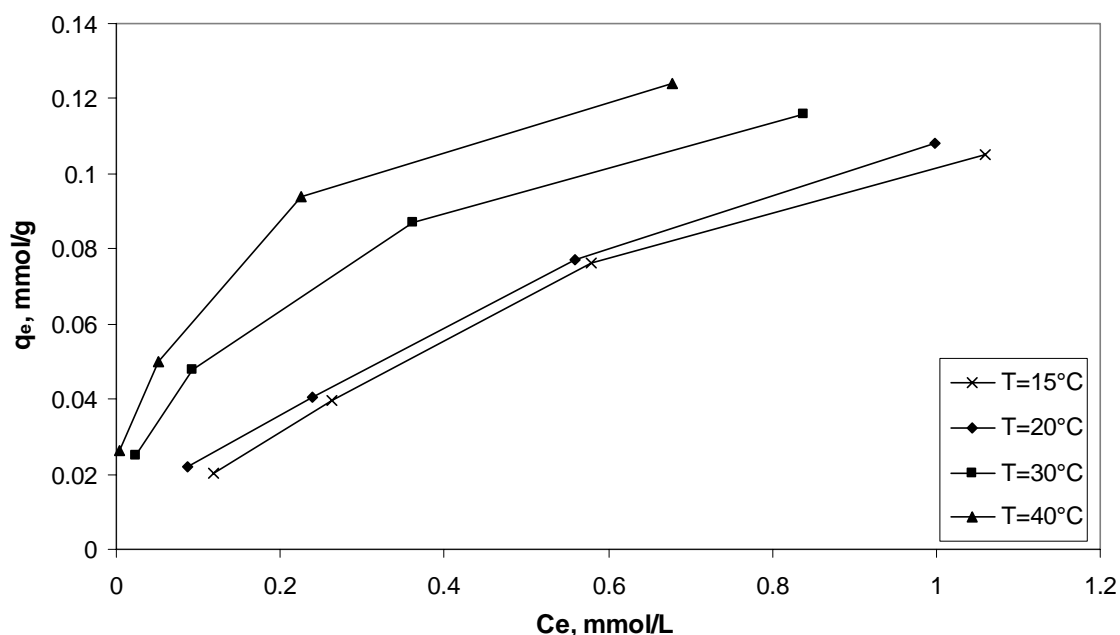


Figure 12 Phosphate adsorption rate at various temperatures using Limestone as adsorbent. (Contact time 10h, dose 10g and pH 6).

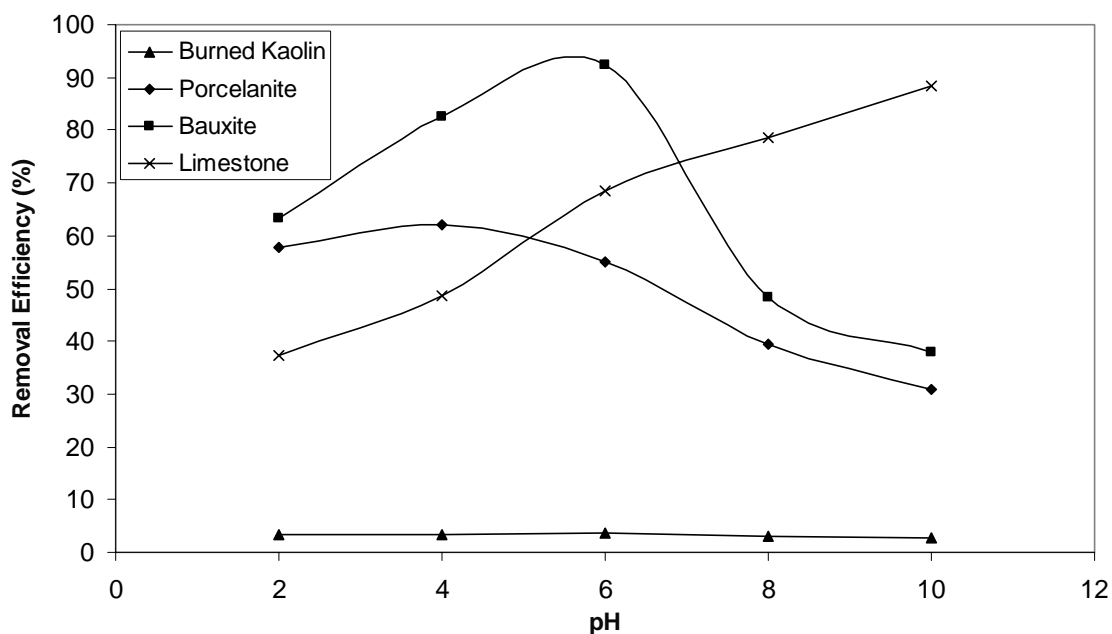


Figure 13 Effect of pH on the adsorption removal efficiency using different adsorption media (initial phosphate concentration 300 mg/l, dose 10g and temperature 20°C and contact time 10 h).





A society development mainly depends on its capability and ability of suitability with the necessary and continuous changing for developed its response with the climatic environment surrounded, and the technology developments take place of direct influence on this understood and an imported positioned to the right direct for our buildings to be in agreement form with the surrounded climatically environment.

()



(693 15 2009)

- :

(77 1985 Bradshaw)

) ()
(

1985 Bradshaw)

(77

(Sensible Heat)

(110 1998 Givoni)

(166 165 1997

)
(
(Latent Heat) (Static Barrier)
(
(

(...) (77 1985 Bradshaw) (Open Structural Frame)
(60 2 2009)

(Thermal Transmittance)



“Labs&Watson)

(1983

—

15 2009)

(702

:

(692 689 15 2009

)

(

...

—:

—

(<http://images.google.com/imgres?imgurl>)

"

"

)

" :

.(

(689-688 15 2009)

(Minimize Heat Loss)

" : ."

Promote Heat)

(Gain

Promote Heat)

()

(Loss

(Minimize Heat Gain)



()

"

(www.biblioislam.net/ar/scholar/card)

(381 234 1986 Rush)

:

(1)

)

(...

- -

(106 46 2007)

:

Visible)

(Integration

1982 Heyne) (360 14-12 1986 Rush) (www.arab-eng.org)

.(549

:(S)

(Tension)

()

:(E)

:Automation (1)

...



(

:(Interior Space System)

Mechanical ()

:System

()

()

()

()

()

(Visible Ducts)

(Duct Work)

)



:()

(+)

:
Menara) :

(Mesiniaga

:_____

– (Subang Jaya) :

(Kenneth Yeang) :

;(417-414 2007 Powell & Yeang)

.(TR Hamzah and Yeang Sdn Bhd)

_____:

.1992 :

. - :

15 (Petronas Towers)
88)

() .(

IBM (International Business

_____:

Machine)

(15)

1950

()

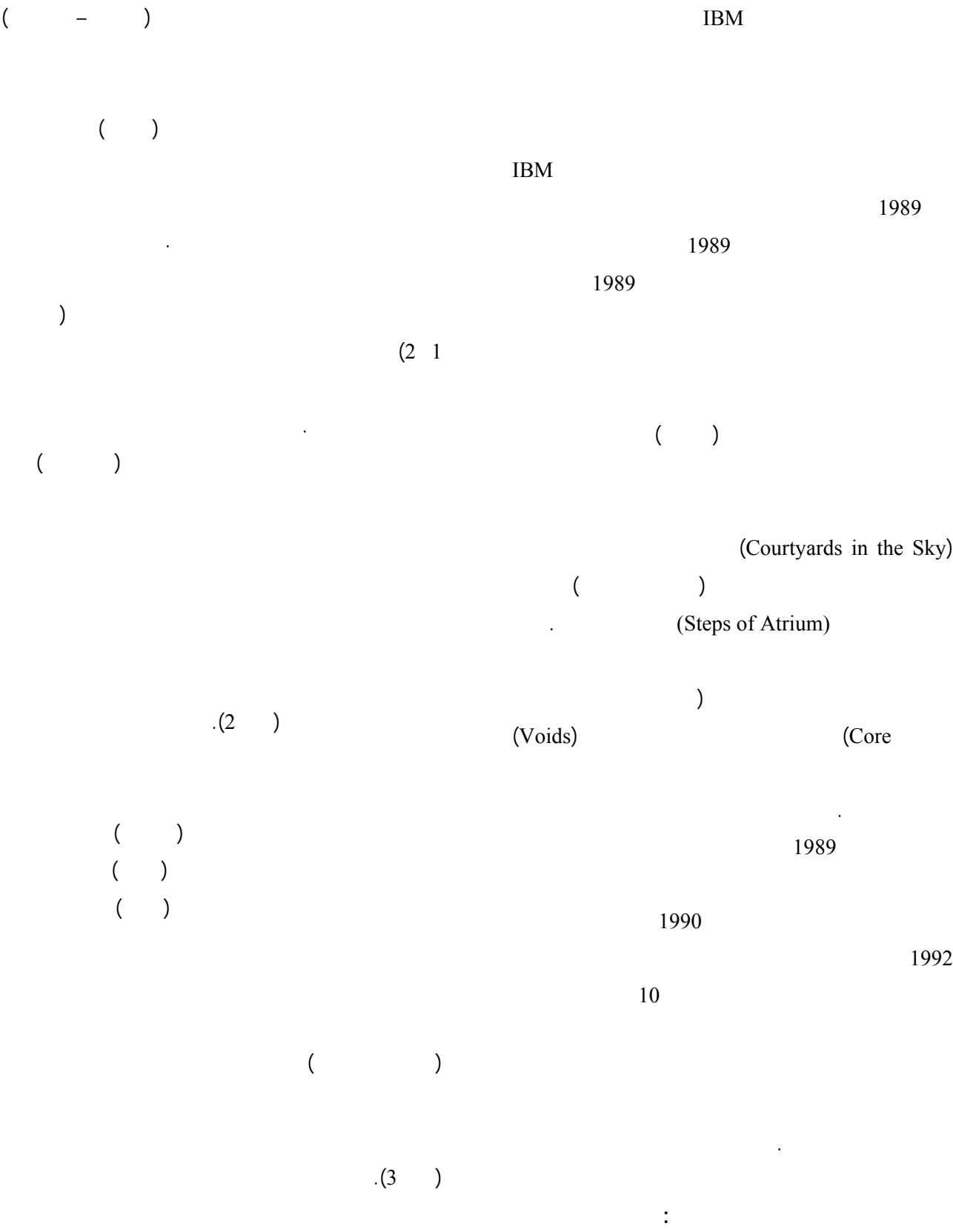
(Bioclimatic Skyscraper)

(Sky Courts)

_____:

(Vertical Landscape)

. 1995





- ()

-. (<http://en.wikipedia.org>) (www.m3mare.com)

(Core)

(Atkins)

2004

.2008

50 :

240 :

()

.(5)

.(4)

Vertical)

(Landscape

50

160

.(6)

.(5)

(1)

(<http://www.yangsquare.com/wp-content/uploads/2008/06/mesiniagaa6.pdf>)
(http://archnet.org/library/sites/one-site.jsp?site_id=1231).

.(7)

(1



55.000

3

.

(1300-1100)

300

(1)

.(8)

:

()

" :

.

.

240

"

.

(225)

(29)

(675)

%3.5

(S)

(45°)

:

-(05/29www.inhabitat.com/2008/)

(Mumbai)

%(15-11)

Mumbai :

James Law Cybertecture International :

2008

:

2009

(1)

.2010

"2008

"

"

.² 4025 :

.² 6676 :

"2008

"

"2008

% 80 =

% 60 =

"2007

EDIE

"

14 =

."2006 LEAF "

3 =



62 =
-: = (Landscape)
2 2800
Cybertecture)
High-) (Egg
(Technology
()
:
() • (Mumbai)
()
(9)
:
(10) (Curtain Wall Exterior)
(13 12 11)
(14)
(Gray Water)
(Cybertecture Egg)



(17 2009) (2)() (1) •

(Cybertecture Egg)

/ 5.5 . / 5.0 •

(60)
10

) (•

(1789)
(<http://www.iraqitimesmg.com/news.php?>)
•

(Renewable Energy)

—

1997 (2) (1)
(4.8) 2000
(17 2009) 2 (200)



•

•

•

•

)
(

)
(

•

•
—

•

—

•

•
•

•

•

•

•

•

•

"

"

/4 /7 – 5

—

—

2009

—

.2

"

•

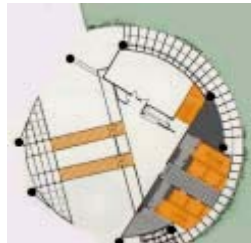
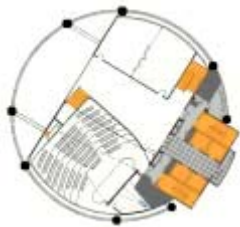
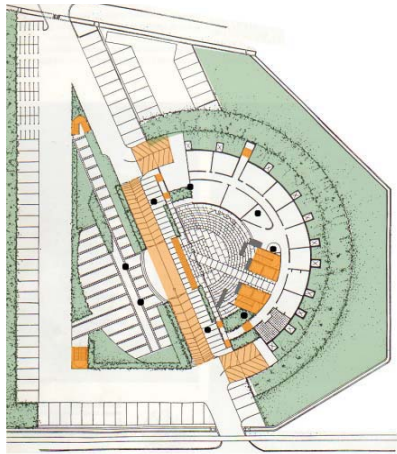
- Yeang & Powell, Ken, Pobert, "Designing the Eco-Skyscraper: Premises for Tall Building Design", structural design tall build, 10, 411-427, Wiley Interscience, 2007.

- http://archnet.org/library/sites/one-site.jsp?site_id=1231
- http://en.wikiarquitectura.com/index.php?title=Bahrain_World_Trade_Center
- http://en.wikipedia.org/wiki/Bahrain_World_Trade_Center
- <http://images.google.com/imgres?imgurl>
- http://jetsongreen.typepad.com/jetson_green/2006/11/skyscraper_sund_3.html
- http://www.akdn.org/architecture/pdf/1356_Mal.pdf
- <http://www.arab-eng.org/vb/>
- <http://www.biblioislam.net/ar/scholar/card>
- <http://www.designboom.com/weblog/cat/9/view/2984/james-law-cybertecture-international-egg-building-mumbai.html>
- <http://www.iraqitimesmg.com/news.php?readmore=130>
- <http://www.m3mare.com/vb/showthread.php?7060>
- <http://www.nbmcw.com/articles/architects-a-project-watch/612-the-cybertecture-egg-new-jewel-in-mumbai.html>
- <http://www.solaripedia.com/files/721.pdf>
- <http://www.yangsquare.com/wp-content/uploads/2008/06/mesiniagaa6.pdf>
- www.inhabitat.com/2008/05/29

- " - .2007
- " " . 1997
- " " . 2009 15 2
- " - 2009 /4 /7 - 5 .2
- Bradshaw, Vaughn, "Building Control System", John Wiley & Sons, 1985.
- Girardet, Herbert, "The Architecture of Ecology", Academy Editions Press, London, 1998.
- Givoni, Baruch, "Climate Consideration in Building and Urban Design", Van Nostrand Reinhold, U. S. A., 1998.
- Heyne, Pamela, "Today's Architecture Mirror", (Interior, Buildings, and Solar Designs), Van Nostrand Reinhold, New York, 1982.
- Rush, Richard D., "Building System Integration Handbook", Canada, 1986.
- Salvadori, Mario and Heller Robert, "Structure in Architecture", Prentic Hall, INC., Englewood Cliffs, New Jersey, 1975.
- Watson, Donald, FAIA & Labs, Kenneth, "Climatic Design", Mc Graw-Hill Book Company, 1983.

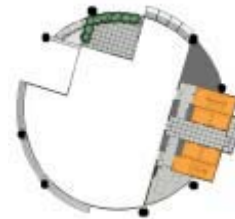
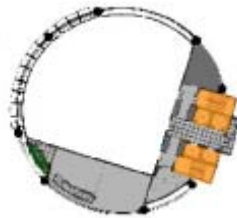
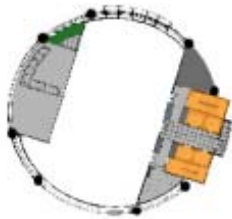


. : (1)
http://www.yangsquare :
.com/wp-content/uploads/
2008/06/mesiniagaa6.pdf



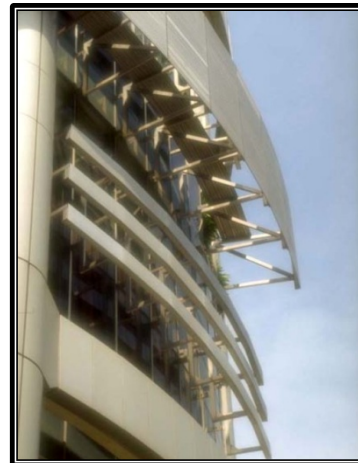
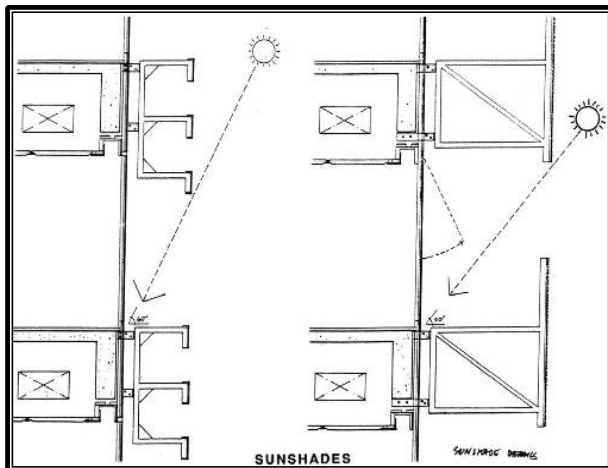
(Mezzanine)

- Circulation
- Service Spaces
- Exterior Spaces
- Green Spaces
- Steel Tubes



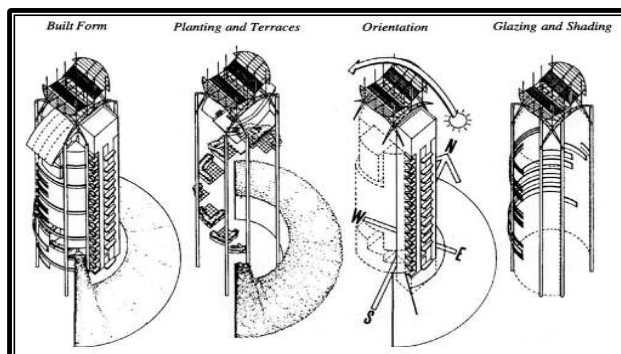
:(2)

<http://www.solaripedia.com/files/721.pdf>:



:(3)

http://www.akdn.org/architecture/pdf/1356_Mal.pdf :



:(5)

.(
http://jetsongreen.typepad.com/jetson_green/2006/11/skyscraper_sund_3.html

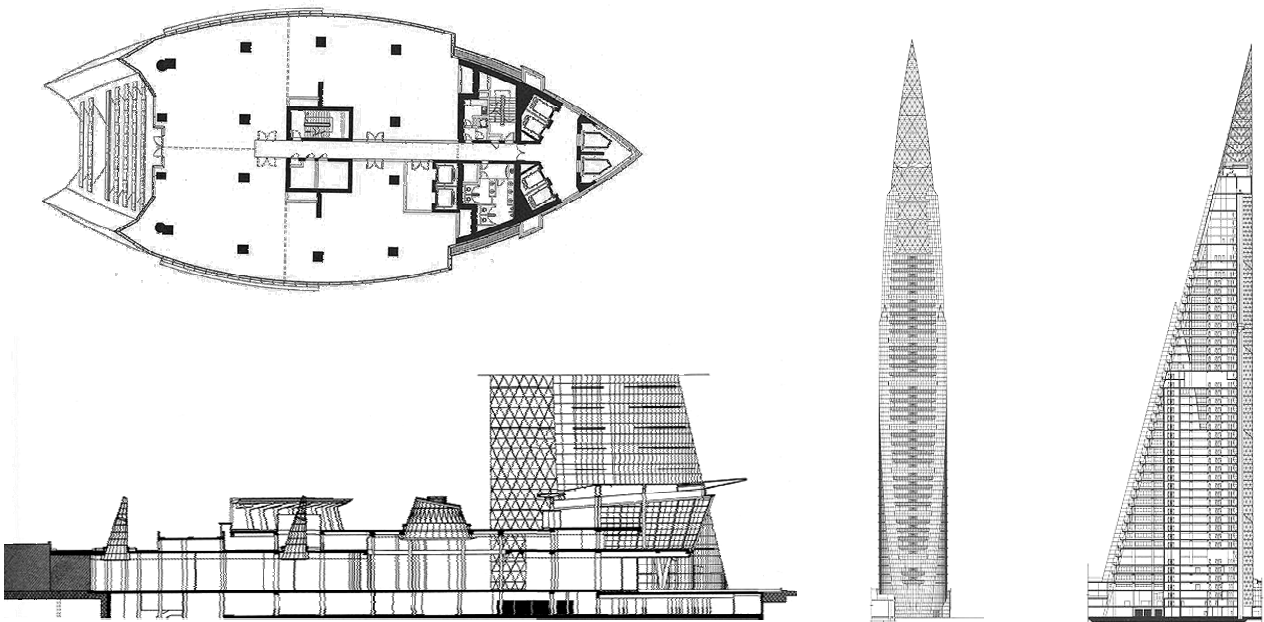
:(4)

http://www.akdn.org/pdf/1356_Mal.pdf architecture/



:(5)

www.m3mare.com :



:(6)

http://en.wikiarquitectura.com/index.php?title=Bahrain_World_Trade_Center :



:(7)

<http://en.wikipedia.org> :



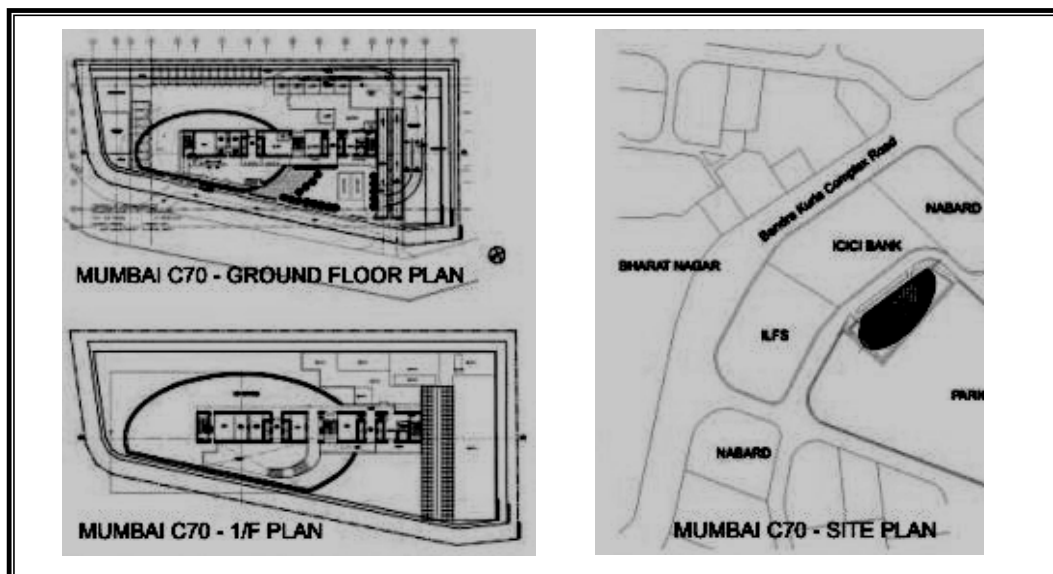
(8)

http://en.wikipedia.org/wiki/Bahrain_World_Trade_Center :



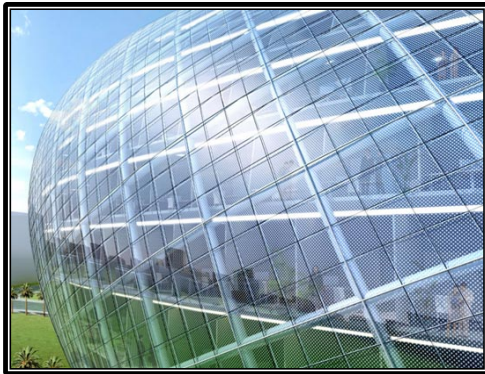
(9)

05/29www.inhabitat.com/2008/ :



(10)

<http://www.nbmcw.com/articles/architects-a-project-watch/612-the-cybertecture-egg-new-jewel-in-mumbai.html>



(12)

05/29www.inhabitat.com/2008/ :

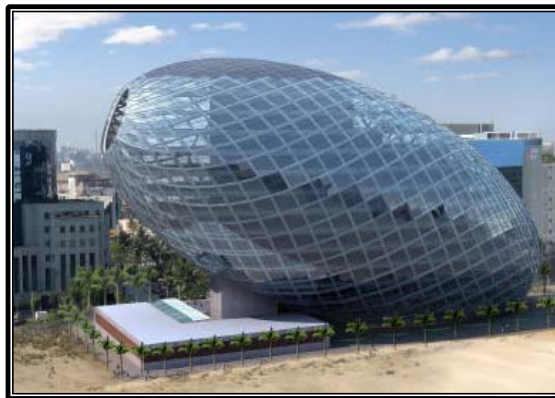


(11)

05/29www.inhabitat.com/2008/ :

(13)

<http://www.designboom.com/weblog/cat/9/view/2984/james-law-cybertecture-international-egg-building-mumbai.html>



(14)

05/29www.inhabitat.com/2008/ :